https://www.sciltp.com/journals/mi
Online ISSN: 2982-2394
Volume 3, Issue 1, 2026

Materials and Interfaces

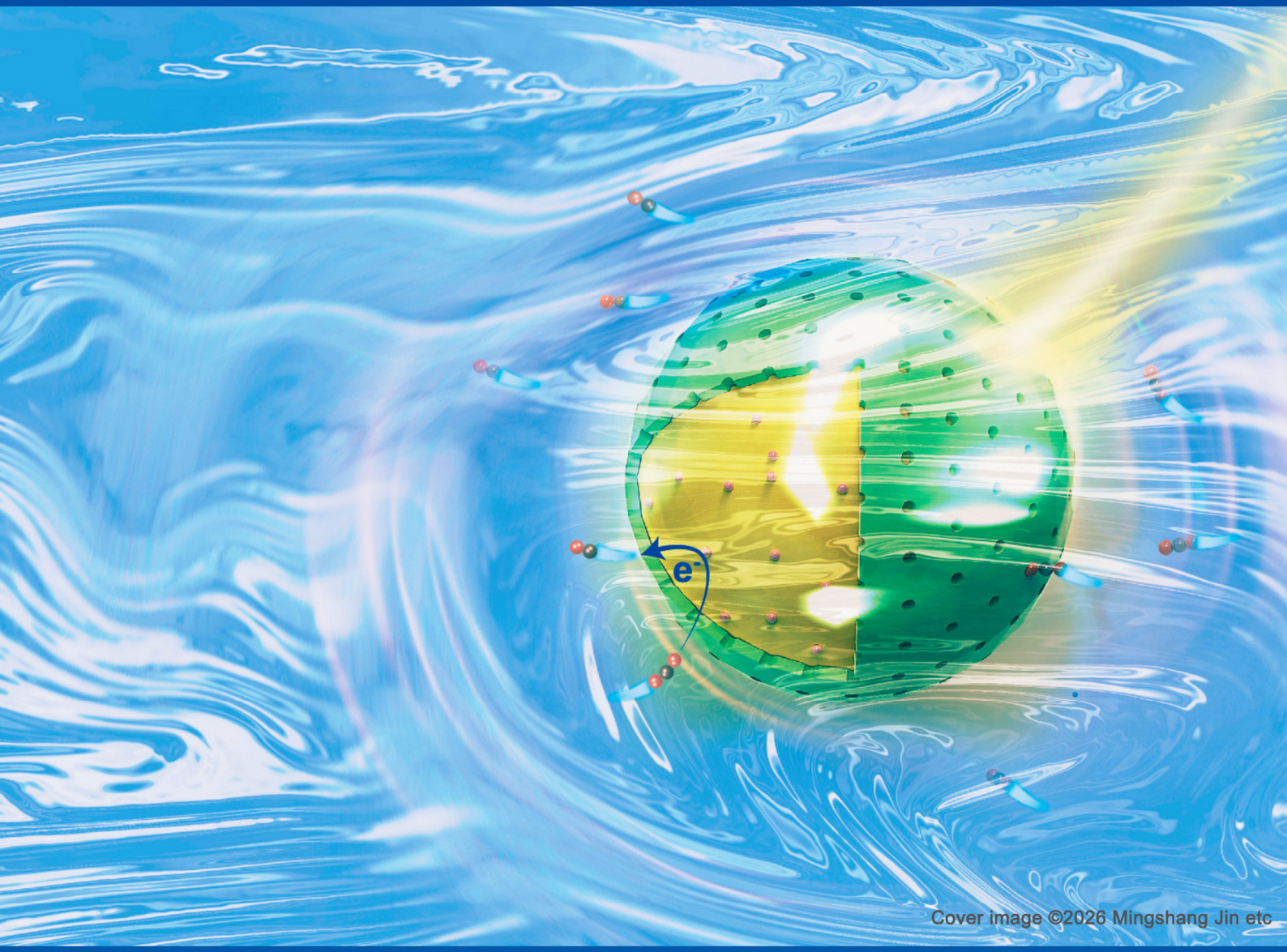

Encapsulation in Porous SiO_2 for Selective Suppression of Hydrogen Evolution in Photocatalytic CO_2 Reduction

Scilight

Contents

Vol. 3 No. 1, March 2026

Article

Encapsulation in Porous SiO_2 for Selective Suppression of Hydrogen Evolution in Photocatalytic CO_2 Reduction

Junhao Lu [1], Yanan Li [1,2,3], Yiduo Wang [1], Qingqing Guan [1], Zixing Ge [1,2,3], Yuan Ren [1,2,3], Yaohui Zhao [1,2,3], Qian Wang [1], and Mingshang Jin [1,2,3,*]

[1] State Key Laboratory of Multiphase Flow in Power Engineering, Xi'an Jiaotong University, Xi'an 710049, China
[2] Frontier Institute of Science and Technology, Xi'an Jiaotong University, Xi'an 710049, China
[3] Interdisciplinary Research Center of Frontier Science and Technology, Xi'an Jiaotong University, Xi'an 710049, China
* Correspondence: jinm@mail.xjtu.edu.cn
Received: 3 December 2025; Revised: 2 February 2026; Accepted: 9 February 2026; Published: 25 February 2026

Abstract: Photocatalytic carbon dioxide reduction reaction (CO_2RR) represents a promising route for sustainable energy conversion. However, in conventional solid-liquid-gas reaction systems, inefficient CO_2 diffusion to the catalyst surface often leads to dominant hydrogen evolution reaction (HER), limiting CO_2 conversion efficiency and product selectivity. Herein, we propose a catalyst encapsulation strategy using porous silicon dioxide (SiO_2) to spatially control molecular transport toward the active sites. By encapsulating Ag-modified titanium dioxide within a porous SiO_2 layer, we effectively restrict water access to the catalytic interface while facilitating CO_2 permeation. As a result, the parasitic HER is significantly suppressed, enabling an exceptional 100% selectivity for CO production from photocatalytic CO_2 reduction in pure water, which is a dramatic improvement from the mere 5.9% CO selectivity of the unencapsulated Ag-TiO_2 catalyst. This design achieves near-complete suppression of HER and 100% selectivity toward CO production under photocatalytic conditions. Our work provides a versatile interfacial engineering approach to overcome mass transfer limitations in three-phase photocatalytic systems, opening avenues for efficient gas-involving photoreactions.

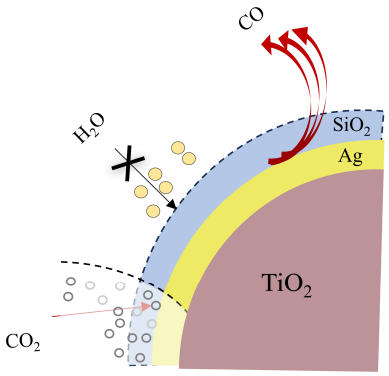

Keywords: CO_2RR; SiO_2 shell; core-shell; HER suppression; interface engineering

1. Introduction

With the rapid development of industry and economy globally, the massive consumption of finite fossil fuels has led to severe environmental issues, notably the greenhouse effect driven by rising atmospheric CO_2 levels [1–4]. In this context, photocatalytic CO_2 reduction reaction (CO_2RR) stands out as a promising strategy for converting solar energy into sustainable fuels, often regarded as the "holy grail" of energy conversion [5–8]. From the perspectives of sustainability and environmental friendliness, using water as the hydrogen source for CO_2RR is highly desirable [9,10]. However, a significant challenge persists in aqueous-phase photocatalytic CO_2RR, which is the severe competition from the hydrogen evolution reaction (HER) [11,12]. In typical aqueous reaction systems, HER tends to dominate over CO_2RR, primarily due to the kinetically more favorable proton reduction pathway. This fierce competition results in unsatisfactory selectivity for carbon-based products and low CO_2RR efficiency in most cases [13,14].

Although substantial efforts have been devoted to enhancing CO_2RR performance through catalyst design, such as developing novel semiconductors, morphology control, doping, and constructing heterojunctions [5,15–19], these strategies often focus on modifying the intrinsic electronic structure of the catalysts. For instance, Sun et al. designed an N, S-codoped Fe-based MIL-88B catalyst with a well-defined bipyramidal hexagonal prism morphology, achieving a high C_2H_4 yield of 17.7 μmol g^{-1} h^{-1} [20]. Meanwhile, Wang et al. anchored Ag single atoms on hollow porous polygonal C_3N_4 nanotubes to form a photocatalyst, showing up to 94% CO selectivity [21]. Despite these advances, effectively suppressing the competing HER to achieve near-unity product selectivity remains a critical and unresolved issue.

Recent studies have highlighted that the interfacial microenvironment of the catalyst plays a decisive role in governing the reaction pathway [22]. The simultaneous presence of water molecules and CO_2 reactants at the catalyst surface creates a direct competition between HER and CO_2RR [23]. Therefore, precisely controlling the transport of key molecules (H_2O and CO_2) to the active sites is crucial for steering the selectivity. Conventional approaches, such as employing organic hole scavengers, can alter the reaction microenvironment but introduce problems like high cost, toxicity, and compromised sustainability [24,25].

To address the fundamental challenge of HER dominance, we propose an interfacial engineering strategy centered on selectively inhibiting the access of water to the catalytic active sites. Herein, we demonstrate a porous silicon dioxide (SiO_2) encapsulation layer coated on Ag-loaded TiO_2 photocatalysts (Ag-TiO_2@SiO_2). This design does not aim to enhance CO_2 diffusion but rather to create a localized hydrophobic microenvironment that preferentially restricts the migration of water molecules to the reaction interface while allowing CO_2 permeation. As a result, the parasitic HER is significantly suppressed, enabling an exceptional 100% selectivity for CO production from photocatalytic CO_2 reduction in pure water, which is a dramatic improvement from the mere 5.9% CO selectivity of the unencapsulated Ag-TiO_2 catalyst. This work provides a distinct and effective solution to the selectivity challenge by managing the interfacial reactant supply, opening new avenues for optimizing various multiphase photocatalytic processes.

2. Experimental Section

2.1. Materials and Methods

All chemicals were of analytical grade and used without further. TiO_2 nanoparticles (P25, Degussa, Germany) were used as the photocatalyst. $AgNO_3$ (99.8%), acetone (99.9%), ethanol (95%), tetraethyl orthosilicate (TEOS) and ammonia aqueous solution (28%) were purchased from Sinopharm Chemical Reagent Co. (Shanghai, China). Hexadecyl trimethyl ammonium Bromide (CTAB) was purchased from Shanghai Aladdin Biochemical Technology Co. (Shanghai, China). Deionized water (H_2O, 18.25 MΩ·cm) supplied by an UP-Water Purification System was used in the whole experimental process.

2.1.1. Synthesis of Ag-TiO_2

Ag nanoparticles were loaded onto the surface of TiO_2 to form Ag-TiO_2 nanoparticles using a photo-loading method. Water, methanol, and $AgNO_3$ were used as solvent, holes sacrificial agent, and Ag source, respectively. For the preparation of Ag-TiO_2, 0.2 g TiO_2 was dispersed in an aqueous solution containing 40 mL H_2O and 10 mL ethanol under sonication. Then, 0.5 mL $AgNO_3$ aqueous solution (50 mM) was added with vigorous stirring and continuously bubbled using high purity Ar gas for 30 min. Subsequently, the mixture was moved to a sealed transparent container and irradiated under a 300 W xenon lamp (Beijing China Education Au-light Co., Ltd. CEL-HXF300-T3) for 60 min. The as-prepared Ag-TiO_2 nanoparticles were separated by centrifugation and washed three times with water, and dried at 60 °C overnight.

2.1.2. Synthesis of Ag-TiO_2@SiO_2

The Ag-TiO_2@SiO_2 particles were prepared according to Stöber method. In a typical procedure, 100 mg Ag-TiO_2 and 300 mg CTAB were dispersed in the mixture of ethanol (80 mL) and water (20 mL) and 1 mL of ammonia aqueous solution (28 wt%) under stirring for 30 min, then 200 μL of TEOS was added slowly with continuous stirring for 2 h. The particles were collected by centrifugation and washed with ethanol and water, respectively. The CTAB surfactant was removed by solvent extraction method using 120 mL of acetone solution and refluxed at 80 °C for 48 h. This extraction process was repeated three times. After centrifugating and washing with ethanol and water, the Ag-TiO_2@SiO_2-2 core-shell nanocarriers were obtained. By altering the amount of TEOS to 50 μL or 400 μL, Ag-TiO_2@SiO_2-1 and Ag-TiO_2@SiO_2-3 were obtained. Ag-TiO_2@SiO_2-2 is commonly abbreviated as Ag-TiO_2@SiO_2.

2.1.3. Synthesis of Ag-TiO_2@D-SiO_2

In a typical procedure, 100 mg Ag-TiO_2 were dispersed in the mixture of ethanol (80 mL) and water (20 mL) and 1 mL of ammonia aqueous solution (28 wt%) under stirring for 30 min, then 200 μL of TEOS was added slowly with continuous stirring for 2 h. The particles were collected by centrifugation and washed with ethanol and water, the Ag-TiO_2@D-SiO_2 core-shell nanocarriers were obtained.

2.1.4. Synthesis of SiO_2

In a typical procedure, 300 mg CTAB were dispersed in the mixture of ethanol (80 mL) and water (20 mL) and 1 mL of ammonia aqueous solution (28 wt%) under stirring for 30 min, then 200 μL of TEOS was added slowly with continuous stirring for 2 h. The particles were collected by centrifugation and washed with ethanol and water, respectively.

2.1.5. Synthesis of Ag-TiO_2-CTAB

In a typical procedure, 100 mg Ag-TiO_2 and 300 mg CTAB were dispersed in the mixture of ethanol (80 mL) and water (20 mL) and 1 mL of ammonia aqueous solution (28 wt%) under stirring for 2 h, The particles were collected by centrifugation and washed with ethanol and water, respectively.

2.1.6. Synthesis of Ag-TiO_2@SiO_2-NaOH

Ag-TiO_2@SiO_2-NaOH were prepared by etching Ag-TiO_2@SiO_2 in 10 mL of 2 M NaOH solution at 80 ℃ for 1 h.

2.2. Characterization

High-resolution TEM (HRTEM) images, high-angle annular dark-field scanning transmission microscopy (HAADF-STEM) images, and energy-dispersive X-ray spectroscopy (EDS) elemental mappings and line scans were performed on a JEM-F200 microscope equipped with a built-in EDS operated at 200 kV. The powder X-ray diffraction (PXRD) patterns were obtained on a Rigaku SmartLab, using Cu Kα (λ = 0.15406 nm) radiation. Textural properties of the catalysts were measured by N_2 physisorption at -196 °C on Micromeritics ASAP 2460 instrument. X-ray photoelectron spectroscopy (XPS) was conducted using a Thermo Fisher ESCALAB Xi+ spectrometer equipped with monochromatic Al Kα radiations. The Ag 3d, Ti 2p, O 1s and Si 2p peaks, as well as the valence bands, were corrected using the C 1s contamination peak (284.8 eV) as a reference. The content of Ag of the samples were determined by inductively coupled plasma mass spectrometry (ICP-MS), using a PerkinElmer NexION 350D (Waltham, MA, USA). Water-droplet contact angle tests were performed on the JY-82B contact angle goniometer. An Intrinsic DVS instrument from Surface Measurement Systems was used to perform the water vapor adsorption and desorption experiments over a humidity range of 0 ~ 95%. Each humidity step was made if less than a 0.002% weight change occurred over 10 min, with a maximum hold time of 240 min.

2.3. Photocatalytic CO_2RR Measurements

The photocatalytic CO_2 reduction measurements were carried out in a sealed reaction system. A 300 W Xe lamp (Beijing China Education Au-light Co., Ltd. CEL-HXF300-T3) was used as the light source providing a full spectrum illumination. In the photocatalytic process, 5 mg catalyst powder and 20 mL water were placed in a quartz reactor with a window area of 16 cm^2 and a volume of 130 mL. Before reaction, the reactor was purged with high purity CO_2 (99.999%) for 30 min. During the reaction, the reactor was placed on a magnetic stirrer, and the stirring speed was set at 800 rpm. The reaction temperature is controlled at 25 °C with a water circulator. Reaction was stopped after 4 h. The gas products were quantitatively analyzed by a gas chromatograph (SHIMANZU GC-2014) equipped with flame ionization detector (FID) and thermal conductivity detector (TCD).

The isotope-labeling experiments were carried out under the same experimental conditions, except that $^{12}CO_2$ was replaced with $^{13}CO_2$. The ^{13}C-labeled products were analyzed using a gas chromatograph-mass spectrometer (GC-MS, Agilent 5977B GC/MSD). In cycling measurements, the catalyst was washed with ultrapure water to remove surface adsorbates before each reaction cycle. In this work the selectivity of catalyst for CO_2 reduction to acetate was calculated by following equation:

$$\textit{Selectivity}\ (\%) = n(CO)/[n(H_2) + n(CO) + n(CH_4) + n(C_2H_4)] \times 100\%$$

where, $n(H_2)$, $n(CO)$, $n(CH_4)$ and $n(C_2H_4)$ are the mole amounts of produced H_2, CO, CH_4 and C_2H_4, respectively.

3. Results and Discussion

The core-shell structured Ag-TiO_2@SiO_2 photocatalyst was synthesized via a two-step procedure, as illustrated in Figure 1a. Initially, Ag nanoparticles were deposited on the surface of TiO_2 through a photo-deposition process to form Ag-TiO_2 nanoparticles (Figure S1) [26]. Subsequently, a porous SiO_2 shell was encapsulated onto the Ag-TiO_2 nanoparticles using the Stöber method [27]. This rational design aims to selectively control the transport of reactant molecules (H_2O and CO_2) to the active sites by creating a physical barrier, thereby

addressing the critical issue of HER competing with CO_2RR in the three-phase photocatalytic system. The X-ray diffraction (XRD) patterns (Figure 1b) of both Ag-TiO_2 and Ag-TiO_2@SiO_2 are identical to that of the pristine TiO_2, showing a mixed phase of anatase and rutile. The absence of distinct Ag diffraction peaks is attributed to its low loading and high dispersion [28]. Transmission electron microscopy (TEM) images (Figure 1c) confirmed the successful encapsulation of Ag-TiO_2 nanoparticles by a uniform SiO_2 shell, typically 5-15 nm thick. High-resolution TEM (HRTEM) analysis (Figures 1d and S2) reveals lattice fringes of 0.352 nm and 0.236 nm, corresponding to the (101) plane of anatase TiO_2 and (111) plane of metallic Ag, respectively. Energy-dispersive X-ray spectroscopy (EDS) mapping (Figure 1e) further verifies the core-shell structure, showing a homogeneous distribution of Ag, Ti, and O elements in the core, while the Si signal forms a distinct shell surrounding the core.

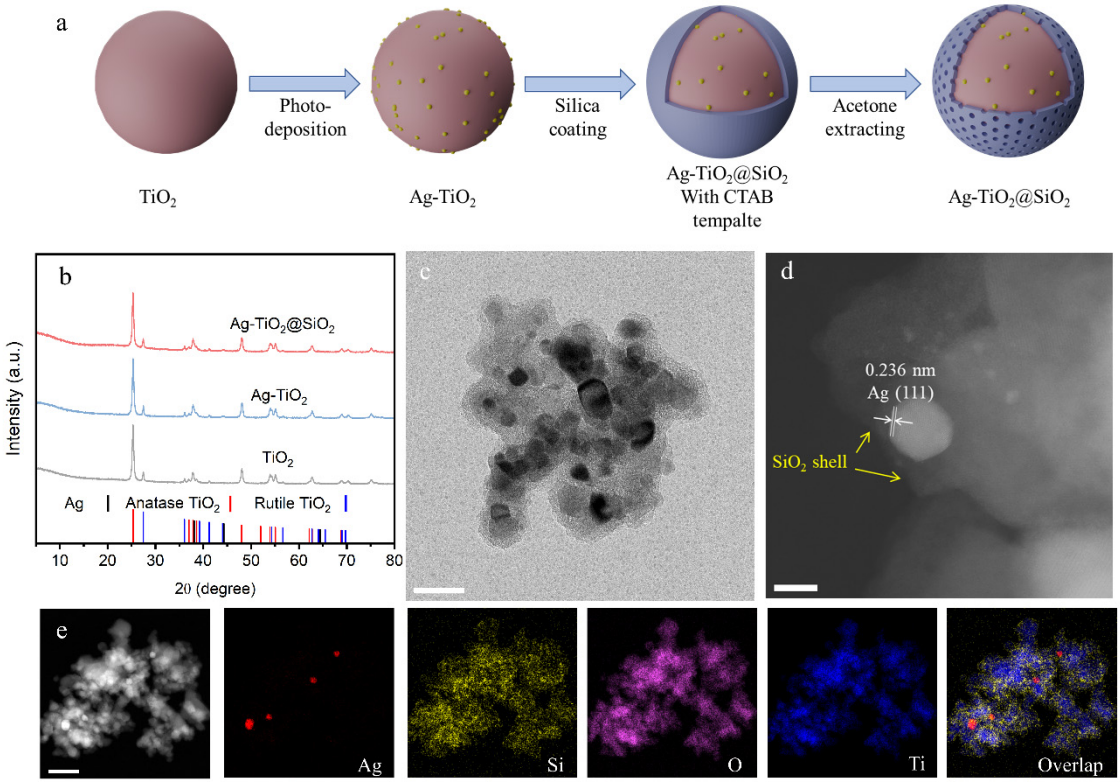

Figure 1. (**a**) Schematic illustration of the formation of Ag-TiO_2@SiO_2. (**b**) XRD patterns of TiO_2, Ag-TiO_2 and Ag-TiO_2@SiO_2. (**c**)TEM image of Ag-TiO_2@SiO_2, scale bars: 50 nm. (**d**) HRTEM image of Ag-TiO_2@SiO_2, scale bars: 5 nm. (**e**) STEM image of Ag-TiO_2@SiO_2 and corresponding element mapping (Ag, Si, O, and Ti), scale bars: 100 nm.

The chemical structures of the Ag-TiO_2 and Ag-TiO_2@SiO_2 nanoparticles were further examined by Fourier transform infrared (FTIR) spectroscopy. As shown in Figure 2a, the FTIR spectra offer clear evidence of functional groups and chemical bonds present in both samples. In each spectrum, the peak at 409 cm^{-1} is associated with the Ti-O-Ti vibration of the TiO_2 crystal framework, confirming its presence as the primary component [29]. Additional peaks at 3445 cm^{-1} and 1632 cm^{-1} correspond to the O-H stretching and bending vibrations, respectively, indicating the presence of adsorbed water molecules on the nanoparticle surfaces. Notably, the Ag-TiO_2@SiO_2 sample exhibits a distinct peak at 1072 cm^{-1}, which is characteristic of the asymmetric stretching vibration of Si-O-Si bonds, confirming the successful formation of a SiO_2 shell. Also observable in the Ag-TiO_2@SiO_2 spectrum are several peaks associated with the structure-directing agent CTAB, including the C-N stretching vibration at 1481 cm^{-1} and the -CH_2- rocking vibrations at 2922 cm^{-1} and 2852 cm^{-1} [27]. The presence of these organic residues suggests that CTAB is incorporated into the SiO_2 shell, which likely influences the material's final porosity and surface properties, which is crucial for forming the porous and hydrophobic shell.

X-ray photoelectron spectroscopy (XPS) was further conducted to probe the surface chemical states and elemental composition of Ag-TiO_2 and Ag-TiO_2@SiO_2 nanoparticles. As illustrated in Figure 2b, the XPS survey spectrum of Ag-TiO_2 exhibits distinct photoelectron peaks corresponding to Ag and Ti, indicating the presence of both metallic Ag and TiO_2 on the surface. In contrast, the survey spectrum of Ag-TiO_2@SiO_2 shows a substantial attenuation of the Ag and Ti signals, while new and prominent peaks corresponding to Si are observed (Figure S3). This marked decrease in signal intensity from the underlying Ag-TiO_2 core, coupled with the emergence of Si-related peaks, provides strong evidence

for the formation of a continuous and conformal SiO_2 shell layer coating the surface, which effectively shields the photoelectrons emitted from the core material, which is consistent with the TEM observations.

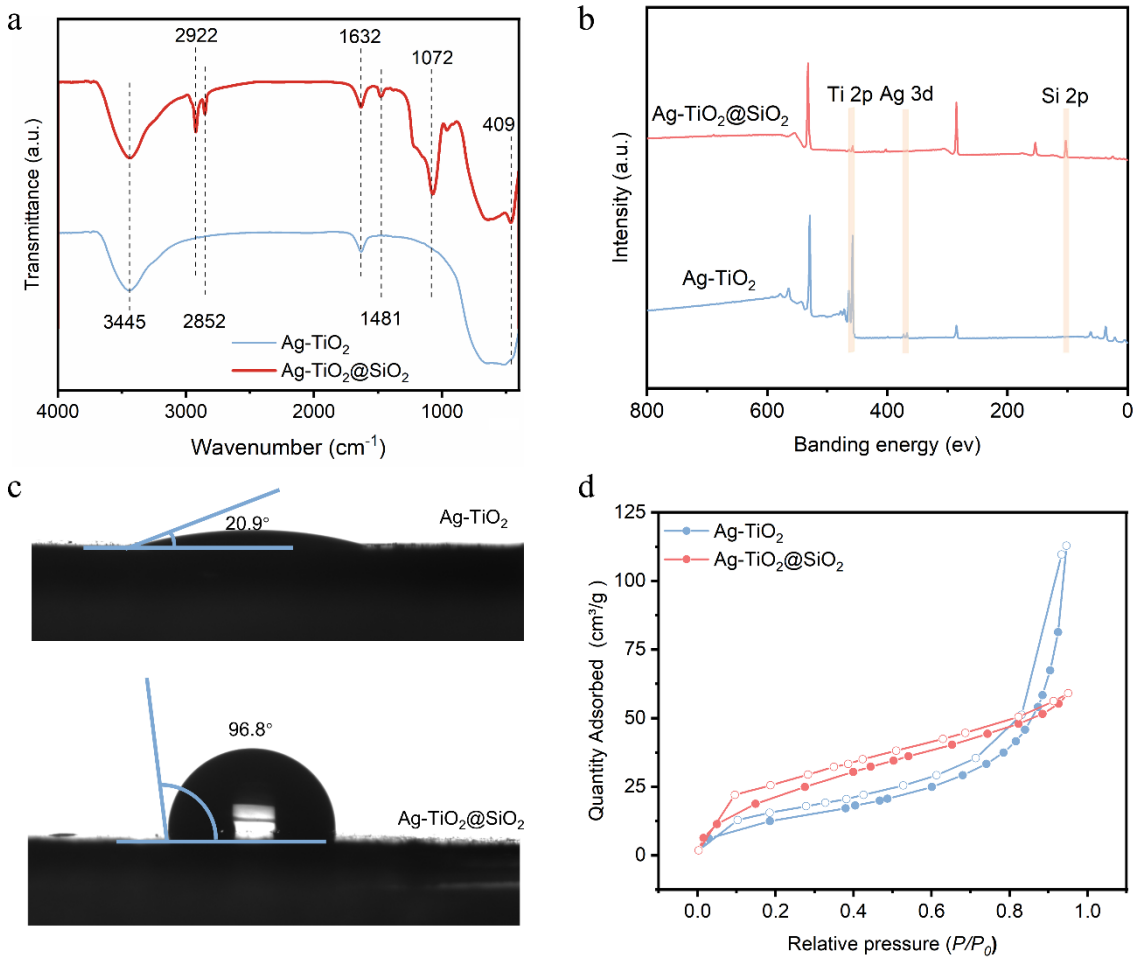

Figure 2. (**a**) FTIR spectra of Ag-TiO_2 and Ag-TiO_2@SiO_2, (**b**) XPS spectra of Ag-TiO_2 and Ag-TiO_2@SiO_2. (**c**) Water-droplet contact angle tests. (**d**) The water vapor adsorption and desorption tests of Ag-TiO_2 and Ag-TiO_2@SiO_2.

To validate the role of the SiO_2 shell in modulating the interfacial microenvironment, we systematically characterized the surface physicochemical properties. Water contact angle measurements (Figure 2c) revealed that the pristine Ag-TiO_2 surface is hydrophilic (contact angle of 20.9°). In stark contrast, the Ag-TiO_2@SiO_2 surface exhibited a significantly increased contact angle of 96.8°, demonstrating that the SiO_2 coating effectively enhanced surface hydrophobicity. This property is pivotal for inhibiting the migration of water molecules to the active interface. Specific surface area and pore size distribution analyses (Figure S4) indicated that Ag-TiO_2 and Ag-TiO_2@SiO_2 possess comparable specific surface areas. However, notable differences were observed in their pore size distributions. Ag-TiO_2 exhibited a broad distribution of micropores, mesopores, and macropores. In contrast, Ag-TiO_2@SiO_2 showed a relatively narrower distribution, primarily centered on micropores and small mesopores with a pronounced peak at 3.6 nm, which is characteristic of the mesopores within the SiO_2 shell. This tailored porosity is expected to facilitate the diffusion of CO_2 gas while imposing mass transfer resistance for water molecules. The isothermal water adsorption curves (Figure 2d) strongly support this inference that Ag-TiO_2@SiO_2 exhibited inferior water adsorption capacity, especially in the high relative pressure region, compared to Ag-TiO_2. This can be directly attributed to its hydrophobic surface and mesoporous-dominated structure, which collectively suppress water accumulation on the catalyst surface.

Based on the structural characterization, the photocatalytic CO_2 reduction performance of the as-prepared samples was systematically evaluated in aqueous medium without any sacrificial agent. The reactions were carried out under irradiation from a 300 W xenon lamp, and the gas products were quantified using gas chromatography (GC). As shown in Figure 3a, no reaction products were detected for the exposed SiO_2 nanoparticles (Figure S5), owing to their inherent insulating properties, the unmodified Ag-TiO_2 exhibited strong hydrogen evolution activity with only 5.9% selectivity toward CO, while producing minor amounts of CH_4 and C_2H_4, consistent with its hydrophilic surface property that favors water adsorption and proton reduction. In contrast, after encapsulation

with a porous SiO_2 shell, Ag-TiO_2@SiO_2 achieved 100% selectivity for CO, with H_2 evolution being completely suppressed. The hydrophobic micropores within the CTAB-templated SiO_2 shell create a locally hydrogen-deficient environment, which significantly lowers the surface concentration of reactive H species. As a result, the CO* intermediate formed on the Ag-TiO_2 surface is also prevented from undergoing further hydrogenation to CH_4 or C-C coupling to C_2H_4, and instead desorbs as CO. Although the CO evolution rate over Ag-TiO_2@SiO_2 (6.20 $\mu mol \cdot g^{-1} \cdot h^{-1}$) did not increase significantly compared to that of Ag-TiO_2. To decouple the mechanistic contributions of the SiO_2 shell from residual CTAB, we synthesized two reference materials: Ag-TiO_2@D-SiO_2 (CTAB-free with a dense SiO_2 shell) and Ag-TiO_2-CTAB (SiO_2-free with only surface-adsorbed CTAB). Performance testing revealed that while Ag-TiO_2-CTAB, lacking the SiO_2 shell, achieved 53.6% CO selectivity, this remained substantially lower than Ag-TiO_2@SiO_2. Conversely, Ag-TiO_2@D-SiO_2 without CTAB exhibited 100% CO selectivity but demonstrated a markedly reduced CO desorption rate (3.00 $\mu mol \cdot g^{-1} \cdot h^{-1}$), primarily due to a significant decrease in specific surface area. To further confirm the origin of hydrophobicity, we removed the SiO_2 shell by NaOH etching. After etching, the CO selectivity of the catalyst dropped to 23% (Figure S6), providing additional evidence that the SiO_2 shell is crucial for inhibiting HER. These findings confirm that the SiO_2 shell serves as the primary barrier against HER, the core function of the porous SiO_2 shell is not to enhance intrinsic activity, but rather to precisely inhibit the hydrocracking pathway by constructing a hydrophobic interfacial microenvironment. This strategic regulation directs the reaction towards near-perfect carbon dioxide reduction selectivity. On the other hand, the SiO_2 shell thickness is another critical parameter influencing catalytic performance. By varying the amount of TEOS added during synthesis, we prepared Ag-TiO_2@SiO_2 samples with different shell thicknesses. Performance evaluation revealed that an excessively thin shell still allows water molecules to reach the reaction interface, resulting in lower CO selectivity. Conversely, an overly thick SiO_2 shell reduces the proportion of active catalytic components in the material, thereby diminishing overall photocatalytic activity. Therefore, rational control of the SiO_2 shell thickness is essential (Figure S7). Inductively coupled plasma (ICP) analysis conducted before and after the 4-h photocatalytic reaction revealed negligible Ag leaching, with a quantified Ag loss of only ~0.16 wt%, thereby confirming the excellent structural stability and retention capability of Ag species in the catalyst under operational conditions (Table S3). The cycling test (Figure 3c) further demonstrated the excellent photocatalytic stability of Ag-TiO_2@SiO_2 over five consecutive runs, confirming the robustness of the core-shell structure [30]. Control experiments (Figure 3d) verified that no CO was detected in the absence of CO_2, light irradiation, or photocatalyst, indicating that the reaction is truly photocatalytic and dependent on all three components. Moreover, isotope labeling experiments using $^{13}CO_2$ (Figure 3e) clearly demonstrated that the produced CO originated from the supplied CO_2, ruling out contributions from carbonaceous impurities [31].

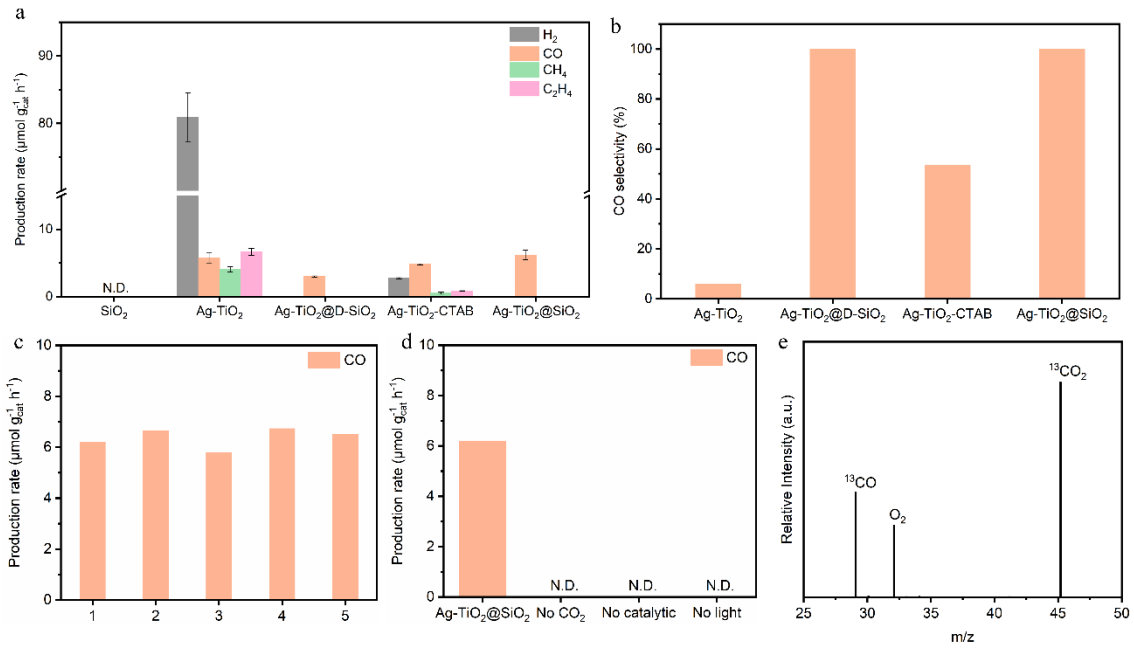

Figure 3. (**a**) The photocatalytic activity of CO_2 reduction. (**b**) CO selectivity. (**c**) Stability tests of CO_2 reduction of Ag-TiO_2@SiO_2. (**d**) Photocatalytic CO_2 reduction performance under different conditions. (**e**) CO evolution of the $^{13}CO_2$ isotope-labeled experiment.

To gain insight into the reaction pathway, in situ diffuse reflectance infrared Fourier transform spectroscopy (DRIFTS) was employed to monitor the intermediate species formed during the CO_2 reduction process [32]. As depicted in Figure 4a, upon irradiation, characteristic peaks emerged at 1706 cm^{-1} (carbonyl stretch ν(C=O) in carboxylic acids), 1550 cm^{-1} (ν_{as}(OCO), the antisymmetric telescopic vibration of OCO), 1409 cm^{-1} (ν_s(COO^-), the symmetrical stretching vibration of COO^-), and 1253 cm^{-1} (ν(C-OH), the stretching vibration of carboxylic acid hydroxyl group) [22,33]. The presence of these signals confirms that *COOH is a key intermediate in the CO_2 reduction pathway. Additionally, a weak peak at 2160 cm^{-1} was identified as adsorbed *CO [34]. Coupled with the fact that CO is the major gas product, a plausible reaction pathway can be inferred that CO_2 is activated and hydrogenated to form the *COOH intermediate, which then undergoes dehydration to yield *CO, followed by rapid desorption as gaseous CO. Based on the above results and discussions, a mechanism for the photocatalytic CO_2 reduction over the porous SiO_2-coated Ag-TiO_2 is proposed schematically in Figure 4b. Under light irradiation, TiO_2 generates electron-hole pairs. Given that the work function of Ag (4.26 eV) is higher than that of TiO_2 (4.20 eV), photogenerated electrons in TiO_2 spontaneously transfer to the Ag nanoparticles upon light irradiation, where they participate in reduction reactions. Concurrently, the photogenerated holes remain on TiO_2 and are involved in oxidation reactions, which predominantly occur at oxygen sites [26,35]. The key innovation lies in the porous SiO_2 shell, which constructs a localized hydrophobic microenvironment. The pore channels preferentially allow the diffusion of gaseous CO_2 molecules to the Ag active sites while effectively hindering the access of water molecules. This selective regulation of reactant supply enriches the local concentration of CO_2 around the active sites, thereby drastically suppressing the competition from the HER and ultimately leading to the high selectivity for CO production.

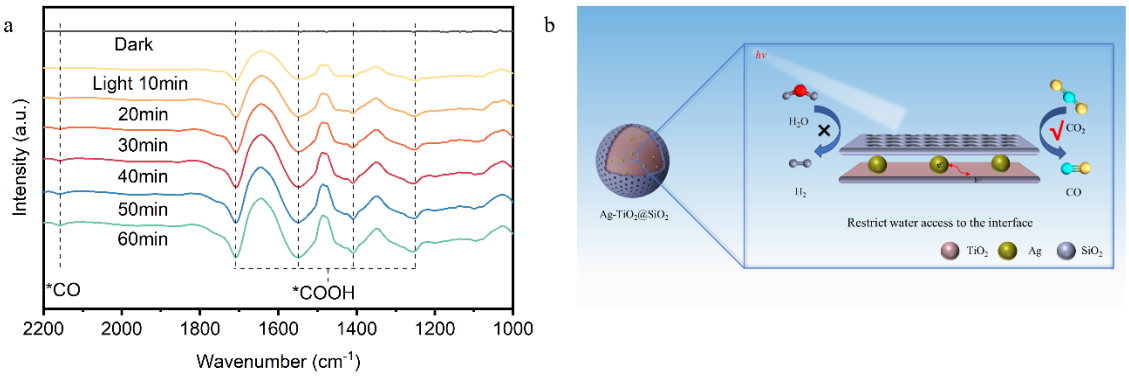

Figure 4. (**a**) In situ IR spectra of Ag-TiO_2@SiO_2. (**b**) The mechanism of CO_2 reduction on Ag-TiO_2@SiO_2.

4. Conclusions

In summary, we have developed a porous SiO_2-encapsulated Ag-TiO_2 photocatalyst that achieves 100% selectivity toward CO in the photocatalytic CO_2 reduction reaction without the use of any sacrificial agent. The remarkable enhancement in selectivity is attributed to the core-shell structure, in which the SiO_2 shell acts as a molecular sieve that preferentially permits the diffusion of CO_2 to the active sites while effectively restricting the access of water molecules to the catalytic interface. This work underscores the critical role of interfacial microenvironment engineering in regulating mass transport and suppressing competing reactions in three-phase photocatalytic systems. We believe this SiO_2 encapsulation strategy offers a versatile and scalable pathway for designing highly selective photocatalysts, and it may inspire further exploration of core-shell architectures for efficient solar fuel production and other gas-involved photocatalytic processes.

Supplementary Materials: The following supporting information can be downloaded at: https://media.sciltp.com/articles/others/2602251115362807/MI-25120017-Supplementary_Materials.pdf.

Author Contributions: M.J. conceived and designed the experiments. J.L. performed the catalyst preparation, characterization, and wrote the manuscript. Y.L., contributed to the HRTEM characterizations. Y.W. and Q.G. performed the catalytic tests. Z.G., Y.R., Y.Z., and Q.W. participated in the catalyst preparation and data analysis. The manuscript was written through the contributions of all authors. All authors have read and agreed to the published version of the manuscript.

Funding: This work was supported by the National Natural Science Foundation of China (NSFC, Nos: 52488201, 22171217), National Key R&D Program of China (No. 2024YFF0506100), the Distinguished Young Scholars in Shaanxi Province (No: 2023JC-JQ-12), and the Fundamental Research Funds for the Central Universities.

Data Availability Statement: The authors confirm that the data supporting the findings of this study are available within the article and its supplementary materials.

Conflicts of Interest: The authors declare no conflict of interest.

Use of AI and AI-assisted Technologies: No AI tools were utilized for this paper.

References

1. Gao, W.; Liang, S.; Wang, R.; Jiang, Q.; Zhang, Y.; Zheng, Q.; Xie, B.; Toe, C.Y.; Zhu, X.; Wang, J.; et al. Industrial carbon dioxide capture and utilization: state of the art and future challenges. *Chem. Soc. Rev.* **2020**, *49*, 8584–8686.
2. Das, S.; Pérez-Ramírez, J.; Gong, J.L.; Dewangan, N.; Hidajat, K.; Gates, B.C.; Kawi, S. Core–shell structured catalysts for thermocatalytic, photocatalytic, and electrocatalytic conversion of CO_2. *Chem. Soc. Rev.* **2020**, *49*, 2937–3004.
3. Xie, Z.K.; Xu, S.J.; Li, L.H.; Gong, S.H.; Wu, X.J.; Xu, D.B.; Mao, B.D.; Zhou, T.; Chen, M.; Wang, X.; et al. Well-defined diatomic catalysis for photosynthesis of C_2H_4 from CO_2. *Nat. Commun.* **2024**, *15*, 2422.
4. Choi, C.; Kwon, S.; Cheng, T.; Xu, M.J.; Tieu, P.; Lee, C.; Cai, J.; Lee, H.M.; Pan, X.Q.; Duan, X.F.; et al. Highly active and stable stepped Cu surface for enhanced electrochemical CO_2 reduction to C_2H_4. *Nat. Catal.* **2020**, *3*, 804–812.
5. Li, X.; Sun, Y.; Xu, J.; Shao, Y.; Wu, J.; Xu, X.; Pan, Y.; Ju, H.; Zhu, J.; Xie, Y. Selective visible-light-driven photocatalytic CO_2 reduction to CH_4 mediated by atomically thin $CuIn_5S_8$ layers *Nat. Energy* **2019**, *4*, 690–699.
6. Fang, S.; Rahaman, M.; Bharti, J.; Reisner, E.; Robert, M.; Ozin, G.A.; Hu, Y.H. Photocatalytic CO_2 reduction. *Nat. Rev. Methods Primers* **2023**, *3*, 61.
7. Kong, T.T.; Low, J.X.; Xiong, Y.J. Catalyst: How Material Chemistry Enables Solar-Driven CO_2 Conversion. *Chem* **2020**, *6*, 1035–1038.
8. Zhou, Q.X.; Guo, Y.; Zhu, Y.F. Reticular copper dual sites embedded with semiconductor particles for selective CO_2-to-C_2H_4 photoreduction. *Nat. Catal.* **2025**, *8*, 728–739.
9. Li, J.; Chen, G.; Zhu, Y.; Liang, Z.; Pei, A.; Wu, C.-L.; Wang, H.; Lee, H.R.; Liu, K.; Chu, S.; et al. Efficient electrocatalytic CO_2 reduction on a three-phase interface. *Nat. Catal.* **2018**, *1*, 592–600.
10. Jiang, Z.F.; Sun, H.L.; Wang, T.Q.; Wang, B.; Wei, W.; Li, H.M.; Yuan, S.Q.; An, T.C.; Zhao, H.J.; Yu, J.G.; et al. Nature-based catalyst for visible-light-driven photocatalytic CO_2 reduction. *Energy Environ. Sci.* **2018**, *11*, 2382–2389.
11. Zhang, Y.Z.; Xia, B.Q.; Ran, J.R.; Davey, K.; Qiao, S.Z. Atomic-Level Reactive Sites for Semiconductor-Based Photocatalytic CO_2 Reduction. *Adv. Energy Mater.* **2020**, *10*, 1903879.
12. Wei, Y.; Mao, Z.J.; Jiang, T.W.; Li, H.; Ma, X.Y.; Zhan, C.; Cai, W.B. Uncovering Photoelectronic and Photothermal Effects in Plasmon-Mediated Electrocatalytic CO_2 Reduction. *Angew. Chem. Int. Ed.* **2024**, *63*, e202317740.
13. Mohata, S.; Das, R.; Koner, K.; Riyaz, M.; Das, K.; Chakraborty, S.; Ogaeri, Y.; Nishiyama, Y.; Peter, S.C.; Banerjee, R. Selective Metal-Free CO_2 Photoreduction in Water Using Porous Nanostructures with Internal Molecular Free Volume *J. Am. Chem. Soc.* **2023**, *145*, 23802–23813.
14. Wu, X.Y.; Li, Y.; Zhang, G.K.; Chen, H.; Li, J.; Wang, K.; Pan, Y.; Zhao, Y.; Sun, Y.F.; Xie, Y. Photocatalytic CO_2 Conversion of $M_{0.33}WO_3$ Directly from the Air with High Selectivity: Insight into Full Spectrum-Induced Reaction Mechanism *J. Am. Chem. Soc.* **2019**, *141*, 5267–5274.
15. Su, H.; Yin, H.; Orbell, W.; Li, Y.; Wang, G.; Wang, Y.; Mori, K.; Chen, Z.; Li, H.; Yamashita, H.; et al. Asymmetric Triple-Atom Sites Combined with Oxygen Vacancy for Selective Photocatalytic Conversion of CO_2 to Propionic Acid *Angew. Chem. Int. Ed.* **2025**, *64*, e202425446.
16. Ren, Y.; Si, Y.; Du, M.; You, C.; Zhang, C.; Zhu, Y.-H.; Sun, Z.; Huang, K.; Liu, M.; Duan, L.; et al. Photothermal Synergistic Effect Induces Bimetallic Cooperation to Modulate Product Selectivity of CO_2 Reduction on Different CeO_2 Crystal Facets. *Angew. Chem. Int. Ed.* **2024**, *63*, e202410474.
17. Wang, J.; Zhang, H.; Nian, Y.; Chen, Y.; Cheng, H.; Yang, C.; Han, Y.; Tan, X.; Ye, J.; Yu, T. Disruption Symmetric Crystal Structure Favoring Photocatalytic CO_2 Reduction: Reduced *COOH Formation Energy Barrier on Al Doped CuS/TiO_2. *Adv. Funct. Mater.* **2024**, *34*, 2406549.
18. Ma, Y.; Jiang, Q.; Li, X.; Yu, H.; Han, X.; Liu, Y.; Li, Q.; Lv, K.; Hu, J. Heterojunction constructed from ZIF-8-on-MIL-68(Ga) precursor for photocatalytic CO_2 reduction. *Chem. Commun.* **2025**, *61*, 6831.
19. Kim, C.; Cho, K.M.; Al-Saggaf, A.; Gereige, I.; Jung, H.T. Z-scheme Photocatalytic CO_2 Conversion on Three-Dimensional BiVO4/Carbon-Coated Cu2O Nanowire Arrays under Visible Light. *ACS Catal.* **2018**, *8*, 4170–4177.
20. Guo, F.; Li, R.-X.; Yang, S.; Zhang, X.-Y.; Yu, H.; Urban, J.J.; Sun, W.-Y. Designing heteroatom-codoped iron metal–organic framework for promotional photoreduction of carbon dioxide to ethylene. *Angew. Chem. Int. Ed.* **2023**, *62*, e202216232.
21. Hu, S.; Qiao, P.; Yi, X.; Lei, Y.; Hu, H.; Ye, J.; Wang, D. Selective Photocatalytic Reduction of CO_2 to CO Mediated by Silver Single Atoms Anchored on Tubular Carbon Nitride *Angew. Chem. Int. Ed.* **2023**, *62*, e202304585.
22. Li, A.; Cao, Q.; Zhou, G.; Schmidt, B.V.K.J.; Zhu, W.; Yuan, X.; Huo, H.; Gong, J.; Antonietti, M. Three-Phase Photocatalysis for the Enhanced Selectivity and Activity of CO_2 Reduction on a Hydrophobic Surface. *Angew. Chem. Int. Ed.* **2019**, *58*, 14549–14555.

23. Wang, R.A.; Zhang, M.J.; Zhang, S.L.; Zheng, J.Z.; Zeng, Y.Q.; Yang, Y.; Ding, J.; Wu, X.; Zhong, Q. Simultaneous Photocatalytic CO2 Reduction and H2O Oxidation Under Non-Sacrificial Ambient Conditions.*ACS Nano* **2023**, *17*, 24363–24373.
24. Wang, Y.; Huang, N.-Y.; Shen, J.-Q.; Liao, P.-Q.; Chen, X.-M.; Zhang, J.-P. Hydroxide Ligands Cooperate with Catalytic Centers in Metal–Organic Frameworks for Efficient Photocatalytic CO_2 Reduction. *J. Am. Chem. Soc.* **2018**, *140*, 38–41.
25. Robert, M.; Zhang, J.-H.; Ge, Z.-M.; Zhong, D.-C.; Zuo, J.-L.; Lu, T.-B. Self-Photosensitizing Cobalt Complexes for Photocatalytic CO_2 Reduction Coupled with CH_3OH Oxidation. *Angew. Chem. Int. Ed.* **2025**, *64*, e202506060.
26. Yu, Y.Y.; He, Y.; Yan, P.; Wang, S.Y.; Dong, F. Boosted C-C coupling with Cu-Ag alloy sub-nanoclusters for CO_2-to-C_2H_4 photosynthesis. *Proc. Natl. Acad. Sci. USA* **2023**, *120*, e2307320120.
27. Deng, Y.; Qi, D.; Deng, C.; Zhang, X.; Zhao, D. Superparamagnetic High-Magnetization Microspheres with an Fe_3O_4@SiO_2 Core and Perpendicularly Aligned Mesoporous SiO_2 Shell for Removal of Microcystins. *J. Am. Chem. Soc.* **2008**, *130*, 28–29.
28. Huang, H.N.; Shi, R.; Li, Z.H.; Zhao, J.Q.; Su, C.L.; Zhang, T.R. Triphase Photocatalytic CO_2 Reduction over Silver-Decorated Titanium Oxide at a Gas–Water Boundary. *Angew. Chem. Int. Ed.* **2022**, *61*, e202200802.
29. Yin, C.; Li, X.; Sun, S.; Wei, X.; Tong, Q.; Tan, W.; Wang, X.; Peng, B.; Wan, H.; Dong, L. High photocatalytic performance over ultrathin 2D TiO_2 for CO_2 reduction to alcohols. *Chem. Commun.* **2024**, *60*, 3531–3534.
30. Xia, P.F.; Antonietti, M.; Zhu, B.C.; Heil, T.; Yu, J.G.; Cao, S.W. Designing Defective Crystalline Carbon Nitride to Enable Selective CO_2 Photoreduction in the Gas Phase. *Adv. Funct. Mater.* 2019, **29**,1900093.
31. Jiang, M.; Gao, Y.L.; Wang, Z.Y.; Ding, Z.X. Photocatalytic CO_2 reduction promoted by a $CuCo_2O_4$ cocatalyst with homogeneous and heterogeneous light harvesters. *Appl. Catal. B* **2016**, *198*, 180–188.
32. Kattel, S.; Yu, W.T.; Yang, X.F.; Yan, B.H.; Huang, Y.Q.; Wan, W.M.; Liu, P.; Chen, J.G.G. CO_2 Hydrogenation over Oxide-Supported PtCo Catalysts: The Role of the Oxide Support in Determining the Product Selectivity. *Angew. Chem. Int. Ed.* **2016**, *55*, 7968–7973.
33. Zhao, Z.J.; Mu, R.T.; Wang, X.H.; Gong, J.L. Fast prediction of CO binding energy via the local structure effect on PtCu alloy surfaces. *Langmuir* **2017**, *33*, 8700–8706.
34. Su, B.; Wang, S.; Xing, W.; Liu, K.; Hung, S.-F.; Chen, X.; Fang, Y.; Zhang, G.; Zhang, H.; Wang, X. Synergistic Ru Species on Poly(heptazine imide) Enabling Efficient Photocatalytic CO_2 Reduction with H_2O beyond 800 nm. *Angew. Chem. Int. Ed.* **2025**, *64*, e202505453.
35. Kaushik, T.; Ghosh, S.; Dolkar, T.; Biswas, R.; Dutta, A. Noble Metal Plasmon–Molecular Catalyst Hybrids for Renewable Energy Relevant Small Molecule Activation. *ACS Nanosci. Au* **2024**, *4*, 273–289.

Article

Reactivity of Perfluorophenyl Azide with Graphene Supported on Cu: Effect of Substrate Crystallinity

Jia Tu and Mingdi Yan *

Department of Chemistry, University of Massachusetts Lowell, Lowell, MA 01854, USA
* Correspondence: mingdi_yan@uml.edu
Received: 1 March 2026; Revised: 14 March 2026; Accepted:16 March; Published: 18 March 2026

Abstract: Effective methods for the covalent functionalization of pristine graphene are limited due to its low chemical reactivity. We developed a covalent chemistry to functionalize graphene using perfluorophenyl azide (PFPA) and demonstrated that the reactivity of graphene can be enhanced by metal substrates. In this work, we investigated the impact of crystalline lattice and morphology of Cu on the reactivity of graphene with PFPA. Graphene grown on single crystalline Cu(111) (Gra/Cu(111)) exhibited the highest degree of functionalization, as evidenced by the largest increase in the D-band intensity obtained from Raman spectroscopy and Raman mapping, along with a low crystallite domain size L_D and a high defect density n_D. In contrast, graphene grown on electropolished polycrystalline Cu (Gra/pCu) showed minimal reactivity toward PFPA reaction. Further Raman analyses demonstrate that Cu(111) induces stronger charge transfer and higher strain in graphene compared to pCu, primarily due to superior lattice matching between graphene and Cu(111), leading to higher reactivity of Gra/Cu(111) toward electron-deficient perfluorophenyl nitrene. Upon transfer of graphene grown on Cu(111) to other substrates, including Cu(111), electropolished pCu, and silicon wafer, the reactivity decreased, and the reactivity of transferred graphene correlates mainly with surface roughness. The decreased reactivity is attributed to weakened graphene–substrate charge interactions after transfer. These findings establish substrate engineering as an effective and non-invasive method for tuning the chemical reactivity of graphene without the need for harsh activation conditions.

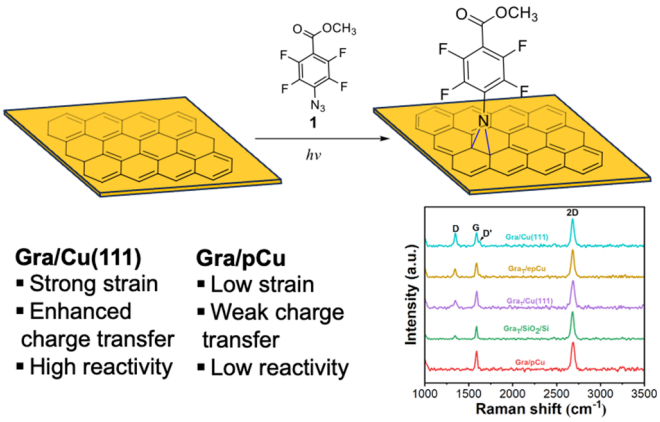

Keywords: graphene; covalent functionalization; perfluorophenyl azide; substrate effect; Cu(111); polycrystalline Cu

1. Introduction

Functionalization of graphene is an important strategy to expand its applications in electronics, sensing, energy storage and biotechnology [1–3]. Various covalent functionalization approaches have been reported, including radical reactions with diazonium salts and peroxides, oxidation, (2+1) cycloadditions with nitrenes, carbenes or malonate derivatives, (2+2) cycloadditions with arynes, (3+2) cycloadditions with azomethine ylides, and (4+2) cycloadditions with dienes or dienophiles [3,4]. Among these, the (2+1) cycloaddition with aryl nitrene is unique in that the reaction can be initiated with UV, heat, or microwave irradiation. Upon the release of N_2, the generated nitrene reacts with graphene to produce covalent adduct. For the reaction of azides with graphene, the (2+1) cycloaddition product aziridine has generally been proposed to be the product structure, analogous to the reaction of azide with other carbon materials such as fullerene [5–7]. However, the exact product structure has not been explicitly confirmed experimentally.

Various azides, including alkyl, silyl, and aryl azides have been used for the covalent functionalization of graphene and highly oriented pyrolytic graphite [8–12]. Literature examples on using azides to functionalize graphene is summarized in Table S1. Compared with perfluorophenyl azides (PFPAs), alkyl, phenyl, and silyl

azides exhibit much lower efficiency. This limitation arises from several intrinsic factors. The short lifetime of singlet nitrenes derived from these azides restricts their ability to engage in productive C-H insertion and cycloaddition reactions [13,14]. Upon photolysis or thermolysis, alkyl and phenyl azides rapidly undergo intersystem crossing (ISC) to the more stable triplet state that is significantly less reactive towards insertion and cycloaddition reactions. In contrast, the strongly electron-withdrawing fluorine atoms of fluorinated aryl azides such as PFPAs suppress ring expansion and ISC, thereby prolonging the singlet nitrene lifetime and enhancing their selectivity toward addition reactions. In the case of silyl azides, steric hindrance plays an important role as silyl azides generate bulky nitrenes in which substituents around the reaction center hinder orbital overlap with graphene's delocalized π network [10,15]. This steric hindrance increases the activation barrier for forming the aziridine ring in the (2+1) cycloaddition, resulting in reduced grafting yields and poor uniformity of functionalization. Safety and stability concerns further limit their practical use [16]. Many alkyl azides are thermally unstable and sensitive to shock or light, posing explosion hazards during synthesis and handling. Silyl azides, while somewhat more stable, are moisture-sensitive and decompose to release toxic gases under ambient conditions. These factors limit reactions with alkyl and silyl azides.

Aryl azides have been increasingly applied in the functionalization of surfaces and nanomaterials, demonstrating remarkable versatility in the covalent functionalization of small organic molecules, polymers, proteins, and carbon materials including fullerenes, carbon tubes, and graphene under ambient, solid state, as well as biological conditions [17,18]. Perfluorophenyl azides (PFPAs) are particularly attractive due to the ease of synthesis from commercially available precursors and the excellent stability under dark conditions. In addition, PFPAs can be readily functionalized with a wide range of reactive groups such as carboxylic acid and its activated esters, e.g., *N*-hydroxysuccinimidyl ester, silanes, phosphates, thiols and disulfide, enabling ready conjugation to both organic and inorganic substrates. Building on these, we and others have employed PFPA chemistry to functionalize graphene to introduce well-defined functional groups, to pattern graphene, and to fabricate graphene-based nanocomposite materials [19–28]. However, the PFPA reaction on graphene typically results in a relatively low degree of functionalization under standard reaction conditions.

Substrate engineering has emerged as a promising strategy in increasing the reactivity of graphene by inducing strain and/or charge doping in the carbon lattice [29,30]. Tensile or compressive strain alters the π-orbital alignment, while charge transfer between graphene and the substrate shifts the Fermi level to favor either electrophilic or nucleophilic reaction. These substrate-induced perturbations directly influence the extent and selectivity of covalent functionalization on graphene. In the reaction with PFPA, computational study revealed that metal-assisted charge transfer lowers the singlet–triplet energy gap, thereby stabilizing the reactive singlet nitrene and enhancing the efficiency of the cycloaddition reaction [21]. Consistent with this prediction, graphene supported on Ni and Cu exhibited higher PFPA reactivity than that on silicon wafer (SiO_2/Si). In this case, the samples were prepared by transferring graphene grown by chemical vapor deposition (CVD) onto polycrystalline Ni and Cu films [21,31].

It has also been reported that the crystal orientation of the metal substrates can influence the reactivity of graphene. For example, graphene grown on single crystalline Cu(111) exhibits higher reactivity than that on polycrystalline Cu (pCu), an effect attributed to substrate-induced strain and charge transfer interactions [32–35]. This substrate-dependent behavior suggests that the crystallographic orientation and morphology of the underlying substrate can be exploited to control the extent of nitrene reaction and thereby fine-tune the degree of covalent functionalization of graphene.

In this work, we investigated how the crystallographic orientation and morphology of the Cu substrate affect the reactivity of graphene toward PFPA functionalization. Graphene was grown via CVD on Cu(111) and pCu. Graphene grown on Cu(111) was also transferred onto Cu(111), electropolished pCu (epCu) and SiO_2/Si (Scheme 1). Using Raman spectroscopy and Raman mapping, we quantified the extent of functionalization and correlated it with substrate-induced strain and charge doping effects. Our results reveal that graphene grown on Cu(111) undergoes the highest degree of functionalization, consistent with its strong substrate coupling with Cu(111). These findings establish substrate crystallography and morphology as an important parameter for tuning the reactivity of graphene towards PFPA reaction.

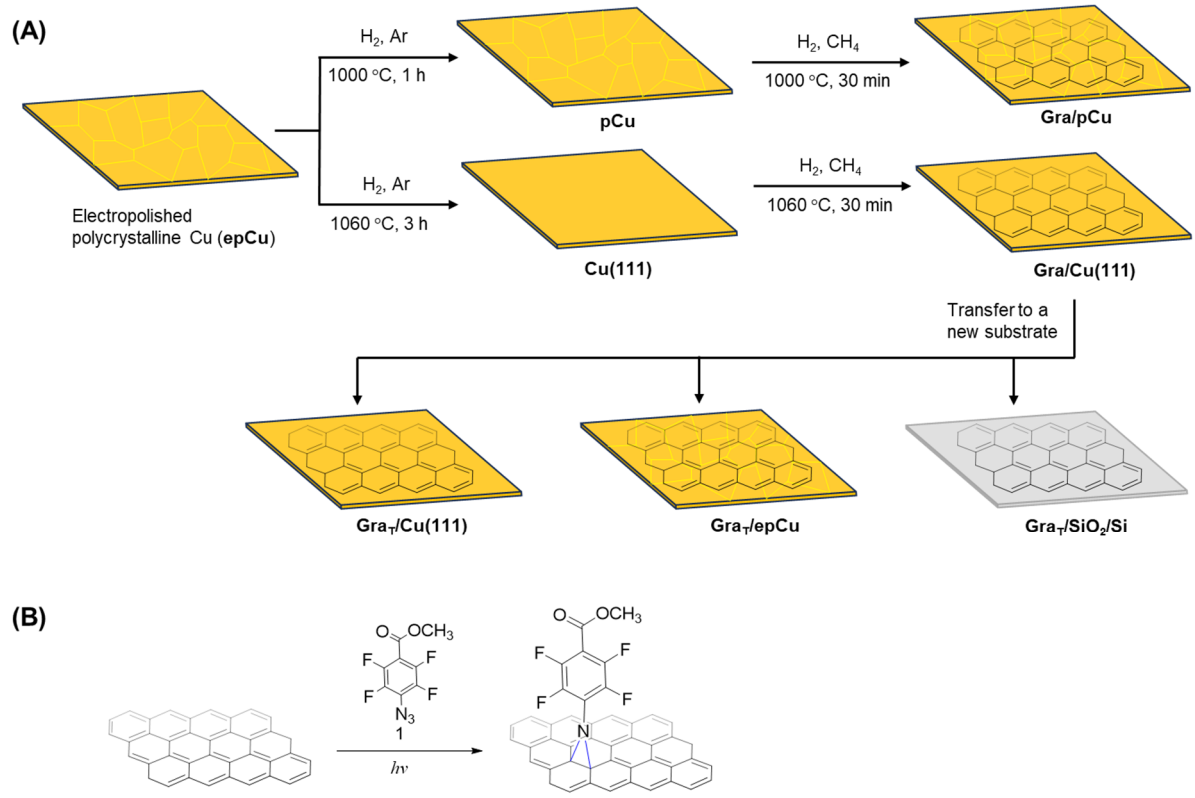

Scheme 1. (**A**) Synthesis of CVD graphene on pCu (Gra/pCu) and on Cu(111) (Gra/Cu(111)), and transfer of graphene grown on Cu(111) to silicon wafer (Gra$_T$/SiO$_2$/Si), electropolished polycrystalline Cu (Gra$_T$/epCu), and Cu(111) (Gra$_T$/Cu(111)). (**B**) Photochemical reaction of graphene with PFPA **1**.

2. Experimental Section

2.1. Materials and Instruments

Copper foils (25 μm thick, annealed, uncoated, 99.8%) and Cu plate (0.675 mm thick, annealed, 99.9%) were purchased from Alfa Aesar (Ward Hill, MA, USA). Silicon wafers with 280 nm thermally grown SiO_2 (single-side polished) were purchased from Fuleda Technology (Wan Chai, China). Ethanol (200 proof) was purchased from Decon Labs, Inc (King of Prussia, PA, USA). Acetone (certified ACS), methanol (certified ACS), isopropanol (>99.5%), and hydrochloric acid (certified ACS Plus) were purchased from Fisher Chemical (Bridgewater, NJ, USA). Urea (99.63%, certified ACS) were purchased from Fisher Chemical (Fair Lawn, NJ, USA) All aqueous solutions were prepared from Milli-Q water (18.2 MΩ·cm). Hydrogen, argon, and methane gases (ultrahigh purity grade) were purchased from Airgas (Billerica, MA, USA). Poly(methyl methacrylate) (PMMA, average molecular weight: 996,000) was purchased from Aldrich Chemical (Milwaukee, WI, USA). Phosphoric acid (>85 wt%) was purchased from Honeywell (USA). Methyl 4-azido-2,3,5,6-tetrafluorobenzoate (PFPA **1**) was synthesized according to a previous procedure [36]. *N*-Methyl-2-pyrrolidone (NMP, anhydrous, 99.5%) and iron(III) chloride (97%) were purchased from Sigma-Aldrich (Milwaukee, WI, USA).

The photochemical reaction was carried out in a UV box equipped with a 450 M medium-pressure mercury lamp. The intensity of the UV lamp was measured to be 36 mW/cm^2 at 280 nm at the location of the reaction using a Coherent FieldMate power meter fitted with a PowerMax PM30 sensor having an active area diameter of 19 mm (Coherent, Inc., Santa Clara, CA, USA). Raman spectra were collected on a Bruker Senterra I spectrometer equipped with a 532 nm laser at the incident power of 1 mW and irradiation time of 10 s. Raman mapping was performed using a HORIBA Scientific Raman microscope equipped with a 532 nm excitation laser. Spectra were acquired with an integration time of 1 s over the range of 1000–3000 cm^{-1}. Each mapping spot covered an area of 2 × 2 μm^2, and a 7 × 7 mapping image (49 spots) was collected for each sample. Atomic force microscopy (AFM) images were obtained using a Bruker Multimode AFM in the tapping mode. Optical images were recorded on a Nikon ECLIPSE L200 microscope using a Moticam 2500 camera. X-ray diffraction (XRD) analysis was carried out on a Rigaku MiniFlex 600 diffractometer equipped with Cu Kα radiation (λ = 1.5418 Å).

2.2. Fabrication of Graphene on pCu and Cu(111)

Monolayer graphene was synthesized by CVD on both pCu and Cu(111) following a previous procedure [37]. The substrates were prepared from commercial Cu foils that were electropolished to remove surface oxides and reduce surface roughness. Electropolishing was carried out by using commercial Cu foils as the anode and a copper plate as the cathode at a constant current of 2.8 A for 180 s. The electropolishing solution was prepared from a stock solution containing 1000 mL of Milli-Q water, 500 mL of phosphoric acid, 500 mL of ethanol, 100 mL of isopropyl alcohol, and 10.0 g of urea. After electropolishing, the Cu foils were thoroughly rinsed with water, ethanol, and acetone, and then dried under an argon stream to give epCu.

To synthesize Gra/pCu, the electropolished Cu foil was first annealed at 1000 °C in a homebuilt CVD furnace [37] under a flow of H_2 (10 sccm) and Ar (~15 sccm) for 1 h to give pCu (Scheme 1). After annealing, the argon valve was closed, and CH_4 (3–6 sccm) was introduced while maintaining the H_2 flow at 10 sccm. Graphene was grown at 1000 °C for 30 min. The furnace was then rapidly cooled to ~50 °C under a continuous flow of H_2 and CH_4, after which the gases were turned off and the chamber was open to ambient environment.

To synthesize Gra/Cu(111), the electropolished Cu foil was annealed at 1060 °C for 3 h under a flow of H_2 (10 sccm) and argon (~15 sccm) to produce Cu(111) (Scheme 1). Graphene growth on Cu(111) was carried out in the same manner as for pCu except at the growth temperature of 1060 °C.

2.3. Transfer of Graphene onto SiO_2/Si, epCu, and Cu(111)

Graphene grown on Cu(111) was transferred to silicon wafer (SiO_2/Si), epCu, and Cu(111) using the PMMA-assisted wet-transfer method [38]. Briefly, a solution of PMMA in acetone (40 mg/mL) was spin-coated on the side of graphene at 1000 rpm for 1 min. The Cu foil was then etched away in a $FeCl_3$/HCl (1 M $FeCl_3$ in 3 M HCl) for 3 h. The PMMA-supported graphene film was rinsed thoroughly in 1 M HCl solution followed by Milli-Q water several times. PMMA-supported graphene was then scooped from Milli-Q water onto the target substrate. After drying at room temperature, the sample was immersed in acetone for 3 h, repeated once more to obtain a clean graphene film on the target substrate, yielding Gra_T/SiO_2/Si, Gra_T/epCu, and Gra_T/Cu(111) (Scheme 1).

2.4. Reaction of Graphene with PFPA

Graphene supported on different substrates was immersed in an anhydrous NMP solution of PFPA **1** (0.1 M). The sample was then irradiated with a 450 M medium-pressure mercury lamp through a 280-nm long-pass optical filter at room temperature for 40 min. After irradiation, the sample was rinsed with acetone three times. Except for Gra_T/SiO_2/Si which was used directly for Raman characterization, other samples were transferred onto silicon wafer prior to Raman characterization.

2.5. Characterization by Raman Spectroscopy and Mapping

For each sample, Raman spectra were collected from randomly selected 76–246 points across the graphene surface to account for spatial inhomogeneity. The peak height of D (~1350 cm^{-1}) and G (~1590 cm^{-1}) bands was used to calculate peak intensity and I_D/I_G. Crystallite domain size (L_D) and defect density (n_D) were calculated using the Tuinstra–Koenig relation [21]. The relative change in I_D/I_G ($\Delta I_D/I_G$) before and after reaction was quantified as

$$\Delta I_D/I_G = \frac{(I_D/I_G)_{\text{after}} - (I_D/I_G)_{\text{before}}}{(I_D/I_G)_{\text{before}}} \times 100$$

3. Results

3.1. Preparation of Monolayer Graphene on Various Substrates

Monolayer graphene on Cu(111) (Gra/Cu(111)) or pCu (Gra/pCu) was prepared in a home-build CVD setup following the protocol developed previously [37]. In the process, commercial polycrystalline copper foils were first subjected to electropolishing to remove surface contaminants and reduce surface roughness, yielding epCu. The foils were then annealed in the furnace at 1000 °C for 1 h or at 1060 °C for 3 h to give pCu or single crystal Cu(111), respectively (Scheme 1). The XRD pattern of commercial pCu, electropolished pCu and annealed pCu all shows multiple prominent diffraction peaks corresponding to (331), (111), (220), and (200) facets, with the (331) being the most intense (Figure 1). On the other hand, as-prepared Cu(111) foil contains a single sharp diffraction peak corresponding to the (111) facet. To grow graphene, annealed pCu and Cu(111) foils were exposed

to 10 sccm H_2 and 3–6 sccm CH_4 at 1000 °C or 1060 °C for 30 min to give Gra/pCu or Gra/Cu(111), respectively. Graphene transferred to other substrates was prepared by transferring Gra/Cu(111) to silicon wafer, epCu, or Cu(111) by PMMA-assisted wet transfer to give $Gra_T/SiO_2/Si$, Gra_T/epCu, and Gra_T/Cu(111) (Scheme 1).

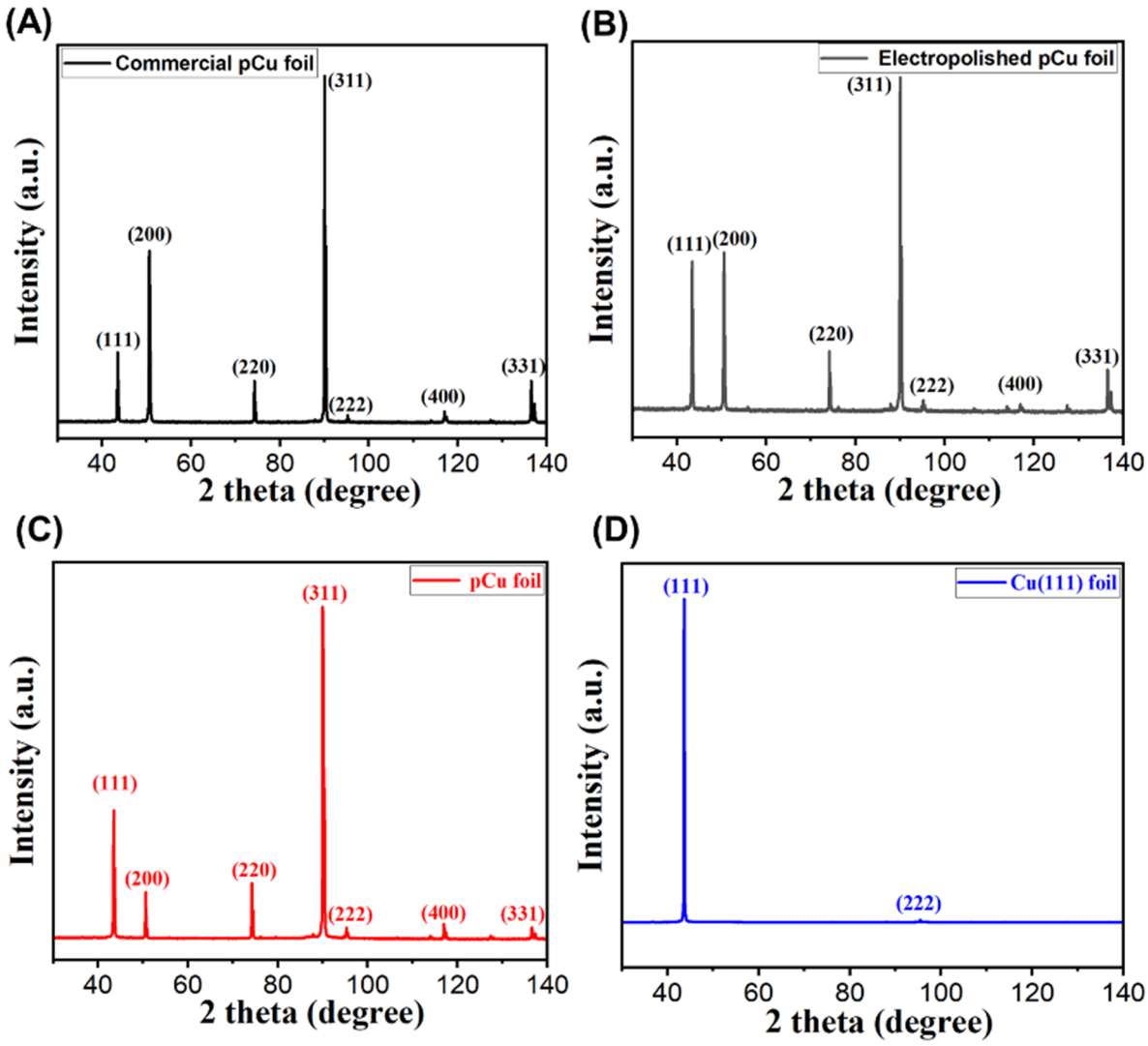

Figure 1. XRD patterns of (**A**) as-received polycrystalline copper foil, (**B**) electropolished polycrystalline copper foil (epCu) (**C**) electropolished polycrystalline copper foil annealed in H_2/Ar at 1000 °C for 1 h (pCu), and (**D**) Cu(111) foil.

3.2. Functionalization of Graphene on Different Substrates

Reactions were carried out by immersing graphene samples in 0.1 M solution of PFPA in anhydrous NMP, covered the vial with a 280-nm long-pass filter, and then irradiated with a medium-pressure Hg lamp at room temperature for 40 min. The irradiation time was selected based on our previous systematic investigation of PFPA reactions with graphene [21]. We have also demonstrated that without PFPA, irradiating graphene in NMP under identical conditions showed no increase in the Raman D band intensity, indicating that neither NMP nor UV irradiation introduces detectable defects in graphene under the reaction conditions [21]. After extensive rinsing with acetone and drying, graphene supported on Cu was transferred onto silicon wafer, and Raman spectra were collected. The as-grown Gra/pCu (Figure S1A) and Gra/Cu(111) (Figure S2A) showed the characteristic single layer graphene features of symmetric 2D peak and $I_{2D}/I_G > 2$, as well as minimal D band, indicative of minimal structural defects in the as-prepared unfunctionalized graphene. After reaction with PFPA, all functionalized graphene samples (Figure 2A) exhibit defect-related D bands at ~1350 cm^{-1} with varying intensities reflecting different extents of defect incorporation [29,39]. After functionalization, Gra/Cu(111) shows the most pronounced D peak together with a D' band at ~1625 cm^{-1} (Figures 2A and S2B). The D band arises from defect-activated intervalley scattering, whereas D' band originates from intravalley scattering and is particularly sensitive to localized point-like sp^3 defects [40,41]. The simultaneous presence of D and D' bands indicate localized symmetry-breaking defects introduced by PFFA

functionalization of graphene. In contrast, Gra/pCu shows the weakest D-band intensity (Figures 2A and S1B). The transferred samples ($Gra_T/SiO_2/Si$, Gra_T/epCu, and Gra_T/Cu(111)) exhibit intermediate D-band intensities, following the trend Gra_T/Cu(111) > Gra_T/epCu > $Gra_T/SiO_2/Si$ (Figures 2A and S2C–E).

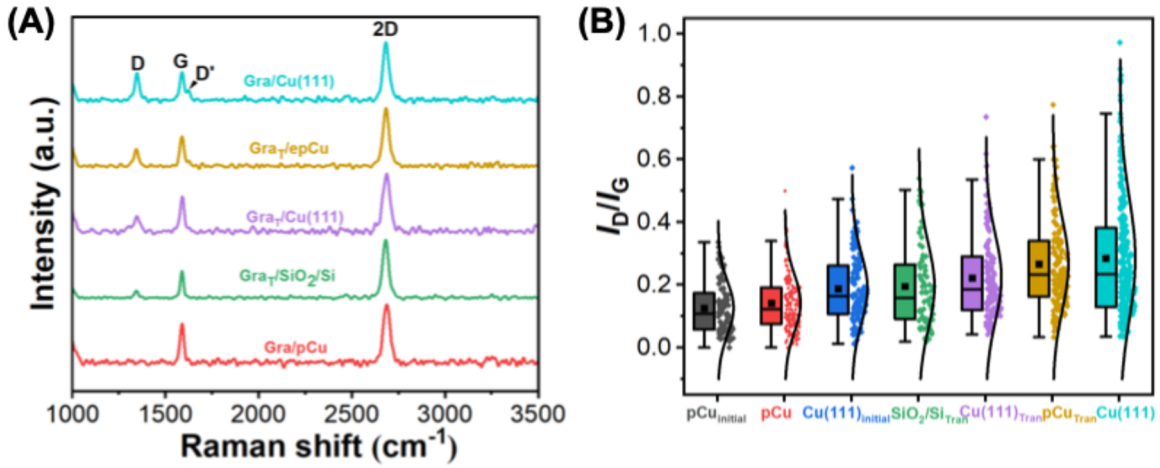

(C)

Sample	Condition	I_D/I_G	$\%\Delta I_D/I_G$	L_D (nm)	n_D ($\times 10^9$ cm^{-2})
Gra/pCu	Initial	0.13 ± 0.08	--	41 ± 16	28 ± 18
	After reaction	0.14 ± 0.09	7.7%	38 ± 16	32 ± 20
Gra/Cu(111)	Initial	0.18 ± 0.11	--	33 ± 13	42 ± 24
Gra$_T$/SiO$_2$/Si	After reaction	0.19 ± 0.14	5.6%	33 ± 14	43 ± 30
Gra$_T$/Cu(111)		0.22 ± 0.14	22%	29 ± 9.1	49 ± 30
Gra$_T$/epCu		0.27 ± 0.15	50%	26 ± 8.6	59 ± 32
Gra/Cu(111)		0.28 ± 0.19	56%	27 ± 10	63 ± 43

Figure 2. Raman analysis of graphene supported on different substrates after reaction with PFPA. (**A**) Typical Raman spectra of PFPA-functionalized Gra/Cu(111), Gra$_T$/epCu, Gra$_T$/Cu(111), Gra$_T$/SiO$_2$/Si, and Gra/pCu. Additional Raman spectra can be found in Figures S1B and S2B–E. (**B**) Box-violin plots showing the distribution of I_D/I_G for PFPA-functionalized graphene samples. The boxes represent the interquartile range (25th–75th percentile), with whiskers indicating the data spread. The surrounding violin plots show the full probability distribution of the data, obtained from 82 (Gra/pCu$_{initial}$), 210 (Gra/pCu), 112 (Gra/Cu(111)$_{initial}$), 76 (Gra$_T$/SiO$_2$/Si), 145 (Gra/Cu(111)), 130 (Gra$_T$/epCu), and 246 (Gra/Cu(111)) Raman spectra, respectively. (**C**) Raman-derived parameters, I_D/I_G, $\%\Delta I_D/I_G$, L_D, and n_D, of graphene samples before and after reaction with PFPA. The L_D, and n_D calculations can be found in Supplementary Materials. Data are presented as mean ± standard deviation.

Further Raman analyses (Figure 2C) show that after reaction with PFPA, the relative change in I_D/I_G, $\%\Delta I_D/I_G$, was 7.7% for Gra/pCu. On the other hand, I_D/I_G of Gra/Cu(111) increased substantially to $\Delta I_D/I_G$ of 56% after reaction with PFPA. The transferred graphene samples show intermediate increase in $\Delta I_D/I_G$, at 5.6%, 22%, and 50% for $Gra_T/SiO_2/Si$, Gra_T/Cu(111), and Gra_T/epCu, respectively. Overall, the extent of defect incorporation follows the trend of Gra/Cu(111) > Gra_T/epCu > Gra_T/Cu(111) > Gra/pCu ≈ $Gra_T/SiO_2/Si$, with Gra/Cu(111) having the highest degree of defect incorporation.

Raman mapping of I_D/I_G was performed to visualize the spatial distribution of PFPA functionalization of graphene across graphene supported on different substrates (Figure 3). Consistent with the Raman spectroscopy data in Figure 2, as-prepared Gra/pCu (Gra/pCu$_{initial}$) exhibits a low and spatially uniform I_D/I_G of 0.13 ± 0.03, which increases only marginally to 0.14 ± 0.02 after PFPA functionalization, indicating minimal structural modification. Similarly, as-prepared Gra/Cu(111) (Gra/Cu(111)$_{initial}$) shows a low average I_D/I_G of 0.16 ± 0.03. After PFPA functionalization, a high I_D/I_G of 0.34 ± 0.13 is observed for Gra/Cu(111), together with localized regions of significantly increased I_D/I_G, indicating that graphene directly grown on Cu(111) undergoes the most extensive functionalization. $Gra_T/SiO_2/Si$ displays a small increase in I_D/I_G to 0.19 ± 0.05, whereas Gra_T/Cu(111) shows a modest increase in I_D/I_G to 0.24 ± 0.10. More pronounced increase in I_D/I_G was observed for Gra_T/epCu, which exhibits an elevated I_D/I_G of 0.29 ± 0.17.

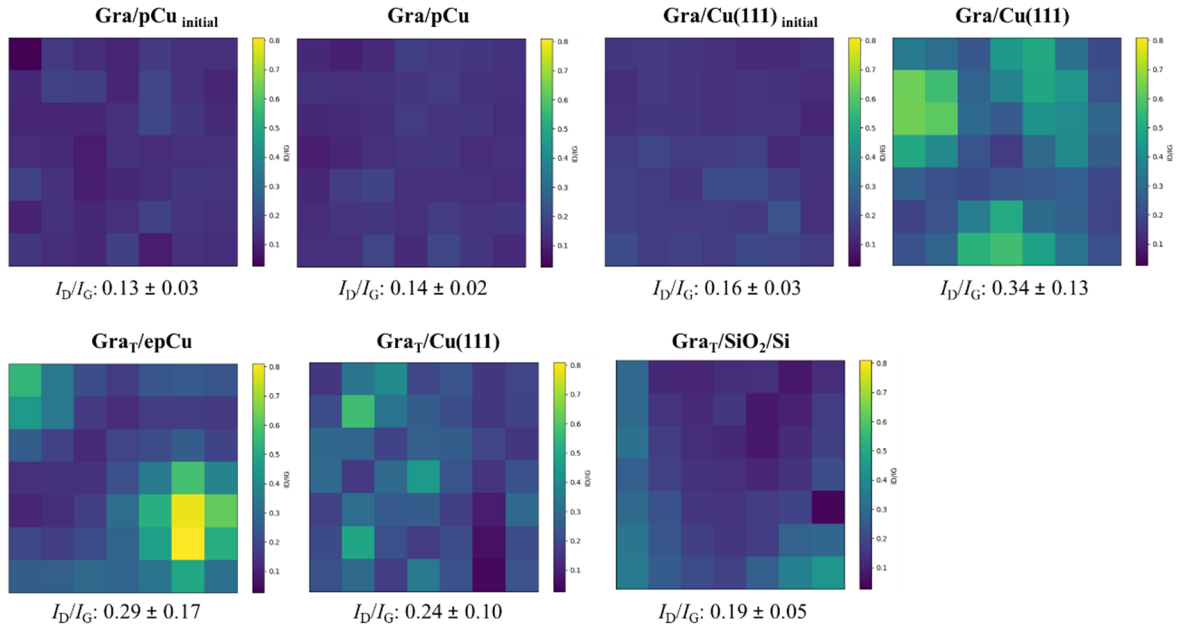

Figure 3. Raman I_D/I_G mapping of graphene on different substrates before (initial) and after PFPA functionalization. Each Raman mapping spot corresponds to an area of 2 × 2 μm^2.

3.3. Extent of Functionalization

To quantify the extent of functionalization, statistical analyses of crystallite domain size (L_D) and defect density (n_D) [40,41] were performed and results are shown in Figure 3C. Here, L_D represents the average distance between neighboring point defects, while n_D denotes the number of defects per area and is inversely proportional to L_D^2. Figure 4A shows box violin plots of L_D for all samples, showing the data as well as statistical distribution. The as-prepared Gra/pCu and Gra/Cu(111) exhibit relatively large L_D values (41 ± 16 nm and 33 ± 13 nm, respectively), indicating large crystallite domain size. After PFPA functionalization, L_D decreases slightly for Gra/pCu (38 ± 16 nm) but more significantly for Gra/Cu(111) (27 ± 10 nm), indicating enhanced defect incorporation on Gra/Cu(111). Transferred samples also show reduced domain sizes, with Gra_T/epCu and Gra_T/Cu(111) yielding L_D values of 26 ± 8.6 nm and 29 ± 9.1 nm, respectively. In contrast, Gra/SiO_2/Si shows only a minimal change (33 ± 14 nm), consistent with its relatively low reactivity. These results clearly demonstrate that smaller domain sizes correlate with higher extent of functionalization. Particularly, Gra/Cu(111) with the smallest L_D reflects its strong substrate–graphene interaction that facilitates reaction with PFPA.

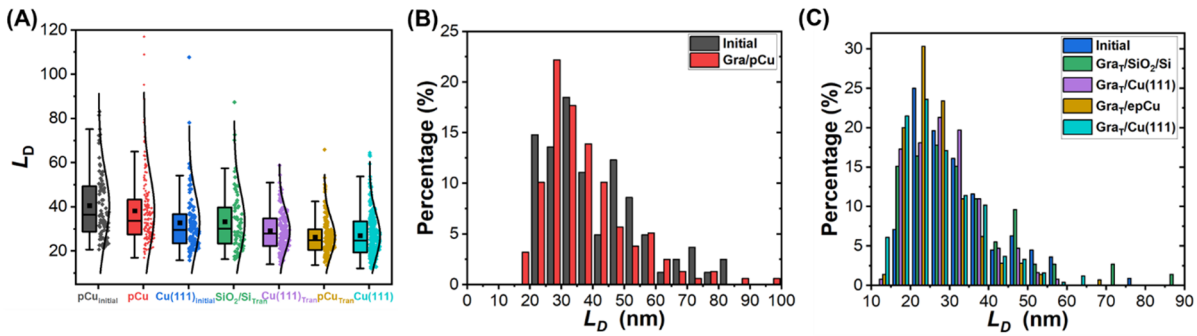

Figure 4. Statistical analysis of crystallite domain size (L_D) in graphene on different substrates before and after PFPA functionalization. (**A**) Box–violin plots of L_D distribution. (**B**) Histograms of L_D values for Gra/pCu before (grey), and after PFPA functionalization (red). (**C**) Histograms of L_D values for Gra/Cu(111) before (blue), and after PFPA functionalization (turquois), and after PFPA functionalization for Gra_T/SiO_2/Si (green), Gra_T/Cu(111) (purple), and Gra_T/epCu (gold).

The defect density (n_D) was also analyzed, and the results are shown in Figure 5. The as-prepared Gra/pCu shows the lowest defect density ((28.1 ± 18.5) × 10^9 cm^{-2}), while as-prepared Gra/Cu(111) exhibits a slightly higher n_D ((41.5 ± 24.5) × 10^9 cm^{-2}). Following functionalization, the defect density increases across all substrates,

with the most pronounced increase observed for Gra/Cu(111), reaching (62.7 ± 42.9) × 10^9 cm^{-2}), followed closely by Gra_T/epCu ((58.7 ± 32.1) × 10^9 cm^{-2}). Gra_T/Cu(111) and Gra_T/SiO_2/Si exhibit more modest increases at (49.0 ± 30.3) × 10^9 cm^{-2} and (43.1 ± 29.5) × 10^9 cm^{-2}, respectively. Gra/pCu shows a slight increase to (31.5 ± 19.9) × 10^9 cm^{-2}. Overall, the combined L_D and n_D analyses reinforce the conclusion that graphene grown on Cu(111) is the most reactive toward PFPA functionalization, while graphene grown on pCu is the least reactive. Transferred samples exhibit intermediate reactivities, indicating partial retention of substrate-induced effects after transfer.

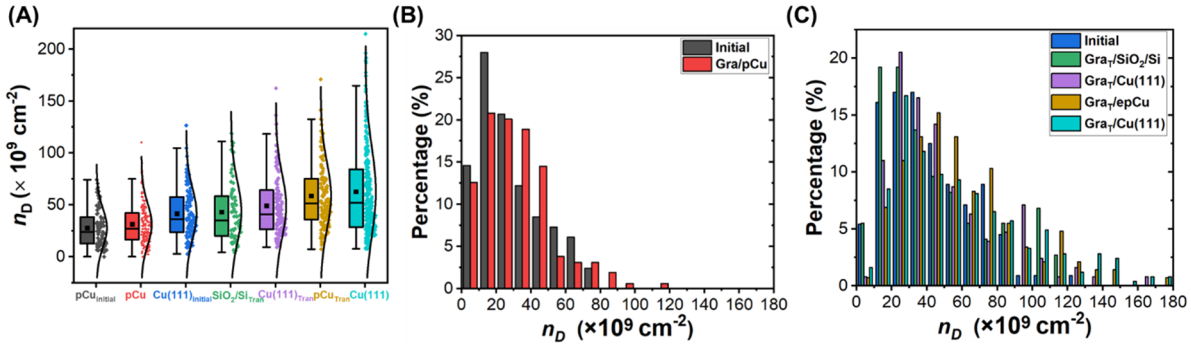

Figure 5. Statistical analysis of defect density (n_D) in graphene on different substrates before and after PFPA functionalization. (**A**) Box violin plots of n_D distribution. (**B**) Histograms of n_D values for Gra/pCu before (grey), and after PFPA functionalization (red). (**C**) Histograms of L_D values for Gra/Cu(111) before (blue), and after PFPA functionalization (turquois), and after PFPA functionalization for Gra_T/SiO_2/Si (green), Gra_T/Cu(111) (purple), and Gra_T/epCu (gold).

4. Discussions

Collectively, the results reveal a clear substrate-dependent reactivity of graphene toward PFPA functionalization. Graphene grown on pCu and Cu(111) exhibits markedly different reactivity toward PFPA functionalization. Gra/Cu(111) showed the highest reactivity, whereas Gra/pCu showed minimal reactivity. Transfer partially diminished or redistributed this reactivity, with transferred graphene on epCu displaying the most significant reactivity among the transferred samples. Below, we discuss the possible reasons for the overall reactivity trend: Gra/pCu < Gra_T/SiO_2/Si < Gra_T/Cu(111) < Gra_T/epCu < Gra/Cu(111).

4.1. Substrate-Induced Strain and Doping Effects

The Raman features of graphene grown on polycrystalline Cu and monocrystalline Cu(111) were compared. The correlation of G- and 2D-band positions (Figure 6A) reveals upshift for Gra/Cu(111) relative to Gra/pCu. The centroids for both bands also shift toward higher wavenumbers. These shifts are shown in the representative spectra in Figure 6B,C), where both the G and 2D bands for Gra/Cu(111) appear at higher wavenumbers than for Gra/pCu.

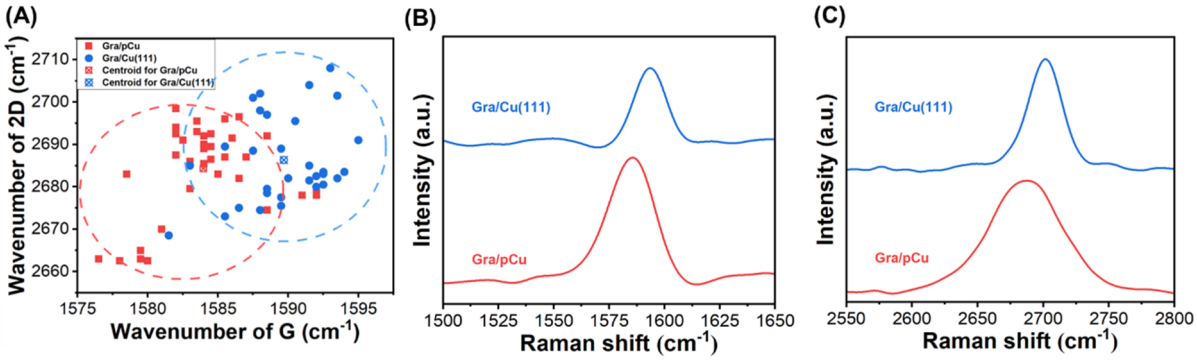

Figure 6. Raman spectral analysis of graphene grown on polycrystalline Cu and monocrystalline Cu(111). (**A**) Correlation plot of G- and 2D-band positions, with the centroid indicated as a red and a blue cross for Gra/pCu and Gra/Cu(111), respectively. Representative (**B**) G-band, and (**C**) 2D-band spectra highlighting the distinct peak positions.

Such wavenumber upshifts in the G and 2D modes are characteristic signatures of substrate-induced effects [33,35,42,43]. The upshifted G band indicates enhanced n-type doping due to stronger charge transfer from Cu(111) to graphene, while the upshifted 2D band suggests compressive strain arising from the epitaxial

relationship and better lattice matching between graphene and the Cu(111) substrate. In contrast, graphene on pCu exhibits comparatively lower band positions, consistent with weaker substrate coupling and less pronounced electronic or strain modulation. These results demonstrate that Cu(111) induces stronger substrate interactions, leading to greater charge transfer and strain effects compared to polycrystalline Cu, thereby contributing to the enhanced reactivity of Gra/Cu(111) observed during PFPA functionalization [33,35].

4.2. Morphology of Graphene on Various Substrates

Optical microscopy and AFM imaging both reveal distinct surface characteristics of graphene grown on pCu and Cu(111). As shown in Figure 7A, Gra/pCu exhibits rough and nonuniform morphology with an average AFM root mean square (RMS) roughness of 8.23 ± 0.92 nm. In contrast, Gra/Cu(111) displays smooth, relatively ordered surface morphology with RMS roughness of 1.87 ± 0.29 nm. From the larger area optical microscopy images, Gra/pCu surface shows interconnected network of grain boundaries (Figure 7A), whereas Gra/Cu(111) appears continuous and shows more homogeneous surface (Figure 7B). As the surface curvature could also lead to enhanced reactivity, the higher reactivity of Gra/Cu(111) than that of Gra/pCu toward PFPA reaction is therefore attributed to charge doping and strain [21,29,44–49].

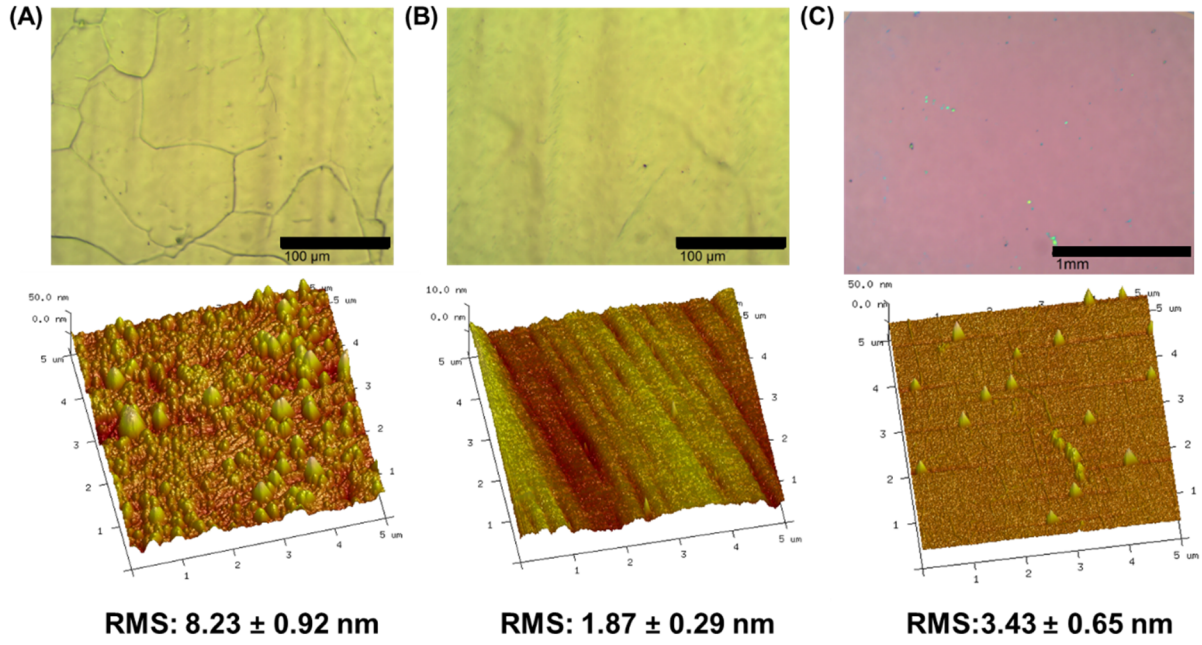

Figure 7. Optical microscopy (**top**) and AFM (**bottom**) images of (**A**) Gra/pCu, (**B**) Gra/Cu(111), and (**C**) $Gra_T/SiO_2/Si$. Additional images can be found in Figures S3 and S4.

For the transferred samples, the graphene morphology is governed by the surface morphology of the supporting substrates through conformal adhesion [44,50–53]. The RMS roughness values of Gra/epCu and Gra/Cu(111) were measured previously as 38.8 ± 12 nm and 21.0 ± 4.2 nm, respectively [37], and $Gra_T/SiO_2/Si$ shows a uniform, continuous graphene film with a significantly lower RMS roughness of 3.43 ± 0.65 nm (Figure 7C). These results indicate a correlation between the reactivity of transferred graphene and the roughness of the supporting substrates. Specifically, the higher surface roughness of Gra/epCu induces greater graphene corrugation, leading to enhanced reactivity of GraT/epCu among the transferred samples. As the substrate roughness decreases, the reactivity decreases, as observed for $Gra_T/Cu(111)$ and $Gra_T/SiO_2/Si$. Despite retaining the Cu(111) crystallographic orientation, $Gra_T/Cu(111)$ exhibits lower reactivity than $Gra_T/epCu$, which can be attributed to weaker graphene–substrate charge interaction in $Gra_T/Cu(111)$ after transfer, leading to reduced strain and charge-doping effects. In contrast, $Gra/SiO_2/Si$ shows the lowest reactivity, attributed to reduced surface roughness and/or distribution of charge puddles that passivates graphene reactivity [21,29,43]. Thus, for transferred substrates, graphene reactivity toward PFPA correlates with graphene roughness.

5. Conclusions

In this work, we carried out the photochemical reaction of PFPA with graphene on different substrates and investigated the role of supporting substrates in modulating graphene reactivity. Graphene grown on Cu(111)

exhibited the highest degree of functionalization, as evidenced by the largest increase in $\Delta I_D/I_G$ obtained from Raman spectroscopy and Raman mapping, along with decrease in L_D and increase in n_D. In contrast, graphene grown on polycrystalline Cu showed minimal reactivity toward PFPA reaction. Raman analyses further demonstrate that Cu(111) induces stronger charge transfer and higher strain in graphene compared to pCu, primarily due to superior lattice matching between graphene and the Cu(111) surface. These substrate-induced electronic and structural effects enhance graphene's reactivity toward the electron-deficient perfluorophenyl nitrene, leading to higher reactivity.

Upon transfer of graphene grown on Cu(111) to other substrates, including Cu(111), electropolished pCu, and SiO_2/Si, the reactivity decreased. The decreased reactivity is attributed to weakened graphene–substrate charge interactions after transfer, and the reactivity of transferred graphene correlates mainly with the surface roughness.

Overall, these findings establish substrate engineering as an effective and non-invasive method for tuning the chemical reactivity of graphene without the need for harsh activation conditions. By leveraging the intrinsic interaction between graphene and the substrate, this approach enables controlled covalent functionalization of graphene, offering a versatile approach for chemical modification of graphene.

Supplementary Materials: The following supporting information can be downloaded at: https://media.sciltp.com/articles/others/260318122437075 7/MI-26030002_Supplementary_Materials.pdf. Reference [54] is cited in the Supplementary Materials.

Author Contributions: J.T.: conceptualization, methodology, software, data curation, writing—original draft preparation, visualization, investigation, and validation; M.Y.: conceptualization, methodology, data curation, visualization, supervision, software, validation, writing—reviewing and editing. All authors have read and agreed to the published version of the manuscript.

Funding: The authors are grateful for the financial support from the National Science Foundation (CHE-2305006).

Data Availability Statement: Not applicable.

Acknowledgments: The authors thank Ji-Xin Cheng and Bethany Weinberg of Boston University for their kind help in Raman mapping.

Conflicts of Interest: The authors declare no conflict of interest.

Use of AI and AI-Assisted Technologies: During the preparation of this work, the authors used ChatGPT to assist with language editing of the manuscript. The authors reviewed and edited the content as necessary and take full responsibility for the content of the published article.

References

1. Liu, J.; Tang, J.; Gooding, J.J. Strategies for chemical modification of graphene and applications of chemically modified graphene. *J. Mater. Chem.* **2012**, *22*, 12435–12452.
2. Park, J.; Yan, M. Covalent functionalization of graphene with reactive intermediates. *Acc. Chem. Res.* **2013**, *46*, 181–189.
3. Stergiou, A.; Cantón-Vitoria, R.; Psarrou, M.N.; Economopoulos, S.P.; Tagmatarchis, N. Functionalized graphene and targeted applications–Highlighting the road from chemistry to applications. *Prog. Mater Sci.* **2020**, *114*, 100683.
4. Chua, C.K.; Pumera, M. Covalent chemistry on graphene. *Chem. Soc. Rev.* **2013**, *42*, 3222–3233.
5. Yan, M.; Cai, S.X.; Keana, J.F.W. Photochemical and Thermal Reactions of C60 with N-Succinimidyl 4-Azido-2,3,5,6-tetrafluorobenzoate: A New Method for Functionalization of C60. *J. Org. Chem.* **2002**, *59*, 5951–5954.
6. Liu, F.; Du, W.; Liang, Q.; Wang, Y.; Zhang, J.; Zhao, J.; Zhu, S. Synthesis of 4-aziridino[C60]fullerene-1,8-naphthalimide (C60-NI dyads) and their photophysical properties. *Tetrahedron* **2010**, *66*, 5467–5471.
7. Khalilov, M.; Tulyabaev, A.R.; Akhmetov, A.R.; Tuktarov, A.R. Synthesis and ^{13}C NMR features of N-substituted aziridino[60]fullerenes. *Russ. Chem. Bull.* **2016**, *64*, 2725–2730.
8. Gross, A.J.; Yu, S.S.; Downard, A.J. Two-component mixed and patterned films on carbon surfaces through the photografting of arylazides. *Langmuir* **2010**, *26*, 7285–7292.
9. Tanaka, M.; Sawaguchi, T.; Sato, Y.; Yoshioka, K.; Niwa, O. Surface modification of GC and HOPG with diazonium, amine, azide, and olefin derivatives. *Langmuir* **2011**, *27*, 170–178.
10. Choi, J.; Kim, K.-j.; Kim, B.; Lee, H.; Kim, S. Covalent functionalization of epitaxial graphene by azidotrimethylsilane. *J. Phys. Chem. C* **2009**, *113*, 9433–9435.
11. Strom, T.A.; Dillon, E.P.; Hamilton, C.E.; Barron, A.R. Nitrene addition to exfoliated graphene: A one-step route to highly functionalized graphene. *Chem. Commun.* **2010**, *46*, 4097–4099.
12. Vadukumpully, S.; Gupta, J.; Zhang, Y.; Xu, G.Q.; Valiyaveettil, S. Functionalization of surfactant wrapped graphene nanosheets with alkylazides for enhanced dispersibility. *Nanoscale* **2011**, *3*, 303–308.
13. Poe, R.; Schnapp, K.; Young, M.J.; Grayzar, J.; Platz, M.S. Chemistry and kinetics of singlet pentafluorophenylnitrene. *J. Am. Chem. Soc.* **1992**, *114*, 5054–5067.

14. Kotzyba-Hibert, F.; Kapfer, I.; Goeldner, M. Recent trends in photoaffinity labeling. *Angew. Chem. Int. Ed.* **1995**, *34*, 1296–1312.
15. Denis, P.A.; Iribarne, F. Monolayer and bilayer graphene functionalized with nitrene radicals. *J. Phys. Chem. C* **2011**, *115*, 195–203.
16. Bräse, S.; Gil, C.; Knepper, K.; Zimmermann, V. Organic azides: An exploding diversity of a unique class of compounds. *Angew. Chem. Int. Ed.* **2005**, *44*, 5188–5240.
17. Wang, X.; Liu, L.H.; Ramstrom, O.; Yan, M. Engineering nanomaterial surfaces for biomedical applications. *Exp. Biol. Med.* **2009**, *234*, 1128–1139.
18. Liu, L.H.; Yan, M. Perfluorophenyl azides: New applications in surface functionalization and nanomaterial synthesis. *Acc. Chem. Res.* **2010**, *43*, 1434–1443.
19. Liu, L.-H.; Yan, M. Functionalization of pristine graphene with perfluorophenyl azides. *J. Mater. Chem.* **2011**, *21*, 3273–3276.
20. Nagel, T.; Jurkiewicz, L.; Hauke, F.; Hirsch, A. Laser-Initiated Covalent Functionalization of Graphene Using Perfluorophenylazides with Local Addend-Binding Control. *Phys. Status Solidi Basic Res.* **2025**, *263*, 2500348.
21. Yang, X.; Chen, F.; Kim, M.A.; Liu, H.; Wolf, L.M.; Yan, M. On the Reactivity Enhancement of Graphene by Metallic Substrates towards Aryl Nitrene Cycloadditions. *Chem. Eur. J.* **2021**, *27*, 7887–7896.
22. Park, J.; Yang, X.; Wickramasinghe, D.; Sundhoro, M.; Orbey, N.; Chow, K.F.; Yan, M. Functionalization of pristine graphene for the synthesis of covalent graphene-polyaniline nanocomposite. *RSC Adv.* **2020**, *10*, 26486–26493.
23. Park, J.; Jin, T.; Liu, C.; Li, G.; Yan, M. Three-dimensional graphene–TiO_2 nanocomposite photocatalyst synthesized by covalent attachment. *ACS Omega* **2016**, *1*, 351–356.
24. Liu, L.-H.; Yan, M. Simple method for the covalent immobilization of graphene. *Nano Lett.* **2009**, *9*, 3375–3378.
25. Liu, L.-H.; Zorn, G.; Castner, D.G.; Solanki, R.; Lerner, M.M.; Yan, M. A simple and scalable route to wafer-size patterned graphene. *J. Mater. Chem.* **2010**, *20*, 5041–5046.
26. Park, J.; Jayawardena, H.S.N.; Chen, X.; Jayawardana, K.W.; Sundhoro, M.; Ada, E.; Yan, M. A general method for the fabrication of graphene–nanoparticle hybrid material. *Chem. Commun.* **2015**, *51*, 2882–2885.
27. Kong, N.; Park, J.; Yang, X.; Ramström, O.; Yan, M. Carbohydrate functionalization of few-layer graphene through microwave-assisted reaction of perfluorophenyl azide. *ACS Appl. Bio Mater.* **2018**, *2*, 284–291.
28. Liu, L.-H.; Lerner, M.M.; Yan, M. Derivitization of pristine graphene with well-defined chemical functionalities. *Nano Lett.* **2010**, *10*, 3754–3756.
29. Tu, J.; Yan, M. Enhancing the Chemical Reactivity of Graphene through Substrate Engineering. *Small* **2024**, *2024*, e2408116.
30. Criado, A.; Melchionna, M.; Marchesan, S.; Prato, M. The Covalent Functionalization of Graphene on Substrates. *Angew. Chem. Int. Ed.* **2015**, *54*, 10734–10750.
31. Yang, X.; Chen, F.; Kim, M.A.; Liu, H.; Wolf, L.M.; Yan, M. Using metal substrates to enhance the reactivity of graphene towards Diels-Alder reactions. *Phys. Chem. Chem. Phys.* **2022**, *24*, 20082–20093.
32. Tu, J.; Zhou, W.; Wolf, L.M.; Yan, M. Inverse-Electron-Demand Diels-Alder Reaction of Tropone with Graphene Supported on Cu(111). *Small* **2025**, *21*, e03669.
33. Zhang, X.; Luo, D.; Zhang, H.; Hwang, D.Y.; Park, S.O.; Li, B.-W.; Biswal, M.; Jiang, Y.; Huang, Y.; Kwak, S.K. Effect of copper substrate surface orientation on the reductive functionalization of graphene. *Chem. Mater.* **2019**, *31*, 8639–8648.
34. Plsek, J.; Kovaricek, P.; Vales, V.; Kalbac, M. Tuning the Reactivity of Graphene by Surface Phase Orientation. *Chem. Eur. J.* **2017**, *23*, 1839–1845.
35. Li, B.W.; Luo, D.; Zhu, L.; Zhang, X.; Jin, S.; Huang, M.; Ding, F.; Ruoff, R.S. Orientation-Dependent Strain Relaxation and Chemical Functionalization of Graphene on a Cu(111) Foil. *Adv. Mater.* **2018**, *30*, 1706504.
36. Perera, H.A.; Raviranga, N.G.H.; Ramstrom, O.; Yan, M. Trehalose-Functionalized Magnetic Affinity Probe Provides Biochemical Evidence of Nanoparticle Internalization in Mycobacteria. *ACS Infect. Dis.* **2025**, *11*, 2847–2858.
37. Tu, J.; Zhou, W.; Kiani, A.; Wolf, L.M.; Yan, M. Chemical Vapor Deposition of Monolayer Graphene on Centimeter-Sized Cu(111) for Nanoelectronics Applications. *ACS Appl. Nano Mater.* **2025**, *8*, 4926–4939.
38. Yang, X.; Yan, M. Removing contaminants from transferred CVD graphene. *Nano Res.* **2020**, *13*, 599–610.
39. Ferrari, A.C.; Basko, D.M. Raman spectroscopy as a versatile tool for studying the properties of graphene. *Nat. Nanotechnol.* **2013**, *8*, 235–246.
40. Cancado, L.G.; Jorio, A.; Ferreira, E.H.; Stavale, F.; Achete, C.A.; Capaz, R.B.; Moutinho, M.V.; Lombardo, A.; Kulmala, T.S.; Ferrari, A.C. Quantifying defects in graphene via Raman spectroscopy at different excitation energies. *Nano Lett.* **2011**, *11*, 3190–3196.
41. Lucchese, M.M.; Stavale, F.; Ferreira, E.M.; Vilani, C.; Moutinho, M.d.O.; Capaz, R.B.; Achete, C.A.; Jorio, A. Quantifying ion-induced defects and Raman relaxation length in graphene. *Carbon* **2010**, *48*, 1592–1597.
42. Lee, J.E.; Ahn, G.; Shim, J.; Lee, Y.S.; Ryu, S. Optical separation of mechanical strain from charge doping in graphene. *Nat. Commun.* **2012**, *3*, 1024.

43. Wang, Q.H.; Jin, Z.; Kim, K.K.; Hilmer, A.J.; Paulus, G.L.; Shih, C.J.; Ham, M.H.; Sanchez-Yamagishi, J.D.; Watanabe, K.; Taniguchi, T.; et al. Understanding and controlling the substrate effect on graphene electron-transfer chemistry via reactivity imprint lithography. *Nat. Chem.* **2012**, *4*, 724–732.
44. Wu, Q.; Wu, Y.; Hao, Y.; Geng, J.; Charlton, M.; Chen, S.; Ren, Y.; Ji, H.; Li, H.; Boukhvalov, D.W.; et al. Selective surface functionalization at regions of high local curvature in graphene. *Chem. Commun.* **2013**, *49*, 677–679.
45. Deng, S.; Rhee, D.; Lee, W.K.; Che, S.; Keisham, B.; Berry, V.; Odom, T.W. Graphene Wrinkles Enable Spatially Defined Chemistry. *Nano Lett.* **2019**, *19*, 5640–5646.
46. Giovannetti, G.; Khomyakov, P.A.; Brocks, G.; Karpan, V.V.; van den Brink, J.; Kelly, P.J. Doping graphene with metal contacts. *Phys. Rev. Lett.* **2008**, *101*, 026803.
47. Kong, L.; Bjelkevig, C.; Gaddam, S.; Zhou, M.; Lee, Y.H.; Han, G.H.; Jeong, H.K.; Wu, N.; Zhang, Z.; Xiao, J. Graphene/substrate charge transfer characterized by inverse photoelectron spectroscopy. *J. Phys. Chem. C* **2010**, *114*, 21618–21624.
48. Khomyakov, P.; Giovannetti, G.; Rusu, P.; Brocks, G.V.; Van den Brink, J.; Kelly, P.J. First-principles study of the interaction and charge transfer between graphene and metals. *Phys. Rev. B.* **2009**, *79*, 195425.
49. Chen, C.; Avila, J.; Asensio, M.C. Chemical and electronic structure imaging of graphene on Cu: A NanoARPES study. *J. Phys. Condens. Matter* **2017**, *29*, 183001.
50. Zhou, L.; Liao, L.; Wang, J.; Yu, J.; Li, D.; Xie, Q.; Liu, Z.; Yang, Y.; Guo, X.; Liu, Z. Substrate-Induced Graphene Chemistry for 2D Superlattices with Tunable Periodicities. *Adv. Mater.* **2016**, *28*, 2148–2154.
51. Cullen, W.G.; Yamamoto, M.; Burson, K.M.; Chen, J.-H.; Jang, C.; Li, L.; Fuhrer, M.S.; Williams, E.D. High-fidelity conformation of graphene to SiO 2 topographic features. *Phys. Rev. Lett.* **2010**, *105*, 215504.
52. Li, T.; Zhang, Z. Substrate-regulated morphology of graphene. *J. Phys. D Appl. Phys.* **2010**, *43*, 075303.
53. Zhang, Y.; Heiranian, M.; Janicek, B.; Budrikis, Z.; Zapperi, S.; Huang, P.Y.; Johnson, H.T.; Aluru, N.R.; Lyding, J.W.; Mason, N. Strain modulation of graphene by nanoscale substrate curvatures: A molecular view. *Nano Lett.* **2018**, *18*, 2098–2104.
54. Negrito, M.; Elinski, M.B.; Hawthorne, N.; Pedley, M.P.; Han, M.; Sheldon, M.; Espinosa-Marzal, R.M.; Batteas, J.D. Using Patterned Self-Assembled Monolayers to Tune Graphene–Substrate Interactions. *Langmuir* **2021**, *37*, 9996–10005.

Article

Understanding the Surface Oxidation of Ag Nanocrystals under Different Environmental Conditions

Kyle D. Gilroy [1], Yutong Wang [2], and Younan Xia [1,2,3,4,*]

[1] The Wallace H. Coulter Department of Biomedical Engineering, Georgia Institute of Technology and Emory University, Atlanta, GA 30332, USA
[2] School of Chemistry and Biochemistry, Georgia Institute of Technology, Atlanta, GA 30332, USA
[3] Department of Materials Science and Engineering, Johns Hopkins University, Baltimore, MD 21218, USA
[4] Department of Biomedical Engineering, Johns Hopkins University, Baltimore, MD 21205, USA
* Correspondence: yxia70@jh.edu

Received: 3 March 2026; Revised: 17 March 2026; Accepted: 20 March 2026; Published: 23 March 2026

Abstract: In many cases, the presence of a shell of surface oxide detrimentally alters the properties of nanomaterials, rendering them ineffective for the targeted applications. This issue is yet to be addressed because the growth and removal of oxide(s) from the surface of nanomaterials is still poorly understood. In this article, we used vapor-phase-derived Ag nanocrystals with controlled sizes to elucidate the mechanisms of surface oxidation by exposing them to ambient atmosphere, aqueous environments, and ethylene glycol. Our experimental data suggested that the thickness of an oxide shell directly correlated with the extent of plasmon damping, and the optical properties of nanocrystals below 8 nm in size were more drastically affected by the presence of an oxide shell relative to larger counterparts. In addition, we found that aqueous environments with a relatively high pH gave rise to higher rates of oxidation. The time-dependent changes in optical properties were also validated using theoretical simulations based on the discrete dipole approximation. We concluded this article by discussing three different strategies for effectively removing the surface oxide, including decomposition through thermal annealing, wet-chemical reduction through the addition of a reducing agent, and decomposition and/or reduction by electron irradiation.

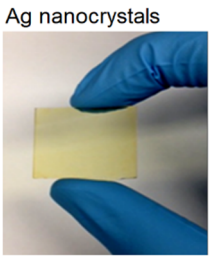

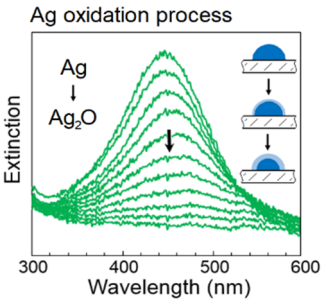

Keywords: oxidation; silver; nanocrystal; plasmon; discrete dipole approximation

1. Introduction

Oxidation is a redox reaction that involves the transfer of electrons from one chemical species to another. This fundamental process can be manipulated strategically to carry out vital electrochemical catalytic reactions, or to engineer the shape and structure of colloidal nanocrystals [1,2]. In other contexts, oxidation can also be considered a barrier, especially when structural materials such as steel are exposed to an oxidative environment, to suppress the continued formation of new materials (e.g., iron oxides in the case of steel) with unfavorable properties. Analogous issues arise in nanotechnology, where materials with nanoscale dimensions have an even higher susceptibility to oxidative environments such as air filled with oxygen or sulfur-containing compounds. Nanomaterials comprised of metals such as Fe, Ni, and Co can react with oxygen to generate metal oxides [3–5], while other metals such as Al, Cu, and Ag often form ultrathin, self-terminating oxide layers on the surface that can, in turn, protect the interior of the structure from further oxidation but at the same time hinder their performance in applications that demand pure metal interfaces [6–8]. Despite the rich history and great amount of work dedicated to the study of surface oxidation, very little is known about the kinetics, mechanisms, dependence on size down to the nanoscale regime, and strategies for preventing or removing the surface oxides.

In this study, we focused on the use of Ag nanocrystals supported on solid substrates as a model system to elucidate the nanoscale size effects and mechanisms that govern surface oxidation. It is worth pointing out that investigations into the oxidation of Ag date as far back as 1887, when Le Chatelier demonstrated the reversible

conversion between Ag and its oxidized form Ag_2O [9]. It was later discovered by Lewis in 1905 that the decomposition of Ag_2O was autocatalytic in nature [10]. In 2002, our group utilized the sensitive localized surface plasmon resonance (LSPR) of colloidal Ag nanocrystals (spectrally located in the visible region) as a direct means to monitor the surface oxidation process [8]. It is generally accepted that the oxidation involves the reaction between surface Ag atoms and gaseous O_2, which can be represented as $4\ Ag + O_2 \rightarrow 2\ Ag_2O$ [10–12]. However, limited work has been conducted to elucidate the mechanisms of oxide formation on Ag nanocrystals, and subsequently, how the oxides degrade the unique optical and chemical properties of nanomaterials. This gap in research likely stems from the fact that nanocrystals generated via wet-chemical methods as colloids are less than ideal for confidently quantifying the surface oxidation process, as they are commonly covered by a multitude of ions, organic capping agents and/or stabilizers, impurities from the solvent, and pre-adsorbed gas molecules. These adsorbates not only redefine the surface energy landscape of the nanocrystals and act as physical barriers to surface reactions, but also, more significantly, influence the optical and chemical properties [13].

To circumvent some of these drawbacks, a number of groups have shifted their focus to Ag nanocrystals supported on solid substrates. In these cases, the Ag nanocrystals can be fabricated *in vacuo* in the absence of the aforementioned chemical species that can obfuscate the oxidation mechanism. Furthermore, like a colloidal system, the ultrasensitive nature of LSPR (in terms of peak position and intensity) can still be used to track and quantify oxide formation [14]. In one study, Kalyanaraman and co-workers examined the oxidation of Ag nanocrystals (supported on SiO_2) formed through pulsed laser deposition (PLD). They found that indoor ambient air conditions led to a drastic change in both the composition and morphology, and subsequently, pronounced LSPR damping [15]. Sukhishvili and co-workers obtained a similar result for colloidal Ag nanocrystals deposited on a glass support and showed that the oxidation process led to deleterious effects in terms of surface-enhanced Raman spectroscopy (SERS), where the enhancement factor dropped by three orders of magnitude after the formation of a sub-monolayer of Ag_2O [11]. In this study, we investigate the oxidation process by subjecting size-controlled Ag nanocrystals on amorphous SiO_2 (a-SiO_2) supports to a variety of media to elucidate the nano-size effects and chemical mechanisms that govern Ag surface oxidation. We also demonstrate effective means for removing the oxide layer without compromising the optical properties of the nanocrystals.

2. Experimental Section

2.1. Chemicals and Materials

Silver (Ag, 99.99%), nitric acid (HNO_3), sodium hydroxide (NaOH), ethylene glycol (EG), amorphous SiO_2 (a-SiO_2) were all obtained from Sigma-Aldrich (St. Louis, MO, USA) and used as received. The SiO_2 TEM grids were purchased from TEMwindows.com (West Henrietta, NY, USA) with catalog number SO100-A40Q33. The deionized (DI) water used in the experiments was obtained from a Millipore ultrapure water system (Billerica, MA, USA) with a resistivity of 18.2 MΩ·cm at room temperature.

2.2. Synthesis of Ag Nanocrystals Supported on a-SiO_2

The Ag nanocrystals were prepared via thermal evaporation of Ag onto amorphous SiO_2 substrates following a previously reported procedure [16], in which the deposition conditions and thickness calibration were both described. Briefly, Ag was thermally evaporated from a tungsten boat to form Ag films with effective thicknesses of approximately 1.7, 0.5, 0.1, and 0.05 nm. The films were subsequently annealed at 600 °C for 2 min under vacuum and then cooled to room temperature over 2 h without breaking vacuum. During annealing, the continuous Ag films dewetted and evolved into discrete nanocrystals.

2.3. Characterizations

Transmission electron microscopy (TEM) was carried out with a Hitachi HT7700 microscope (Tokyo, Japan). For TEM analysis, the same deposition and annealing procedure described above were carried out on Si grids coated with a 40 nm a-SiO_2 layer. Optical extinction spectra were measured using a Cary 60 ultraviolet–visible (UV–vis) spectrometer. Samples were mounted inside the spectrometer so that the incident light beam was normal to the substrate surface. X-ray photoelectron spectroscopy (XPS) analyses were conducted using a Thermo K-Alpha system (Waltham, MA, USA). High-angle annular dark-field (HAADF) scanning transmission electron microscopy (STEM) images were acquired using a spherical aberration-corrected Hitachi HD2700 STEM microscope operated at 200 keV.

2.4. pH-Dependent Oxidation Studies

The pH of water derived from a Millipore system was controlled by adding HNO_3 or NaOH to decrease or increase the pH, respectively. After pH adjustment, the pH was measured using a standard electrode-based pH meter. To measure the pH-dependent rate of oxidation for the 4-nm Ag nanocrystals, the samples were placed in cuvettes filled with water with different pH values. It is found that samples derived from different batches would give inconsistent rates of oxidation because there always exists some degree of variation among different batches. To mitigate this issue, we deposited Ag on a relatively large piece of glass (~2.5 cm × 1 cm), annealed the sample, and then used a diamond scribe to cut the substrate into three similar-sized samples. Then, each sample was placed in a cuvette containing 1 mL of water with a pre-measured pH, and optical absorbance spectra were measured periodically at intervals of 3 min. It is assumed that each of the three pieces derived from the same batch had the same initial LSPR spectrum, and thus, this initial spectrum was used to represent the first data point for each of the three samples reported.

2.5. Formation of Thick Oxide Shells

To grow a thick oxide shell, Ag nanocrystals were first prepared and deposited on SiO_2 TEM grids, which were then mounted on a standard TEM holder. Then, the holder was inserted into a ZONE Desktop Sample Cleaner and Desiccator for SEM/TEM for roughly 5 min. The sample was then transferred to an aberration-corrected Hitachi HD-2700 TEM to monitor changes under the 200 keV electron beam.

3. Results and Discussion

3.1. Synthesis and Characterization of Ag Nanocrystals

We prepared the Ag nanocrystals by thermally evaporating Ag onto the surface of *a*-SiO_2 to form Ag films (Figure 1, top) following a reported procedure [16]. Specifically, we prepared Ag films of ca. 1.7, 0.5, 0.1, and 0.05 nm in effective thicknesses, annealed the samples at 600 °C for 2 min and then cooled to room temperature under vacuum. In each case, heating caused the film to evolve into discrete nanocrystals, changing the sample color from purple to vibrant yellow (Figure 1, bottom).

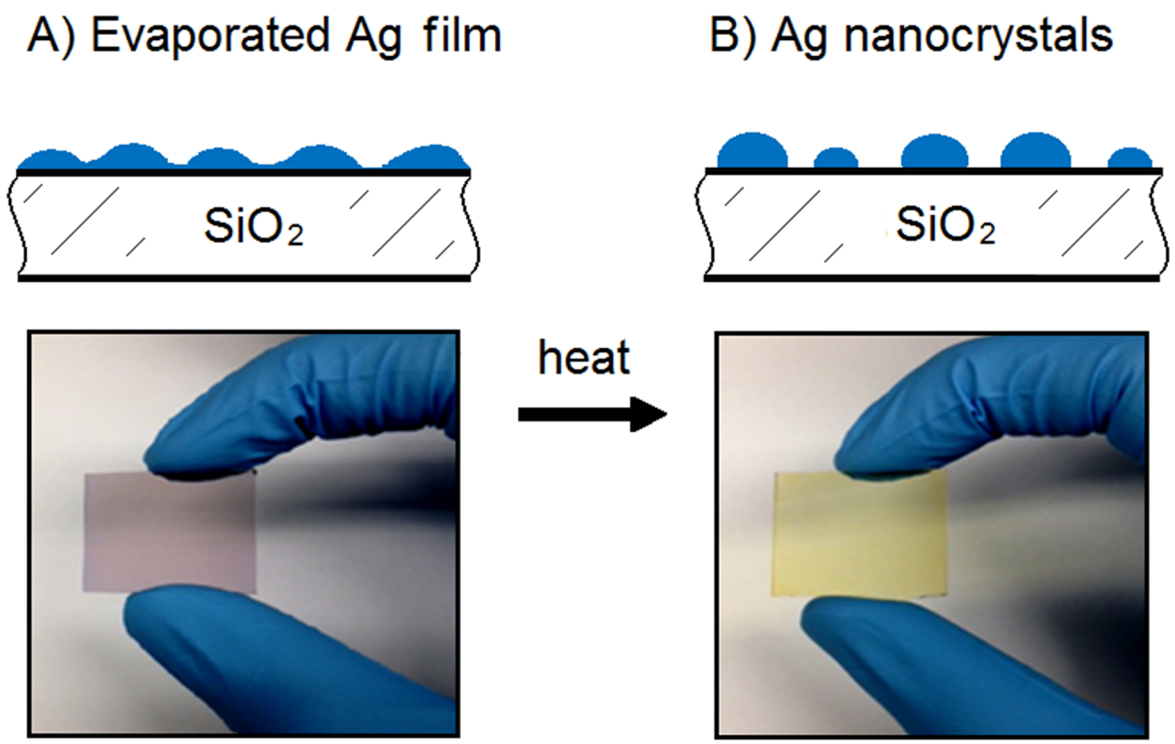

Figure 1. (**A**) Schematic illustration of a 1.7-nm Ag film deposited on an *a*-SiO_2 substrate by thermal evaporation with a corresponding photograph showing that the film appeared purple. (**B**) Upon annealing *in vacuo* at 600 °C and then cooling to room temperature, the Ag film dewetted and broke into discrete Ag nanocrystals, causing the sample to turn yellow.

Transmission electron microscopy (TEM) images revealed that the Ag nanocrystals derived from Ag films with effective thicknesses of ca. 1.7, 0.5, and 0.1 nm, respectively, had average diameters of 16, 8, and 4 nm (Figure 2A–C). Their size distributions were shown in Figure 2D. Note that the error in deposition thickness can be up to ±0.2 nm, and because the average diameter of the resultant particles trended logarithmically with deposition thickness [16], the average size can have an error of roughly ±2 nm. As another note, our group previously established that the internal defect structure (i.e., number and orientation of twin defects) trended with particle size post equilibration [16]. Under these conditions, Ag nanocrystals with icosahedral, decahedral, and single-crystal structures were found to be favored at sizes below 7 nm, between 7–11 nm, and greater than 11 nm, respectively. The optical properties of the Ag nanocrystals were further examined using UV–vis spectroscopy. Figure S1 shows the extinction spectra of Ag nanocrystals prior to oxidation. The LSPR peaks of all samples investigated in this work were positioned between 430–450 nm, and the LSPR peak intensity increased in proportion to the thickness of the Ag film.

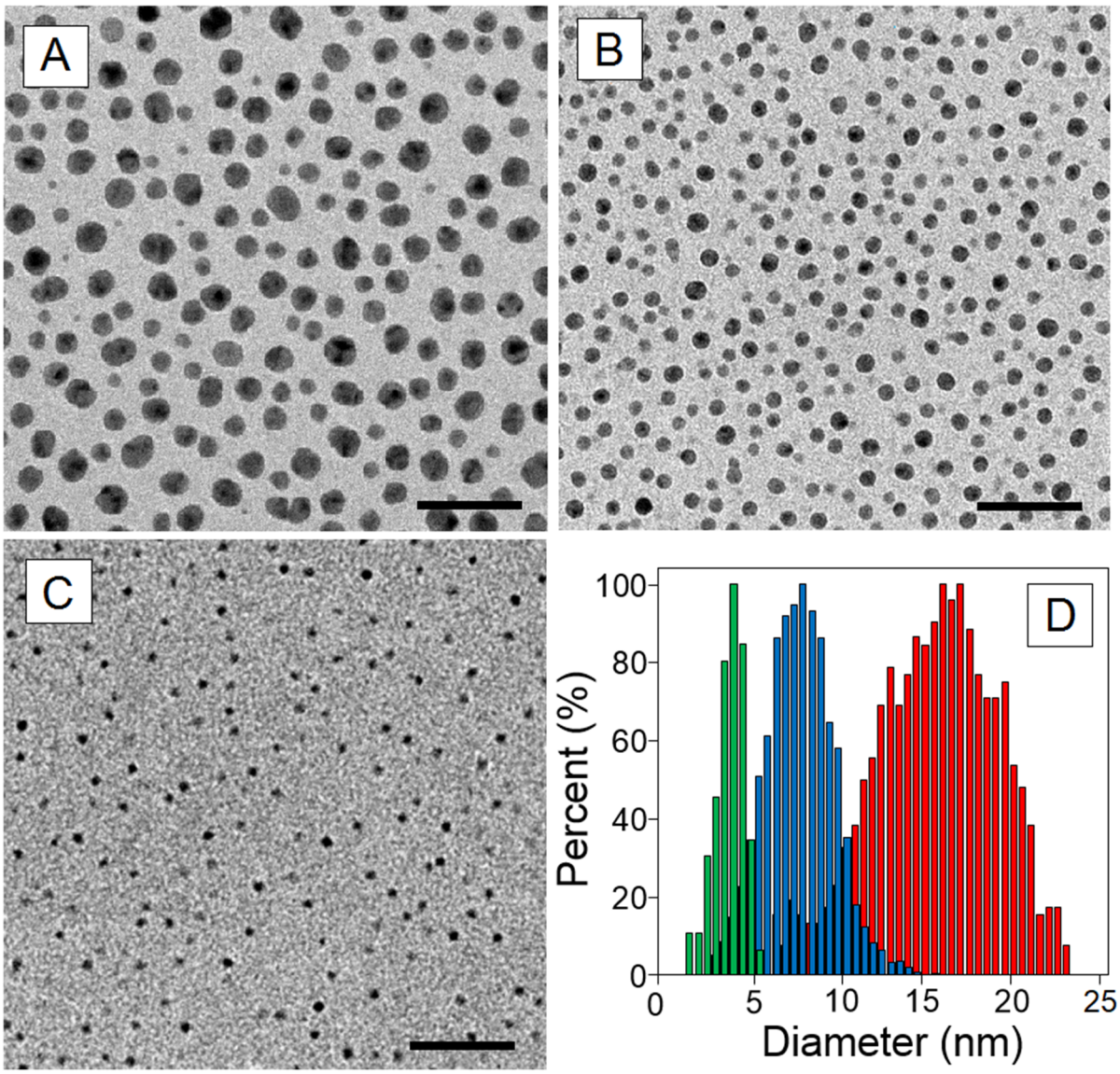

Figure 2. TEM images of Ag nanocrystals obtained by annealing Ag films of (**A**) 1.7; (**B**) 0.5; and (**C**) 0.1 nm, respectively, in thickness. (**D**) Histograms overlaid to show the size distributions of the Ag nanocrystals resulting from the films of 1.7, 0.5, and 0.1 nm in thickness, as represented by orange, blue, and green colors. All scale bars are 50 nm.

3.2. Oxidation Behaviors of Ag Nanocrystals under Diverse Conditions

We first examined the oxidation behavior of the Ag nanocrystals under ambient air conditions (23 °C, 50–60% humidity) by monitoring changes to their optical spectra in real time. Remarkably, for Ag nanocrystals of 4 nm or 8 nm in size, the changes could even be observed with the naked eye, with the sample changing from yellow to

transparent. For all three samples, the changes in spectral profile appeared to reach a steady state after 14 h, suggesting that (i) smaller particles generated thicker oxide layers and thereby underwent a greater degree of LSPR damping or (ii) the thickness of the oxide layer was size-independent, but the LSPR intensity of smaller particles was more heavily impacted by oxidation. For the LSPR peak position and intensity of the 16-nm Ag nanocrystals, only a slight red-shift and minor decrease in intensity were observed (Figure 3A). In the case of 8-nm Ag nanocrystals, optical changes consisted of a LSPR peak intensity drop of ca. 30% and a spectral red-shift of ca. 3 nm (Figure 3B). The greatest changes in optical signal corresponded to a ca. 85% drop in LSPR peak intensity along with a red-shift of ca. 40 nm, which were observed for Ag nanocrystals with an average diameter of 4 nm or below (Figure 3C).

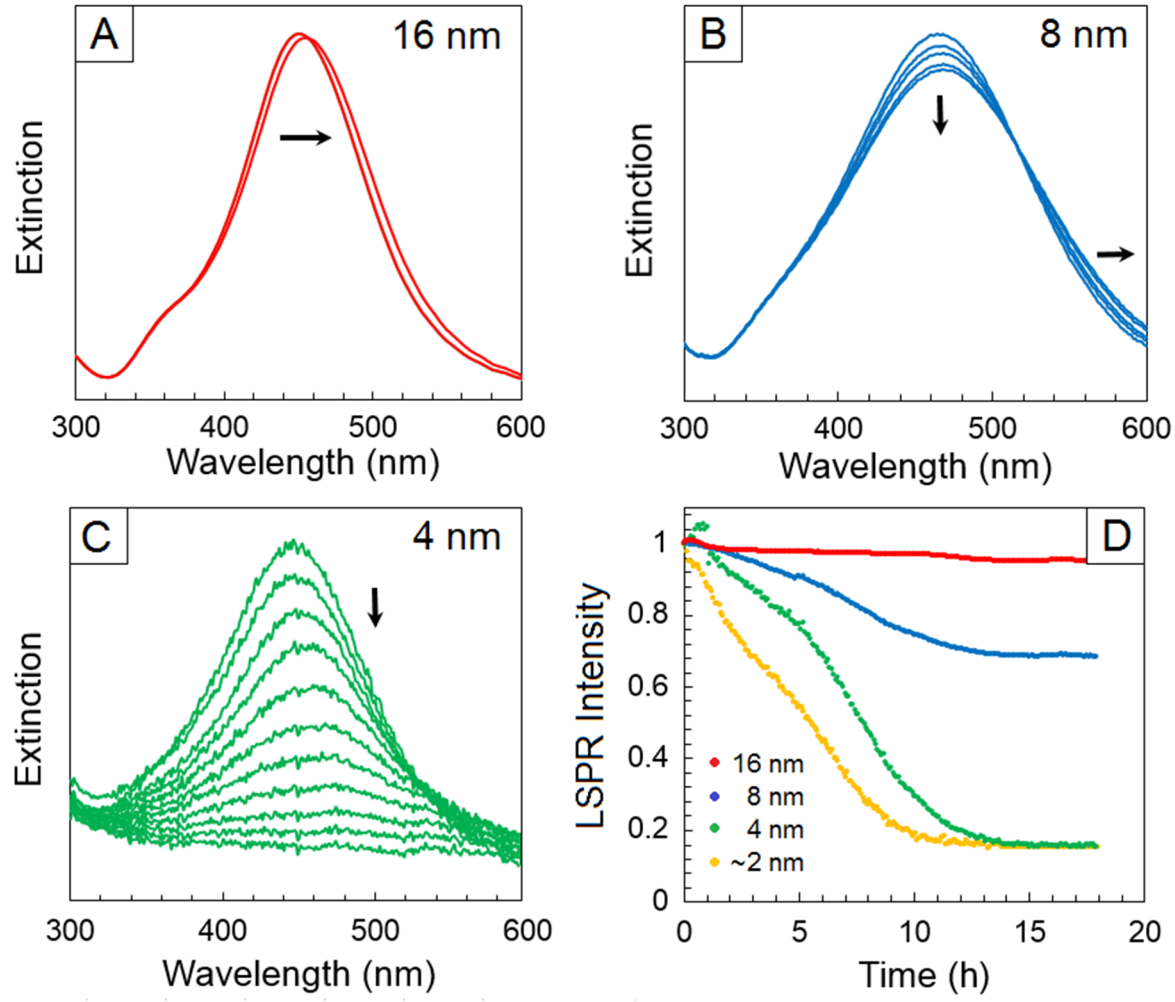

Figure 3. Spectral evolution of Ag nanocrystals with average diameters of (**A**) 16; (**B**) 8; and (**C**) 4 nm; respectively, upon exposure to the ambient air for up to 18 h. (**D**) Plots comparing the normalized extinction at the LSPR peak position as a function of the exposure time, revealing that atmospheric oxidation impacts the smaller particles more significantly.

To elucidate the role played by surface oxidation in determining the optical properties of Ag nanocrystals, we carried out simulations using the discrete dipole approximation (DDA) method [17]. To simulate the changes in LSPR upon oxidation, we designed a continuum model, as illustrated in Figure 4A, which consisted of an individual Ag_2O-coated Ag nanocrystal supported on a SiO_2 slab. At all sizes investigated, the calculated results indicated that increasing the thickness of the oxide shell led to peak damping and a slight red-shift, as shown for a 4-nm particle in Figure 4B. A red-shift in the LSPR band was generally attributable to an increase in the refractive index of the surrounding medium, which is consistent with the change from air to Ag_2O. In addition to this refractive index effect, the damping of the LSPR can be attributed to interband transitions in Ag_2O. Specifically, the band gap of Ag_2O falls within the visible region, enabling optical excitation of interband transitions that overlap with the plasmon resonance. These transitions introduce a significant imaginary component (ε_2) to the dielectric function, leading to additional absorption and energy dissipation, and thus damping the LSPR. The $\varepsilon_{Ag}(\lambda)$ and $\varepsilon_{Ag_2O}(\lambda)$ can be found in Figure S2. The degree of peak damping was found to trend exponentially with Ag_2O

thickness, while the LSPR peak intensities of smaller particles were more affected by oxide formation (Figure 4C). The inset in Figure 4C shows the changes in LSPR peak intensity as the thickness of the Ag_2O shell was increased up to 0.5 nm, with the experimentally measured LSPR damping, which was used to estimate an effective oxide thickness based on the DDA simulations, shown as squares. The peak intensity of the 4-nm Ag nanocrystals showed a drop of ca. 80% when the thickness of Ag_2O reached 0.25 nm (roughly one monolayer). However, for the same thickness of Ag_2O, the LSPR peak intensities of the 8- and 16-nm nanocrystals were only damped by ca. 70% and 30%, respectively; both values were significantly greater than what was observed experimentally (30% and 3%, respectively). These discrepancies suggested that only sub-monolayers of oxide were formed on the larger nanocrystals, as reported previously [11,18]. Since the surface free energy (and thus reactivity) of nanoparticles trended exponentially with size [19], it was feasible that the smaller nanocrystals were more prone to oxidation due to their higher reactivity.

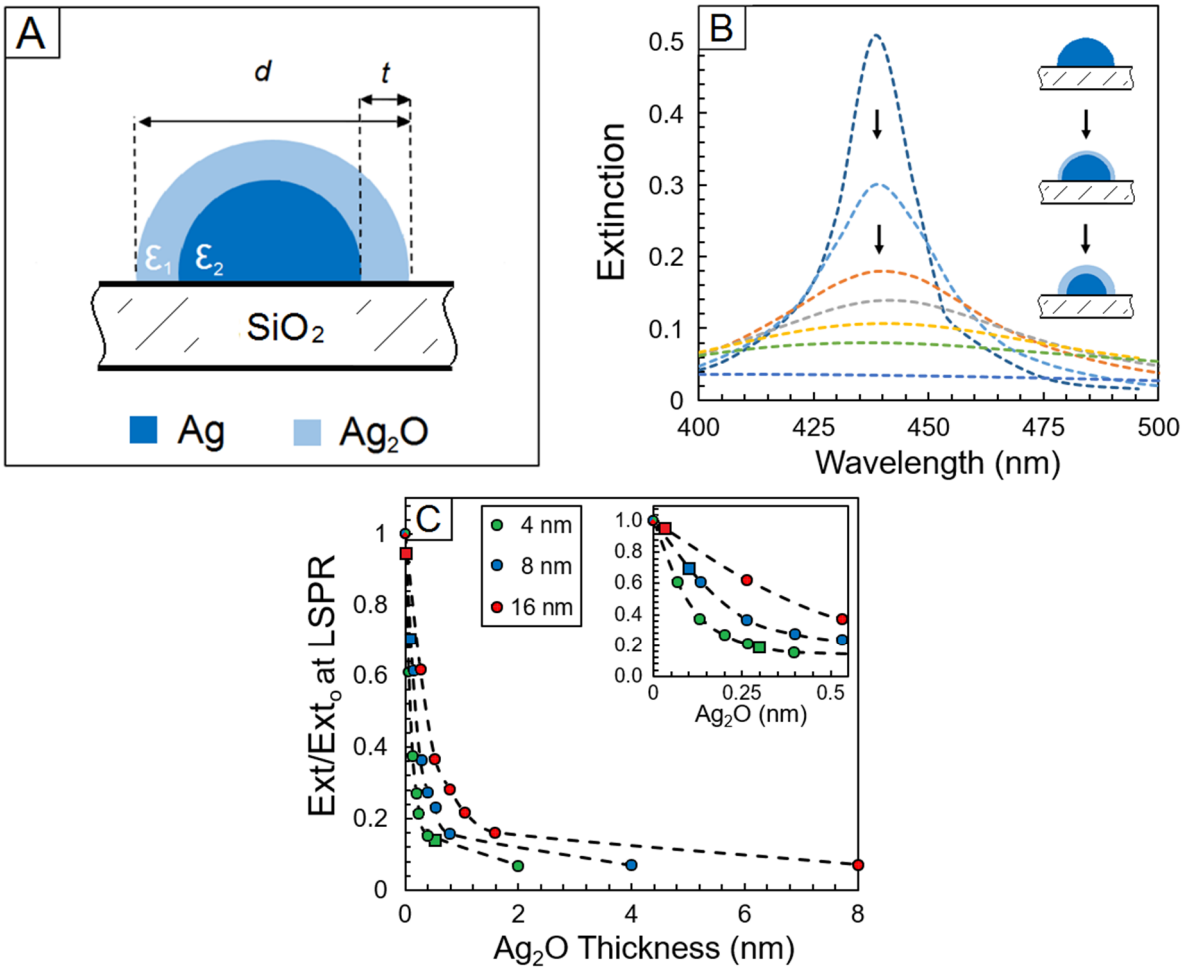

Figure 4. (**A**) Schematic illustration showing the continuum model on which all DDA simulations are based. The model consists of a Ag_2O-coated Ag hemisphere supported on a SiO_2 substrate. (**B**) Calculated extinction spectra of a 4-nm Ag hemisphere undergoing oxidation, where the increase in Ag_2O thickness leads to increased damping. (**C**) Theoretical trends showing the fractional change in LSPR peak intensity as a function of increasing Ag_2O thickness for Ag nanocrystals of 4, 8, and 16 nm in diameter. The experimentally measured LSPR damping, which was used to estimate an effective oxide thickness based on the DDA simulations, is represented by squares. The inset in (**C**) shows a zoomed-in view of the fractional change in peak intensity as the thickness of the Ag_2O shell is increased up to 0.5 nm.

LSPR damping upon the formation of an ultrathin oxide layer was similar to what has been observed when the surface of a metal nanocrystal with LSPR in the visible regime (e.g., Au, Ag, and Cu) is conformally coated with a platinum-group metal such as Pt, Pd, or Ir [20,21]. In essence, when the overlayer is sufficiently thick, it shields the inner core and severely damps the LSPR. In a similar fashion, formation of an ultrathin Ag_2O shell substantially damped the LSPR. It is important to note that the damping effect (due to oxide shell formation) is not unique to supported nanocrystals as our simulations also showed that 4-nm spherical Ag nanocrystals (i.e., reminiscent of Ag

colloids) also underwent substantial damping after the formation of a 0.25-nm complete Ag_2O shell (Figure S3). However, while the LSPR peak position and shift matched the experimental data, the calculated linewidth, and thus theoretical damping constant (Γ) was underestimated ($\Gamma_{exp} \sim 4\Gamma_{theory}$), as expected from the dielectric constants provided by Johnson and Christy [22]. In addition, further peak broadening is expected from enhanced electron-surface scattering for nanoparticles smaller than the electron mean-free path of bulk Ag ($l_{Ag}^{\infty} = 52$ nm) [23,24]. This effect was evident when the full width at half maximum (FWHM) of the LSPR peaks measured from the 4- and 16-nm Ag nanocrystals were compared, where the FWHM of the 4 nm nanocrystals was broader by 14 nm when compared to those of 16 nm in size (Figure S4).

To further evaluate the role of the surrounding medium, we next examined the oxidation behavior of the Ag nanocrystals in liquid environments. In practical applications, plasmonic nanocrystals are often used in solvents such as water or polyols [13,19]. To this end, it is critical to know how Ag nanocrystals respond to these environments as well. As another advantage of our system, the relatively strong interaction between the Ag nanocrystals and the substrate allowed us to immerse the sample in a solution prepared with a specific pH, ionic strength, and/or dielectric constant and then monitored the changes caused by the liquid environment [25]. Similar to the air-exposure experiments, we related the changes in optical properties to the thickness of the oxide grown at the surface of the Ag nanocrystals. All experiments involved submerging the samples in the liquid and placing them against the inside wall of a cuvette with the nanocrystal side of the sample facing the bulk of the solution. It should be noted that removing samples from water and allowing them to dry would cause some of the particles to lift off the surface. However, when the samples were submerged in water and then subjected to ultrasonication, the sample color remained bright yellow for hours (in the case of the 16-nm structures), suggesting that particles left the surface at a negligible rate during the oxidation experiments.

Realizing these aforementioned advantages, we investigated the oxidation of the 4-nm Ag nanocrystals in water and ethylene glycol (EG) and compared the results with what was obtained in the case of air (Figure 5A). To make a quantitative comparison among the three media in terms of oxidation rate, we derived rate constants based on the time-dependent change in LSPR peak intensity. Specifically, the time-dependent LSPR peak intensity changes were fitted using a first-order exponential decay function. The rate constant can then be extracted from the slope of the linear plot of $-\ln(I/I_0)$ versus time (Figure S5). The obtained rate constants ares primarily used for comparative analysis among different chemical conditions. The Ag nanocrystals exposed to EG showed the slowest oxidation rate, likely due to a number of effects but primarily from the formation of EG multilayers that could prevent the surface atoms from interacting with the oxygen dissolved in EG [26]. These adsorbed EG multilayers, with n and k of 1.4 and 4.3×10^{-8} at 450 nm [27], respectively, were not expected to induce a time-dependent change in optical properties. Furthermore, EG is a well-known reducing agent [28], which provides an additional measure against oxidation. In contrast, nanocrystals exposed to water showed the fastest rate of oxidation, where a steady state was reached within 1 h (pH = 6.8) with respect to the change in LSPR peak intensity.

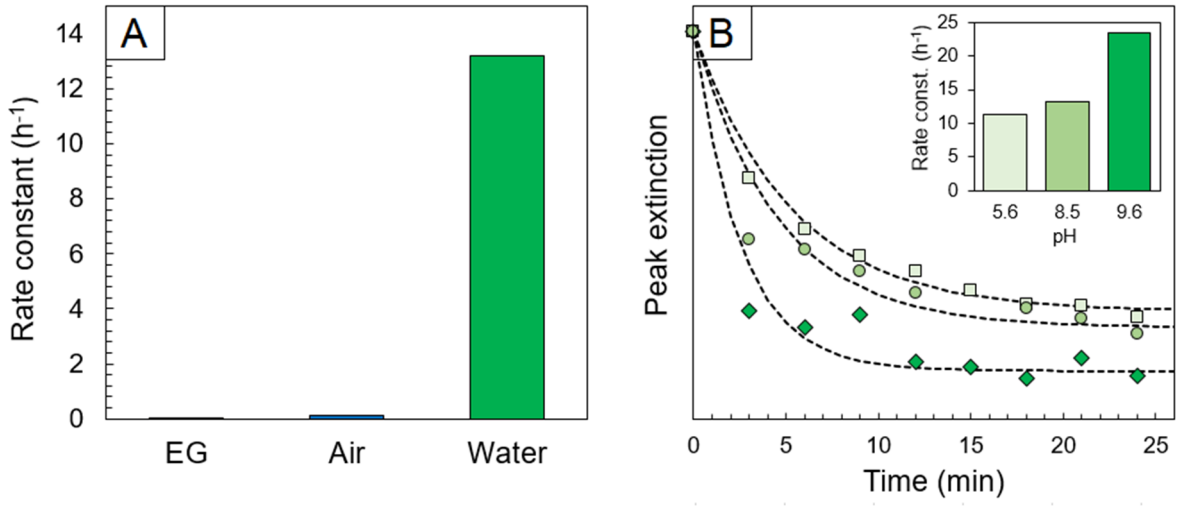

Figure 5. (**A**) Bar graph comparing the oxidation rate constant of 4-nm Ag nanocrystals in ethylene glycol (EG), air, and water (pH = 8.5). (**B**) Scatter plot showing the decrease in extinction intensity at the normalized LSPR peak for 4-nm Ag nanocrystals when subjected to aqueous environments at three different pH values (5.6, 8.5, and 9.6).

To further investigate the chemical mechanism, we measured the oxidation rate of the Ag nanocrystals derived from samples of the same batch in aqueous systems with different pH values. Our experimental results

clearly demonstrated that the oxidation rates correlated positively with increasing pH (Figure 5B). However, it should be noted that the rate of oxidation varied greatly between different batches, illustrating the high sensitivity of this process. Based on our results, we believed that the enhanced oxidation rate in water, relative to air and EG, was likely due to the high concentration of hydroxide ions (OH^-). This suggested that the oxidation process was accelerated in alkaline solutions due to the presence of OH^- species as depicted in Equations (1) and (2), in which the hydroxyl species are consumed in (1) and regenerated in (2). This led to the formation of AgOH that could easily decompose into Ag_2O and H_2O according to Equation (3). Taken together, these steps constitute the overall reaction scheme shown in Equation (4). For the same reason, oxidation under the ambient air conditions could also be driven by the presence of water molecules, which is supported by the work of Jiu and co-workers who showed that electrical contacts comprised of Ag-nanowire films oxidized more rapidly when exposed to atmospheric conditions at relatively high humidity [29].

$$4Ag + 4OH^- \rightarrow 4AgOH + 4e^- \quad (1)$$

$$2H_2O + O_2 + 4e^- \rightarrow 4OH^- \quad (2)$$

$$4AgOH \rightarrow 2Ag_2O + 2H_2O \quad (3)$$

$$4Ag + O_2 \rightarrow 2Ag_2O \quad (4)$$

To ensure that the observed oxidation behavior was intrinsic rather than arising from extrinsic factors, we also investigated the possible involvement of chemical contaminants. One common mode of Ag corrosion is sulfidation, where sulfur-containing compounds (e.g., H_2S) react with the Ag surface to form Ag_2S [30], a semiconducting material with drastically different optical properties. To rule out this possibility, X-ray photoelectron spectroscopy (XPS) was carried out, and no signals from sulfur-containing species were detected (Figure S6A). As another possibility, tungsten from the evaporation boat could also contaminate the Ag during the deposition process. However, the XPS measurements showed no evidence of tungsten-containing species (Figure S6B).

A contaminant that was naturally found within the sample was carbon, which could arise at any stage of sample preparation, including substrate cleaning and loading, during the deposition process, or even after the annealing through interactions with atmospheric hydrocarbons or gaseous CO_2. We carried out a series of XPS measurements before and after exposure to atmospheric conditions which revealed two distinct and universal spectral changes: (i) an increase in binding energy for the peak positions of both Ag $3d_{3/2}$ and Ag $3d_{5/2}$ and (ii) the disappearance of the energy loss feature. The XPS spectra in Figures 6A−C suggested the presence of carbonates (i.e., CO_3^{2-}) even prior to the long exposure to atmospheric conditions. Specifically, the initial Ag 3d peak position was located at 367.9 eV, which lies between the binding energies for Ag^0 (368.2 eV) and Ag_2CO_3 (367.7 eV). It is well-known that CO_2 strongly interacts with Ag_2O to produce Ag_2CO_3 through the following reaction: $Ag_2O + CO_2 \rightarrow Ag_2CO_3$ [30]. In fact, bulk Ag_2O has been actively explored as a thermally regenerable sorbent of CO_2 for purifying breathing air within space suits worn by astronauts during extravehicular activities [31]. We were able to rule out significant carbonation after the annealing step since Ag_2CO_3 readily decomposes at temperatures >200 °C. Interestingly, this carbonate layer has been attributed to the unique corrosion resistance properties of Ag [32]. Furthermore, previous XPS studies based on AgO and Ag_2O powders had shown that the CO_2 present in the air was responsible for generating Ag_2CO_3 on their surface [33,34]. In another study, by using XPS and SERS, it was found that exposing Ag nanocrystals to atmospheric conditions resulted in an exponential increase in the percentage of oxygen and carbon contamination after only 48 h, with the elemental percentages of Ag, O, and C reaching steady-state values of 66, 10, and 24%, respectively [35]. Despite the potential presence of Ag_2CO_3 at the surface, the optical characterization and simulation results suggested that it played a minor role in LSPR damping. Unfortunately, since the optical constants of Ag_2CO_3 are currently unavailable, we were unable to simulate its effect with our continuum model.

Our results also indicated that as the oxidation process proceeded, the Ag $3d_{5/2}$ peak increased in energy until it centered at 368 eV (the peak center for Ag_2O was located at 367.9 eV). As the Ag $3d_{5/2}$ peak shifted to a higher energy, the loss features in all the XPS spectra decreased in intensity (Figure 6D−F). This trend was consistent with optical measurements that showed substantial LSPR damping following surface oxidation. In essence, the loss features could serve as a qualitative indicator of plasmon-related energy loss, since this signal was comprised of electrons that were extrinsic in nature, emanating from the released Ag $3d_{3/2}$ electrons that lost energy by stimulating the LSPR of the Ag nanocrystals before making it to the detector [36]. By subtracting the energy of the loss peak from that of the Ag $3d_{3/2}$ peak, it was found that these electrons lost 2.7 eV, a value almost equal to the energy of the LSPR located at ca. 450 nm (E_p = 2.76 eV) (see Figure S7 for clarification). It should be noted

that the changes in loss features may also be influenced by the sensitivity of XPS and the formation of Ag_2O layer, which can reduce the contribution from the underlying metallic Ag. Therefore, the decrease in the loss features is interpreted as being consistent with, rather than a direct measure of, the plasmon damping observed in the optical spectra. This conclusion was supported by Figures 3 and 4, which showed that Ag_2O-shell formation damped the LSPR peak, especially for the particles smaller than 4 nm.

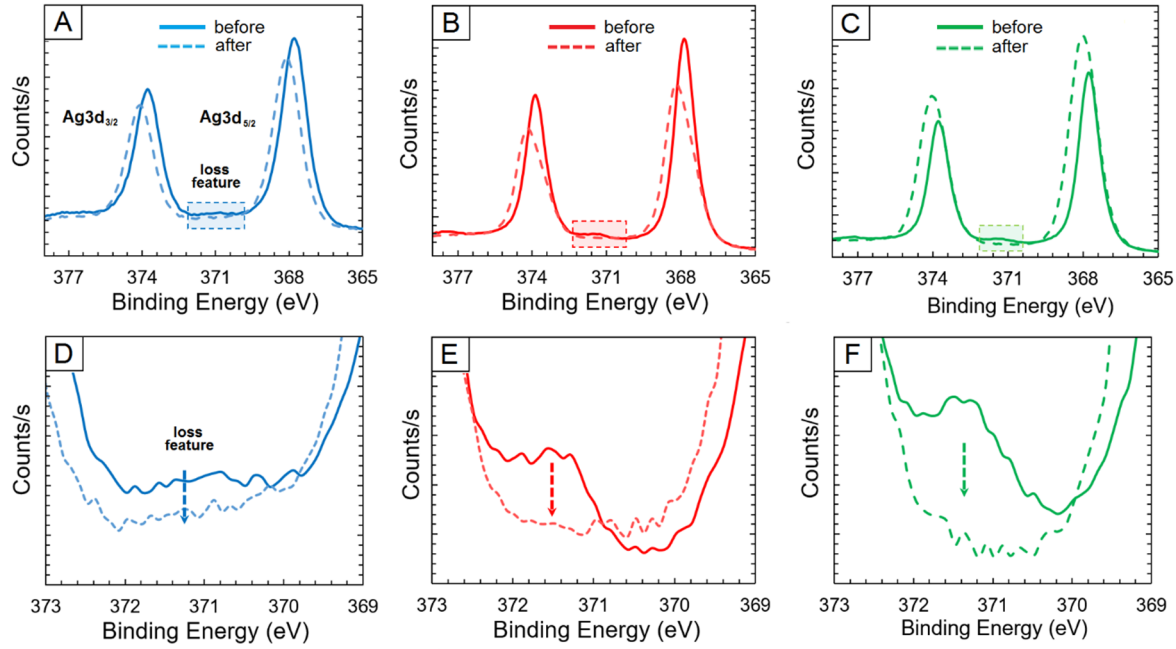

Figure 6. XPS spectra measured over the Ag $3d_{3/2}$ and Ag $3d_{5/2}$ spectral regions for (**A**) 4-nm nanocrystals; (**B**) 16-nm nanocrystals; and (**C**) a 1.5-nm Ag thin film before and after oxidation under ambient conditions; (**D**–**F**) XPS spectra showing the loss features associated with the corresponding spectra in (**A**–**C**) (highlighted by a rectangular box) before and after the oxidation.

Taken together, our data suggest a multi-step oxidation process that begins with the formation of surface carbonates, followed by subsurface oxidation events leading to the formation of an ultrathin Ag_2O shell, a process that correlated positively with pH. This scenario fits well within the framework of the known literature, where the synthesis of Ag_2O nanocrystals was often found to be most effective when performed at elevated pH [37–39]. This was roughly consistent with what was expected from the Pourbaix diagram, which provides potential–pH boundaries for the most thermodynamically favorable oxidation processes of Ag metal (e.g., Ag, Ag^+, and Ag_2O), but with differences expected for the surface of Ag nanocrystals as compared to bulk Ag [40]. In essence, under wet conditions, the surface-based Ag_2O phase was likely to be the most stable in systems that had high pH values. As a final note, those who have investigated oxidation of Ag bulk electrodes in alkaline media have found the surface oxidation process to be highly complex, involving a series of steps, including the adsorption of OH^- ions, solid-state diffusion, Ag or Ag oxide dissolution, and a change in surface roughness [41].

3.3. Removal of Surface Oxides from Ag Nanocrystals

The surface oxidation of Ag nanocrystals is detrimental to many applications that rely on either the strong LSPR or the unique electronic structure of surface Ag atoms. Therefore, it is essential to develop methods capable of removing the surface oxide layer without compromising the underlying Ag atoms. Here we focused on three methods, including thermal decomposition, chemical reduction, and electron beam irradiation.

The most straightforward way to remove surface oxide and carbonaceous species is through thermal annealing. Heating to temperatures within the interval of 167−194 °C has been shown previously to decompose Ag_2CO_3 [42]. In terms of silver oxide removal, previous studies have shown that heating Ag_2O powders to temperatures upwards of 490 °C effectively removes both oxides and carbonaceous contaminants through decomposition, leaving behind pure Ag [33]. This same strategy was adopted for nanocrystals, as evidenced by the complete recovery of the LSPR after annealing for 2 min at 600 °C, as shown in Figure 7A. The slight decrease in intensity post annealing was likely due to the loss of Ag atoms or some small amount of residual oxide.

Another effective strategy involved the addition of a reducing agent. Since Ag_2O has a standard reduction potential (E^o) of 0.34 V vs. standard hydrogen electrode (SHE), the formation of Ag^0 via reduction of Ag^+ is thermodynamically favored when a reducing agent with $E^o_{Red} < E^o_{Ag_2O}$ is used [43]. To illustrate this concept, we simply subjected a partially oxidized sample to a 1 mL solution of ethanol (E^o = 0.20 V vs. SHE), which immediately led to recovery of the LSPR signal, as shown in Figure 7B.

As the least convenient oxide removal strategy, we found that electron irradiation was also viable. To illustrate this concept, we first synthesized Ag@Ag_2O core-shell nanocrystals with thick shells by exposing the 16-nm Ag nanocrystals to O_3 for ~5 min (by placing the sample in an ozone cleaner). This led to the formation of a thick Ag_2O oxide shell that encapsulated a Ag core (see Figure 7C). Notably, the oxide shells derived from atmospheric oxidation were undetectable by scanning transmission electron microscopy (STEM), likely due to the fact that ultrathin oxide shells rapidly decomposed upon exposure to the electron beam. When irradiating an individual Ag@Ag_2O particle with 200 keV electrons for 30 min, the core-shell particle transformed into a pure Ag nanocrystal, as demonstrated by the high-angle annular dark-field (HAADF) images in Figure 7C. In terms of mechanism, removal of the oxide shell could be driven by thermal decomposition or by reduction of Ag^+ by the high-energy electrons. Taken together, either chemically reducing Ag^+ or decomposing the Ag^+ compounds could be used to generate Ag nanocrystals with clean, oxide-free surfaces.

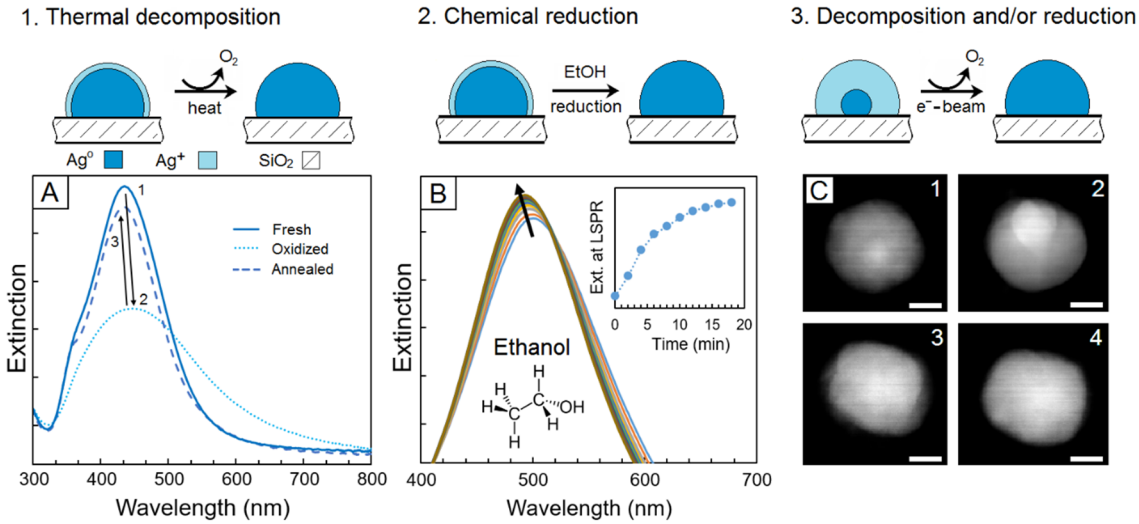

Figure 7. Summary of three effective strategies for removing the oxide layer from the surface of Ag nanocrystals. (**A**) Thermal decomposition, in which the sample was annealed at 600 °C post-oxidation from air, resulted in recovery of the LSPR to its initial spectral profile. (**B**) Chemical reduction, in which the structures were exposed to pure ethanol at room temperature after partial oxidation, also resulted in recovery of the LSPR signal. (**C**) Decomposition and/or reduction, in which an individual Ag@Ag_2O core-shell structure was monitored using HAADF-STEM, showing the growth of the Ag core (brighter region) at the expense of the Ag_2O shell (dimmer region) under 200 keV electron irradiation. The scale bars in (**C**) are all 5 nm.

4. Conclusions

In summary, surface-based Ag nanocrystals were synthesized with sizes ranging from 4–16 nm and then exposed to a variety of conditions while their LSPR spectra were monitored. It was found that the smaller particles underwent a much greater degree of plasmonic damping over the same period of time. All changes in the LSPR peak position and intensity were in agreement with theoretical modeling based on the DDA method, which showed that the degree of damping was commensurate with the thickening of a surface layer of Ag_2O. We also found that the rate of oxidation was greatest in aqueous environments relative to air and ethylene glycol, which we attributed to the presence of hydroxide ions that promoted the oxidation process. We measured the oxidation rate of the 4-nm Ag nanocrystals in a series of aqueous solutions with increasing pH, which revealed that the increased concentration of hydroxide ions accelerated the oxidation process. Analysis of the surface chemistry by XPS suggested that the oxidation process occurred in a series of steps, including a rapid two-step oxidation/carbonation process that was followed by subsurface oxidation events leading to Ag_2O formation. In addition to XPS measurements, these conclusions were supported by the time-dependent LSPR damping as well as the decrease in intensity of the XPS loss peak. Ultimately, after oxidation, the steady-state configuration was an Ag nanocrystal encapsulated by a self-terminating ultrathin Ag_2O shell, together with Ag_2CO_3 on the outermost surface.

In addition to understanding the size effect on the oxidation of Ag nanocrystals, we also demonstrated a variety of methods for removing the oxide and carbonate layers, including thermal decomposition through annealing, chemical reduction through the addition of a reducing agent, and electron irradiation during STEM. In the first two cases, recovery of the LSPR to its initial state provided direct evidence of oxide removal. In the latter case, we directly observed a decrease in the Ag_2O shell thickness as the Ag core increased in size. While all methods were effective in removing the oxide layer, these results also raise a number of additional perspectives. For example, those working with colloidal nanomaterials in aqueous systems likely have ultrathin oxide layers encapsulating their particles. However, if these particles are maintained in the presence of a reducing agent or at relatively low pH values, formation of the oxide layer can be minimized. These results are also important to those employing Ag nanocrystals as heterogeneous catalysts, since their performance is directly linked to the chemical state of the outermost atoms. To develop a more meaningful correlation between the substantial literature on colloidal Ag nanocrystals and the results discussed herein, future investigations must include systematic studies involving chemical adsorbates typical of colloidal systems (e.g., stabilizers, ligands, and reducing agents).

Supplementary Materials: The following supporting information can be downloaded at: https://media.sciltp.com/articles/others/2603231122380529/MI-26030014-SM.pdf. Figure S1: Extinction spectra of Ag nanocrystals derived from Ag films with effective thicknesses of <1, 1, 5, and 15 Å. The inset shows the LSPR peak intensity as a function of Ag film thickness, revealing a linear relationship; Figure S2: The dielectric constants of (A) Ag and (B) Ag_2O used for the DDA simulation. The dielectric functions (ε_1 and ε_2) of Ag and Ag_2O were obtained from literature reports [1,2] and used to generate the plots; Figure S3: DDA simulation of the extinction spectra of a 4-nm Ag nanocrystal before oxidation (blue) and after formation of a 0.25-nm shell of Ag_2O (green). These results suggest that the high sensitivity of LSPR to surface oxidation is not unique to the hemispherical nanoparticles supported on a substrate. The simulation was carried out with a surrounding dielectric constant equal to that of water ($\varepsilon_m = 1.78$); Figure S4: Normalized extinction spectra of the 4- and 16-nm Ag nanocrystals, showing that the FWHM of the LSPR was broader for the 4-nm sample; Figure S5: Plot of the LSPR peak intensity as a function of time (blue line), which is fitted with an exponential decay function with a rate constant of *k*. The rate constant can also be obtained from the slope of the linear plot of –ln(y) versus time (orange line); Figure S6: XPS spectra of the (A) sulfur 2p region and (B) tungsten 4f region measured from a typical Ag sample (derived from the 0.4-nm film), confirming the absence of sulfur- and tungsten-based contaminants; Figure S7: XPS spectrum of the Ag $3d_{3/2}$ region and associated loss feature, showing an energy separation of 2.7 eV. References [44,45] are cited in supplementary materials.

Author Contributions: K.D.G.: conducted experiments on materials preparation, oxidation monitoring, and analyzed the data; K.D.G. and Y.W.: prepared the manuscript. Y.X.: conceptualization, supervision, writing—reviewing and editing. All authors have read and agreed to the published version of the manuscript

Funding: This research was funded by a grant from NSF (CHE 2504965) and start-up funds from the Georgia Institute of Technology.

Data Availability Statement: The data that support the findings of this study are available from the corresponding author Y.X. upon reasonable request.

Acknowledgments: The authors gratefully acknowledge Zachary D. Hood, Madeline Vara, Thenner Silva Rodrigues, Anderson Gabriel Marques da Silva, and Jane Howe for their contributions to materials characterization.

Conflicts of Interest: The authors declare no conflicts of interest. Given the role as Editor-in-Chief, Y.X. was not involved in the peer review of this paper and had no access to information regarding its peer-review process. Full responsibility for the editorial process of this paper was delegated to another editor of the journal.

Use of AI and AI-Assisted Technologies: No AI tools were utilized for this paper.

References

1. Long, R.; Zhou, S.; Wiley, B.J.; Xiong, Y. Oxidative Etching for Controlled Synthesis of Metal Nanocrystals: Atomic Addition and Subtraction. *Chem. Soc. Rev.* **2014**, *43*, 6288–6310.
2. Sun, X.; Kim, J.; Gilroy, K.D.; Liu, J.; König, T.A.F.; Qin, D. Gold-Based Cubic Nanoboxes with Well- Defined Openings at the Corners and Ultrathin Walls Less Than Two Nanometers Thick. *ACS Nano* **2016**, *10*, 8019–8025.
3. Ling, D.; Lee, N.; Hyeon, T. Chemical synthesis and assembly of uniformly sized iron oxide nanoparticles for medical applications. *Acc. Chem. Res.* **2015**, *48*, 1276–1285.
4. Prieto, P.; Nistor, V.; Nouneh, K.; Oyama, M.; Abd-Lefdil, M.; Díaz, R. XPS Study of Silver, Nickel and Bimetallic Silver–Nickel Nanoparticles Prepared by Seed-Mediated Growth. *Appl. Surf. Sci.* **2012**, *258*, 8807–8813.
5. Ha, D.H.; Moreau, L.M.; Honrao, S.; Hennig, R.G.; Robinson, R.D. The Oxidation of Cobalt Nanoparticles into Kirkendall-Hollowed CoO and Co_3O_4: The Diffusion Mechanisms and Atomic Structural Transformations. *J. Phys. Chem. C* **2013**, *117*,14303–14312.
6. Knight, M.W.; King, N.S.; Liu, L.; Everitt, H.O.; Nordlander, P.; Halas, N.J. Aluminum for Plasmonics. *ACS Nano* **2014**, *8*, 834–840.

7. Jeong, S.; Woo, K.; Kim, D.; Lim, S.; Kim, J.S.; Shin, H.; Xia, Y.; Moon, J. Controlling the Thickness of the Surface Oxide Layer on Cu Nanoparticles for the Fabrication of Conductive Structures by Ink-Jet Printing. *Adv. Funct. Mater.* **2008**, *18*, 679–686.
8. Yin, Y.; Li, Z.Y.; Zhong, Z.; Gates, B.; Xia, Y.; Venkateswaran, S. Synthesis and Characterization of Stable Aqueous Dispersions of Silver Nanoparticles Through the Tollens Process. *J. Mater. Chem.* **2002**, *12*, 522–527.
9. Le Chatelier, H.; Über die Oxydation des Silbers. *Z. Phys. Chemie* **1887**, *1*, 516–518.
10. Lewis, G.N.; Zersetzung von Silberoxyd durch Autokatalyse. *Z. Phys. Chemie* **1905**, *52*, 310–326.
11. Han, Y.; Lupitskyy, R.; Chou, T.-M.; Stafford, C.M.; Du, H.; Sukhishvili, S. Effect of Oxidation on Surface-enhanced Raman Scattering Activity of Silver Nanoparticles: A Quantitative Correlation. *Anal. Chem.* **2011**, *83*, 5873–5880.
12. L'vov, BV. Kinetics and Mechanism of Thermal Decomposition of Silver Oxide. *Thermochimica Acta* **1999**, *333*, 13–19.
13. Xia, Y.; Xiong, Y.; Lim, B.; Skrabalak, S.E. Shape-controlled Synthesis of Metal Nanocrystals: Simple Chemistry Meets Complex Physics? *Angew. Chem. Intl. Ed.* **2009**, *48*, 60–103.
14. Mayer, K.M.; Hafner, J.H. Localized Surface Plasmon Resonance Sensors. *Chem. Rev.* **2011**, *111*, 3828–3857.
15. Sachan, R.; Ramos, V.; Malasi, A.; Yadavali, S.; Bartley, B.; Garcia, H.; Duscher, G.; Kalyanaraman, R. Oxidation-resistant Silver Nanostructures for Ultrastable Plasmonic Applications. *Adv. Mater.* **2013**, *25*, 2045–2050.
16. Gilroy, K.D.; Puibasset, J.; Vara, M.; Xia, Y. On the Thermodynamics and Experimental Control of Twinning in Metal Nanocrystals. *Angew. Chem. Int. Ed.* **2017**, *129*, 8773–8777.
17. Draine, B.T.; Flatau, P.J. Discrete-dipole Approximation for Scattering Calculations. *J. Opt. Soc. Am.* **1994**, *11*, 1491–1499.
18. Graedel, T. Corrosion Mechanisms for Silver Exposed to the Atmosphere. *J. Electrochem. Soc.* **1992**, *139*, 1963–1970.
19. Medasani, B.; Park, Y.H.; Vasiliev, I. Theoretical Study of the Surface Energy, Stress, and Lattice Contraction of Silver Nanoparticles. *Phys. Rev. B* **2007**, *75*, 235436.
20. Gilroy, K.D.; Ruditskiy, A.; Peng, H.C.; Qin, D.; Xia, Y. Bimetallic Nanocrystals: Syntheses, Properties, and Applications. *Chem. Rev.* **2016**, *116*, 10414–10472.
21. Cortie, M.B.; McDonagh, A.M. Synthesis and Optical Properties of Hybrid and Alloy Plasmonic Nanoparticles. *Chem. Rev.* **2011**, *111*, 3713–3735.
22. Blaber, M.G.; Henry, A.I.; Bingham, J.M.; Schatz, G.C.; Van Duyne, R.P. LSPR Imaging of Silver Triangular Nanoprisms: Correlating Scattering with Structure Using Electrodynamics for Plasmon Lifetime Analysis. *J. Phys. Chem. C* **2012**, *116*, 393–403.
23. Kreibig, U.; Vollmer, M. *Optical Properties of Metal Clusters*; Springer: Berlin/Heidelberg, Germany, **1995**, p. 79.
24. Hartland, G.V. Optical Studies of Dynamics in Noble Metal Nanostructures. *Chem. Rev.* **2014**, *111*, 3858–3887.
25. Gilroy, K.D.; Xia, Y. Dimerization of Colloidal Particles Through Controlled Aggregation for Enhanced Properties and Applications, *Chem. Asian J.* **2016**, *11*, 2341–2351.
26. Vodyankina, O.V.; Kurina, L.N.; Izatulina, G.A. Surface Interaction of Ethylene Glycol with Silver. *React. Kinet. Catal. Lett.* **1998**, *64*, 103–108.
27. Sani, E.; Dell'Oro, A. Optical Constants of Ethylene Glycol Over an Extremely Wide Spectral Range. *Opt. Mater.* **2015**, *37*, 36–41.
28. Li, C.; Shuford, K.L.; Park, Q.H.; Cai, W.; Li, Y.; Lee, E.J.; Cho, S.O.; High-Yield Synthesis of Single-Crystalline Gold Nano-octahedra. *Angew. Chem.* **2007**, *119*, 3328–3332.
29. Jiu, J.; Wang, J.; Sugahara, T.; Nagao, S.; Nogi, M.; Koga, H.; Suganuma, K.; Hara, M.; Nakazawa, E.; Uchida, H. The Effect of Light and Humidity on the Stability of Silver Nanowire Transparent Electrodes. *RSC Adv.* **2015**, *5*, 27657−27664.
30. Levard, C.; Hotze, E.M.; Colman, B.P.; Dale, A.L.; Truong, L.; Yang, X.Y.; Bone, A.J.; Brown, G.E.; Tanguay, R.L.; Di Giulio, R.T.; et al. Sulfidation of Silver Nanoparticles: Natural Antidote to their Toxicity. *Environ. Sci. Technol.* **2013**, *47*, 13440−13448.
31. Atwater, J.E.; Holtsnider, J.T.; Wheeler, R.R., Jr. *Microwave Regenerable Air Purification Device*; National Technical Information Service: Springfield, VA, USA, 1996.
32. Hoflund, G.B.; Hazos, Z.F. Surface Characterization Study of Ag, AgO, and Ag_2O Using X-ray Photoelectron Spectroscopy and Electron Energy-loss Spectroscopy. *Phys. Rev. B* **2000**, *62*, 11126.
33. Weaver, J.F.; Hoflund, G.B. Surface Characterization Study of the Thermal Decomposition of Ag_2O. *Chem. Mater.* **1994**, *6*, 1693–1699.
34. Weaver, J.F.; Hoflund, G.B. Surface Characterization Study of the Thermal Decomposition of AgO. *J. Phys. Chem.* **1994**, *98*, 8519–8524.
35. Matikainen, A.; Nuutinen, T.; Itkonen, T.; Heinilehto, S.; Puustinen, J.; Hiltunen, J.; Lappalainen, J.; Karioja, P.; Vahimaa, P. Atmospheric Oxidation and Carbon Contamination of Silver and its Effect on Surface-enhanced Raman Spectroscopy (SERS). *Sci. Rep.* **2016**, *6*, 37192.

36. Bates, C.W.; Wertheim, G.K.; Buchanan, D.N.E. Nature of the 3.8 eV Plasmon in X-ray Photoemission from Silver. *Phys. Lett. A.* **1979**, *72*, 178–180.
37. Kim, M.J.; Cho, Y.S.; Park, S.H.; Huh, Y.D. Facile Synthesis and Fine Morphological Tuning of Ag_2O. *Cryst. Growth Des.* **2012**, *12*, 4180−4185.
38. Wang, X.; Wu, H.F.; Kuang, Q.; Huang, R.B.; Xie, Z.X.; Zheng, L.S. Shape-dependent Antibacterial Activities of Ag_2O Polyhedral Particles. *Langmuir* **2010**, *26*, 2774–2778.
39. Kim, M.J.; Kim, S.; Park, H.; Huh, Y.D. Morphological Evolution of Ag_2O Microstructures from Cubes to Octapods and their Antibacterial Activities. *Bull. Korean Chem. Soc.* **2011**, *32*, 3793–3795.
40. Holewinski, A.; Idrobo, J.C.; Linic, S. High-performance Ag–Co Alloy Catalysts for Electrochemical Oxygen Reduction. *Nature Chem.* **2014**, *6*, 828–834.
41. Mayer, S.T.; Muller, R.H. Nucleation of Silver (I) Oxide Investigated by Spectroscopic Ellipsometry. *J Electrochem. Soc.* **2005**, *152*, A179–A185.
42. Kadlec, O.; Dubinin, M.M. Investigation of Kinetics of Thermal Decomposition of Solids. Communication 2. Thermal Decomposition of Silver Carbonate. *Izv. AN. SSSR. Otd. Khim. Nauk.* **1961**, *3*, 390–396. (In Russian)
43. Bratsch, S.G.J. Standard Electrode Potentials and Temperature Coefficients in Water at 298.15 K. *Phys. Chem. Ref. Data* **1989**, *18*, 1–21.
44. Johnson, P.B.; Christy, R.W. Optical Constants of the Noble Metals. *Phys. Rev. B* **1972**, *6*, 4370–4379.
45. Gao, X.Y.; Wang, S.Y.; Li, J.; Zheng, Y.X.; Zhang, R.J.; Zhou, P.; Yang, Y.M.; Chen, L.Y. Study of Structure and Optical Properties of Silver Oxide Films by Ellipsometry, XRD and XPS Methods. *Thin Solid Films* **2004**, *455–456*, 438–442.

Perspective

From Static to Dynamic: Rethinking Interface Passivation in Inverted Perovskite Solar Cells

Qingyun Xiao [1], Xiaofen Jiang [2], Xiaonan Wang [2,3], Qinggui Li [2,3], Rui Wang [2], and Jingjing Xue [3,*]

[1] Department of Electronic and Information Engineering, School of Engineering, Westlake University, Hangzhou 310024, China
[2] Department of Materials Science and Engineering, School of Engineering, Westlake University, Hangzhou 310024, China
[3] State Key Laboratory of Silicon and Advanced Semiconductor Materials, School of Materials Science and Engineering, Zhejiang University, Hangzhou 310027, China
* Correspondence: jjxue@zju.edu.cn

Received: 30 January 2026; Revised: 3 March 2026; Accepted: 23 March 2026; Published: 25 March 2026

Abstract: Interface passivation is central to efficiency improvement in inverted perovskite solar cells, yet its effectiveness is fundamentally limited by the assumption of a static picture. Herein, we argue that the perovskite/electron transport layer interface is intrinsically dynamic under operation, continuously evolving under illumination, thermal stress, and electrical bias owing to ion migration, interfacial redistribution, passivator destabilization, and chemical reactions. These coupled processes progressively reconstruct interfacial energetics and defect landscapes, leading to voltage loss, fill-factor decay, hysteresis re-emergence, and irreversible performance degradation even in devices with high initial efficiencies. By reframing the interface as a time-dependent system rather than a fixed structure, this perspective highlights dynamic interfacial evolution as the origin of long-term instability and calls for interface regulation strategies that prioritize sustained functional stability under realistic operating conditions.

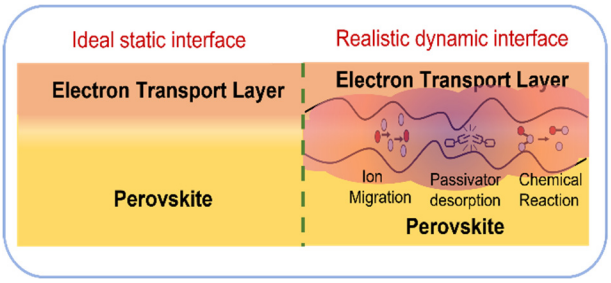

Keywords: dynamic interface; interface passivation; ion migration; operational stability; interfacial evolution

1. Introduction

Over the past decade, organic-inorganic halide perovskite solar cells (PSCs) have demonstrated an unprecedented increase in power conversion efficiency (PCE). This progress has emerged from coordinated advances in materials composition regulation, thin-film fabrication processing, and increasingly refined interface engineering [1]. Among these efforts, passivation of the contact interface between the perovskite absorber and the electron transport layer (ETL) has attracted particular attention [2]. By implementing a variety of interface passivation approaches, non-radiative recombination at the perovskite/ETL interface can be substantially suppressed, leading to measurable improvements in both the open-circuit voltage (V_{OC}) and fill factor (FF) [3]. These passivation approaches have contributed decisively to the rapid efficiency improvements achieved in laboratory-scale devices, underscoring the increasingly prominent role of interface engineering in advancing the performance of PSCs [4].

However, the achievement of high efficiency does not inherently ensure stable performance under prolonged operational conditions, a phenomenon that has been consistently observed across a wide range of device architectures and material systems. Even devices featuring rigorously engineered and well-passivated interfaces often exhibit gradual performance degradation during continuous illumination, thermal stress, or electrical bias [5]. This discrepancy between efficiency and stability indicates that prevailing interface engineering strategies, while highly effective at improving static performance indicators, remain insufficient in sustaining device functionality over extended timescales. Implicitly, the most existing approaches are founded on the assumption that an interface optimized at fabrication remains structurally and electronically static throughout device operation.

Such a static interface assumption, however, is fundamentally incompatible with the intrinsic physical characteristics of halide perovskites. Owing to their soft lattices and pronounced ion mobility, the distribution of ions, defect configurations, and local electrostatic modulations at perovskite surfaces and near-interface regions are inherently susceptible to gradual reorganization under external stimuli, including illumination, electric fields, and thermal stress [6]. In contrast, ETLs are predominantly composed of organic semiconductors with constrained ion migration and comparatively rigid structures, whose electronic structure and chemical composition change much more slowly during device operation [7]. This asymmetry in structural flexibility and kinetic responsiveness between the two contacting materials renders the perovskite/ETL interface a natural locus for the redistribution of charge carriers, mobile ions, and localized electric potentials.

Under sustained operating conditions, the combined effects of photoexcitation, electrical bias, and thermal stress progressively reshape the interfacial electronic landscape, driving the interface to progressively deviate from the initial configuration. As the interfacial state evolves over time, passivation strategies designed to address a specific, static interface condition may no longer remain chemically or electronically effective. Consequently, interfacial defects can re-emerge or transform, undermining charge extraction and accelerating performance degradation during long-term operation.

This perspective highlights a conceptual gap in prevailing interface engineering: the long-term performance of perovskite solar cells is constrained not merely by incomplete passivation, but by a predominantly static view of an interface that is intrinsically dynamic in nature. Bridging this gap requires a fundamental shift in how to understand and engineer the perovskite/ETL interface, moving beyond its treatment as a static structural entity towards recognizing it as a time-dependent, operating-state-coupled system.

Within this framework, interface passivation should not be regarded solely as a one-time structural modification, but rather as an adaptive process capable of accommodating interfacial evolution under realistic operating conditions. Incorporating this dynamic perspective may provide critical insights into the origins of operational instability, help alleviate existing stability bottlenecks, and ultimately guide perovskite photovoltaics toward practical and commercially viable deployment.

2. Current Interface Passivation Strategy: Achievements and Limitations

Before considering how interface strategies might evolve to accommodate time-dependent interfacial processes, it is instructive to examine the conceptual foundations, achievements, and underlying assumptions of the classical passivation approaches that have dominated the field to date. Such an analysis not only highlights the origins of the remarkable efficiency gains achieved thus far, but also reveals the structural limitations that emerge when these strategies are confronted with realistic operational stress.

Non-radiative recombination and charge-transport losses originating from the perovskite/ETL interface have long been recognized as critical limitations to device performance [8]. As the mechanistic understanding of this interface has deepened, passivation strategies have progressively evolved from isolated defect-repair efforts towards more systematic regulation of interfacial chemical states, electrostatic environments, and structural configurations. Among these, chemical defect passivation represents the most direct and widely adopted approach.

2.1. Chemical Defect Passivation: Local Bonding Optimization

Chemical defect passivation primarily targets the intrinsic atomic-scale imperfections of perovskite surfaces. Extensive theoretical calculations and experimental characterizations consistently indicate that incomplete lattice termination and compositional volatility at perovskite surfaces lead to the accumulation of halide vacancies, under-coordinated Pb^{2+} species, and their associated shallow and deep electronic states, which act as high-density non-radiative recombination centers when located at the perovskite/ETL interface [9]. The introduction of molecules possessing Lewis acid, Lewis base or hydrogen-bonding functionalities enables coordination or electrostatic interactions with these under-coordinated species, effectively saturating dangling bonds and compensating local charge imbalance (Figure 1a). At its core, this strategy seeks to establish a chemically well-terminated perovskite surface at the final stage of device fabrication, characterized by reduced defect density and more idealized stoichiometry and bonding configurations.

2.2. Field-Effect Passivation: Electrostatic Regulation without Direct Defect Elimination

Building upon this understanding, it has become increasingly clear that interfacial recombination losses are not solely governed by point defects that can be eliminated through specific chemical bonding. Long-range electrostatic effects arising from subtle energy-level mismatches, interfacial dipole disorder and inhomogeneous charge distributions can also exert a decisive influence on carrier-transport dynamics in the interfacial region [10].

This recognition has motivated the development of field-effect passivation strategies, which aim to regulate the interfacial electrostatic environment rather than directly modifying atomic-scale defect structures.

By inserting interlayers with tailored electronic structures between the perovskite and the ETL, a predefined local electrostatic potential profile can be established. Whether achieved through interfacial band bending, dipole-induced vacuum-level shifts, or electric double-layer formation, the unifying objective is to reshape carrier-transport pathways such that photogenerated electrons are steered away from recombination-prone regions and efficiently extracted towards the collecting electrode (Figure 1b). Within this framework, defects are not necessarily removed but rendered less active as recombination centers through physical modulation of the carrier-transport environment.

2.3. Structurally Engineered Interfacial Layers: Transitional Architectures

More recently, interface engineering has further progressed from defect- and field-centric strategies toward the deliberate construction of structurally defined interfacial regions. By introducing low-dimensional perovskite layers, molecular cation reconstruction layers, or composite interfacial architectures between the perovskite absorber and the ETL, researchers seek to construct a structurally defined transition region that alleviates abrupt discontinuities in crystal structure, dielectric response, and polarization behavior [11,12].

These engineered interlayers often exhibit ionic distributions and dielectric properties distinct from those of bulk perovskites, enabling partial screening of Coulomb interactions, redistribution of local electric fields, and suppression of interfacial ionic disorder [13]. Through the synergistic integration of defect passivation, energy-level alignment, and electrostatic field remodeling (Figure 1c), such approaches have delivered notable improvements in device efficiency and short-term operational stability.

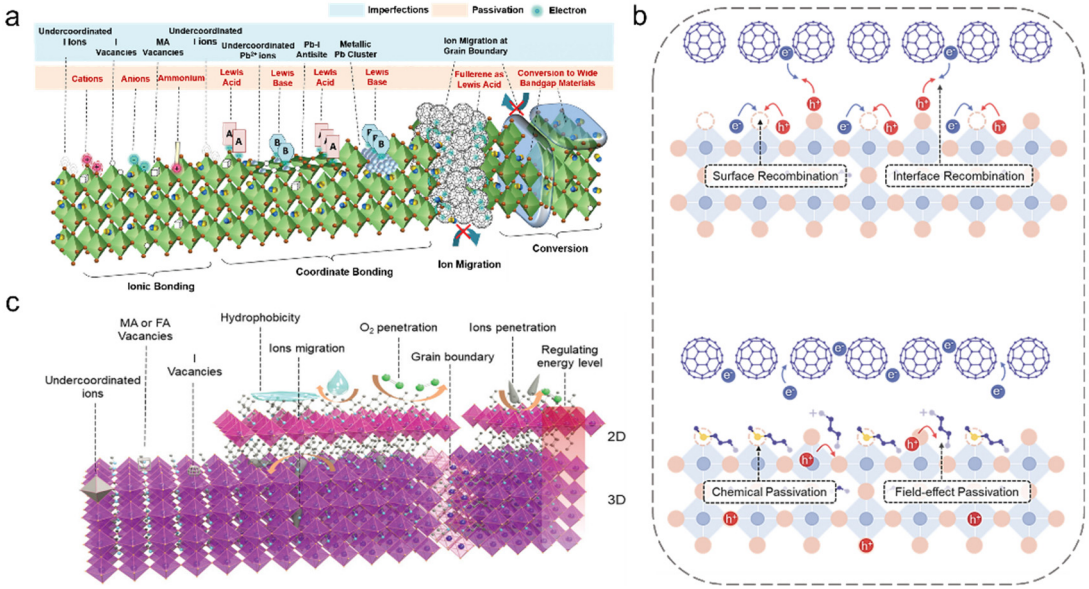

Figure 1. Schematic Diagram of the Current Interface Passivation Strategy Mechanism. (**a**) Imperfections in organic-inorganic halide perovskite film and their passivation by ionic bonding, coordinate bonding, and conversion to wide bandgap materials, and suppression of ion migration at extended defects. Reprinted with permission from Ref. [14]. (**b**) Schematic of the perovskite surface without passivation (**up**) and with diammonium-methylthio dual passivation (DMDP) composed by chemical and field-effect passivation (**down**). Reprinted with permission from Ref. [15]. (**c**) Schematic illustration of the surface passivation using 2D perovskites, in which vacancy/excess defects are well repaired, and the formation of a 2D capping layer with outstanding robustness effectively blocks the penetration of oxygen/moisture. Moreover, the modified energy level facilitates charge transfer and collection. Reprinted with permission from Ref. [16].

2.4. A Shared Paradigm: Static Optimization of a Dynamic Interface

Despite their diverse material implementations and microscopic mechanisms, these classical interface passivation strategies share a common conceptual foundation. They are predominantly implemented during device fabrication or post-treatment stages, with the central objective of maximizing photovoltaic performance by establishing an interfacial configuration that minimizes initial defect density, optimizes energy-level alignment, and suppresses non-radiative

recombination. Consequently, performance assessments typically emphasize post-fabrication gains in V_{OC}, FF and PCE, alongside stability tests conducted under relatively mild and controlled conditions.

Implicit in this framework is the assumption that interface passivation constitutes a largely "one-off" structural optimization, namely that an optimally configured interface established at the outset can be preserved throughout subsequent device operation. This paradigm has been instrumental in enabling the rapid efficiency advances achieved over the past decade and has underpinned sustained progress in interface engineering [17,18].

However, an increasing number of experimental evidence suggests that its implicit premise does not universally hold under realistic operating conditions [19]. Even in devices employing multiple passivation strategies and exhibiting high initial efficiencies, pronounced performance degradation is frequently observed under prolonged illumination, thermal stress, applied electric fields, or their combined influence. Typical manifestations include gradual V_{OC} loss, J_{SC} decay, etc.

3. The Origin and Concrete Manifestations of Dynamic Evolution

From a dynamic viewpoint, the perovskite/ETL interface cannot be regarded as a static entity fixed at the fabrication stage, but rather as an evolving system that continuously responds to external operating environments. Metal halide perovskites possess a soft and adaptive lattice, low activation barriers for ion migration, and metastable surface coordination, making their interfacial structure highly sensitive to temperature, mechanical stress, illumination, and moisture. These external stimuli drive persistent reorganization of lattice geometry, defect populations, and ionic distributions at the interface, progressively shifting it away from its initial equilibrium configuration.

Thermal stimuli induce pronounced lattice expansion, phase transitions, and strain accumulation within the perovskite layer (Figure 2a). Temperature cycling not only alters octahedral tilting and crystal symmetry, but also accelerates ion diffusion and defect activation near the perovskite/ETL interface, leading to dynamically evolving band alignment and interfacial recombination pathways [20].

Similarly, mechanical and lattice mismatch-induced strain further modulates the interfacial energy landscape (Figure 2b). Local strain fields alter Pb-X bond lengths and angles, thereby shifting band edges and lowering the formation energy of defects. This strain-defect coupling creates spatially heterogeneous electronic properties at the interface, enhancing non-radiative recombination and amplifying degradation under prolonged operation [21,22].

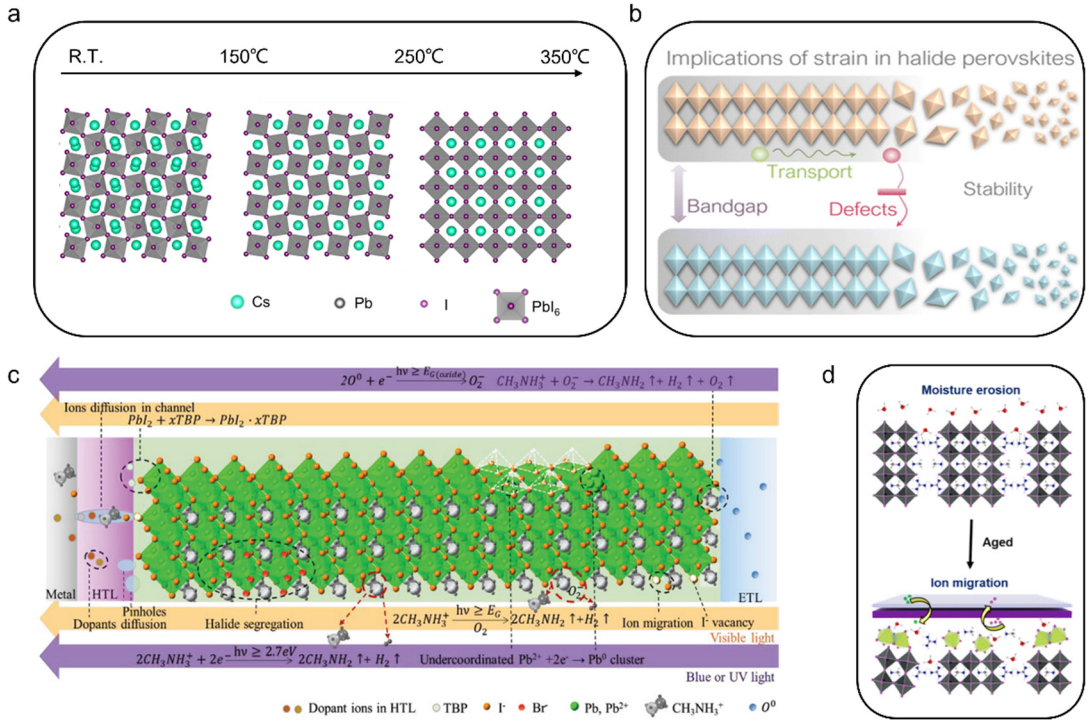

Figure 2. (**a**) Schematics of the thermal-induced change in the lattice of $CsPbI_3$ samples. Reprinted with permission from Ref. [23]. (**b**) Implications of strain on perovskite films. Reprinted with permission from Ref. [24]. (**c**) Impacts of visible, blue, and UV light illumination on PSCs. (E_G represents the bandgap of perovskite). Reprinted with permission from Ref. [25]. (**d**) Schematic diagram of perovskite films adsorbing water. Reprinted with permission from Ref. [26].

Under illumination, photoexcited carriers modify defect charge states and drive light-assisted ionic migration, while high-energy photons can directly induce bond cleavage and interfacial chemical reactions (Figure2c). These photoinduced effects are particularly pronounced at the perovskite/ETL interface, where electric fields, carrier accumulation, and chemical gradients are intrinsically coupled.

In parallel, environmental moisture interacts strongly with the ionic lattice, triggering hydration reactions, lattice swelling, and preferential degradation at interfacial regions with incomplete coordination or enhanced ion accessibility (Figure 2d). Such humidity-induced processes promote ion migration and chemical reconstruction at the interface, rather than uniform bulk degradation.

Collectively, temperature, strain, illumination and humidity do not act as isolated stressors but synergistically converge at the perovskite/ETL interface, rendering it the most dynamically active and vulnerable region in inverted perovskite solar cells. This intrinsic dynamic nature fundamentally challenges passivation strategies that rely on a fixed interfacial configuration, underscoring the need to reconsider interface design from a time-dependent and adaptive perspective.

3.1. Ion Migration and Photo-Induced Phase Separation

Among various forms of interfacial dynamic evolution, ion migration and photo-induced halide phase separation represent two closely coupled and mutually reinforcing destabilization mechanisms. Rather than acting as isolated bulk phenomena, these processes cooperatively drive the continuous reconstruction of interfacial structure, composition, and electrostatic landscape over operational time.

Under continuous illumination or electrical bias, the activation of halide ionic species, for example iodide in mixed-halide $MAPb(I_{1-x}Br_x)_3$, is generally enhanced, enabling directional ionic redistribution driven by internal electric fields and chemical potential gradients (Figure 3a). This ionic motion not only promote photo-induced halide phase separation but also perturbs local charge density and interfacial band bending, giving rise to iodide-rich and bromide-rich domains that evolve progressively under high excitation intensity [27]. Such coupled ionic and compositional rearrangements are now widely recognized as a fundamental source of interfacial instability rather than isolated bulk effects.

The consequences of this dynamic evolution are consistently reflected across electrical, optical, and structural characterizations. From an operational perspective, device parameters including PCE, J_{SC}, V_{OC}, and FF commonly exhibit pronounced scan-rate dependence after aging, with suppressed performance at slow scan rates and reduced hysteresis under fast sweeps (Figure 3b–e). This behavior is generally attributed to ion-induced field screening at functional interfaces, where accumulated mobile ions dynamically modulate the built-in electric field and charge-extraction barriers [28]. In parallel, time-dependent photoluminescence measurements frequently reveal red-shifted emission and intensity redistribution during prolonged illumination (Figure 3f), a characteristic optical signature of halide phase separation and the formation of low-bandgap iodide-rich domains that act as preferential recombination centers. Complementary PXRD analyses before and after illumination further corroborate this picture, with the emergence or evolution of diffraction features indicative of halide redistribution and lattice distortion (Figure 3g). Collectively, these recurring observations point to a continuous, time-dependent reconstruction of the perovskite interface, manifested through evolving interfacial dipoles, fluctuating electrostatic landscapes, and progressively enhanced interface-dominated recombination. Such intrinsically dynamic behavior fundamentally challenges the assumption of a static, permanently passivated interface, underscoring the limitations of conventional static passivation strategies under realistic operating conditions.

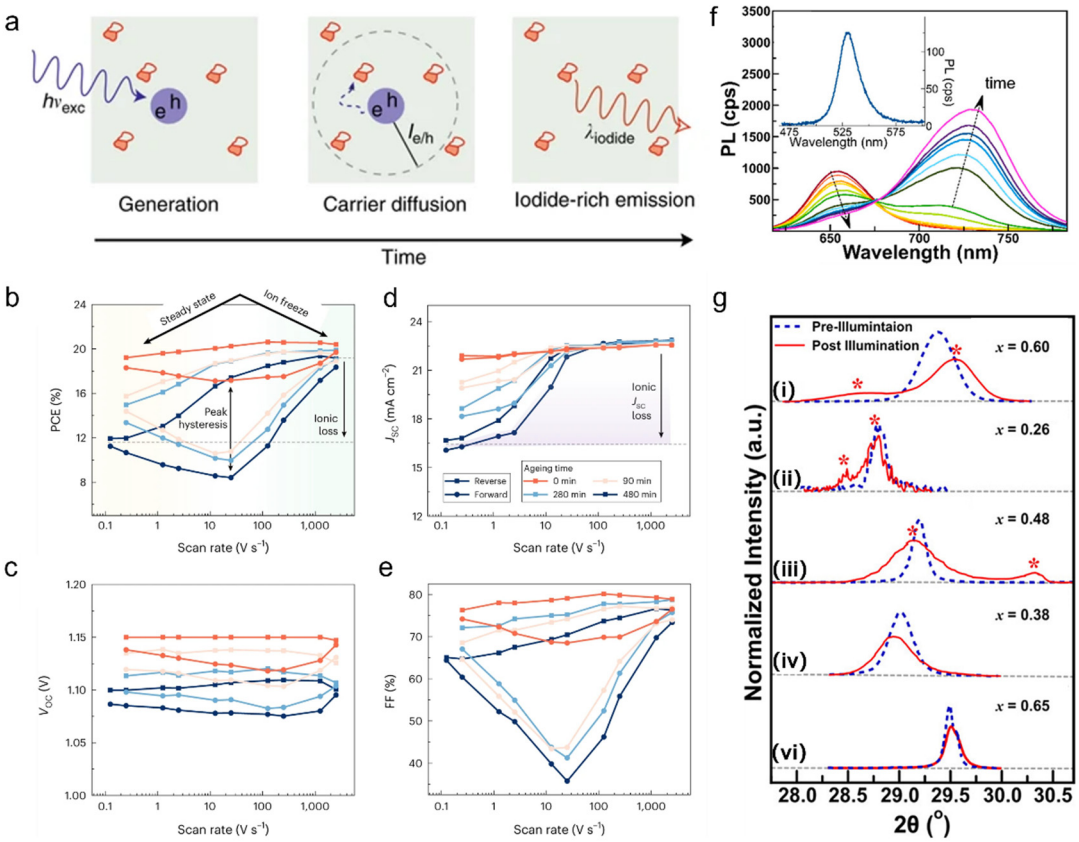

Figure 3. (**a**) High excitation intensity light-induced phase separation of $MAPb(I_{1-x}Br_x)_3$ (MA = $CH_3NH_3^+$). Reprinted with permission from Ref. [29]. The PCE (**b**), V_{OC} (**c**), J_{SC} (**d**) and FF (**e**) obtained from *J-V* characteristics measured at different scan speeds in reverse (squares) and forward (circles) scan direction for $Cs_{0.05}(FA_{0.83}MA_{0.17})_{0.95}Pb(I_{0.83}Br_{0.17})_3$ perovskite solar cells after different ageing times. Reprinted with permission from Ref. [30]. (**f**) Time evolution of $MAPb(I_{0.5}Br_{0.5})_3$ emission spectra under λ_{exc} = 405 nm CW excitation (I_{exc} = 20 mW cm^{-2}) over the course of 3 s. Times for selected spectra (from *red* to *purple*): 0.05, 1.41. 1.64, 1.69, 1.83, 1.93, 2.26, 2.40, 2.58, 2.68, 2.87, and 3.10 s. Inset: Emission spectrum between 475 and 600 nm indicative of Br-rich emission. Reprinted with permission from Ref. [29]. (**g**) Summary of $MAPb(I_{1-x}Br_x)_3$ literature pXRD powder patterns before (dashed blue) and after (solid red) illumination. Initial halide compositions given by x at the top right corner of each panel. Red asterisks denote post illumination peak positions for split I-rich and Br-rich domains. (i) reprinted with permission from Ref. [31]. (ii) reprinted with permission from Ref. [32]. (iii) reprinted with permission from Ref. [33]. (iv) reprinted with permission from Ref. [34]. (vi) reprinted with permission from Ref. [35].

3.2. Desorption of Passivating Molecules

Beyond ion migration and halide phase separation, the intrinsic instability of interface passivation layers constitutes another widely observed manifestation of dynamic interface evolution in perovskite solar cells. Under realistic operating conditions, passivation layers should not be regarded as chemically inert or permanently anchored components. Instead, they represent reactive and adaptive interfacial species whose molecular configuration, bonding state, and surface coverage can evolve continuously under illumination, thermal stress, and electrical bias [36]. In particular, increasing evidence shows that ultraviolet and high-energy visible photons can directly trigger chemical reactions or electronic excitation within commonly used organic passivators, initiating their gradual desorption or transformation (Figure 4a).

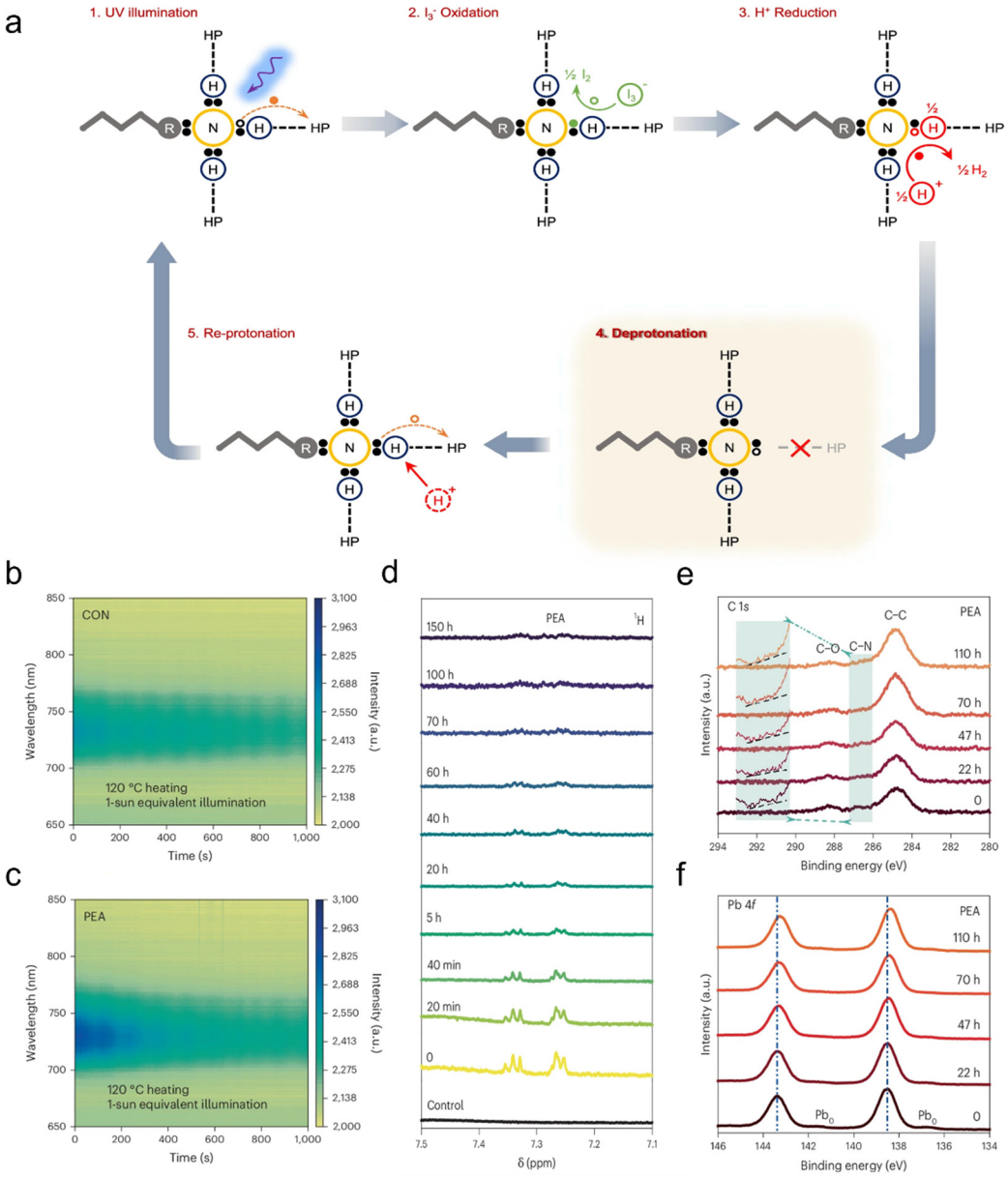

Figure 4. (**a**) Diagram of the violet/UV light-triggered photoreaction cycle. Hollow circles denote holes, solid circles denote electrons, and colored holes/electrons denote the charge carriers participating in the corresponding kinetics. Reprinted with permission from Ref. [36]. The evolution of the PL profile of as-prepared control (**b**), PEA^+ (**c**) perovskite films under continuous 120 °C heating and 1-sun equivalent illumination. (**d**) ^{1}H NMR spectra of control perovskite film, time-evolved ^{1}H NMR spectra of PEA^+ perovskite films under 100 °C heating and 1-sun equivalent illumination. δ denotes the chemical shift. (**e**,**f**) Evolution of the C 1s (**e**) and Pb 4f (**f**) XPS spectra of PEA^+ perovskite films under 100 °C heating and 1-sun equivalent illumination. The C-N signal is highlighted with green shading, and the green dashed lines are used to connect the two green shaded areas of the initial and enlarged regions. The black dashed lines in the left-hand side shade are guides to the eye, used to distinguish the changes in the C-N signal. The vertical dashed lines in (**f**) mark the initial binding energy position of the Pb 4f. Reprinted with permission from Ref. [37].

Representative experimental observations consistently reveal that passivators such as phenethylammonium (PEA^+), which are widely employed to suppress surface defects through ionic or coordinative interactions, undergo progressive desorption or chemical modification under operational conditions [37]. Time-dependent absorption spectroscopy under 1-sun illumination and elevated temperature shows pronounced spectral evolution for PEA-modified interfaces, in contrast to relatively stable control systems (Figure 4b,c), while the rapid decay and finally approaching the intensity close to the control film indicates the failure passivation effects of PEA^+ under continuous photothermal stress. Complementary solid-state characterizations further substantiate this dynamic behavior: 1H NMR spectra reveal a gradual attenuation of characteristic proton signals over extended aging

periods (Figure 4d). XPS analysis shows that the C–N peak of PEA^+ at 286.6 eV disappears after 22 h, indicating complete surface desorption of PEA^+, while deeper PEA^+ persists, and the Pb 4f shift confirms that PEA^+ does not inhibit perovskite surface chemical changes (Figure 4e,f). Collectively, these signatures point to a progressive loss or reconfiguration of passivation molecules at the interface rather than abrupt failure. Such desorption processes inevitably re-expose undercoordinated lead or halide sites, reactivate interfacial non-radiative recombination pathways, and facilitate subsequent ion accumulation, thereby accelerating device performance degradation. These observations underscore that interface passivation in perovskite solar cells is intrinsically dynamic, fundamentally challenging the conventional assumption of static and permanent defect passivation and highlighting the necessity of passivation strategies that explicitly account for chemical and structural evolution under operating conditions.

3.3. Interfacial Chemical Reactions and Electrode Corrosion

Once interface passivation integrity is progressively compromised, the perovskite/ETL interface can no longer be regarded as a chemically inert boundary but instead evolves into an increasingly reactive and structurally unstable region. Under the coupled influence of illumination, thermal stress, and electric-field-driven carrier injection, halide ions, especially iodide, tend to accumulate preferentially at grain boundaries and functional interfaces, where defect density and local electric fields are inherently higher. This enrichment leads to a pronounced increase in PbI_2 content at grain boundaries and interfaces, as directly visualized by high-resolution transmission electron microscopy, which reveals the gradual emergence and expansion of PbI_2-rich regions during aging (Figure 5a–c). Photoelectron spectroscopy further confirms this trend by showing a progressive deviation of the Pb/I atomic ratio from stoichiometry at degraded interfaces, indicating sustained halide depletion and chemical reconstruction rather than reversible ionic redistribution (Figure 5d). Together, these observations demonstrate that the interface undergoes a transition from defect-mediated electronic degradation to genuine chemical decomposition.

As halide depletion continues, mobile iodine species generated from perovskite decomposition, which include I^-, HI, and I_2, can further migrate across the ETL toward the top electrode under thermal stress and illumination. Upon reaching the Ag electrode, these iodine species readily participate in interfacial redox reactions with metallic Ag, leading to the formation of insulating AgI and establishing a chemically driven degradation pathway that couples ionic migration with electrode corrosion (Figure 5f). This process not only accelerates iodine loss from the perovskite lattice but also introduces a growing interfacial barrier for charge extraction, thereby amplifying both chemical and electrical instability.

As degradation proceeds, this chemically activated interface no longer evolves uniformly but instead propagates in a layer-by-layer manner [38]. At later stages, localized chemical reactions preferentially nucleate at pre-existing defects or weak points, progressively developing into pinholes and discontinuities that are clearly resolved in cross-sectional STEM images under accelerated thermal conditions (Figure 5g). These morphological failures permanently disrupt interfacial contact, resulting in abrupt losses in current density and V_{OC} and ultimately driving the device into an irreversible failure regime [39].

From an interfacial evolution perspective, these phenomena collectively represent the terminal manifestation of dynamic interface instability in perovskite solar cells. Chemical reactions, electrode corrosion, and morphological collapse do not occur as isolated degradation events but instead emerge from a self-amplifying interplay between ion migration, interfacial reactivity, and structural fragility. This final failure pathway underscores that perovskite interfaces are intrinsically dynamic systems whose chemical and morphological states continuously evolve under realistic operating conditions. Consequently, passivation strategies based solely on static defect coverage are fundamentally insufficient to prevent long-term degradation, highlighting the urgent need for interfacial designs that can suppress or accommodate chemically driven evolution throughout device operation.

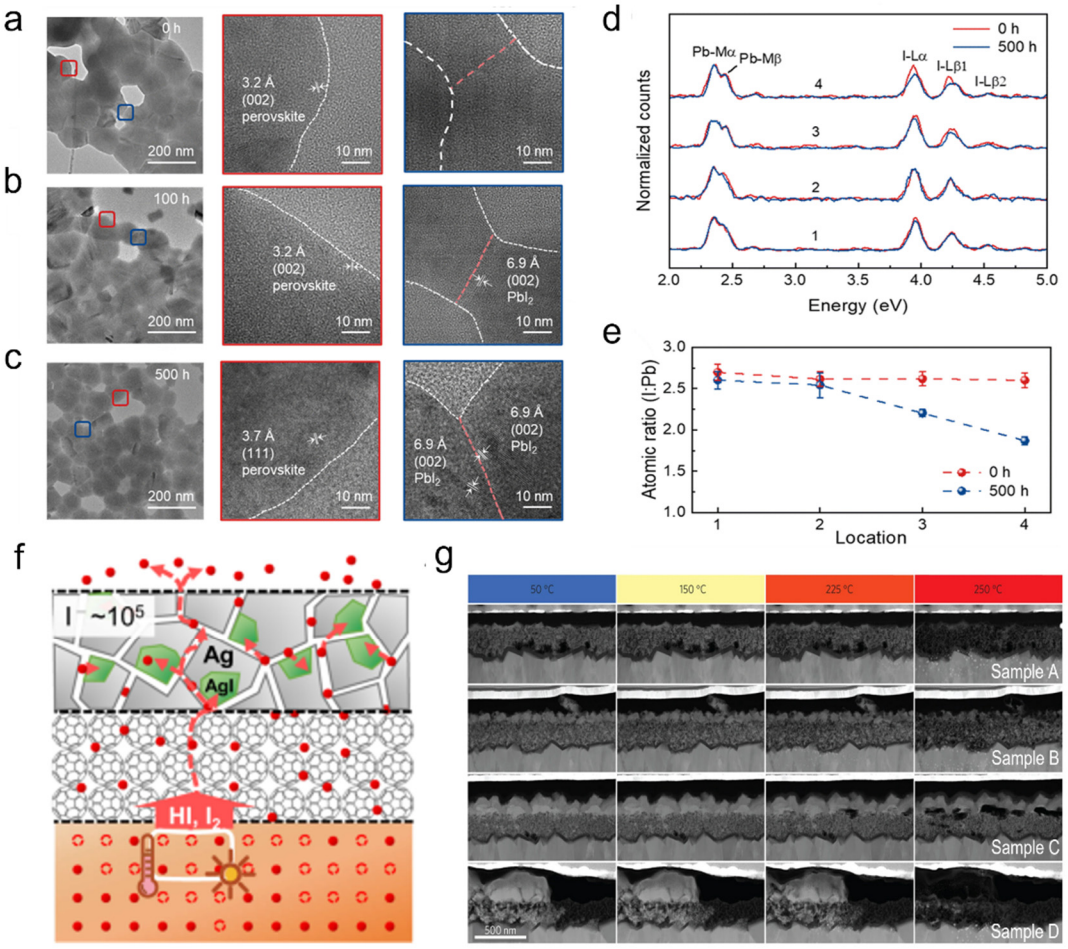

Figure 5. TEM images and the corresponding enlarged views of the perovskite films under AM 1.5G illumination for (**a**) 0 h, (**b**) 100 h, and (**c**) 500 h. The regions highlighted in red and blue boxes indicate the non-contacted and contacted GBs, respectively. (**d**) EDS profiles of the four different regions before and after light illumination. Bulk grains, non-contacted GBs, contacted GBs without PbI_2, and contacted GBs with PbI_2 are represented by 1, 2, 3, and 4, respectively. (**e**) Atomic I: Pb ratios in the four regions determined by EDS before and after light illumination. Reprinted with permission from Ref. [40]. (**f**) Schematic diagram of the iodine ions migration within the devices with Ag. Reprinted with permission from Ref. [41]. (**g**) A high-angle annular dark-field (HAADF) imaging technique to study the sample at various heating stages. Reprinted with permission from Ref. [42].

4. Dynamic Interface-Oriented Strategies and Outlook

The above analysis indicates that the interface between the perovskite absorber and the ETL undergoes a series of dynamically coupled transformations during real device operation. These include sustained ion migration, interfacial structural reconstruction, passivator destabilization, chemically driven interfacial reactions, and localized micro-fracturing or partial delamination. Rather than occurring independently, these processes interact and reinforce one another, collectively governing the long-term operational stability of perovskite solar cells. However, prevailing interface passivation strategies remain predominantly rooted in the assumption that the interface is static and thus chemically and structurally invariant once initially optimized. Such a framework struggles to account for the continuous evolution of interfacial states under prolonged exposure to light, heat, and electrical bias. Consequently, future interface engineering must shift its core objective from maximizing initial passivation efficacy toward developing interface systems capable of sustaining functional stability under dynamic photothermal and electrical operating conditions.

At the stage of materials screening, theoretical modelling and data-driven approaches should go beyond predicting static interfacial configurations and instead prioritize the evolution pathways and stability windows of interfaces under realistic operating stresses [43]. By integrating high-throughput computation with machine learning models, it is possible to simultaneously assess the intrinsic stability of interface materials, their chemical compatibility with perovskite and transport layers, and their ability to maintain dynamically stable interfaces under temperature,

humidity, and bias perturbations [44]. This shift from evaluating single-point performance to predicting evolutionary behavior will establish a theoretical foundation for addressing long-term dynamic interface failure.

Beyond predictive screening, interface material design itself must embrace controlled dynamics. Recent studies on thermally or environmentally activated dynamic passivation systems provide compelling experimental evidence for the feasibility to develop an adaptive interface. In such a system, reversible chemical bonds or latent Lewis-base precursor motifs can be activated under illumination, heating, or hydrothermal stress, enabling the formation of new coordination or bonding sites in response to freshly generated interfacial defects [45]. This dynamic defect compensation mechanism allows for sustained passivation during ongoing interfacial evolution, effectively delaying performance degradation under harsh operating conditions. These findings demonstrate that the interface does not need to be chemically static; instead, deliberately engineered reconfigurability can preserve low defect densities and stable charge transport over extended operation.

In parallel, the construction of gradient and multilayer interfacial architectures offers an effective strategy to mitigate interfacial chemical reactions and morphological degradation. Compared with single-layer passivation schemes, gradient or multilayer interface can spatially decouple ion accumulation zones, charge transport regions, and reaction-sensitive areas, thereby reducing local chemical potential build-up and suppressing reaction driving forces. Rationally designed gradients in energy level alignment, composition, or polarity can also modulate the migration pathways and local accumulation tendencies of halide ions and charge carriers, diminishing the formation of reactive phases and lowering the risk of electrode corrosion. Moreover, by dispersing localized stresses associated with ion migration and lattice mismatch, such architectures can suppress pinhole expansion and interfacial fracture, enhancing both structural and electrical robustness during long-term operation.

Ultimately, a comprehensive understanding and effective regulation of dynamic interfaces rely on in situ and real-time characterization techniques tailored to realistic working conditions. Conventional pre- and post-ageing comparisons often obscure the initial triggers and critical transition stages of interfacial evolution. In contrast, concurrent in situ spectroscopic, microscopic, and compositional analyses performed under illumination, electrical bias, and thermal stress enable direct observation of ion migration, reactive phase formation, and defect state evolution [46]. These time-resolved insights are essential not only for elucidating failure mechanisms but also for establishing quantitative correlations between interfacial dynamics and performance degradation, thereby feeding back into predictive and data-driven design frameworks (Figure 6).

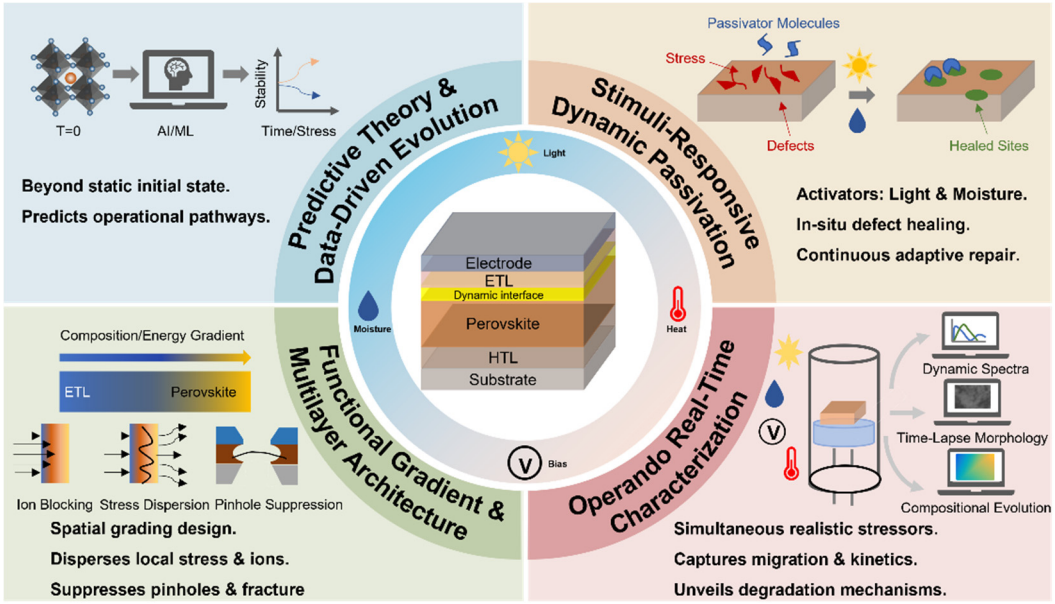

Figure 6. Strategies for dynamic perovskite/ETL interface.

In summary, interface engineering between the perovskite layer and the electron transport layer is undergoing a necessary paradigm shift. Interfaces should no longer be regarded as static structures requiring permanent chemical stability, but rather as dynamically evolving systems whose functionality can be actively regulated during operation. Through the coordinated advancement of predictive modelling, adaptive material design, and in situ characterization, it is increasingly feasible to develop genuinely dynamic passivation and regulation strategies. Such approaches hold the key to overcoming the fundamental stability constraints imposed by interfaces and to enabling the long-term operational reliability of perovskite solar cells.

Author Contributions: J.X. and R.W. directed and supervised the project. Q.X. conceived the idea and wrote the manuscript. X.J., X.W. and Q.L. assisted with the content modification. All authors have read and agreed to the published version of the manuscript.

Funding: This work was supported by the National Natural Science Foundation of China (grant no. 62474143), the Scientific Research Innovation Capability Support Project for Young Faculty (SRICSPYF-BS2025014), Natural Science Foundation of Zhejiang Province of China (grant nos. LD24E020001 and QKWL25E1301), and support from the Key R&D Program of Zhejiang (2024SSYS0061). J.X. acknowledges grants (grant nos. LR24F040001, LDG25E020001) from the Natural Science Foundation of Zhejiang Province of China, the grant from the National Natural Science Foundation of China (grant no. 62274146), the support from the Fundamental Research Funds for the Central Universities (226-2022-00200), the grant from the Research and Development Foundation of Dongfang Electric (Hangzhou) Innovation Institute Co., Ltd. (grant no. 4F-CSC24005), and Zhejiang Province's Vanguard and Leader Geese Research and Development Program (2024C01246(SD2)).

Data Availability Statement: Not applicable.

Conflicts of Interest: The authors declare no conflict of interest.

Use of AI and AI-Assisted Technologies: During the preparation of this work, the authors used ChatGPT to polish the language of the article. After using this tool, the authors reviewed and edited the content as needed and take full responsibility for the content of the published article.

References

1. Rajagopal, A.; Yao, K.; Jen, A.K.Y. Toward Perovskite Solar Cell Commercialization: A Perspective and Research Roadmap Based on Interfacial Engineering. *Adv. Mater.* **2018**, *30*, 1800455. https://doi.org/10.1002/adma.201800455.
2. Kim, D.H.; Park, N.-G. Advanced Interface Engineering for Perovskite Solar Cells: The Way to Ensure Efficiency and Stability. *Acc. Mater. Res.* **2025**, *6*, 1147–1157. https://doi.org/10.1021/accountsmr.5c00170.
3. Tao, J.; Zhao, C.; Wang, Z.; Chen, Y.; Zang, L.; Yang, G.; Bai, Y.; Chu, J. Suppressing non-radiative recombination for efficient and stable perovskite solar cells. *Energy Environ. Sci.* **2025**, *18*, 509–544. https://doi.org/10.1039/D4EE02917H.
4. Shin, S.S.; Park, B.; Noh, J.H.; Seok, S.I. Interlayer engineering in metal halide perovskite photovoltaics. *Nat. Photonics* **2026**, *20*, 11–23. https://doi.org/10.1038/s41566-025-01809-8.
5. Shen, Y.; Zhang, T.; Xu, G.; Steele, J.A.; Chen, X.; Chen, W.; Zheng, G.; Li, J.; Guo, B.; Yang, H.; et al. Strain regulation retards natural operation decay of perovskite solar cells. *Nature* **2024**, *635*, 882–889. https://doi.org/10.1038/s41586-024-08161-x.
6. Jin, B.; Cao, J.; Yuan, R.; Cai, B.; Wu, C.; Zheng, X. Strain Relaxation for Perovskite Lattice Reconfiguration. *Adv. Energy Sustain. Res.* **2023**, *4*, 2200143. https://doi.org/10.1002/aesr.202200143.
7. Lin, Z.; Zhang, W.; Cai, Q.; Xu, X.; Dong, H.; Mu, C.; Zhang, J.-P. Precursor Engineering of the Electron Transport Layer for Application in High-Performance Perovskite Solar Cells. *Adv. Sci.* **2021**, *8*, 2102845. https://doi.org/10.1002/advs.202102845.
8. Luo, D.; Su, R.; Zhang, W.; Gong, Q.; Zhu, R. Minimizing non-radiative recombination losses in perovskite solar cells. *Nat. Rev. Mater.* **2020**, *5*, 44–60. https://doi.org/10.1038/s41578-019-0151-y.
9. Kang, J.; Li, J.; Wei, S.-H. Atomic-scale understanding on the physics and control of intrinsic point defects in lead halide perovskites. *Appl. Phys. Rev.* **2021**, *8*, 031302. https://doi.org/10.1063/5.0052402.
10. Chen, H.; Zhang, W.; Li, M.; He, G.; Guo, X. Interface Engineering in Organic Field-Effect Transistors: Principles, Applications, and Perspectives. *Chem. Rev.* **2020**, *120*, 2879–2949. https://doi.org/10.1021/acs.chemrev.9b00532.
11. Li, J.; Jin, C.; Jiang, R.; Su, J.; Tian, T.; Yin, C.; Meng, J.; Kou, Z.; Bai, S.; Müller-Buschbaum, P.; et al. Homogeneous coverage of the low-dimensional perovskite passivation layer for formamidinium–caesium perovskite solar modules. *Nat. Energy* **2024**, *9*, 1540–1550. https://doi.org/10.1038/s41560-024-01667-8.
12. Guan, H.; Zhang, W.; Liang, J.; Wang, C.; Hu, X.; Pu, D.; Huang, L.; Ge, Y.; Cui, H.; Zou, Y.; et al. Low-Dimensional 2-thiopheneethylammonium Lead Halide Capping Layer Enables Efficient Single-Junction Methylamine-Free Wide-Bandgap and Tandem Perovskite Solar Cells. *Adv. Funct. Mater.* **2023**, *33*, 2300860. https://doi.org/10.1002/adfm.202300860.
13. Su, R.; Xu, Z.; Wu, J.; Luo, D.; Hu, Q.; Yang, W.; Yang, X.; Zhang, R.; Yu, H.; Russell, T.P.; et al. Dielectric screening in perovskite photovoltaics. *Nat. Commun.* **2021**, *12*, 2479. https://doi.org/10.1038/s41467-021-22783-z.
14. Chen, B.; Rudd, P.N.; Yang, S.; Yuan, Y.; Huang, J. Imperfections and their passivation in halide perovskite solar cells. *Chem. Soc. Rev.* **2019**, *48*, 3842–3867. https://doi.org/10.1039/C8CS00853A.
15. Liu, C.; Yang, Y.; Chen, H.; Xu, J.; Liu, A.; Bati, A.S.R.; Zhu, H.; Grater, L.; Hadke, S.S.; Huang, C.; et al. Bimolecularly passivated interface enables efficient and stable inverted perovskite solar cells. *Science* **2023**, *382*, 810–815. https://doi.org/10.1126/science.adk1633.
16. Wu, G.; Liang, R.; Ge, M.; Sun, G.; Zhang, Y.; Xing, G. Surface Passivation Using 2D Perovskites toward Efficient and Stable Perovskite Solar Cells. *Adv. Mater.* **2022**, *34*, 2105635. https://doi.org/10.1002/adma.202105635.
17. Tress, W.; Domanski, K.; Carlsen, B.; Agarwalla, A.; Alharbi, E.A.; Graetzel, M.; Hagfeldt, A. Performance of perovskite solar cells under simulated temperature-illumination real-world operating conditions. *Nat. Energy* **2019**, *4*, 568–574.

https://doi.org/10.1038/s41560-019-0400-8.

18. Wu, L.; Hu, S.; Yang, F.; Li, G.; Wang, J.; Zuo, W.; Jerónimo-Rendon, J.J.; Turren-Cruz, S.-H.; Saba, M.; Saliba, M.; et al. Resilience pathways for halide perovskite photovoltaics under temperature cycling. *Nat. Rev. Mater.* **2025**, *10*, 536–549. https://doi.org/10.1038/s41578-025-00781-7.
19. Zhu, H.; Teale, S.; Lintangpradipto, M.N.; Mahesh, S.; Chen, B.; McGehee, M.D.; Sargent, E.H.; Bakr, O.M. Long-term operating stability in perovskite photovoltaics. *Nat. Rev. Mater.* **2023**, *8*, 569–586. https://doi.org/10.1038/s41578-023-00582-w.
20. Hu, J.; Chen, P.; Luo, D.; Wang, D.; Chen, N.; Yang, S.; Fu, Z.; Yu, M.; Li, L.; Zhu, R.; et al. Tracking the evolution of materials and interfaces in perovskite solar cells under an electric field. *Commun. Mater.* **2022**, *3*, 39. https://doi.org/10.1038/s43246-022-00262-2.
21. Meggiolaro, D.; Motti, S.G.; Mosconi, E.; Barker, A.J.; Ball, J.; Andrea Riccardo Perini, C.; Deschler, F.; Petrozza, A.; De Angelis, F. Iodine chemistry determines the defect tolerance of lead-halide perovskites. *Energy Environ. Sci.* **2018**, *11*, 702–713. https://doi.org/10.1039/C8EE00124C.
22. Li, Z.; Jia, C.; Wu, H.; Tang, Y.; Zhao, J.; Su, Z.; Gao, X.; Qiu, S.; Yuan, H.; Li, M. In-Situ Cross-Linked Polymers for Enhanced Thermal Cycling Stability in Flexible Perovskite Solar Cells. *Angew. Chem. Int. Ed.* **2025**, *64*, e202421063. https://doi.org/10.1002/anie.202421063.
23. Ma, M.; Zhang, X.; Chen, X.; Xiong, H.; Xu, L.; Cheng, T.; Yuan, J.; Wei, F.; Shen, B. In situ imaging of the atomic phase transition dynamics in metal halide perovskites. *Nat. Commun.* **2023**, *14*, 7142. https://doi.org/10.1038/s41467-023-42999-5.
24. Yang, B.; Bogachuk, D.; Suo, J.; Wagner, L.; Kim, H.; Lim, J.; Hinsch, A.; Boschloo, G.; Nazeeruddin, M.K.; Hagfeldt, A. Strain effects on halide perovskite solar cells. *Chem. Soc. Rev.* **2022**, *51*, 7509–7530. https://doi.org/10.1039/D2CS00278G.
25. Wei, J.; Wang, Q.; Huo, J.; Gao, F.; Gan, Z.; Zhao, Q.; Li, H. Mechanisms and Suppression of Photoinduced Degradation in Perovskite Solar Cells. *Adv. Energy Mater.* **2021**, *11*, 2002326. https://doi.org/10.1002/aenm.202002326.
26. Xing, Z.; Fan, B.; Meng, X.; Li, D.; Huang, Z.; Li, L.; Zhang, Y.; Wang, F.; Hu, X.; Hu, T.; et al. Repairing humidity-induced interfacial degradation in quasi-2D perovskite solar cells printed in ambient air. *Energy Environ. Sci.* **2024**, *17*, 3660–3669. https://doi.org/10.1039/D4EE00912F.
27. Lan, Z.; Yang, Y.; Huang, H.; Du, S.; Zhang, Q.; Wang, Z.; Jiang, T.; Sun, C.; Qu, S.; Li, L.; et al. Interfacial electrostatic repulsion inhibits iodide ion migration for enhancing reverse-bias stability of perovskite solar cells. *Nat. Commun.* **2025**, *16*, 11407. https://doi.org/10.1038/s41467-025-66224-7.
28. Xu, J.; Boyd, C.C.; Yu, Z.J.; Palmstrom, A.F.; Witter, D.J.; Larson, B.W.; France, R.M.; Werner, J.; Harvey, S.P.; Wolf, E.J.; et al. Triple-halide wide–band gap perovskites with suppressed phase segregation for efficient tandems. *Science* **2020**, *367*, 1097–1104. https://doi.org/10.1126/science.aaz5074.
29. Draguta, S.; Sharia, O.; Yoon, S.J.; Brennan, M.C.; Morozov, Y.V.; Manser, J.S.; Kamat, P.V.; Schneider, W.F.; Kuno, M. Rationalizing the light-induced phase separation of mixed halide organic–inorganic perovskites. *Nat. Commun.* **2017**, *8*, 200. https://doi.org/10.1038/s41467-017-00284-2.
30. Thiesbrummel, J.; Shah, S.; Gutierrez-Partida, E.; Zu, F.; Peña-Camargo, F.; Zeiske, S.; Diekmann, J.; Ye, F.; Peters, K.P.; Brinkmann, K.O.; et al. Ion-induced field screening as a dominant factor in perovskite solar cell operational stability. *Nat. Energy* **2024**, *9*, 664–676. https://doi.org/10.1038/s41560-024-01487-w.
31. Hoke, E.T.; Slotcavage, D.J.; Dohner, E.R.; Bowring, A.R.; Karunadasa, H.I.; McGehee, M.D. Reversible photo-induced trap formation in mixed-halide hybrid perovskites for photovoltaics. *Chem. Sci.* **2015**, *6*, 613–617. https://doi.org/10.1039/C4SC03141E.
32. Hu, M.; Bi, C.; Yuan, Y.; Bai, Y.; Huang, J. Stabilized Wide Bandgap $MAPbBr_xI_{3-x}$ Perovskite by Enhanced Grain Size and Improved Crystallinity. *Adv. Sci.* **2016**, *3*, 1500301. https://doi.org/10.1002/advs.201500301.
33. Duong, T.; Mulmudi, H.K.; Wu, Y.; Fu, X.; Shen, H.; Peng, J.; Wu, N.; Nguyen, H.T.; Macdonald, D.; Lockrey, M.; et al. Light and Electrically Induced Phase Segregation and Its Impact on the Stability of Quadruple Cation High Bandgap Perovskite Solar Cells. *ACS Appl. Mater. Interfaces* **2017**, *9*, 26859–26866. https://doi.org/10.1021/acsami.7b06816.
34. Yang, Z.; Rajagopal, A.; Jo, S.B.; Chueh, C.C.; Williams, S.; Huang, C.C.; Katahara, J.K.; Hillhouse, H.W.; Jen, A.K.Y. Stabilized Wide Bandgap Perovskite Solar Cells by Tin Substitution. *Nano Lett.* **2016**, *16*, 7739–7747. https://doi.org/10.1021/acs.nanolett.6b03857.
35. Barker, A.J.; Sadhanala, A.; Deschler, F.; Gandini, M.; Senanayak, S.P.; Pearce, P.M.; Mosconi, E.; Pearson, A.J.; Wu, Y.; Srimath Kandada, A.R.; et al. Defect-Assisted Photoinduced Halide Segregation in Mixed-Halide Perovskite Thin Films. *ACS Energy Lett.* **2017**, *2*,1416–1424. https://doi.org/10.1021/acsenergylett.7b00282.
36. Yu, D.; Cao, F.; Qiu, X.; Chen, Y.; Zhang, Z.; Wang, G.; Mao, Y.; Zhong, J.; Su, C.; Huang, W.; et al. Violet/ultraviolet light-induced depassivation in halide perovskite solar cells. *Nat. Commun.* **2025**, *16*, 11409. https://doi.org/10.1038/s41467-025-66227-4.
37. Pei, F.; Lin, S.; Zhang, Z.; Lin, S.; Huang, X.; Zhao, M.; Xu, J.; Zhuang, X.; Zhang, Y.; Tang, J.; et al. Inhibiting defect passivation failure in perovskite for perovskite/Cu(In,Ga)Se2 monolithic tandem solar cells with certified efficiency

27.35%. *Nat. Energy* **2025**, *10*, 824–835. https://doi.org/10.1038/s41560-025-01761-5.

38. Li, H.; Xie, G.; Fang, J.; Peng, H.; Huang, N.; Wang, X.; Lin, D.; Qiu, L. Revealing the Relationship between Interfacial Morphology Degradation and Unsatisfied Stability in Phenethylamine-Treated Perovskite Solar Cell. *Small* **2025**, *21*, e03623. https://doi.org/10.1002/smll.202503623.
39. Li, X.; Fu, S.; Zhang, W.; Ke, S.; Song, W.; Fang, J. Chemical anti-corrosion strategy for stable inverted perovskite solar cells. *Sci. Adv.* **2020**, *6*, eabd1580. https://doi.org/10.1126/sciadv.abd1580.
40. Wang, H.; Li, Q.; Zhu, Y.; Sui, X.; Fan, X.; Lin, M.; Shi, Y.; Zheng, Y.; Yuan, H.; Zhou, Y.; et al. Photomechanically accelerated degradation of perovskite solar cells. *Energy Environ. Sci.* **2025**, *18*, 2254–2263. https://doi.org/10.1039/D4EE04878D.
41. Zhou, J.; Liu, Z.; Yu, P.; Tong, G.; Chen, R.; Ono, L.K.; Chen, R.; Wang, H.; Ren, F.; Liu, S.; et al. Modulation of perovskite degradation with multiple-barrier for light-heat stable perovskite solar cells. *Nat. Commun.* **2023**, *14*, 6120. https://doi.org/10.1038/s41467-023-41856-9.
42. Divitini, G.; Cacovich, S.; Matteocci, F.; Cinà, L.; Di Carlo, A.; Ducati, C. In situ observation of heat-induced degradation of perovskite solar cells. *Nat. Energy* **2016**, *1*, 15012. https://doi.org/10.1038/nenergy.2015.12.
43. Correa-Baena, J.-P.; Hippalgaonkar, K.; van Duren, J.; Jaffer, S.; Chandrasekhar, V.R.; Stevanovic, V.; Wadia, C.; Guha, S.; Buonassisi, T. Accelerating Materials Development via Automation, Machine Learning, and High-Performance Computing. *Joule* **2018**, *2*, 1410–1420. https://doi.org/10.1016/j.joule.2018.05.009.
44. Zhang, C.; Jia, Y.; Zhang, B.; Zhao, Q.; Xu, R.; Pang, S.; Wang, H.; De Wolf, S.; Wang, K. Machine learning-driven interface material design for high-performance perovskite solar cells with scalability and band-gap universality. *Joule* **2025**, *10*, 102264. https://doi.org/10.1016/j.joule.2025.102264.
45. Wang, W.-T.; Holzhey, P.; Zhou, N.; Zhang, Q.; Zhou, S.; Duijnstee, E.A.; Rietwyk, K.J.; Lin, J.-Y.; Mu, Y.; Zhang, Y.; et al. Water- and heat-activated dynamic passivation for perovskite photovoltaics. *Nature* **2024**, *632*, 294–300. https://doi.org/10.1038/s41586-024-07705-5.
46. Mao, L.; Xiang, C. A comprehensive review of machine learning applications in perovskite solar cells: Materials discovery, device performance, process optimization and systems integration. *Mater. Today Energy* **2025**, *47*, 101742. https://doi.org/10.1016/j.mtener.2024.101742.

Commentary

Kinetic Trapping of High-Entropy Alloys via Fast Reduction and Mixing in a Liquid Metal

Zhiheng Lyu

Department of Chemical and Biological Engineering, The University of Alabama, Tuscaloosa, AL 35401, USA; zlyu2@ua.edu

Received: 16 March 2026; Revised: 28 March 2026; Accepted: 30 March 2026; Published: 31 March 2026

Abstract: High-entropy alloy nanoparticles have emerged as a promising material platform for catalysis, sensing, energy storage, and biomedical applications, but their synthesis is often constrained by high temperature or energy inputs, as well as the intrinsic immiscibility of the constituent elements. A recent study in *Nature* introduces an isothermal solidification approach, in which metals are rapidly reduced and mixed in a sacrificial liquid metal, enabling the formation of nanoparticles containing up to 20 elements with controlled structure and morphology.

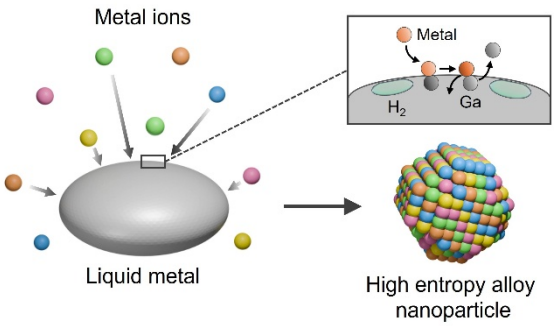

Keywords: high-entropy alloy; isothermal solidification; liquid metal; nanoparticle synthesis; *in-situ* transmission electron microscopy

Alloying elements has been employed to modify material properties since the Bronze Age, with well-known examples including the addition of tin into copper and chromium into iron to enhance hardness and corrosion resistance [1]. At the nanoscale, tuning the composition of nanoparticles (NPs) can similarly optimize their chemical, physical, and mechanical properties, such as surface reactivity, chemical stability, structural robustness, and stiffness, enabling superior performance in catalysis, sensing, energy storage, and biomedicine. While earlier studies mostly focused on bi- or tri-metallic NPs, since first proposed in 2004 [2], the concept of high-entropy alloys (HEAs) introduced materials composed of five or more elements in near-equiatomic proportions. These multicomponent NPs offer highly tunable chemical compositions and improved structural stability, as the increased entropic contribution with increasing number of elements can overcome the enthalpic contribution and stabilize solid solutions.

The most typical method in synthesizing HEA NPs involves high temperature/energy annealing followed by rapid cooling, which promotes mixing of elements while skipping their structural aggregation, phase segregation, and surface reconstruction. Notable examples include carbothermal shock [3], electroshock [4], and laser scanning ablation [5], techniques that typically require specialized and sometimes complex instrumentation. Alternatively, wet-chemical strategies such as multi-cation exchange [6] or co-reduction [7,8] have emerged as convenient approaches, usually operating at relatively low reaction temperatures by carefully controlling metal insertion or reduction rates. However, these methods are often limited by the miscibility of elements involved, and the products are majorly governed by thermodynamics.

Aside from co-reduction, galvanic replacement provides another strategy for alloying metals driven by differences in reduction potentials, in which a sacrificial metal template reacts with ions of more noble metals. Liquid metal, in particular gallium (Ga), stands out as a unique substrate due to its non-toxicity, low melting point, high metal solubility, and low reduction potential ($E_0[Ga^{3+}/Ga]$ = −0.529 V vs. standard hydrogen electrode), endowing it with strong reducing capability and an ideal medium for atomic-level metal mixing [9]. Reporting in *Nature*, Zheng and co-workers demonstrated an isothermal solidification approach to synthesize HEA NPs containing up to 20 elements at temperatures below 100 °C by employing Ga as both the reductant and reaction

medium (Figure 1A) [10]. Beyond simple galvanic replacement [11], this approach can produce Ga-free HEA NPs with tunable size, structure, and morphology.

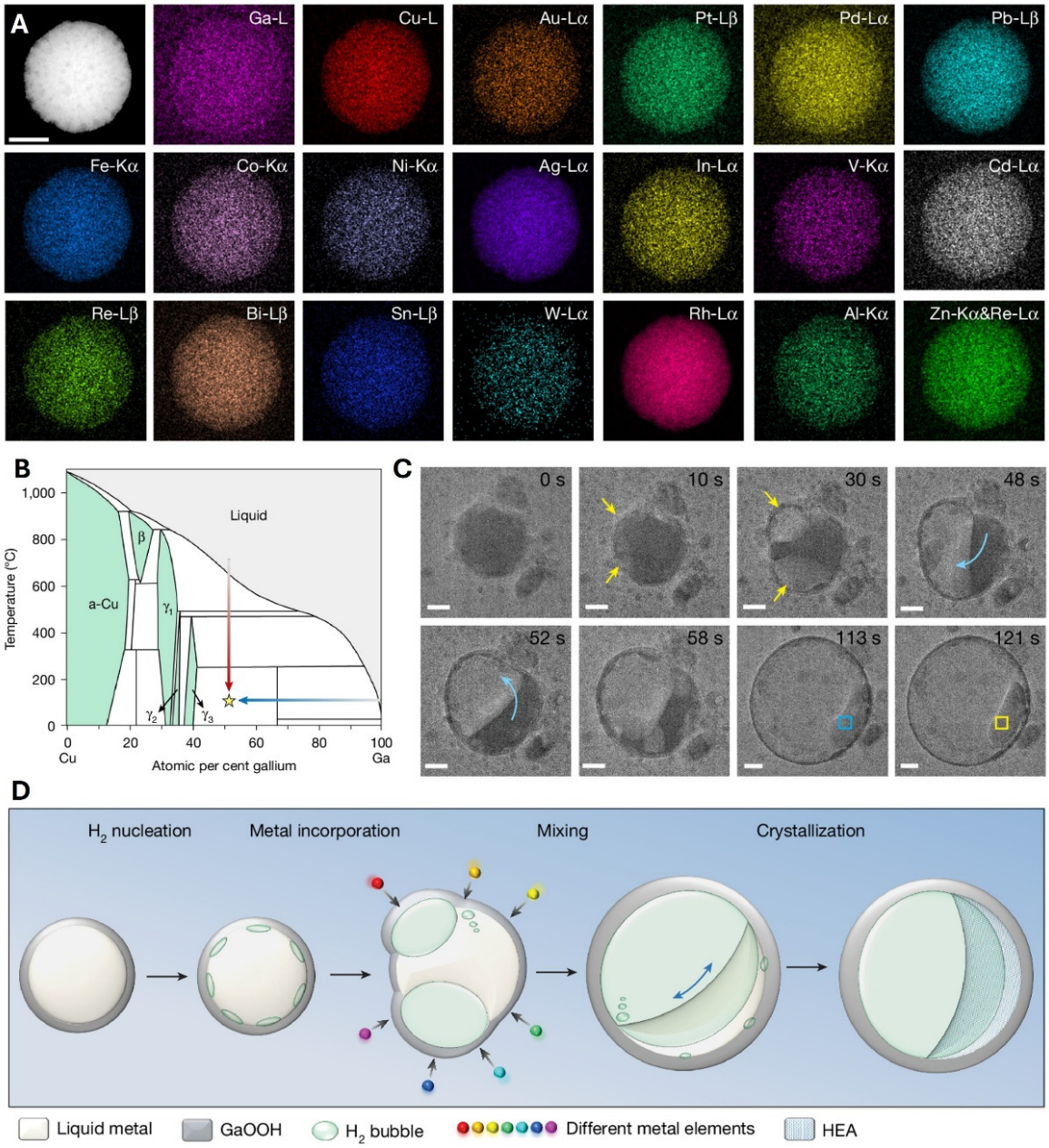

Figure 1. (**A**) Elemental mapping by energy dispersive X-ray spectroscopy (EDS) showing a HEA NP containing up to 20 metals, which was synthesized using isothermal solidification. (**B**) Phase diagram of a representative Cu–Ga binary alloy, demonstrating two solidification routes. The rapid cooling solidification traps the high-temperature states to form HEAs, as indicated by the red arrow. The isothermal solidification, in contrast, traps high-entropy state by rapidly changing the composition at low temperatures, as marked by the blue arrow. (**C**) *In-situ* TEM images capture the formation of a HEA NP (GaInSnZnCu) within a liquid environment at 60 °C. Yellow arrows highlight H_2 bubble nucleation and growth, whereas the blue arrow indicates the stirring direction of the liquid metal alloy. (**D**) Schematic of the formation of HEA NPs, showing the steps of H_2 nucleation, metal reduction and incorporation, metal mixing and crystallization.

Two steps are involved in isothermal solidification: (i) fast reduction of metal salts at the interfaces between the Ga-based liquid metal and aqueous metal ion solution ($Ga + \frac{3}{n} Me^{n+} \rightleftharpoons Ga^{3+} + \frac{3}{n} Me$), and (ii) dissolution of the reduced metal atoms into Ga, followed by their dynamic mixing. Different from the rapid cooling solidification which kinetically traps the high-temperature states to form HEAs (indicated by the red arrow in Figure 1B), isothermal solidification traps the high-entropy state by rapidly changing the composition at low temperatures (as highlighted by the blue arrow). The abrupt composition change leads to the liquid metal alloy

entering a supercooled state, triggering elemental oversaturation in the liquid metal and their precipitation as HEA NPs. Note that Ga can be largely excluded in the final product by controlling its consumption and metal solidification rates, leaving alloys made of only desired elements. This distinguishes isothermal solidification from previously reported liquid metal-assisted synthesis of HEA NPs at high temperatures [12], where Ga remains incorporated in the final product.

The solidification process was further captured by in-situ transmission electron microscopy (TEM) to unveil the atomistic mechanisms (Figure 1C,D). This state-of-the-art imaging technique allows two interesting observations: (i) hydrogen bubbles were generated during the reduction process, and their stirring effectively enhanced the metal element mixing; (ii) oscillatory nucleation and disruption were observed, which supports the proposed rapid solidification. The disruption to the formation of crystals is likely induced by the stirring of evolving hydrogen bubbles.

Beyond simply producing HEA NPs, isothermal solidification also has capability in controlling crystal structure and morphology by tuning reaction temperature and metal salt concentration. With increasing temperature, mesocrystalline (at 60 °C) and polycrystalline (at 80 °C) NPs were obtained, which can be attributed to rapid solidification, dynamic heterogeneities, and mobility asymmetry of supercooled liquids. Reacting at a lower temperature (40 °C) while doubling the concentrations of metal precursors led to the formation of amorphous spherical NPs, potentially arising from the swift dissolution of metal atoms, deep undercooling of the liquid alloy, and prompt solidification. In terms of morphology, with increasing reaction temperature, HEA NPs tended to exhibit more uniform elemental distribution, more porous structures, and more diversified morphologies. A variety of shapes including solid spheres, porous spheres, flow-like, dendritic, and snowflake-like structures have been observed. The size of HEA NPs could also be tuned from 140–250 nm by controlling the size of the liquid metal droplets.

Despite its advantages, the isothermal solidification method still requires further development. For instance, scalable synthesis is necessary to meet the demand of a large quantity for practical applications. Additionally, since the shape and size of the HEA NPs are also affected by liquid metal droplets, achieving high-purity products remains a challenge. Nevertheless, this approach based on rapid reduction and mixing of metals in liquid metal nanoreactors offers an innovative platform for producing NPs that are otherwise difficult or tedious to synthesize, such as single-atom alloys and multi-layer structures, potentially through careful control of metal salt concentrations and drop-wise precursor addition. Moreover, its coupling with density functional theory (DFT) and machine learning (ML) holds great promise for accelerating the identification of elemental compositions for specific applications [13]. The nanoreactors could also be extended beyond liquid metals to micelles or bioreactors, enabling selective element incorporation or alternative reduction mechanisms (e.g., photocatalysis). In summary, isothermal solidification provides a one-step, low-temperature route to HEA NPs with controllable size, morphology, and crystal structure, offering significant promise for applications in catalysis, batteries, and beyond.

Funding: This work was supported by start-up funds from the University of Alabama.

Data Availability Statement: Not applicable.

Conflicts of Interest: The author declares no conflict of interest.

Use of AI and AI-Assisted Technologies: No AI tools were utilized for this paper.

References

1. George, E.P.; Raabe, D.; Ritchie, R.O. High-Entropy Alloys. *Nat. Rev. Mater.* **2019**, *4*, 515–534.
2. Yeh, J.W.; Chen, S.K.; Lin, S.J.; Gan, J.Y.; Chin, T.S.; Shun, T.T.; Tsau, C.H.; Chang, S.Y. Nanostructured High-Entropy Alloys with Multiple Principal Elements: Novel Alloy Design Concepts and Outcomes. *Adv. Eng. Mater.* **2004**, *6*, 299–303.
3. Yao, Y.G.; Huang, Z.N.; Xie, P.F.; Lacey, S.D.; Jacob, R.J.; Xie, H.; Chen, F.J.; Nie, A.M.; Pu, T.C.; Rehwoldt, M.; et al. Carbothermal Shock Synthesis of High-Entropy-Alloy Nanoparticles. *Science* **2018**, *359*, 1489–1494.
4. Glasscott, M.W.; Pendergast, A.D.; Goines, S.; Bishop, A.R.; Hoang, A.T.; Renault, C.; Dick, J.E. Electrosynthesis of High-Entropy Metallic Glass Nanoparticles for Designer, Multi-Functional Electrocatalysis. *Nat. Commun.* **2019**, *10*, 2650.
5. Wang, B.; Wang, C.; Yu, X.W.; Cao, Y.; Gao, L.F.; Wu, C.P.; Yao, Y.F.; Lin, Z.Q.; Zou, Z.G. General Synthesis of High-Entropy Alloy and Ceramic Nanoparticles in Nanoseconds. *Nat. Synth.* **2022**, *1*, 138–146.
6. McCormick, C.R.; Schaak, R.E. Simultaneous Multication Exchange Pathway to High-Entropy Metal Sulfide Nanoparticles. *J. Am. Chem. Soc.* **2021**, *143*, 1017–1023.
7. Liu, Y.H.; Hsieh, C.J.; Hsu, L.C.; Lin, K.H.; Hsiao, Y.C.; Chi, C.C.; Lin, J.T.; Chang, C.W.; Lin, S.C.; Wu, C.Y.; et al. Toward Controllable and Predictable Synthesis of High-Entropy Alloy Nanocrystals. *Sci. Adv.* **2023**, *9*, eadf9931.
8. Kang, Y.Q.; Cretu, O.; Kikkawa, J.; Kimoto, K.; Nara, H.; Nugraha, A.S.; Kawamoto, H.; Eguchi, M.; Liao, T.; Sun, Z.Q.; et al. Mesoporous Multimetallic Nanospheres with Exposed Highly Entropic Alloy Sites. *Nat. Commun.* **2023**, *14*, 2023.

9. Wang, M.; Lin, Y.L. Gallium-Based Liquid Metals as Reaction Media for Nanomaterials Synthesis. *Nanoscale* **2024**, *16*, 6915–6933.
10. Zhang, Q.B.; Gallant, M.C.; Chen, Y.; Song, Z.G.; Liu, Y.; Zheng, Q.; Chen, L.F.; Bustillo, K.C.; Huang, Y.; Persson, K.A.; et al. Isothermal Solidification for High-Entropy Alloy Synthesis. *Nature* **2025**, *646*, 323–330.
11. Gan, T.S.; Shang, W.H.; Handschuh-Wang, S.; Zhang, Y.K.; Zhou, X.C. Liquid Metal Nanoreactor Enables Living Galvanic Replacement Reaction. *Chem. Mater.* **2024**, *36*, 3042–3053.
12. Cao, G.H.; Liang, J.J.; Guo, Z.L.; Yang, K.A.; Wang, G.; Wang, H.L.; Wan, X.H.; Li, Z.Y.; Bai, Y.J.; Zhang, Y.L.; et al. Liquid Metal for High-Entropy Alloy Nanoparticles Synthesis. *Nature* **2023**, *619*, 73–77.
13. Kubik, M.; Wang, S.; Camargo, P.H.C. Chemically Interpretable Machine Learning for Predicting HER Activity in Au-Based Alloys. *Mater. Interfaces* **2025**, *2*, 406–417.

Review

Interfacial Engineering of Biofunctional Materials for Soft Tissue Repair

Xueyan Li [1], Xinyu Wang [1], Meimeng Dai [1], Lisi Liu [1], Urszula Stachewicz [2], Jianyong Yu [1], Xiaoran Li [1,*], and Bin Ding [1,*]

[1] Innovation Center for Textile Science and Technology, College of Textiles, Donghua University, Shanghai 201620, China
[2] Faculty of Metals Engineering and Industrial Computer Science, AGH University of Krakow, 30-059 Kraków, Poland
* Correspondence: xiaoranli@dhu.edu.cn (X.L.); binding@dhu.edu.cn (B.D.)
Received: 5 February 2026; Revised: 23 March 2026; Accepted: 30 March 2026; Published: 31 March 2026

Abstract: Interfacial materials provide an emerging platform for regulating biomaterial-tissue interactions to improve the therapeutic efficacy. Herein, this review systematically examines the latest progress in interfacial-engineered biomaterials, emphasizing the design principles and the benefits for soft tissue repair. This review begins with a discussion on material selection, structural design, and functionalization aimed at steering the physical, chemical, and biological interactions at the interfaces. Then, the basic regulatory strategies are highlighted, including biophysical modulation, intermolecular interaction regulation, and microenvironment tuning. Additionally, the applications of the functional interfacial materials in diverse soft tissues are discussed. Finally, this review presents the current challenges for interface design, and proposes future directions for improving therapeutic outcomes and translation.

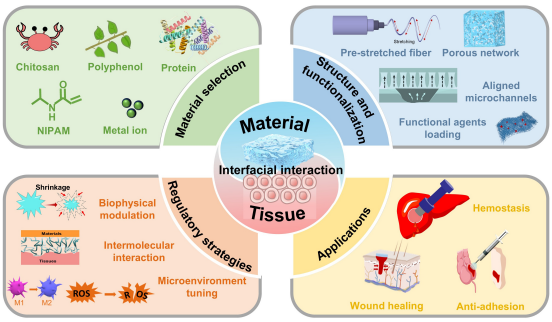

Keywords: biofunctional materials; interfacial engineering; intermolecular interaction regulation; microenvironment tuning; soft tissue repair

1. Introduction

Soft tissues refer to the non-mineralized structures within the body that connect, support, or surround other organs and skeletal frameworks [1]. The repair of damaged or lost soft tissues, such as skin, muscle, tendon, and nerve, remains a significant clinical challenge. Biomaterials show great potential for repair and regeneration of the damaged soft tissues [2–4]. However, poor biomaterial-soft tissue interfaces often trigger adverse events, such as abnormal adhesion, chronic inflammation, and impaired tissue integration. Such interfacial dysfunction compromises the therapeutic efficacy and may even lead to repair failure. Whereas biomaterials with feasible interfacial properties are capable of promoting material-tissue integration and improving eventual outcomes [5,6]. Therefore, the interfacial engineering of functional biomaterials is urgently needed to improve the therapeutic efficacy.

Currently, the common limitations of biomaterials for soft tissue repair include poor adhesion in a wet wound environment, mechanical mismatch-induced tissue stress or isolation, and inability to modulate the pathological conditions, such as persistent inflammation or excessive oxidative stress, resulting in treatment failure. Thus, an ideal interfacial biomaterial should provide adaptive and dynamic physical, chemical, and biological regulation rather than passive coverage or filling. The emergence of interfacial engineered materials provides promising platforms for soft tissue repair by enhancing the interactions at the material-tissue interfaces. By leveraging the interaction mechanisms between materials and tissues, the engineered biomaterials can transmit beneficial mechanical signals [7], establish strong molecular linkages [8], and regulate local microenvironments [9], thereby actively promoting soft tissue repair. For example, polymers with thermal-responsive shrinkage behaviors have been designed into wound dressings to deliver mechanical cues for inducing wound contraction [10]. Similarly, self-expanding sponges have been engineered to provide continuous compression on surrounding tissues via

volume expansion, enabling non-compressible hemostasis [11–13]. Another strategy is to regulate the adhesion state between materials and soft tissues by modulating intermolecular forces [14–16]. For example, strong adhesion is required for dressings to ensure excellent fitting with the wounds, while low adhesion is desired during dressing changing to avoid secondary damage. Furthermore, biomaterials functionalized with therapeutic agents, such as polyphenols, peptides, drugs, and growth factors, can actively regulate the interfacial microenvironment to promote tissue regeneration [17–19].

This article provides a comprehensive review of engineered interfacial biomaterials, covering design principles, regulatory strategies, and applications in soft tissue repair. First, the principles of raw material selection, structural design, and biofunctionalization of interfacial biomaterials are reviewed. Next, we explore the regulatory strategies, including biophysical modulation, intermolecular interaction regulation, and microenvironment tuning. Afterward, the applications in the repair of diverse soft tissues are discussed. Finally, current challenges and future directions for rational design of next-generation materials are highlighted.

2. Design Principles of Interface-Engineered Biomaterials

The composition of biomaterials lays the foundation for regulating the mechanical property, degradation behavior, cell response and tissue integration. Meanwhile, the structural design of the materials plays a crucial role in engineering interfacial interactions. Furthermore, biofunctionalization endows the interfacial materials with desired bioactivities to improve soft tissue regeneration.

2.1. Material Selection

The chemical composition determines the basic properties of the materials, including physical, chemical, and biological characteristics, which directly dictate the efficacy of material-tissue interactions [20,21]. The material hydrophilicity and mechanical compliance directly govern cell adhesion and mechanical matching with the host tissue. Furthermore, the chemical groups provide active sites for additional functionalities, such as microenvironmental responsiveness, antibacterial activity, and antioxidant property. The biomaterials are typically classified into natural and synthetic materials. Natural materials possess superior biocompatibility and biological properties. In contrast, synthetic polymers provide versatile platforms for programmable engineering of mechanical property, degradation behavior, and surface modification.

Derived from biological sources, natural materials exhibit excellent biocompatibility and inherent bioactivity, making them ideal candidates for soft tissue repair. Additionally, natural biomolecules are crucial to build active interfaces with host tissues [22]. Polysaccharides, including sodium alginate [23], hyaluronic acid (HA) [24], chitosan (CS) [25], and cellulose acetate [26], possess abundant hydroxyl, carboxyl, and amino groups that can form physical or chemical crosslinking networks, serving as hydrophilic backbones of the substrates. Additionally, the abundance of active groups facilitates the formation of hydrogen bonds and other chemical interactions with tissue surfaces, which is essential for stable wet adhesion [27,28]. Cationic polymers, such as CS, enable electrostatic interactions with negatively charged cell membranes, and have been widely used as anti-bacterial wound dressings [29]. Oxidized natural polymers are able to achieve strong interfacial adhesion through dynamic Schiff base bonds, which are formed by their aldehyde groups and amino groups on tissue proteins [30]. Proteins such as collagen, gelatin, and silk fibroin play a vital role in mediating specific cellular interactions. Their cell-adhesive motifs directly engage integrin receptors on cell surfaces to promote focal adhesion, spreading, and migration. Gelatin, a denatured collagen that retains biologically active sites and exhibits temperature-dependent sol-gel transition properties, has been widely utilized for injectable delivery and in-situ gelling strategies [31]. Furthermore, methacrylation of proteins such as gelatin methacryloyl (GelMA) enables the construction of photo-crosslinkable systems, combining the inherent bioactivity with tunable *in situ* formability [32,33]. However, the practical applications of natural materials are limited by batch-to-batch variability and mechanical instability.

Synthetic materials offer distinct advantages, including tunable degradation behavior, tailorable mechanical properties, and versatile functionalization. The degradation behavior is of decisive significance for the success of tissue repair [34]. It has been well known that tissue repair scaffolds require suitable degradation behavior that provides structural support yet does not hinder tissue regeneration and growth [35]. In addition, degradation products interact with the surrounding environment and cells, leading to local pH change and inflammatory responses. The synthetic polymers can be designed and synthesized to offer exceptional tunability in chemical, mechanical and degradation behaviors to meet the specific requirements of diverse soft tissues. Notably, mechanical properties such as elasticity and toughness can be precisely tailored by selection of synthetic polymers, adjustment of the compositional ratios, and engineering of the crosslinking network, minimizing mechanical mismatch at the material-tissue interface [36,37]. As an example, polyurethane (PU) has become an ideal

material for fibrous membranes that endure cyclic deformation owing to its exceptional toughness, elasticity, and biocompatibility [38]. Poly(L-lactide-*co*-ε-caprolactone) (PLCL) has been readily electrospun into nanofibrous scaffolds as soft tissue-compatible bioresorbable materials [39]. Similarly, synthetic materials composed of polyacrylamide (PAAm) or poly(ethylene glycol) (PEG) provide inert networks and tunable mechanical properties.

Stimuli-responsive polymers play an essential role in creating active interfaces. For example, poly(N-isopropylacrylamide) (PNIPAM) represents a typical thermoresponsive material, with a lower critical solution temperature (LCST) close to body temperature [40]. Upon warming to 37 °C, PNIPAM chains embedded in the hydrogels or fibers undergo a hydrophilic-to-hydrophobic transition, generating considerable contractile force [41]. The body temperature-responsive contraction property has been widely used to construct materials that actively apply mechanical tension to wound edges for promoting wound closure [27]. The responsive mechanisms based on reactive oxygen species (ROS)- or pH-sensitive dynamic bonds, such as boronate esters and Schiff bases, have been employed for microenvironment-stimulated drug delivery. In addition, enzyme-responsive materials have been designed to react with specific enzymes in the microenvironment for on-demand drug delivery [42]. A typical example is the pH- and enzyme- dual-responsive microgel, which enables on-demand release of antibiotics [43]. Another example involves photo-responsive systems for on-demand drug delivery [32]. Collectively, the stimulus-responsive platforms enable the construction of programmable interfacial materials for adaptive and dynamic therapeutic interventions.

In practical applications, natural and synthetic materials are often hybridized to combine their specific advantages, such as biocompatibility, mechanical properties, biodegradability, etc. By tailoring the key behaviors, the interfacial interactions between the biomaterials and the surrounding biological environment can be effectively optimized.

2.2. Structural Design

Apart from material selection, the structural design plays a critical role in engineering interfacial interactions. Biofunctional materials can be rationally engineered by designing the structure to provide interfacial interactions, such as mechanical signal transmission, exudate management, and biological signal delivery. The structural design transforms the materials into active platforms, which are beneficial for the construction of a favorable interfacial microenvironment for soft tissue repair.

As a representative strategy, a “stiff-elastic” binary component fibrous tape with body temperature shrinkage behavior was developed via electrospinning to provide tensile force for wound closure [44]. In this study, highly elastic PU and stiff poly(vinyl butyral) (PVB) were used for electrospinning, during which PU chains could be stretched under the electrostatic field followed by fixation within the rigid PVB network, resulting in considerable elastic energy storage (Figure 1Ai). A rapid and large isotropic shrinkage of the fibrous membrane was observed upon exposure to 37 °C, due to the retraction of the PU/PVB molecular chains (Figure 1Aii). Notably, the shrunk membrane could be highly stretched, and an almost full recovery could be achieved after exposure to 37 °C (Figure 1Aiii). The thermal-triggered shape recovery was attributed to the mobility of polymer chains and exchanges of H-bonds (Figure 1Aiv). The generated contractile force was capable of inducing significant wound closure and promoting wound healing. In addition, the contraction directionality of dressings can be readily adjusted by controlling the fiber alignment. As an example, a nanofibrous membrane with biaxial orientation was fabricated by regulating the collector geometry during electrospinning. Interestingly, a distinct centripetal contraction was achieved upon thermal stimulation, providing favorable peripheral-to-center mechanical drawing of wound edges [45]. Alternatively, controlled wound contraction can be achieved by a hydration-based shape-memory mechanism. Zhao et al. developed a strain-programmed patch, which was pre-stretched and maintained in a temporary state [46]. Upon water absorption, the adhesive layer of the patch recovered from the glassy to the rubbery state, releasing the predetermined strain, and thereby providing contraction force.

Alternatively, the rational structural design endows the materials with a liquid-triggered self-expansion behavior, generating interfacial compression, which facilitates rapid hemorrhage control in irregular and deep wounds. For instance, Ding et al. developed a highly porous bioactive glass nanofibrous cryogel (BGNC), which was composed of flexible BG electrospun fibers and citric acid-crosslinked poly(vinyl alcohol) (PVA) via homogenization of electrospun fibrous membranes and freeze-drying (Figure 1Bi) [47]. The cryogel could be injected into a deep cavity, followed by a rapid expansion triggered by fluid absorption, resulting in a full filling of the cavity (Figure 1Bii). The expansion stress was measured during fluid absorption. Upon water absorption, BGNC exhibited an ultrafast expansion within 3 s and generated a substantial expansion stress of 2.72 kPa, which was about 4.7 times that of PVA cryogels (Figure 1Biii). Moreover, BGNCs exhibited underwater resilience with near zero Poisson’s ratios during cyclic compression (Figure 1Biv). These findings indicate that BGNC holds great potential for treating deep bleeding wounds, even under dynamic conditions such as movement. Alternatively, *in*

situ gas foaming provides a robust approach for generating expansive pressure within injectable hydrogels. Specifically, the hydrogels containing calcium carbonate and acetic acid are able to generate carbon dioxide bubbles due to the decomposition reaction, resulting in hydrogel expansion and self-propelling (Figure 1Ci) [48]. Figure 1Cii shows the changes in stress during expansion process. The hydrogels with self-expanding and self-propelling action would access deep perforating and conform to the irregular wound cavities.

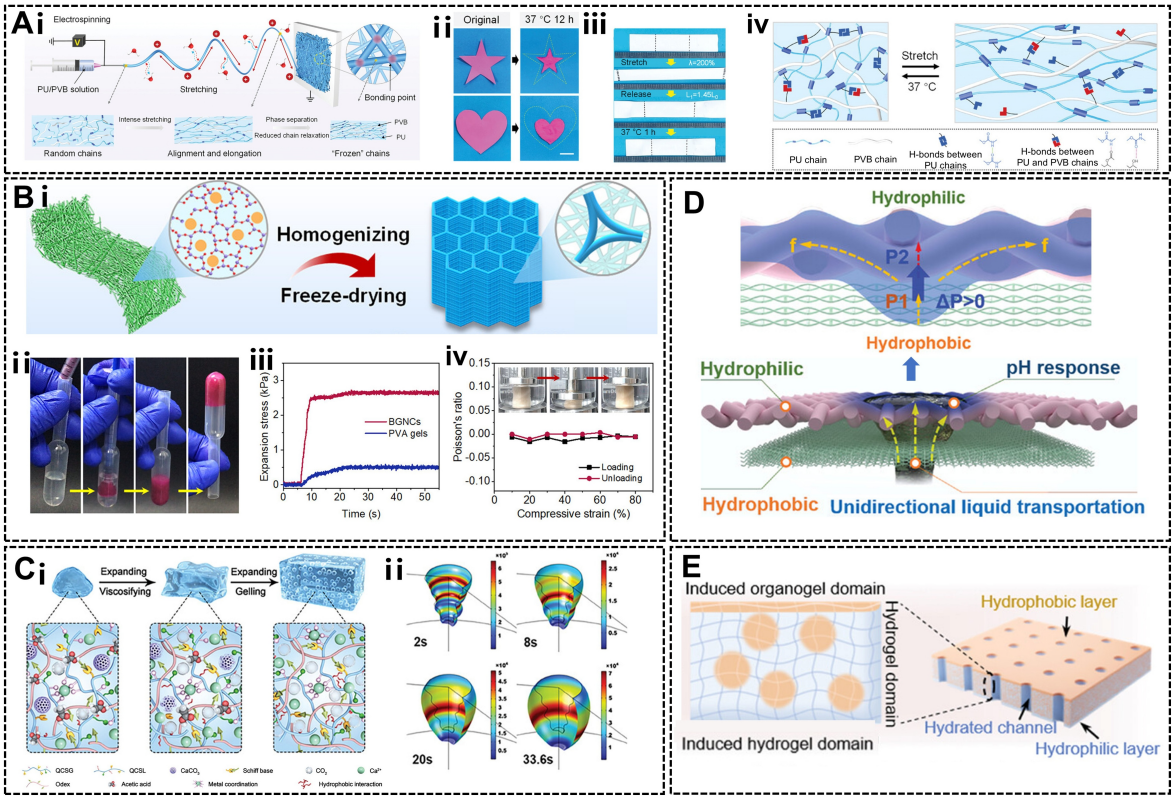

Figure 1. Structural design of interface-engineered biomaterials. (**A**) The electrospun "stiff-elastic" binary-component fibrous membrane with thermal-triggered shrinkable capability. (**i**) Schematic showing the stretching process of PU/PVB chains followed by fixation induced by phase separation during electrospinning. **(ii)** Shrinkage behavior at 37 °C. Scale bar indicates 1 cm. (**iii**) The stretching-release-thermal recovery behavior and (**iv**) mechanism of the shrunk membrane. Reproduced with permission [44]. Copyright 2024, Wiley-VCH. (**B**) Highly porous fibrous cryogels with self-expanding behavior. (**i**) Schematic showing fabrication process by homogenization of electrospun membranes and freeze-drying. (**ii**) Injectability and fluid absorption triggered self-expansion performance. (**iii**) Expansion stress upon water absorption. (**iv**) Poisson's ratio and photographs of the fibrous cryogel under cyclic compression. Reproduced with permission [47]. Copyright 2023, American Chemical Society. (**C**) Carbon dioxide bubble generating hydrogel with self-expanding performance. (**i**) Schematic showing the hydrogel expansion mechanism. (**ii**) Stress during expansion. Reproduced with permission [48]. Copyright 2024, Wiley-VCH. (**D**) Janus fibrous dressing with unidirectional fluid transportation capability. Reproduced with permission [49]. Copyright 2024, Wiley-VCH. (**E**) Self-pumping organohydrogels with aligned hydrated hydrogel channels. Reproduced with permission [50]. Copyright 2024, Wiley-VCH.

The material architectures can be engineered to harness fluidic forces, facilitating wound exudate management. Excessive wound exudate poses risks of delayed healing, wound degeneration, infection, and persistent inflammation. In clinical practice, it is crucial to remove excessive exudate timely. However, it is difficult for traditional materials to remove biological fluids with high viscosity from the wound surface. The Janus dressing with asymmetric wettability represents a typical example of driving fluid transport. As an example, a bilayered dressing consisting of a hydrophobic poly(ε-caprolactone) (PCL) electrospun membrane and a hydrophilic cellulose nonwoven was prepared, resulting in Laplace pressure difference (Figure 1D) [49]. Therefore, a unidirectional fluid transport was achieved from the wound-facing hydrophobic layer to the hydrophilic absorbent layer, effectively draining exudate from the wound beds. A step forward has been made by engineering fluidic pathways with improved capillary pumping effect. For instance, hydrogel dressings with directional hydration channels were prepared by 3D-templated wetting-enabled-transfer polymerization, followed by integration with hydrophobic and hydrophilic gel layers, achieving self-pumping of viscous biofluids (Figure 1E) [50]. The synergistic

effect of guided channels and Janus wettability gradient led to an exceptionally high unidirectional fluid drainage capability at a speed up to 41.67 $\mu L \cdot s^{-1}$, far surpassing that of conventional asymmetric dressings (less than 5.0 $\mu L \cdot s^{-1}$).

2.3. Functionalization with Bioactive Ions or Biomolecules

Biofunctionalization provides a pivotal strategy to endow the interfacial materials with biological capabilities. The addition of bioadhesive substances such as catechol derivatives is favorable for enhancing intermolecular bonding forces at the tissue interface [51]. The immobilization of therapeutic agents, such as active ions, antioxidants, anti-inflammatory drugs, and growth factors, offers rich opportunities to improve the hostile tissue microenvironment [52–54], including alleviating chronic inflammation [55], suppressing excessive oxidative stress [56], and promoting angiogenesis.

Bioactive metal ions can be directly integrated into material networks to impart multifunctionality. For example, zinc ions (Zn^{2+}) exhibit broad-spectrum antibacterial property while facilitating human umbilical vein endothelial cell proliferation and angiogenesis [57]. Iron ions (Fe^{3+}) can serve as crosslinking agents to form strong coordination complexes and participate in the Fenton reaction to clear ROS, thereby improving therapeutic outcomes [28,58]. Nanocarriers, including metal-organic frameworks (MOFs), nanoparticles, nanofibers and nanohydrogels, act as versatile reservoirs for controlled drug delivery. Diverse biomolecules and bioagents have been readily encapsulated into the nanocarriers for controlled release. It can be engineered in response to microenvironmental stimulus such as pH, ROS, and proteinases. Certain MOFs based on Zn^{2+}, Mg^{2+}, or Fe^{3+} possess superoxide dismutase (SOD)-like, or catalase (CAT)-like activities, showing great potential for ROS scavenging [59,60]. In addition, the released bioactive metal ions contribute to antibacterial and angiogenesis functions. The MOF hydrogel loaded with functional small molecules is able to regulate local immune response and accelerate wound healing [61]. Overall, owing to excellent drug delivery efficiency and outstanding antioxidant capacity, MOFs have shown great potential in soft tissue repair [62].

Polyphenols, such as tannic acid (TA) and its derivatives, serve dual roles as versatile interfacial adhesives and bioactive modulators [63,64]. The high density of catechol/pyrogallol groups facilitates strong adhesion through hydrogen bonding, hydrophobic interactions, and coordination bonds. The excellent ROS scavenging capability makes them effective antioxidants for tissue regeneration [65]. Furthermore, their metal-chelating ability allows the formation of functional complexes to achieve additional activities [66]. Curcumin, a polyphenolic compound, was encapsulated into microneedle patches to reshape the microenvironment and improve the repair of chronic soft tissue defects [67]. As another example, epigallocatechin gallate was introduced to the microneedle patches, which showed antibacterial and antioxidant capacity in healing process of infected diabetic wounds [68]. Various herbal preparations, including flavonoids and terpenoids, have been proven to reduce oxidative stress, regulate signaling pathways, and promote angiogenesis [69].

Overall, through diverse functionalization approaches, biomaterials can be endowed with tissue adhesion, specific bioactivities, and improved tissue-interfacing properties. More recently, the advancement of stimuli-responsive delivery system can provide more intelligent systems, which are conducive to controlling cell response and improving tissue regeneration.

3. Regulatory Strategies of Material-Tissue Interfacial Interactions

The material-tissue interface represents a dynamic spatiotemporal system, involving interactions between the implanted materials and biological components, such as proteins, cells, and tissue fluids [70,71]. It has been widely recognized that interfacial molecular interactions constitute the basis underlying most biological processes in nature [72]. The interfacial interactions ultimately drive multi-level physical, chemical, and biological events. Thus, the material-tissue interfacial interactions are of importance for modulating cell behavior and tissue function. The basic regulatory strategies include biophysical modulation, intermolecular interaction regulation, and microenvironment tuning, which collectively influence cell adhesion, migration, and differentiation, and consequently govern tissue adhesion, integration, and regeneration. Notably, biophysical modulation delivers physical force cues, including tension and compression, and also mediates capillary action, thereby promoting wound closure, hemostasis, and exudate drainage. The intermolecular interactions, including hydrogen bonds and dynamic chemical bonds, can directly mediate the interface between materials and tissues. Specifically, strong intermolecular interaction leads to robust adhesion ability, whereas the repulsive force results in superior anti-adhesion performance. Furthermore, increasing evidence suggests that biofunctionalized interfaces capable of modulating microenvironment exhibit a powerful ability to recapitulate the *in vivo* conditions through biochemical cues, such as pH, ROS, growth factor expression, and cell phenotypes.

3.1. Biophysical Modulation

As a non-invasive strategy, the biophysical modulation harnesses biophysical cues to promote the healing process. For instance, the interfacial materials can be engineered to generate tensile forces through contraction, apply compressive pressure via expansion, and drive fluid transport by capillary action. By delivering such active biophysical cues, these materials guide critical repair outcomes, including wound closure, hemostasis, and exudate drainage, in a direct and effective way.

Contractile forces can be generated by engineering the materials to undergo programmable dimensional changes. For instance, a moisture-adaptive fiber composed of sodium alginate, gelatin, and hydroxyl-rich silica nanoparticles was prepared by Di et al. (Figure 2Ai) [73]. Specifically, upon fluid absorption, the disruption of intermolecular hydrogen bonds caused molecular chain relaxation and fiber elongation. Subsequent drying process triggered the reconstruction of hydrogen bonds, forcing the polymer chains into a contracted conformation and generating substantial uniaxial contractile force, which actively drew wound edges together in a simulated wound model (Figure 2Aii). Alternatively, thermal activation offers a facile approach for providing contractile forces [74]. Hydrogels formulated with temperature-sensitive polymers exhibited volume shrinkage upon reaching their LCST. When bridged across a wound, this contraction generated a continuous closing force. The stress-shielding effect directly relieved mechanical tension at wound edges, effectively promoting healing and mitigating scar formation (Figure 2B).

In addition to contractile forces, the interfacial materials can be engineered to offer controlled expansion for providing compression, which is beneficial for hemostasis. To this end, shape memory materials that undergo liquid-triggered self-expansion have been developed to deliver interfacial compression. For instance, a porous scaffold composed of carboxymethyl cellulose (CMC) fibers and acetalized PVA expanded to more than 20 times its original volume within seconds upon blood contact, attributed to the volumetric expansion of the porous network and the swelling of embedded hydrophilic fibers [75]. The expansion forces exerted mechanical compression to the bleeding blood vessels at the lesion sites, similar to manual pressure for stopping bleeding. As another example, Wu et al. developed a self-expanding cuttlefish bone elastomeric sponge (CBES) with ordered microchannels, which was composed of cuttlefish bone powder, poly (glycerol sebacate) (PGS) and PCL by 3D-printing (Figure 2Ci) [76]. It was found that the sponges absorbed fluid rapidly upon blood contact, leading to red blood cell enrichment for blood clotting, along with shape recovery for exerting expansion pressure at the bleeding sites. Moreover, the ordered microchannel architecture provided guiding cues for blood flow, and the incorporated bioactive cuttlefish bone powder was capable of enhancing the coagulation cascade (Figure 2Cii).

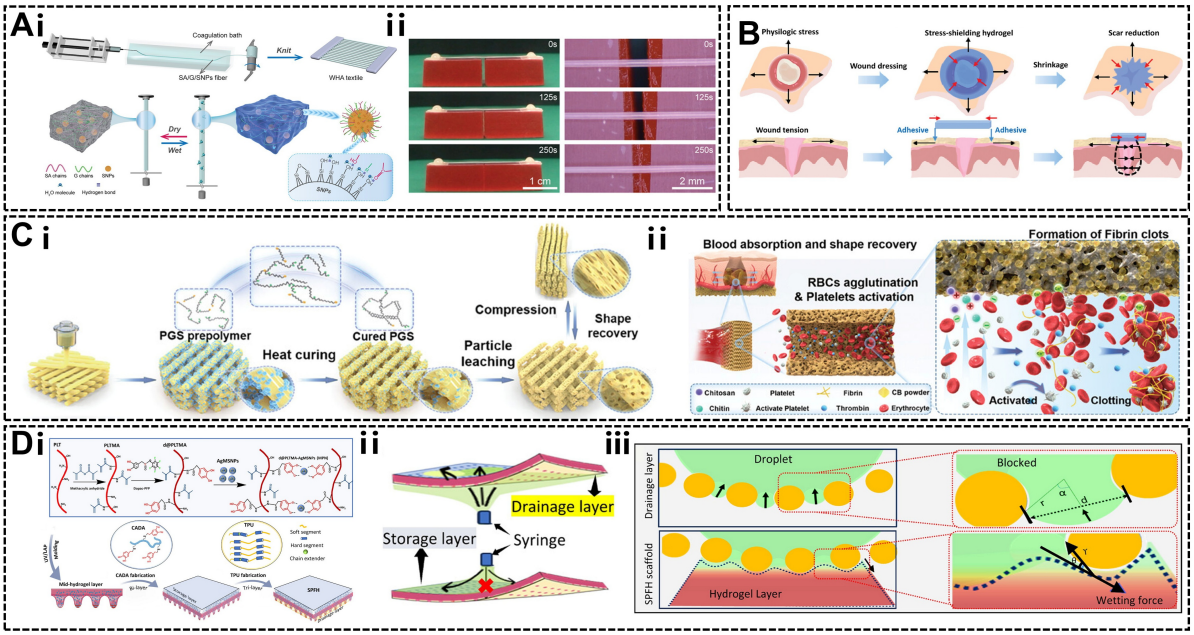

Figure 2. Interfacial biomaterials for biophysical modulation. (**A**) Contractile force provided by the humidity-responsive fibers. (**i**) Schematic showing fabrication of the textile knitted by the composite fibers. (**ii**) The simulated contraction process by using an agarose model. Reproduced with permission [73]. Copyright 2023, Wiley-VCH. (**B**) Schematic illustrating contractile force provided by the stress-shielding hydrogel for reducing scar formation. Reproduced under the terms of the CC BY 4.0 license [74]. Copyright 2024, the authors, published by Wiley-VCH. (**C**) Compressive pressure provided by the self-expanding elastomeric sponge. (**i**) Schematic showing fabrication

process of the sponge with ordered channels and porous structures. (**ii**) Schematic illustrating the hemostatic mechanism of the sponge, combining mechanical compression by rapid self-expansion, red blood cell aggregation, and Ca^{2+} triggered coagulation. Reproduced with permission [76]. Copyright 2023, Wiley-VCH. (**D**) Capillary force provided by the tri-layered Janus scaffold integrating hydrophobic/hydrophilic asymmetric wettable layers and aligned hollow microneedle channels. (**i**) Schematic showing fabrication of the mid-layer featuring aligned hollow microneedle channels. (**ii**) Schematic showing transport process when droplet contacts with different layers. (**iii**) The schematic showing the self-pumping mechanism of SPFH scaffolds in which the wetting force generated by the hydrogel layer pulled the droplets from the contacting points. Reproduced with permission [77]. Copyright 2025, Wiley-VCH.

The capillary force of the materials based on the Laplace pressure gradients, offers a simple and versatile strategy for guiding fluid transport, which is beneficial for wound exudate drainage. The dressings constructed by depositing a hydrophilic layer on a hydrophobic layer create asymmetric wettability, offering a directional capillary force [78,79]. The principle was further amplified in an advanced design by integrating aligned hollow hydrophilic microchannels or microneedle arrays with the hydrophilic/hydrophobic Janus dressing. As shown in Figure 2Di, Pei et al. fabricated a tri-layer self-pumping Janus fibrous hydrogel scaffold (SPFH) composed of an inner hydrophobic electrospun drainage layer, an outer hydrophilic storage layer, and a middle supramolecular hydrogel layer with hollow microneedle channels [77]. The combination of hydrophobic/hydrophilic asymmetric wettability and microchannels synergistically enhanced the drainage performance (Figure 2(Dii,Diii)). In addition to highly efficient exudate drainage, the superhydrophobic surface is able to repel the wound fluid and minimize adhesive contact, facilitating easy and non-traumatic removal [80].

3.2. Intermolecular Interaction Regulation

The dynamic molecularly engineered interfaces have attracted considerable attention. Interfacial biofunctional materials for soft tissue repair rely on sophisticated intermolecular interactions to modulate the biological response at different stages. For example, Cao et al. developed a timescale-dependent bioadhesive, enabling strong wet adhesion, along with fault-tolerant and convenient surgical operations (Figure 3Ai) [81]. In the initial stage which lasts only seconds, the hydrogel formed instant and reversible physical interactions with wet tissue surfaces, allowing repositioning or detachment of misplaced adhesives without causing secondary tissue damage, which was superior to the conventional covalent-based tapes (Figure 3(Aii,Aiii)). Subsequently, a transition from physical interactions to strong covalent linkages occurred in hours, and an interfacial toughness of approximately 1268 J m^{-2} was achieved.

The interface water layer, which mediates the material-tissue interactions dramatically, poses a significant challenge to the adhesion effect [82]. To overcome this challenge, various strategies have been developed, including disruption of hydration layer, enhancement of intermolecular interactions, introduction of covalent bonds, and design of water absorption structures [83]. For example, self-gelling coacervate powders were developed to achieve robust adhesion on wet tissue surface, through a liquid-liquid phase separation process mediated by intermolecular hydrogen bonds and hydrophobic interactions between TA, CS, and PEG (TCP) [84]. Upon absorption of interfacial water, *in situ* self-gelling occurred for the powders, leading to a tight adhesion to various material surfaces, attributed to the formation of hydrogen bonding, cation-π interactions, and coordination bonding (Figure 3Bi). A higher adhesion strength was achieved for the TCP gel compared with fibrin sealant (Figure 3Bii). Moreover, loading of bioactive substances such as platelet-rich plasma and deferoxamine was beneficial for wound healing. Apart from adhesion materials, the anti-adhesive materials play a crucial role in preventing postoperative adhesions. For example, Wang et al. developed a self-fused, antifouling, and injectable hydrogel to prevent postoperative peritoneal adhesions [85]. The hydrogel was constructed through reversible hydrogen-bonding networks between methacrylate hyaluronic acid (HA-GMA) and ultra-hydrophilic N-(2-hydroxypropyl) methacrylamide (HPMA) side chains (Figure 3Ci). Interestingly, the dense hydrated layer consisting of ultra-hydrophilic HPMA chains functioned as an antifouling barrier, effectively repelling proteins and fibroblasts (Figure 3Cii). The hydrogel facilitated peritoneal repair by modulating mesothelial-to-mesenchymal transition. In another example, a microgel assembly with programmable self-contraction, robust adhesiveness, and triggerable detachment, was developed to provide a mechanically active interface for wound healing by activating mechanotransduction [86]. Specifically, the self-contraction N-isopropyl acrylamide (NIPAM)-*co*-acrylic acid (AAC) microgel assembly with robust tissue adhesion featured a secondary network of polyacrylic acid and calcium ions (Figure 3Di). Interestingly, the adhesion decreased dramatically after spraying of sodium bicarbonate solution, allowing noninvasive removal of the dressings (Figure 3(Dii,Diii)). Importantly, the microgel was capable of temperature-triggered self-contraction, which enabled mechanical traction directly to

the wound surface. The mechanical cue activated mechanotransduction pathways, such as Hippo and TGF-β/Smad, to promote cell conversion and collagen synthesis. Simultaneously, the contraction of exosome-laden microgel assembly (SMART-EXO) facilitated the on-demand release of exosomes to accelerate re-epithelialization through PI3K/AKT and MAPK/Erk signaling, indicating a transition from passive barriers to active mechanical and biochemical regulators.

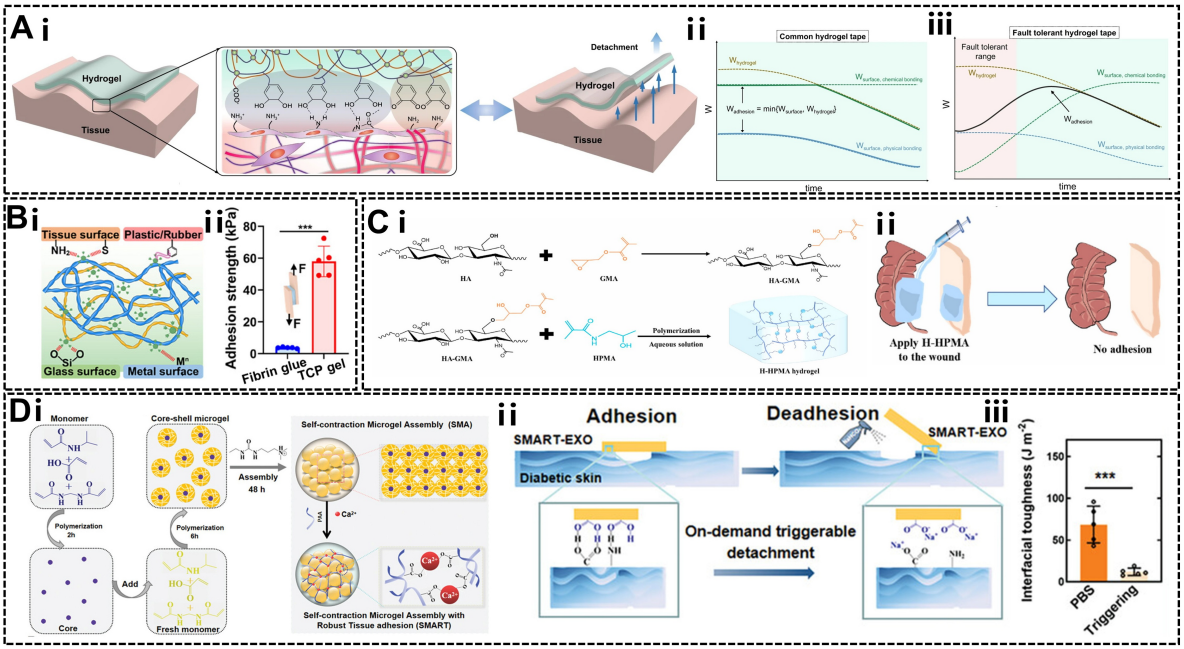

Figure 3. Interfacial biomaterials for intermolecular interaction regulation. (**A**) The fault-tolerant hydrogel tape with reversible adhesion at the initial stage and long-term strong adhesion capability. (**i**) Schematic showing the fault-tolerant mechanism due to the formation of non-covalent interactions in seconds. The time-dependent adhesion strength of (**ii**) common hydrogel tapes and (**iii**) fault-tolerant hydrogel tapes. Reproduced under the terms of the CC BY 4.0 license [81]. Copyright 2021, the authors, published by Springer Nature. (**B**) Coacervate powder-derived adhesive hydrogel. (**i**) Schematic showing adhesion mechanism to different substrates. (**ii**) Adhesion strength on porcine skin. Reproduced with permission [84]. Copyright 2025, Wiley-VCH. (**C**) Hydrogel with anti-adhesion capability. (**i**) Schematic showing hydrogel preparation. (**ii**) Schematic showing its application on a rat cecum-abdominal wall adhesion model. Reproduced under the terms of the CC BY 4.0 license [85]. Copyright 2022, the authors, published by KeAi Publishing. (**D**) Microgel assembly with self-contraction, adhesive, and triggerable detachment capabilities. (**i**) Schematic showing the fabrication process of the microgel. (**ii**) Schematic showing the wet adhesion and triggerable detachment of the microgel. (**iii**) The interfacial toughness of the microgel on wet porcine skin decreased significantly upon application of triggering solution for 5 min. Reproduced with permission [86]. Copyright 2024, Wiley-VCH.

3.3. Microenvironment Tuning

Beyond biophysical modulation and intermolecular interaction regulation, advanced interfacial material functions as an active platform that dynamically regulates the local biochemical and cellular microenvironment of the lesion sites. Significant efforts have been devoted to the development of biofunctionalized materials to regulate hostile microenvironment with excessive ROS, dysregulated inflammation, and aberrant cellular signaling, creating a conducive niche for promoting efficient regeneration. The active intervention strategy is capable of addressing the pathological imbalances of chronic or impaired healing, offering a sophisticated approach for microenvironmental reprogramming.

ROS scavenging and oxidative stress alleviation have been recognized as critical and primary issues for mitigating the deleterious ROS-inflammation cascade in injured tissues. Thus, the antioxidative materials that can protect cells from oxidative damage and activate pro-survival and pro-migration pathways have been widely used as interfacial agents. Nanomaterials engineered with enzyme-mimicking nanozymes can directly scavenge multiple types of ROS [87]. For instance, metal-polyphenol coordination nanoparticles not only exhibit SOD-like activity to catalyze the conversion of superoxide anions, but also upregulate endogenous antioxidant enzymes (e.g., SOD, CAT) in cells. The dual-action, at the material-tissue interface, effectively decreases the local oxidative

burden, protects mitochondrial integrity from damage, and subsequently downregulates harmful pathways such as AGE-RAGE, thereby rescuing cellular function and creating a redox-balanced microenvironment conducive to healing [88].

The sustained inflammation and compromised angiogenesis pose major obstacles for soft tissue regeneration. It has been reported that the nuclear factor-κB (NF-κB) signaling pathway is the key mechanistic target of ROS-inflammatory cascade. Therefore, a tetrahedral framework DNA hydrogel (TDH) was prepared for effective ROS scavenging (Figure 4Ai), which could inhibit the activation of NF-κB pathway, leading to downregulated expression of pro-inflammatory cytokines such as tumor necrosis factor-α (TNF-α) and interleukin-1β (IL-1β) and improved macrophage switching from a pro-inflammatory (M1) to an anti-inflammatory (M2) state (Figure 4(Aii–Aiv)) [89]. The precise immunomodulation at the tissue interface is capable of eliminating chronic inflammation and fostering a restorative microenvironment.

Integration of biochemical regulation and biophysical stimulation provides a comprehensive strategy for promoting wound healing. For example, an antioxidative and thermosensitive active shrinking hydrogel was constructed to enhance re-epithelization and skin constriction [90]. It was found that the gel activated the mechanosensitive epidermal growth factor receptor/Akt pathway, thereby promoting cell proliferation. Furthermore, electrical stimulation offers robust regulatory cues to modulate cell proliferation and migration. A self-powered thermoelectric hydrogel Ag_2Se@GelMA was developed to generate stable electrical stimulation at the material-tissue interface by taking advantage of the temperature difference between the skin and the environment (Figure 4Bi) [91]. Electrical stimulation activated voltage-gated calcium channels on adjacent cells, triggering calcium ion (Ca^{2+}) influx (Figure 4Bii). Subsequently, the increase of free Ca^{2+} levels in the cytoplasm activated Ca^{2+}/calmodulin-dependent protein kinase β (CaMKKβ), which phosphorylated AMP-activated protein kinase (AMPK) at the threonine 172 (Thr172). Modulation of AMPK activity through Ca^{2+} signaling enhanced mitochondrial function and dynamics, significantly promoting key cellular activities including proliferation, migration, and angiogenesis. Therefore, interfacial materials can transmit biochemical and biophysical signals that directly regulate the cellular activities necessary for tissue repair. The active regulation of cell behavior through favorable interfacial interactions provides essential support for guiding soft tissue repair.

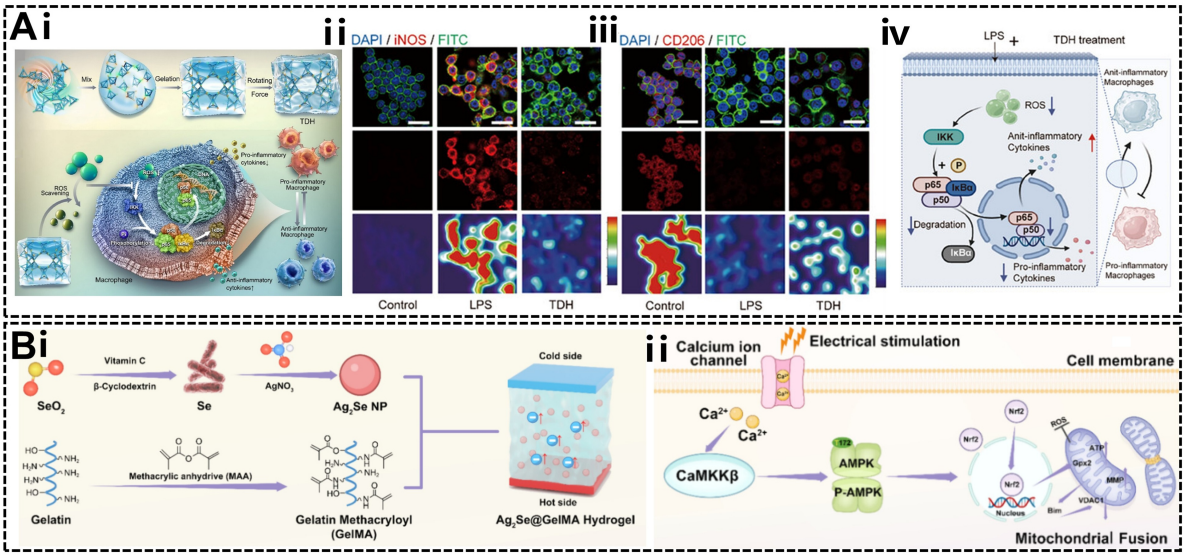

Figure 4. Interfacial biomaterials for microenvironment tuning. (**A**) DNA hydrogel with inflammation regulation capability. (**i**) Schematic showing hydrogel formation via cross-linking of tetrahedral DNA nanostructures based on complementary base pairing. Representative immunofluorescence images and heatmaps of (**ii**) iNOS and (**iii**) CD206 staining. (**iv**) Schematic showing that the hydrogel disrupted the ROS-inflammatory cascade in macrophages via downregulation of NF-κB pathway. Reproduced with permission [89]. Copyright 2025, Wiley-VCH. (**B**) The thermoelectric hydrogels with cell behavior regulation capability. (**i**) Schematic showing the fabrication of hydrogel-based electrical stimulation device. (**ii**) Schematic showing the mechanism and pathway of hydrogels for promoting wound healing. Reproduced with permission [91]. Copyright 2025, American Chemical Society.

4. Applications in Soft Tissue Repair

The repair of severe soft tissue defects remains a huge challenge. Interfacial biomaterials are designed to serve as temporary yet instructive matrices for actively guiding tissue regeneration. The ultimate goal is long-term

integration followed by functional restoration. Thus, these constructs are engineered to not only fill the defect but also interact dynamically with the host tissues, directing key processes such as stem cell fate, tissue-specific regeneration, or the prevention of pathological adhesions. To date, the biomaterials have been constructed in the forms of injectable hydrogels, electrospun patches, decellularized matrix composites, etc., for the applications in repair of various soft tissues including skin, tendon, nerve, muscle, fascia, etc.

4.1. Skin Repair

As a critical component of soft tissue, the skin repair faces several challenges of rapid hemostasis, accelerated wound closure and complete restoration of skin function. Biofunctional interfacial materials have emerged as a versatile platform to manage bleeding or modulate wound microenvironment. Consequently, these materials demonstrate enormous potential beyond traditional wound dressings.

As the first stage of wound healing, uncontrollable bleeding remains the main cause of preventable death. Additionally, hemostasis establishes a provisional matrix enriched with activated platelets, which subsequently play a critical role in tissue repair and regeneration [92,93]. Therefore, hemostasis represents a crucial step that lays the foundation for subsequent soft tissue regeneration. Rapid and effective hemostatic materials should be capable of minimizing blood loss, preventing rebleeding, and facilitating wound healing.

The asymmetric dressing features a self-pumping action that unidirectionally transports excessive serum from the hydrophobic layer to the hydrophilic layer, concentrating coagulation factors and promoting hemostasis. As an example, a Janus amphipathic Fiber@Gel/Ca^{2+}/KL dressing was developed by combining multiple hemostatic mechanisms to enhance the efficiency [94]. Upon application to the bleeding wounds, the dressing enabled unidirectional self-pumping of serum, which effectively concentrated red blood cells and platelets, while simultaneously releasing calcium ions to activate the coagulation cascade (Figure 5Ai). The multifunctional interfacial action promoted a rapid formation of stable clots in the rabbit ear artery bleeding models, resulting in reduced blood loss and hemostatic time (Figure 5(Aii,Aiii)). Notably, the anti-adhesive property of its hydrophobic surface allowed for easy and safe removal of the dressing without causing secondary hemorrhage.

Non-compressible hemorrhage control in deep wounds represents a significant challenge. The self-expanding porous materials have been extensively studied to provide interfacial compression for physical tamponade, and absorb liquid for concentrating coagulation factors, resulting in improved blood clotting [95]. Freeze-drying offers a straightforward approach to develop interconnected porous sponges. The porous sponges, fabricated via freeze-drying, could rapidly absorb blood and expand within seconds to exert mechanical pressure on damaged vessels (Figure 5Bi) [96]. The hemostasis time of the hemostatic sponges in the mouse liver injury model was 41 s, which was much shorter than that of the commercial chitosan sponge group (77 s) (Figure 5Bii). Furthermore, on-demand removal was achieved via a simple rinsing that disrupted the ionic crosslinks, enabling safe debridement without disrupting the fresh clot. Moving forward, an approach combining cryogelation, solvent exchange and ambient-temperature drying has been developed to offer a potential strategy for reducing production costs (Figure 5Ci) [97]. By using this approach, a chitosan fiber (CSF)-based cryogel with fast expanding capability has been fabricated. When applied in the rabbit axillary artery and vein complete transection model, the compressed CSF sponge rapidly absorbed blood, expanded, and sealed the cross-section of the artery, leading to reduced blood loss and hemostatic time (Figure 5Cii).

In addition to hemorrhage control, the main challenges facing skin wound healing include exudate management, persistent inflammation, and tissue regeneration disorders. Through precise engineering of interfacial interactions, including rapid exudate drainage, delivery of mechanical forces, and spatiotemporal modulation of the biochemical signals, the advanced wound dressings enable transformation of the hostile wound bed into a regenerative microenvironment. The dressings have been designed in various forms, including film, hydrogel, sponge, and nanofibrous scaffold, demonstrating superior efficacy in accelerating wound closure, enhancing tissue regeneration, and restoring function across diverse wound models.

Management of hostile wound microenvironments combines multiple interfacial functions to address co-existing challenges such as heavy exudation and persistent inflammation. For treatment of burn wounds with massive exudates, Wang et al. developed a self-pumping organohydrogel dressing with hydrophilic fractal microchannels [98]. By utilizing creaming-assistant emulsion interfacial polymerization, the dressing was constructed with gradient-distributed poly-lauryl methacrylate (PLMA) organogel particles embedded within PAAm hydrogel networks (Figure 6Ai). Owing to the multilevel capillary effects, the organohydrogel dressing enabled ~30 times enhancement in fluid drainage compared to the pure hydrogel. In a murine burn model, a ~42.5% reduction in dermal cavity was achieved compared to that of commercial Tegaderm dressings (Figure 6Aii). Moreover, microenvironment regulation via bioactive agent delivery focuses on governing pathological

imbalances and directing cellular behavior. For treatment of diabetic wounds, a double-layered dressing composed of a ROS-degradable conjugated polymer poly(deca-4,6-diynedioic acid) (PDDA) and CS was employed for microenvironment modulation [99]. The dressing continuously scavenged ROS to alleviate inflammation, in parallel with sustained succinic acid delivery to promote angiogenesis and tissue regeneration. The double-layered dressing significantly promoted wound healing in both diabetic mouse and porcine models. In another example, a wound dressing composed of radially aligned nanofibers and near-infrared responsive microparticles was developed for spatiotemporal release of growth factors [100]. The nanofiber scaffolds facilitated wound healing by activating PI3K-Akt, MAPK, and immune pathways in a porcine model.

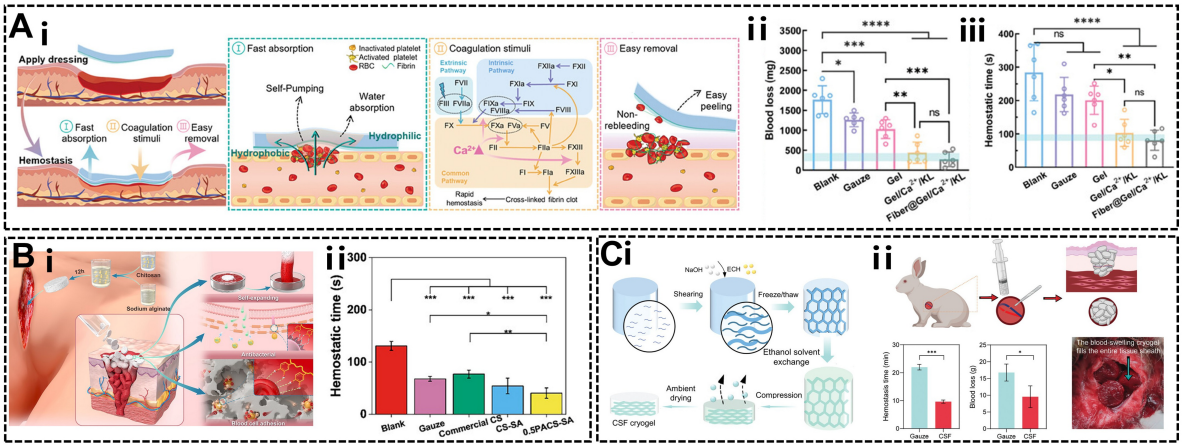

Figure 5. Applications of interfacial biomaterials for hemostatic management. (**A**) Janus self-pumping dressing for hemostasis. (**i**) Schematic showing the hemostasis mechanism. (**ii**) Blood loss and (**iii**) hemostatic time in the rabbit ear artery bleeding model. Reproduced with permission [94]. Copyright 2024, Wiley-VCH. (**B**) Self-expanding sponge prepared by freeze-drying method for non-compressible hemorrhage. (**i**) Schematic showing the self-expansion, blood cell adhesion, and aggregation processes. (**ii**) Hemostatic time of the sponges in the mouse liver injury model. Reproduced with permission [96]. Copyright 2025, Wiley-VCH. (**C**) Self-expanding fibrous cryogels prepared via a non-freeze-drying strategy for non-compressible hemorrhage. (**i**) Schematic showing the fabrication of cryogels by assembling micro-hydrogels. (**ii**) Hemostatic capability of the self-expanding fibrous cryogels. Reproduced with permission [97]. Copyright 2023, Wiley-VCH.

To meet the demands of strong adhesion and painless removal for wound dressing, a multifunctional thermoresponsive hydrogel dressing (DA-Hyd-Doxy) was developed by copolymerization of N-isopropylacrylamide and dopamine-modified zwitterionic poly(amidoamine)s as the matrix, loaded with doxycycline [101]. The hydrogel exhibited smart interfacial adhesion, providing strong attachment to the dynamic wound site at body temperature, while allowing painless removal upon cooling (Figure 6Bi). In addition, antibacterial activity was mediated by doxycycline delivery, and antioxidant and anti-inflammatory effects were provided by the dopamine moiety directly. In the infected skin wound model established on the nape and dorsum of diabetic rats, this multifunctional interfacial strategy significantly promoted wound healing with a near-complete closure (wound area of 1.1 ± 0.4%) at day 15, which markedly outperformed conventional gauze (Figure 6Bii).

Active mechanical intervention for wound closure involves materials that provide physical forces directly to the wound edges, counteracting skin tension and promoting contraction. For example, a core-ring structured hydrogel (CR-gel) was fabricated via two-step photopolymerization, in which the C-gel was composed of methacrylate hyaluronic acid (HAMA) and N-isopropylacrylamide (NIPAAm) and the R-gel consisted of N, N'-methylene bisacrylamide (MBA), acrylic acid (AA) and TA (Figure 6Ci) [102]. The CR-gel exerted localized functions, with a temperature-responsive core generating a contractile force (~3.4 kPa), and an adhesive ring transferring the stress to the wound periphery. The dressing provided effective mechanical force while resisting exudate-mediated swelling, leading to an accelerated epidermal closure of 85% on day 8 in miniature swine skin (Figure 6(Cii,Ciii)). The gel group exhibited a shorter epidermal gap and denser collagen fibers, indicating better healing quality (Figure 6(Civ,Cv)). Furthermore, a mechanically active adhesive and immune regulative dressing was fabricated, to provide strong adhesion, temperature-triggered contraction, and immune regulation [103]. The mouse and porcine wound models validated the synergistic effect of contractile and immunomodulatory functions for promoting wound healing.

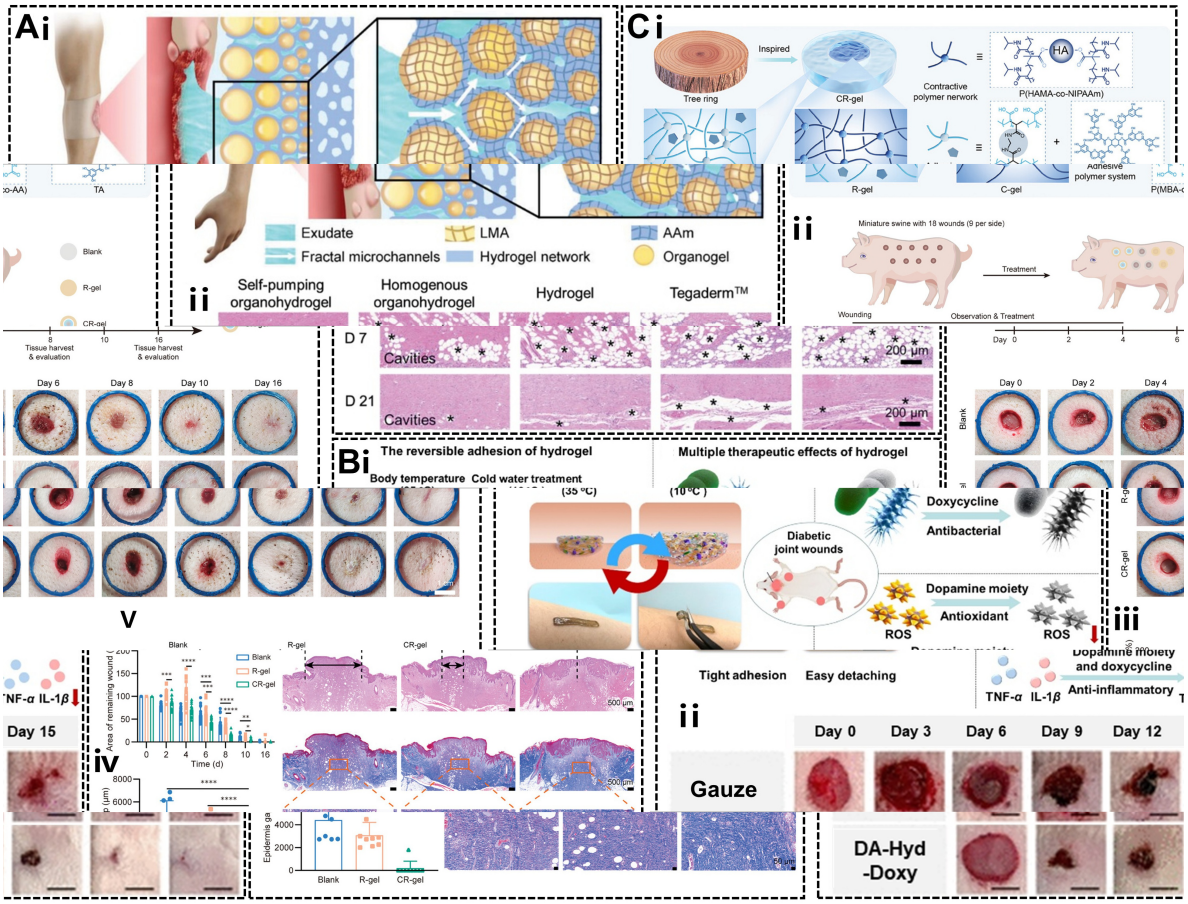

Figure 6. Applications of interfacial biomaterials for wound healing. (**A**) Dressing with self-pumping capability for burn wound healing. (**i**) Schematic showing the design of dressing with hydrophilic fractal microchannels. (**ii**) H&E staining images of burn wounds showing dermal cavities marked by black asterisks. Reproduced with permission [98]. Copyright 2023, Wiley-VCH. (**B**) Reversible adhesive hydrogel for infected diabetic joint wound healing. (**i**) The schematic showing reversible adhesion based on a thermo-stimulated autoshrinkage mechanism and the multiple therapeutic effects of hydrogel for wound healing. (**ii**) Photographs of the infected diabetic joint wounds on the nape area of rats. Scale bar indicates 5 mm. Reproduced with permission [101]. Copyright 2025, American Chemical Society. (**C**) Core-ring structured hydrogel with mechanical regulation capability to promote skin wound repair. (**i**) Schematic showing the hydrogel fabrication. (**ii**) Hydrogel treatment of full-thickness skin wounds in miniature swine: experimental protocol and representative wound photographs. (**iii**) Quantified remaining wound area. (**iv**) Epidermis gap on day 8. (**v**) H&E and Masson staining images of wound tissues on day 8. Reproduced with permission [102]. Copyright 2024, Wiley-VCH.

4.2. Tendon Repair

As a typical soft tissue, tendons including rotator cuff and Achilles tendon, play an important role in force transmission and joint movement. Given the limited regenerative ability, effective tendon repair remains a significant challenge. Since the sliding behavior of tendon relies on low friction, the engineered interfacial materials are highly desirable for tendon repair. Moreover, it is crucial to modulate the microenvironment by scavenging ROS, mitigating inflammatory response, and promoting tenogenic differentiation, to facilitate functional regeneration.

The substantial presence of ROS causes acute oxidative stress, collagen degradation, and M1 macrophage polarization. With the aim of improving tendon repair, the scaffolds with ROS scavenging capability have been developed. As shown in Figure 7Ai, Li et al. developed a decellularized tendon (DT) fibrous membrane decorated with MnO_2 using TA as the cross-linking and reducing agent [104]. MnO_2@DT efficiently scavenged excessive ROS, significantly accelerating the proliferation and remodeling stages during repair of injured tendon. In the rat model of patellar tendon defect, the arrangement of collagen fibers was enhanced under treatment of MnO_2@DT, showing a significant promoting effect on tendon tissue repair (Figure 7Aii).

A motion lubrication layer can be formed by the hydrogel, which is able to form abundant hydrogen bonds with water molecules, to enable interfacial lubrication during tendon movement. Thus, the hydrogel patches

with lubrication and drug delivery properties have been developed to provide anti-adhesion and regenerative capability [105]. Mooney et al. developed a tough hydrogel with a tissue adhesion side, a sliding surface and high drug-loading performance [106]. The tough hydrogel, comprising calcium ion crosslinked alginate along with covalently crosslinked PAAM, functioned as the high-capacity depot for local drug release. And CS adhesive on one side generated strong adhesion to the tissue, while the other non-adhesive side supported tendon sliding. In a rat model of Achilles-tendon rupture, the hydrogel promoted healing along with reduced scar formation, while in a rat model of patellar tendon injury, it inhibited inflammation, improved chemokine secretion, and promoted tendon stem and progenitor cell recruitment.

Electrical stimulation has emerged as a promising approach for tissue repair. A piezoelectric injectable anti-adhesive hydrogel (PE-IAH) composed of cross-linked carboxymethyl chitosan (cCMCS) and HA, incorporating piezoelectric poly-L-lactic acid (PLLA) electrospun short fibers, was developed (Figure 7Bi) [107]. This implant acted as a physical barrier against peritendinous adhesion while providing piezoelectric stimulation that facilitated proliferation and differentiation of tendon stem/progenitor cells (TSPCs), as well as the expression of tenascin C (TNC) and secretion of collagen I under ultrasound (US) excitation. A clear boundary with the surrounding tissues, and dense collagen fibers were found in the PE-IAH group on day 8 in a rat ruptured Achilles tendon model (Figure 7Bii). Moreover, a significant improvement in tendon functional recovery was achieved with enhanced Achilles Functional Index (Figure 7Biii).

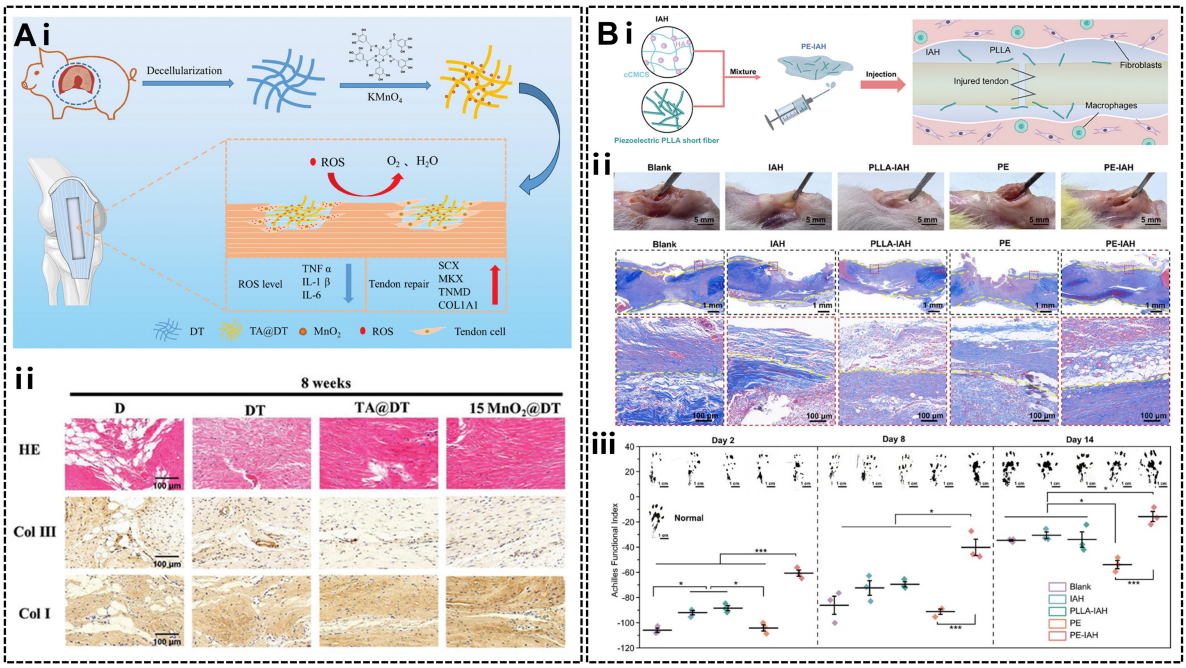

Figure 7. Applications of interfacial biomaterials for tendon repair. (**A**) MnO_2-modified decellularized tendon membrane with ROS scavenging ability to promote tissue regeneration. (**i**) Schematic showing the preparation process. (**ii**) H&E staining and immunohistochemical staining images of patellar tendon at 8 weeks post-surgery. Reproduced with permission [104]. Copyright 2024, Wiley-VCH. (**B**) Injectable piezoelectric anti-adhesive hydrogel to improve tendon functional recovery. (**i**) Schematic showing the preparation of hydrogels. (**ii**) Photographs and Masson staining images of hydrogel treated Achilles tendon on day 8. (**iii**) Paw prints and Achilles Functional Index of rats. Reproduced with permission [107]. Copyright 2025, Wiley-VCH.

4.3. Nerve Repair

Nerve represents one of the most challenging soft tissues to repair. Natural nerves feature a hierarchical structure composed of parallel myelinated axon bundles and multi-layered sheaths, offering electrical conduction. The repair of nerve injury has evolved from suturing of nerve stumps to microenvironment reconstruction. Thus, the biomaterial interfaces can be engineered with topographical guidance for axonal extension, electrical signals for stimulating Schwann cell migration and myelination, and biomolecules for regenerative niche modulation.

In recent years, stem cell therapy has opened up emerging avenues for nerve repair. Aimed to modulate endogenous neural stem cells for facilitating nerve repair, Dai et al. developed an aligned collagen-fibrin fibrous hydrogel (Col-FB), consisting of collagen and fibrin, with superior adhesive, stretchable, and spatiotemporal delivery abilities for spinal cord injury repair (Figure 8Ai) [108]. The fibrous hydrogels with stromal cell-derived

factor-1α (SDF1α) gradient release and sequential delivery of SDF1α/paclitaxel (PTX) directed endogenous neural stem/progenitor cells (NSPCs) toward the lesion site at an early stage (Figure 8Aii) followed by neuronal differentiation, resulting in restoration of hindlimb locomotion. In addition, nerve guidance conduit (NGC) engineered with US-triggered electrical stimulation and controlled drug delivery has been developed for peripheral nerve repair. For example, Chai et al. constructed an aligned piezoelectric nanofiber-derived hydrogel NGC, which was composed of barium titanate piezoelectric nanoparticle (BTNP)-doped polyvinylidene fluoride-trifluoroethylene [BTNPs/P(VDF-TrFE)] electrospun nanofibers loading with nerve growth factor (NGF) (Figure 8Bi) [109]. The NGC utilized US-triggered electrical stimulation to facilitate directional neurite outgrowth, while enabling controllable release of NGF through hydrogel shrinkage upon heating, thereby actively accelerating nerve repair. The *in vivo* results of rat sciatic nerve defect repair model showed that the NGCs combined with US treatment exhibited significant nerve regeneration (Figure 8Bii). In another study, a self-healing electroconductive hydrogel composed of HA, cystamine, and pyrrole-1-propionic acid (HASPy) was developed [110]. HASPy promoted the expression of genes and proteins associated with Schwann cell myelination primarily by activating the interleukin 17 (IL-17) signaling pathway, thus facilitating nerve regeneration. Apart from axonal regeneration, supportive angiogenesis is another key challenge for nerve repair. To address this issue, an NGC consisting of polydopamine (PDA) modified GelMA hydrogel nanofibers with sustained drug release was developed to synergistically promote nerve regeneration and angiogenesis (Figure 8Ci) [111]. The interfacial platform enabled the loading of Secreted Frizzled-Related Protein-2 (SFRP2) *via* π-π stacking and hydrogen bonding for sustained release. The *in vivo* findings demonstrated that the NGCs significantly enhanced angiogenesis and promoted peripheral nerve repair. A significant increase in myelin sheath thickness was achieved (Figure 8Cii), leading to functional recovery. Despite the considerable advances, the long-gap nerve regeneration, including bridging of nerve stumps, effective electrophysiological signal transmission, and full restoration of motor function remains a critical challenge.

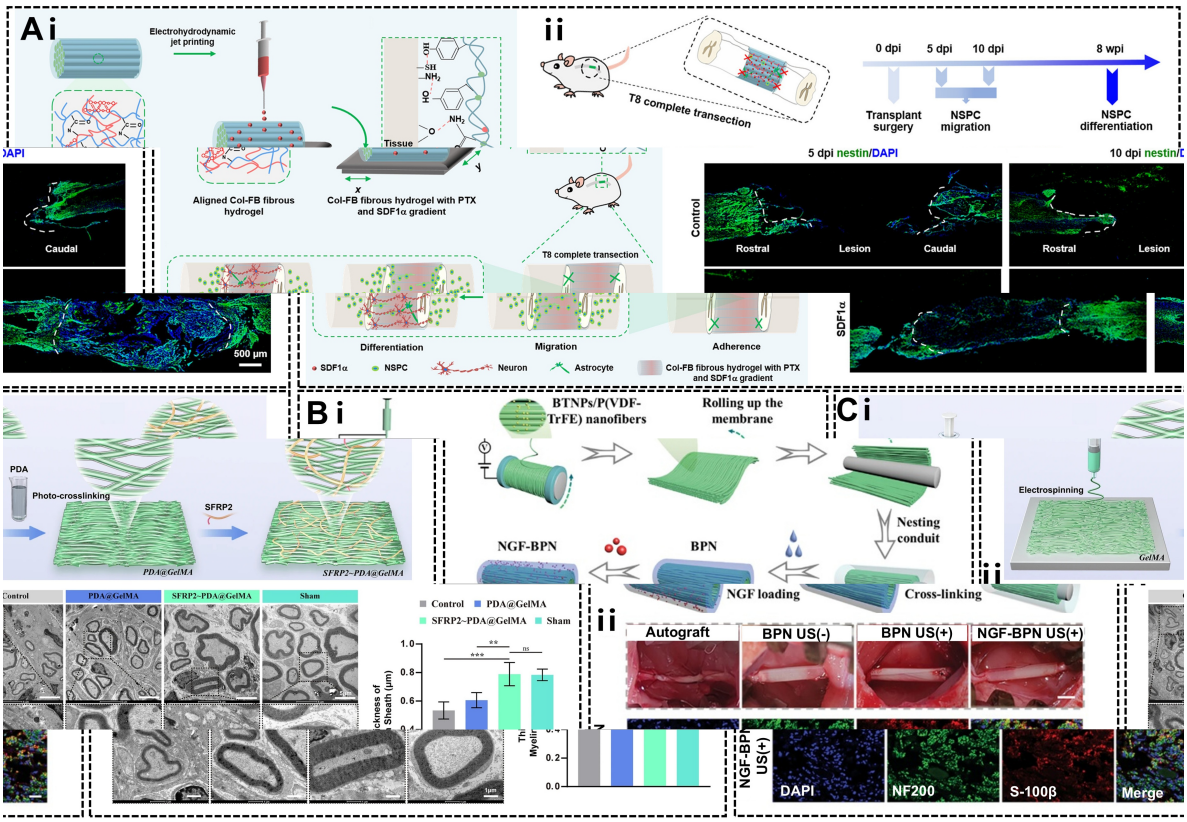

Figure 8. Applications of interfacial biomaterials for nerve repair. (**A**) Adhesive fibrous hydrogel with spatiotemporal delivery capability for spinal cord injury repair. (**i**) Schematic showing the fabrication process. (**ii**) The aligned fibrous hydrogels with gradient SDF1α induced endogenous NSPC migration after implantation in the transected site of the rats with spinal cord injury. Reproduced with permission [108]. Copyright 2021, American Chemical Society. (**B**) US-responsive piezoelectric NGC for peripheral nerve repair. (**i**) Schematic showing the preparation process. (**ii**) Photographs of implantation after surgery (scale bar indicates 2 mm), and immunofluorescence staining images at 8 weeks post-surgery (scale bar indicates 20 μm). Reproduced with permission [109]. Copyright 2024, Wiley-VCH. (**C**) Hydrogel nanofiber-based NGC with sustained release of SFRP2 for angiogenesis and nerve regeneration in peripheral nerve injury repair. (**i**) Schematic showing the

preparation process. (**ii**) TEM images of sciatic nerves and quantitative analysis of myelin sheath thickness in different groups. Reproduced under the terms of the CC BY 4.0 license [111]. Copyright 2025, the authors, published by Springer Nature.

4.4. Other Soft Tissue Repair

Given the highly heterogeneous microenvironments of diverse soft tissue types, interfacial design employs spatiotemporally dynamic physical and biological signals to orchestrate complex tissue regeneration. Deep soft tissue injury refers to acute trauma involving all tissue layers from the skin to the bone, including muscles, ligaments, fascia, etc. Aiming to utilize traditional Chinese medicine external prescriptions for deep soft tissue injury, Mu et al. fabricated a hydrogel adjuvant composed of gallic acid-coupled ε-poly-L-lysine (EPL-GA) and partially oxidized hyaluronic acid (OHA) for loading Chinese medicine ultramicro-powder (μCMP) (EG-OHA@μCMP) (Figure 9Ai) [112]. A deep soft tissue injury model was established by striking the thigh muscles of rats with a heavy hammer. It was found that EG-OHA@μCMP group exhibited almost complete dissipation of blood stasis, and dense and continuous muscle fibers (Figure 9(Aii,Aiii)).

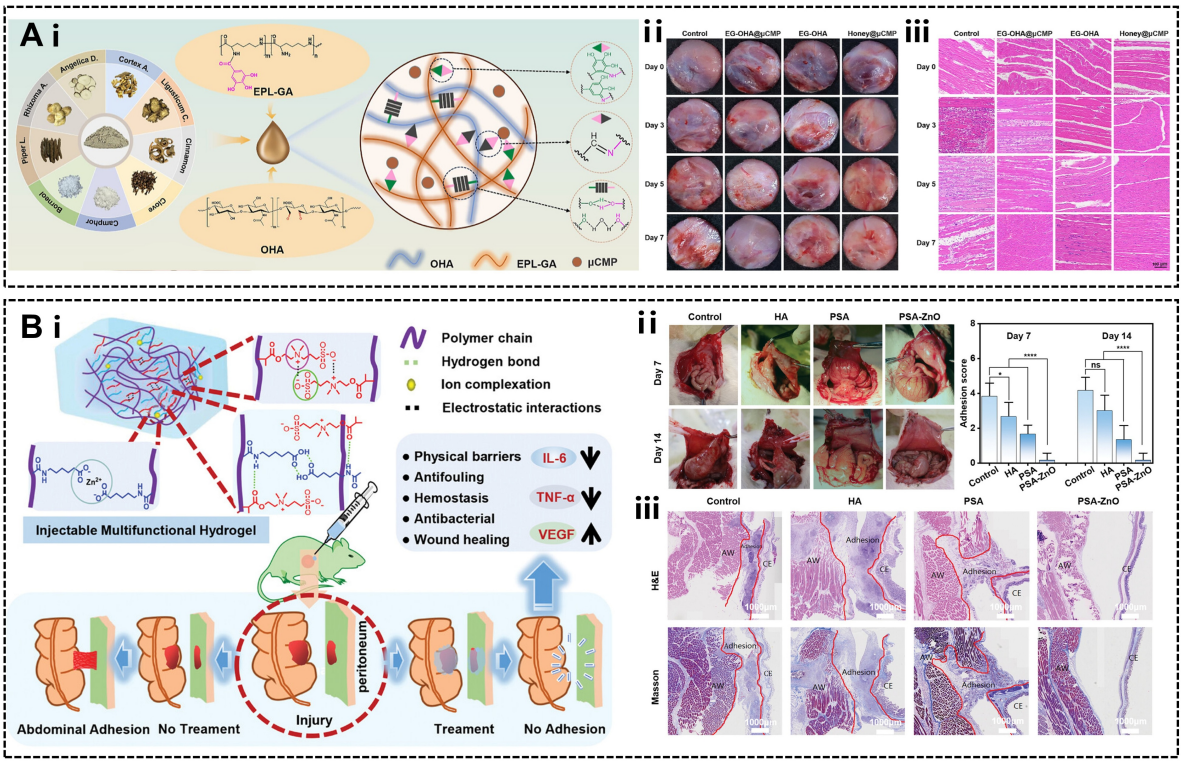

Figure 9. Applications of interfacial biomaterials for other soft tissue repair. (**A**) A hydrogel adjuvant combined with Chinese medicine external prescriptions for the repair of deep soft tissue injury. (**i**) Schematic showing the preparation of the hydrogel. (**ii**) Representative photographs of the muscle tissue in the damaged area. (**iii**) H&E staining images of the muscle tissue. Reproduced with permission [112]. Copyright 2024, American Chemical Society. (**B**) Injectable zwitterionic hydrogel for preventing abdominal adhesions. (**i**) Schematic showing the multiple intermolecular interactions of the hydrogel and its application for abdominal adhesion prevention. (**ii**) Photographs and scores of abdominal adhesions in different groups. (**iii**) H&E and Masson staining images on day 14. Reproduced under the terms of the CC BY 4.0 license [113]. Copyright 2025, the authors, published by Wiley-VCH.

Volumetric muscle loss (VML) refers to extensive and irreversible loss of skeletal muscle tissue caused by trauma or disease, resulting in permanent tissue deformity, and motor function impairment. Although stem cell therapy shows great potential for VML repair, its therapeutic efficacy is limited by inadequate control over stem cell fate. To address this issue, Rando et al. developed a decellularized extracellular matrix loaded with polymeric nanocapsules for sequential release of growth factors [114]. The transplanted muscle stem cells were stimulated to proliferate and differentiate by basic fibroblast growth factor and insulin-like growth factor 1, which were sequentially delivered by the bioinstructive scaffolds. In the murine VML defect model, the transplanted scaffolds restored muscle structure and function.

The peritoneum, a type of delicate soft tissue, is highly susceptible to damage during abdominal surgery, leading to postoperative adhesions. Various types of anti-adhesion barriers have been developed to prevent postoperative adhesions and promote peritoneal repair. For example, a sprayable body temperature-activated in situ gel barrier was prepared using sulfated hyaluronic acid, CS and thermal responsive polymer [115]. A wide spread to the damaged peritoneal wall was formed, followed by a significant reduction in adhesion and anti-inflammatory effect in the rat ischemic button model. Similarly, Huang et al. developed an injectable hydrogel (PSA-ZnO) containing sulfobetaine, modified aminocaproic acid (A6ACA) and ZnO nanoparticles to prevent adhesion and inhibit inflammation (Figure 9Bi) [113]. Importantly, PSA-ZnO prevented foreign body reaction through the inhibition of blood clot formation and pathological fibrin accumulation. In the side wall defect cecum abrasion model of rats, a hydration layer was established at the hydrogel surface for antifouling, while the released Zn^{2+} showed antibacterial and anti-inflammatory performance, cooperatively inhibiting peritoneal adhesion and promoting peritoneal repair (Figure 9Bii). The H&E and Masson staining images validated the inhibited peritoneal adhesion and promoted repair (Figure 9Biii). Moreover, a microneedle array with a double-layer structure was constructed to provide physical barriers and immune regulation [116]. Since calcium signaling plays a role in adhesion formation, poly(lactic-*co*-glycolic acid) (PLGA) nanoparticles containing calcium channel blockers were loaded in the microneedle arrays to regulate the calcium concentration in cells and enhance anti-adhesion effects. The microneedle patch provided a promising strategy to prevent adhesion by destroying the fibrotic process of adhesion.

5. Conclusions and Outlook

To improve the material-tissue integration and therapeutic efficacy, a variety of interfacial engineered biomaterials have been developed. In this article, we have discussed the optimization of material selection, structural design, and biofunctionalization to enhance the interfacial performance. Various regulatory strategies have been developed, such as biophysical modulation, intermolecular interaction regulation, and microenvironment tuning. As a result, functional interfacial materials have been explored to promote diverse soft tissue repair.

With the deepening understanding of interfacial interactions and the advancement in fabrication techniques, an increasing number of products based on interfacial engineering have been approved for clinical use. These products cover a range of soft tissue repair scenarios, including wound healing (Kerecis® Omega3 wound patch [117]), rotator cuff repair (Rotium® nanofiber scaffold [118]), nerve repair (NeuraGen® nerve conduit [119]), adhesion prevention (Seprafilm® adhesion barrier [120]), and soft tissue repair (NovoSorb® biodegradable temporizing matrix [121]). Despite significant progress in engineering biomaterial interfaces, the clinical applicability of these materials remains limited. Several critical challenges, especially concerning biosafety, *in vivo* stability, and scale-up production, are yet to be addressed, which hinder their translation.

The biosafety concern of the interfacial materials is the primary issue. The toxic risks originate from not only the main materials and residual solvents, but also their degradation products. Therefore, the eco-friendly, non-/low-toxic, sustainable materials and solvents should be selected, along with complete removal of monomers and residual solvents after material fabrication. Future work may consider development of fabrication methods with biocompatible solvents, such as water, ethanol, and ionic liquids, or solvent-free techniques such as melt-processing to reduce the toxicity.

The *in vivo* stability of interfacial materials poses a critical challenge, largely arising from the complexity of sophisticated engineering and advanced functionalization. For example, although mechanical actuation such as compression and tension, shows great potential in hemostasis and wound closure, its long-term effectiveness is significantly determined by their *in vivo* expansion, shrinkage, and degradation features. In the complex pathological microenvironment, the engineered interfaces are susceptible to structural compromise and uncontrollable degradation due to body fluids, blood, enzymes and other biological factors. Thus, future research may consider designing interfaces with superior biochemical resistance and tuning the *in vivo* biodegradation profiles.

Another translational challenge is the scalable and reproducible manufacturing of complex interfacial materials. As an example, the intricate structural features, such as hierarchical porosity, Janus wettability gradients, and aligned multichannels, provide essential support for therapeutic outcomes. However, the advanced and complex designs pose huge challenges for large-scale production. Future progress should be achieved by integrating artificial intelligence (AI) for process parameter screening and real-time quality monitoring. The breakthrough in design of functionally active interfaces and the advancement of mass production systems will drive the development of next-generation interfacial biomaterials for soft tissue repair.

Author Contributions: X.L. (Xueyan Li): conceptualization, writing—original draft; X.W.: writing-original draft; M.D. investigation; L.L.: investigation; U.S.: conceptualization, writing—original draft; J.Y.: conceptualization, writing—review &

editing; X.L. (Xiaoran Li): conceptualization, writing—review & editing; B.D.: conceptualization, writing-review & editing. All authors have read and agreed to the published version of the manuscript.

Funding: This work was supported by the Shanghai Eastern Talent Plan Leading Project (BJKJ2024019), the Regional Innovation and Development Joint Fund administered by the National Natural Science Foundation of China (U24A2073), the Science and Technology Commission of Shanghai Municipality (24xtcx00300), and the Fundamental and Interdisciplinary Disciplines Breakthrough Plan of the Ministry of Education of China (JYB2025XDXM402).

Institutional Review Board Statement: Not applicable.

Informed Consent Statement: Not applicable.

Data Availability Statement: Not applicable.

Conflicts of Interest: The authors declare no competing financial interests.

Use of AI and AI-Assisted Technologies: No AI tools were utilized for this paper.

References

1. Horn, C.; Uzor, N.; Fierro, A.; Abeshouse, M.; Ray, K.; Lantis, J.C. Implantable Biologics for Soft Tissue Surgery Reinforcement. *Surg. Technol. Int.* **2023**, *42*, 31–44.
2. Van Damme, L.; Blondeel, P.; Van Vlierberghe, S. Injectable Biomaterials as Minimal Invasive Strategy towards Soft Tissue Regeneration—An Overview. *J. Phys. Mater.* **2021**, *4*, 022001.
3. Capella-Monsonís, H.; Crum, R.J.; Hussey, G.S.; Badylak, S.F. Advances, Challenges, and Future Directions in the Clinical Translation of ECM Biomaterials for Regenerative Medicine Applications. *Adv. Drug Deliv. Rev.* **2024**, *211*, 115347.
4. Mazzoni, E.; Iaquinta, M.; Lanzillotti, C.; Mazziotta, C.; Maritati, M.; Montesi, M.; Sprio, S.; Tampieri, A.; Tognon, M.; Martini, F. Bioactive Materials for Soft Tissue Repair. *Front. Bioeng. Biotechnol.* **2021**, *9*, 613787.
5. Wu, T.; Li, X.; Xue, J.; Xia, Y. Rational Fabrication of Functionally-Graded Surfaces for Biological and Biomedical Applications. *Acc. Mater. Res.* **2024**, *5*, 1507–1519.
6. Wang, Y.; Wang, T.; Tang, R.; Wang, D.; Zhang, X.; Nagaumi, H.; Yang, B.; Ren, X.; Huang, J.; Zhang, Y.; et al. Multiscale Interface Engineering in Biohybrid Composites for Biomedical Applications. *Mater. Today Bio* **2025**, *35*, 102382.
7. Ma, P.; Liu, Y.; Yang, C.; Yang, J.; Cao, Z.; Ren, B.; He, Z.; An, B.; Huang, C.; Liu, J.; et al. A Multifunctional Bilayer Hydrogel Patch with Photothermal-Driven Directional Contraction and Bioregulation for Enhanced Wound Healing. *Mater. Today* **2025**, *90*, 297–313.
8. Karami, P.; Rana, V.; Zhang, Q.; Boniface, A.; Guo, Y.; Moser, C.; Pioletti, D.P. NIR Light-Mediated Photocuring of Adhesive Hydrogels for Noninvasive Tissue Repair via Upconversion Optogenesis. *Biomacromolecules* **2022**, *23*, 5007–5017.
9. Lee, D.; Tran, H.; Sharma, N.; Andrabi, S.; Yan, Z.; Killeen, A.C.; Reinhardt, R.A.; Zhu, W.; Xie, J. 3D-Printed Microfluidic Platform for Creating Porous Nanofibrous Microspheres to Regulate Cell Response and Enhance Tissue Regeneration. *Small* **2025**, *21*, 2502033.
10. Ji, Z.; Wei, T.; Zhu, J.; Hu, J.; Xiao, Z.; Bai, B.; Lv, X.; Miao, Y.; Chen, M.; Wang, C.; et al. Actively Contractible and Antibacterial Hydrogel for Accelerated Wound Healing. *Nano Res.* **2024**, *17*, 7394–7403.
11. Zhang, Y.; Li, J.; Soleimani, M.; Giacomini, F.; Friedrich, H.; Truckenmüller, R.; Habibovic, P. Biodegradable Elastic Sponge from Nanofibrous Biphasic Calcium Phosphate Ceramic as an Advanced Material for Regenerative Medicine. *Adv. Funct. Mater.* **2021**, *31*, 2102911.
12. Shi, Y.; Yu, W.; Liang, X.; Cheng, J.; Cao, Y.; Liu, M.; Fang, Y.; Yang, Z.; Liu, H.; Wei, H.; et al. Interpenetrating Network Expansion Sponge Based on Chitosan and Plasma for Ultrafast Hemostasis of Arterial Bleeding Wounds. *Carbohydr. Polym.* **2023**, *307*, 120590.
13. Zhou, M.; Liao, J.; Li, G.; Yu, Z.; Xie, D.; Zhou, H.; Wang, F.; Ren, Y.; Xu, R.; Dai, Y.; et al. Expandable Carboxymethyl Chitosan/Cellulose Nanofiber Composite Sponge for Traumatic Hemostasis. *Carbohydr. Polym.* **2022**, *294*, 119805.
14. Ni, P.; Huang, H.; Zhang, L.; Chen, Y.; Liang, Z.; Weng, Y.; Fang, Y.; Liu, H. Mussel Foot Protein Inspired Tape-Type Adhesive with Water-Responsive, High Conformal, Tough, and On-Demand Detachable Adhesion to Wet Tissue. *Adv. Healthc. Mater.* **2023**, *12*, 2203342.
15. Ji, M.; Su, J.; Li, J.; Li, F.; Wang, Y.; Wang, X.; Zhang, C.; Peng, S.; Li, J.; Man, J. Asymmetric Wettability Janus Aerogel Dressing for Enhanced Unidirectional Exudate Drainage through a Structural Gradient. *J. Mater. Sci. Technol.* **2026**, *242*, 102–114.
16. Gao, Y.; Guo, J.; Li, S.; Ye, L.; Lu, B.; Liu, J.; Luo, J.; Zhu, Y.; Chen, L.; Peng, T.; et al. A Bio-Adaptive Janus-Adhesive Dressing with Dynamic Lubrication Overlayer for Prevention of Postoperative Infection and Adhesion. *Adv. Sci.* **2025**, *12*, 2500138.

17. Wang, X.; Huo, H.; Cao, L.; Zhong, Y.; Gong, J.; Lin, Z.; Xie, X.; Bao, Z.; Zhang, P. Curcumin-Release Antibacterial Dressings with Antioxidation and Anti-Inflammatory Function for Diabetic Wound Healing and Glucose Monitoring. *J. Control. Release* **2025**, *378*, 153–169.
18. Zhou, Z.; Chen, Y.; Li, J.; Shen, J.; Zeng, H. Silk Nonwoven Fabric-Based Dressing with Antibacterial and ROS-Scavenging Properties for Modulating Wound Microenvironment and Promoting Diabetic Wound Healing. *Adv. Healthc. Mater.* **2025**, *14*, 2405151.
19. Zhou, Z.; Wang, Y.; Liu, N.; Zhang, X.; Ning, X.; Miao, Y.; He, C.; Wu, T.; Leng, X. Multifunctional Nanofiber-Based Dressings in Coordination with Adipose-Derived Stem Cells for Accelerated Burn Wound Healing. *Mater. Des.* **2025**, *253*, 113929.
20. Xue, J.; Wu, T.; Dai, Y.; Xia, Y. Electrospinning and Electrospun Nanofibers: Methods, Materials, and Applications. *Chem. Rev.* **2019**, *119*, 5298–5415.
21. Chen, S.; Li, R.; Li, X.; Xie, J. Electrospinning: An Enabling Nanotechnology Platform for Drug Delivery and Regenerative Medicine. *Adv. Drug Deliv. Rev.* **2018**, *132*, 188–213.
22. Tang, Y.; Gong, G.; He, X.; Dai, M.; Chen, M.; Wang, B.; Wang, Y.; Wang, X.; Guo, J. Multifunctional Dual Cross-Linked Bioadhesive Patch with Low Immunogenic Response and Wet Tissues Adhesion. *Adv. Healthc. Mater.* **2023**, *12*, 2201578.
23. Liang, Y.; Xu, H.; Li, Z.; Zhangji, A.; Guo, B. Bioinspired Injectable Self-Healing Hydrogel Sealant with Fault-Tolerant and Repeated Thermo-Responsive Adhesion for Sutureless Post-Wound-Closure and Wound Healing. *Nano-Micro Lett.* **2022**, *14*, 185.
24. Lei, X.; Liu, M.; Lu, C.; Han, L.; Jia, J.; Li, Z.; Xu, N.; Li, J.; Fu, X.; Jin, Y.; et al. A Self-Hygroscopic, Rapidly Self-Gelling Polysaccharide-Based Sponge with Robust Wet Adhesion for Non-Compressible Hemorrhage Control and Infected Wounds Healing. *Bioact. Mater.* **2025**, *46*, 311–330.
25. Aussel, A.; Boiziau, C.; L'Azou, B.; Siadous, R.; Delmond, S.; Montembault, A.; David, L.; Bordenave, L.; Thébaud, N.B. Cell and Tissue Responses at the Interface with a Chitosan Hydrogel Intended for Vascular Applications: *In Vitro* and *in Vivo* Exploration. *Biomed. Mater.* **2019**, *14*, 025009.
26. Mehmood, S.; Dawit, H.; Hussain, Z.; Ullah, S.; Ullah, I.; Liu, X.; Liu, Y.; Cao, Y.; Wang, Z.; Pei, R. Harnessing Bi-Layered Supramolecular Janus Tissue-Adhesive/Anti-Adhesive Fibrous Hydrogel for Efficient Hemostasis, Wound Healing, and Suppressing Postoperative Tissue Adhesion. *Chem. Eng. J.* **2024**, *495*, 153095.
27. Hu, Q.; Xu, J.; Cheng, J.; Wen, J.; He, W.; Yang, X.; Zhai, G.; Liu, A.; Ye, L. Four-Dimensional Adhesive and Shrinkable Hydrogels with Hemostasis, Antibiosis and Immunoregulation for Enhanced Scarless Healing of Skin Wounds. *Chem. Eng. J.* **2025**, *519*, 164915.
28. Zheng, Z.; Chen, X.; Wang, Y.; Wen, P.; Duan, Q.; Zhang, P.; Shan, L.; Ni, Z.; Feng, Y.; Xue, Y.; et al. Self-Growing Hydrogel Bioadhesives for Chronic Wound Management. *Adv. Mater.* **2024**, *36*, 2408538.
29. Zhou, Z.; Li, J.; Hu, J.; Fu, H. Towards Promoting Wound Healing: A Near-Infrared Light-Triggered Persistently Antibacterial, Synergistically Hemostatic Nanoarchitecture-Integrated Chitosan Hydrogel. *Carbohydr. Polym.* **2024**, *329*, 121783.
30. Wang, R.; Zheng, W.; Huang, Y.; Zhang, R.; Zhang, Y.; Yan, J.; Gu, Y.; Xi, J.; Yuan, T.; Su, H.; et al. A Single-Component Adhesive Sponge Based on Blood-Triggered and Autopenetrative Adhesion for Robust Vascular Closure. *Adv. Sci.* **2025**, *12*, e10377.
31. Mao, Q.; Hoffmann, O.; Yu, K.; Lu, F.; Lan, G.; Dai, F.; Shang, S.; Xie, R. Self-Contracting Oxidized Starch/Gelatin Hydrogel for Noninvasive Wound Closure and Wound Healing. *Mater. Des.* **2020**, *194*, 108916.
32. Du, J.; Rybak, D.; Su, Q.; Wang, Q.; Yuan, Q.; Gao, J.; Wang, Y.; Nakielski, P.; Wang, X.; Pierini, F.; et al. Sprayable Photothermal Fiber-Embedded Hydrogels to Engineer Microenvironment for Infected Wound Healing. *Adv. Funct. Mater.* **2025**, *35*, 2501242.
33. Wang, M.; Du, J.; Li, M.; Pierini, F.; Li, X.; Yu, J.; Ding, B. *In Situ* Forming Double-Crosslinked Hydrogels with Highly Dispersed Short Fibers for the Treatment of Irregular Wounds. *Biomater. Sci.* **2023**, *11*, 2383–2394.
34. Umemori, K.; Little, D. Impact of Polymer Degradation on Cellular Behavior in Tissue Engineering. *Bioprinting* **2025**, *50*, e00429.
35. Mohseni, M.; Cometta, S.; Klein, L.; Wille, M.L.; Vaquette, C.; Hutmacher, D.W. *In Vitro* and *in Vivo* Degradation Studies of a Dual Medical-Grade Scaffold Design for Guided Soft Tissue Regeneration. *Biomater. Sci.* **2025**, *13*, 2115–2133.
36. Tian, M.; Wan, J.; Wang, X.; Liu, J.; Pan, M.; Tan, H.; Pan, Z. Anisotropic Nanocomposite Hydrogel Dressings with Thermo-Responsive Contraction for Actively Stimulated Tissue Regeneration. *Chem. Eng. J.* **2025**, *514*, 163202.
37. Chen, M.; Wu, Y.; Chen, B.; Tucker, A.M.; Jagota, A.; Yang, S. Fast, Strong, and Reversible Adhesives with Dynamic Covalent Bonds for Potential Use in Wound Dressing. *Proc. Natl. Acad. Sci. USA* **2022**, *119*, e2203074119.

38. Liu, W.; Zhao, W.; Xie, K.; Li, X.F.; Wang, Y.; Kong, D.; Liu, Y.; Leng, J. Toughening and Responsive Contractile Shape Memory Fibrous Membrane via Water for Mechanically Active Wound Dressing. *Adv. Fiber Mater.* **2024**, *6*, 1942–1954.
39. Xu, W.; Xu, T.; Yu, L.; Ning, X.; Zhang, C.; Yi, B.; Dai, W.; Zhu, Z.; Zhao, H. Nanofibrous Dressings Incorporating a Synergistic Antibacterial-Anti-Inflammatory Effect for Infected Wound Healing. *Mater. Today Bio* **2025**, *34*, 102155.
40. Kai, K.; Taiki, H.; Yukikazu, T. Development of a Temperature-Responsive Polymer Network with Enhanced Transparency and Volume Shrinkage via Star-Shaped PEG-b-PNIPA Block Copolymer. *Mater. Interfaces* **2025**, *2*, 285–301.
41. Zhong, Q.; Zhang, R.; Chen, Y.; Tan, S.; Huang, L.; Zhang, J.; Luo, Z. A Mechanical Contraction-Driven Hydrogel Dressing for pH Visualization and Tailored Acute/Chronic Wound Healing. *Adv. Funct. Mater.* **2025**, *36*, e12807.
42. Pi, Y.; Ganabady, K.; Celiz, A.D. Enzyme-Responsive Biomaterials for Biomedical Applications. *Commun. Mater.* **2025**, *6*, 263.
43. Li, H.; Li, X.; Jain, P.; Peng, H.; Rahimi, K.; Singh, S.; Pich, A. Dual-Degradable Biohybrid Microgels by Direct Cross-Linking of Chitosan and Dextran Using Azide-Alkyne Cycloaddition. *Biomacromolecules* **2020**, *21*, 4933–4944.
44. Dong, Y.; Zhang, X.; Chen, Y.; Yu, J.; Li, X.; Ding, B. "Stiff-Elastic" Binary Synergistic Fibrous Tape with Thermal-Triggered Shrinkable and Shape Recoverable Performances for Wound Closure. *Adv. Funct. Mater.* **2024**, *34*, 2402252.
45. Huang, Y.; Song, M.; Li, X.; Du, Y.; Gao, Z.; Zhao, Y.-Q.; Li, C.; Yan, H.; Mo, X.; Wang, C.; et al. Temperature-Responsive Self-Contraction Nanofiber/Hydrogel Composite Dressing Facilitates the Healing of Diabetic-Infected Wounds. *Mater. Today Bio* **2024**, *28*, 101214.
46. Theocharidis, G.; Yuk, H.; Roh, H.; Wang, L.; Mezghani, I.; Wu, J.; Kafanas, A.; Contreras, M.; Sumpio, B.; Li, Z.; et al. A Strain-Programmed Patch for the Healing of Diabetic Wounds. *Nat. Biomed. Eng.* **2022**, *6*, 1118–1133.
47. Lu, X.; Liu, Z.; Jia, Q.; Wang, Q.; Zhang, Q.; Li, X.; Yu, J.; Ding, B. Flexible Bioactive Glass Nanofiber-Based Self-Expanding Cryogels with Superelasticity and Bioadhesion Enabling Hemostasis and Wound Healing. *ACS Nano* **2023**, *17*, 11507–11520.
48. Zhao, X.; Huang, Y.; Li, Z.; Chen, J.; Luo, J.; Bai, L.; Huang, H.; Cao, E.; Yin, Z.; Han, Y.; et al. Injectable Self-Expanding/Self-Propelling Hydrogel Adhesive with Procoagulant Activity and Rapid Gelation for Lethal Massive Hemorrhage Management. *Adv. Mater.* **2024**, *36*, 2308701.
49. Xu, Z.; Fan, J.; Tian, W.; Ji, X.; Cui, Y.; Nan, Q.; Sun, F.; Zhang, J. Cellulose-Based pH-Responsive Janus Dressing with Unidirectional Moisture Drainage for Exudate Management and Diabetic Wounds Healing. *Adv. Funct. Mater.* **2024**, *34*, 2307449.
50. Xiao, W.; Wan, X.; Shi, L.; Ye, M.; Zhang, Y.; Wang, S. A Viscous-Biofluid Self-Pumping Organohydrogel Dressing to Accelerate Diabetic Wound Healing. *Adv. Mater.* **2024**, *36*, 2401539.
51. Li, W.; Kong, M.; Yang, T.; Li, J.; Sun, H.; Li, Z.; Wang, Q.; Teng, W. "One Stone Four Birds" Strategy of Advanced Hydrogel System Based on Eight-Arm Nanocages to Promote Chronic Wound Healing in Diabetes. *Chem. Eng. J.* **2023**, *475*, 146174.
52. Chen, Y.; Wang, Q.; Ning, F.; Du, C.; Chen, M.; Feng, C.; Dong, C.M. Dynamic Hyaluronic Acid Hydrogels for Comprehensively Regulating Inflammation, Angiogenesis, and Metabolism to Effectively Proheal Diabetic Wounds. *ACS Appl. Mater. Interfaces* **2024**, *16*, 70256–70273.
53. Lu, B.; Han, X.; Zou, D.; Luo, X.; Liu, L.; Wang, J.; Maitz, M.F.; Yang, P.; Huang, N.; Zhao, A. Catechol-Chitosan/Polyacrylamide Hydrogel Wound Dressing for Regulating Local Inflammation. *Mater. Today Bio* **2022**, *16*, 100392.
54. Sha, Z.; Li, J.; Song, Y.; Li, H.; Liu, H.; Fan, J.; Li, X.; Fei, X.; Zhu, M. Self-Pumping, pH-Responsive Janus Fibrous Dressing for Enhanced Immunomodulation and Accelerated Diabetic Wound Healing. *Nano Today* **2025**, *65*, 102847.
55. Qi, X.; Cai, E.; Xiang, Y.; Zhang, C.; Ge, X.; Wang, J.; Lan, Y.; Xu, H.; Hu, R.; Shen, J. An Immunomodulatory Hydrogel by Hyperthermia-Assisted Self-Cascade Glucose Depletion and ROS Scavenging for Diabetic Foot Ulcer Wound Therapeutics. *Adv. Mater.* **2023**, *35*, 2306632.
56. Fang, Y.; Xiu, L.; Xiao, D.; Zhang, D.; Wang, M.; Dong, Y.; Ye, J. Sandwich-Structured Nanofiber Dressings Containing MgB_2 and Metformin Hydrochloride with ROS Scavenging and Antibacterial Properties for Wound Healing in Diabetic Infections. *Adv. Healthc. Mater.* **2024**, *13*, 2402452.
57. Cai, J.; Liu, S.; Zhong, Q.; Shang, Y.; Chen, Z.; Yao, Y.; Zhou, B.; Yin, F.; Zhao, J.; Zheng, L. Multifunctional PDA/ZIF8 Based Hydrogel Dressing Modulates the Microenvironment to Accelerate Chronic Wound Healing by ROS Scavenging and Macrophage Polarization. *Chem. Eng. J.* **2024**, *487*, 150632.
58. Li, Y.; Sun, Z.; Chai, S.; Zhang, Z.; Li, Y.; Zhu, C.; Fan, D. Tissue-Like Soft Dual-Network Hydrogel Patch with Instant/Tunable Adhesion and Microenvironment Modulation for Infected Wound Healing. *ACS Nano* **2025**, *19*, 27714–27730.

59. Zhao, Y.; Zhao, S.; Du, Y.; Gao, Z.; Li, Y.; Ma, H.; Li, H.; Ren, X.; Fan, Q.; Wu, D.; et al. Inverse Oxide/Alloy-Structured Nanozymes with NIR-Triggered Enzymatic Cascade Regulation of ROS Homeostasis for Efficient Wound Healing. *Adv. Mater.* **2025**, *37*, 2418731.
60. Lian, C.; Liu, J.; Wei, W.; Wu, X.; Goto, T.; Li, H.; Tu, R.; Dai, H. Mg-Gallate Metal-Organic Framework-Based Sprayable Hydrogel for Continuously Regulating Oxidative Stress Microenvironment and Promoting Neurovascular Network Reconstruction in Diabetic Wounds. *Bioact. Mater.* **2024**, *38*, 181–194.
61. Kang, X.; Wang, Y.; Zhao, X.; Chen, C.; Li, F.; Weng, J.; Li, J.; Chen, X. Dual-Functional Photonic Crystal Hydrogel: Drug Release Monitoring and Immunomodulation for Chronic Infected Wounds. *Adv. Healthc. Mater.* **2026**, e71039. https://doi.org/10.1002/adhm.71039.
62. Li, Z.; He, M.; Wang, Y.; Yang, J.; He, Y.; Chen, X.; Zhang, W.; Wu, H.; Chai, R.; Wang, B. Advances in Biocompatible Metal-Organic Frameworks for Biomedical Applications. *Adv. Mater.* **2025**, *37*, 2503946.
63. Park, J.; Kim, T.Y.; Kim, Y.; An, S.; Kim, K.S.; Kang, M.; Kim, S.A.; Kim, J.; Lee, J.; Cho, S.W.; et al. A Mechanically Resilient and Tissue-Conformable Hydrogel with Hemostatic and Antibacterial Capabilities for Wound Care. *Adv. Sci.* **2023**, *10*, 2303651.
64. An, H.; Zhang, M.; Zhou, L.; Huang, Z.; Duan, Y.; Wang, C.; Gu, Z.; Zhang, P.; Wen, Y. Anti-Dehydration and Rapid Trigger-Detachable Multifunctional Hydrogels Promote Scarless Therapeutics of Deep Burn. *Adv. Funct. Mater.* **2023**, *33*, 2211182.
65. Liu, M.; Ding, R.; Li, Z.; Xu, N.; Gong, Y.; Huang, Y.; Jia, J.; Du, H.; Yu, Y.; Luo, G. Hyaluronidase-Responsive Bactericidal Cryogel for Promoting Healing of Infected Wounds: Inflammatory Attenuation, ROS Scavenging, and Immune Regulation. *Adv. Sci.* **2024**, *11*, 2306602.
66. Li, S.; Li, R.; Zhang, X.; Zhu, Y.; Wang, D.; Cui, W.; Chai, H.; Hou, Y.; Li, S. Core-Shell Structure-Based Smart Hydrogel Wound Dressing with Endogenous and Exogenous Dual Adhesion Dynamic Response to Promote Wound Healing. *Adv. Funct. Mater.* **2025**, *35*, 2500329.
67. Zhu, C.; Fan, Z.; Cheng, Z.; Qin, L.; Zhao, X. Nature-Derived Microneedles with Metal-Polyphenolic Networks Encapsulation for Chronic Soft Tissue Defects Repair: Responding and Remodeling the Regenerative Microenvironment. *Mater. Today Bio* **2025**, *31*, 101539.
68. Wang, Y.; Guan, P.; Tan, R.; Shi, Z.; Li, Q.; Lu, B.; Hu, E.; Ding, W.; Wang, W.; Cheng, B.; et al. Fiber-Reinforced Silk Microneedle Patches for Improved Tissue Adhesion in Treating Diabetic Wound Infections. *Adv. Fiber Mater.* **2024**, *6*, 1596–1615.
69. Alberts, A.; Lungescu, I.A.; Niculescu, A.G.; Grumezescu, A.M. Natural Products for Improving Soft Tissue Healing: Mechanisms, Innovations, and Clinical Potential. *Pharmaceutics* **2025**, *17*, 758.
70. Kasemo, B.; Lausmaa, J. Surface Properties and Processes of the Biomaterial-Tissue Interface. *Mater. Sci. Eng. C* **1994**, *1*, 115–119.
71. Kingshott, P.; Andersson, G.; McArthur, S.L.; Griesser, H.J. Surface Modification and Chemical Surface Analysis of Biomaterials. *Curr. Opin. Chem. Biol.* **2011**, *15*, 667–676.
72. Gomes, B.S.; Simoes, B.; Mendes, P.M. The Increasing Dynamic, Functional Complexity of Bio-Interface Materials. *Nat. Rev. Chem.* **2018**, *2*, 0120.
73. Dong, L.; Zhang, W.; Ren, M.; Li, Y.; Wang, Y.; Zhou, Y.; Wu, Y.; Zhang, Z.; Di, J. Moisture-Adaptive Contractile Biopolymer-Derived Fibers for Wound Healing Promotion. *Small* **2023**, *19*, 2300589.
74. Chen, Q.; Li, S.; Li, K.; Zhao, W.; Zhao, C. A Skin Stress Shielding Platform Based on Body Temperature-Induced Shrinking of Hydrogel for Promoting Scar-Less Wound Healing. *Adv. Sci.* **2024**, *11*, 2306018.
75. Wang, Y.; Zhao, Y.; Qiao, L.; Zou, F.; Xie, Y.; Zheng, Y.; Chao, Y.; Yang, Y.; He, W.; Yang, S. Cellulose Fibers-Reinforced Self-Expanding Porous Composite with Multiple Hemostatic Efficacy and Shape Adaptability for Uncontrollable Massive Hemorrhage Treatment. *Bioact. Mater.* **2021**, *6*, 2089–2104.
76. Zhang, X.; Wang, X.; Yuan, P.; Ma, C.; Wang, Y.; Zhang, Z.; Wang, P.; Zhao, Y.; Wu, W. A 3D-Printed Cuttlefish Bone Elastomeric Sponge Rapidly Controlling Noncompressible Hemorrhage. *Small* **2024**, *20*, 2307041.
77. Mehmood, S.; Ullah, I.; Hussain, Z.; Dawit, H.; Ullah, S.; Liu, X.; Ahmed, W.; Xu, M.; Cao, Y.; Pei, R. Bioactive Self-Pumping Janus Fibrous Hydrogel Dressings with Aligned Microneedle Channels for Chronic Wound Healing. *Adv. Funct. Mater.* **2025**, *36*, e04317.
78. Wang, Y.; Zhang, Q.; Liu, Z.; Jin, C.; Rao, Y.; Yuan, X.; He, Q.; Lu, L.; Guo, J.; Yan, F. Janus Fibrous Dressing with Controllable Nitric Oxide-Releasing and Unidirectional Exudate Transport Activities for Bacteria-Infected Burn Wound Therapy. *Adv. Funct. Mater.* **2025**, *35*, 2503992.
79. Yang, S.; Yang, S.; Cai, Y.; Zou, J.; Qiao, X.; Wang, R.; Zheng, X.; Xiong, H.; Zhou, Z. Substitution-Degree-Engineered Acetylated Curdlan Janus Dressing: Unidirectional Self-Pumping for Efficient Wound Exudate Management and Accelerated Healing. *Carbohydr. Polym.* **2026**, *378*, 124944.
80. Lu, B.; Wang, D.; Guo, J.; Shen, Y.; Feng, Q.; Yang, J.; Han, X.; Yu, H.; Li, L.; Liu, J.; et al. High-Efficiency Exudates Drainage of Anti-Adhesion Dressings for Chronic Wound. *Chin. Chem. Lett.* **2025**, *36*, 110601.

81. Xue, B.; Gu, J.; Li, L.; Yu, W.; Yin, S.; Qin, M.; Jiang, Q.; Wang, W.; Cao, Y. Hydrogel Tapes for Fault-Tolerant Strong Wet Adhesion. *Nat. Commun.* **2021**, *12*, 7156.
82. Zhang, L.; Wang, L.; Li, W.; Bai, X.; Wang, X.; Lu, C.; Yuan, Z.; Ge, W.; Liu, Y. Bioinspired Hydrogels for Enhanced Wet Adhesion: From Natural Mechanisms to Biomedical Applications. *Chem. Eng. J.* **2025**, *520*, 165878.
83. Yao, P.; Deng, X.; Zhang, R.; Liu, Z. Hydrogel-Based Implantable Medical Devices: Pioneering Therapies and Monitoring. *Adv. Funct. Mater.* 2026, *e31960*.
84. Zhang, J.; Fu, C.; Tian, T.; Batur, S.; Lv, J.; Xie, Q.; Kong, L.; Yang, C.; Zhang, Z. *In Situ* Ultrafast Self-Gelling Coacervate Powder with Antibacterial, Antioxidant, and Robust Wet Adhesion Properties for Hemostasis and Wound Healing. *Adv. Funct. Mater.* **2025**, *35*, 2502577.
85. Gao, J.; Wen, J.; Hu, D.; Liu, K.; Zhang, Y.; Zhao, X.; Wang, K. Bottlebrush Inspired Injectable Hydrogel for Rapid Prevention of Postoperative and Recurrent Adhesion. *Bioact. Mater.* **2022**, *16*, 27–46.
86. Xie, Q.; Yan, C.; Liu, G.; Bian, L.; Zhang, K. *In Situ* Triggered Self-Contraction Bioactive Microgel Assembly Accelerates Diabetic Skin Wound Healing by Activating Mechanotransduction and Biochemical Pathway. *Adv. Mater.* **2024**, *36*, 2406434.
87. Kim, Y.E.; Kim, J. ROS-Scavenging Therapeutic Hydrogels for Modulation of the Inflammatory Response. *ACS Appl. Mater. Interfaces* **2022**, *14*, 23002–23021.
88. Zhang, S.; Zhao, X.; Zhang, W.; Wei, X.; Chen, X.; Wang, X. Zn-DHM Nanozymes Regulate Metabolic and Immune Homeostasis for Early Diabetic Wound Therapy. *Bioact. Mater.* **2025**, *49*, 63–84.
89. Liu, Z.; Chen, X.; Xu, Z.; Li, S.; Ma, W.; Wang, Y.; Chen, Y.; Yao, L.; Liang, J.; Liao, S.; et al. Diamond-Inspired DNA Hydrogel Based on Tetrahedral Framework Nucleic Acids for Burn Wound Healing. *Adv. Mater.* **2025**, *37*, e09727.
90. Sun, J.; Jia, W.; Qi, H.; Huo, J.; Liao, X.; Xu, Y.; Wang, J.; Sun, Z.; Liu, Y.; Liu, J.; et al. An Antioxidative and Active Shrinkage Hydrogel Integratedly Promotes Re-Epithelization and Skin Constriction for Enhancing Wound Closure. *Adv. Mater.* **2024**, *36*, 2312440.
91. Qin, Y.; Jia, S.; Shi, X.L.; Gao, S.; Zhao, J.; Ma, H.; Wei, Y.; Huang, Q.; Yang, L.; Chen, Z.G.; et al. Self-Powered Thermoelectric Hydrogels Accelerate Wound Healing. *ACS Nano* **2025**, *19*, 15924–15940.
92. Kizhakkedathu, J.N.; Conway, E.M. Biomaterial and Cellular Implants: Foreign Surfaces Where Immunity and Coagulation Meet. *Blood* **2022**, *139*, 1987–1998.
93. Gawaz, M.; Vogel, S. Platelets in Tissue Repair: Control of Apoptosis and Interactions with Regenerative Cells. *Blood* **2013**, *122*, 2550–2554.
94. Yu, Q.; Wang, W.; Deng, N.; Su, B.; Zhao, W.; Zhao, C. Janus Amphipathic Dressing with Liquid Self-Pumping and Blood-Clot Anti-Adhesion for Satisfactory Hemostasis. *Adv. Healthc. Mater.* **2024**, *13*, 2400993.
95. Cai, M.; Huang, L.; Lv, S.; Jiang, X. Synthesis and Characterization of Thermosensitive 2-Hydroxypropyl-Trimethylammonium Chitin and Its Antibacterial Sponge for Noncompressible Hemostasis and Tissue Regeneration. *Carbohydr. Polym.* **2024**, *331*, 121879.
96. Zhang, P.; Yu, C.; Hu, Z.; Li, Y.; Wan, G.; Tang, K.; Fan, X. On-Demand Removal of Rapid Hemostatic Sponge for Non-Compressible Hemorrhage through Disrupting Ionic Bonds. *Adv. Healthc. Mater.* **2025**, *14*, 2404894.
97. Qi, L.; Mu, L.; Guo, X.; Liu, A.; Chen, C.; Ye, Q.; Zhong, Z.; Shi, X. Fast Expandable Chitosan-Fibers Cryogel from Ambient Drying for Noncompressible Bleeding Control and *In Situ* Tissue Regeneration. *Adv. Funct. Mater.* **2023**, *33*, 2212231.
98. Lan, J.; Shi, L.; Xiao, W.; Zhang, X.; Wang, S. A Rapid Self-Pumping Organohydrogel Dressing with Hydrophilic Fractal Microchannels to Promote Burn Wound Healing. *Adv. Mater.* **2023**, *35*, 2301765.
99. Cheng, L.; Zhuang, Z.; Yin, M.; Lu, Y.; Liu, S.; Zhan, M.; Zhao, L.; He, Z.; Meng, F.; Tian, S.; et al. A Microenvironment-Modulating Dressing with Proliferative Degradants for the Healing of Diabetic Wounds. *Nat. Commun.* **2024**, *15*, 9786.
100. Zhang, X.; Gong, B.; Rao, F.; Hu, H.; Tian, F.; Lu, Y.; Zhang, L.; Xia, Y.; Xue, J. Spatiotemporally Controlled Delivery of Biological Effectors from Nanofiber Scaffolds Accelerates Skin Wound Healing in Porcine Models. *Sci. Adv.* 2025, *11*, eadz5302.
101. Song, P.; Sun, Q.; Liang, X.; Li, J.; Shi, J.; Zhu, Y.; Du, J. Reversible Adhesive Hydrogel Balancing Conflicting Needs of Strong Adhesion and Painless Removal for Diabetic Joint Wound Healing. *ACS Nano* **2025**, *19*, 25466–25479.
102. Chen, H.; Zhang, R.; Zhang, G.; Liang, X.; Xu, C.; Li, Y.; Xu, F. Naturally Inspired Tree-Ring Structured Dressing Provides Sustained Wound Tightening and Accelerates Closure. *Adv. Mater.* **2024**, *37*, 2410845.
103. Hu, J.; Wei, T.; Zhao, H.; Chen, M.; Tan, Y.; Ji, Z.; Jin, Q.; Shen, J.; Han, Y.; Yang, N.; et al. Mechanically Active Adhesive and Immune Regulative Dressings for Wound Closure. *Matter* **2021**, *4*, 2985–3000.
104. Lun, W.; Wang, H.; Li, M.; Ma, J.; Ding, Y.; Zheng, X.; Cao, X.; Li, Q. Fabrication of MnO_2-Modified Decellularized Tendon Membrane for Enhancing Tendon Repair. *Adv. Healthc. Mater.* **2024**, *14*, 2402584.
105. Xiang, L.; Liang, J.; Wang, Z.; Lin, F.; Zhuang, Y.; Saiding, Q.; Wang, F.; Deng, L.; Cui, W. Motion Lubrication Suppressed Mechanical Activation via Hydrated Fibrous Gene Patch for Tendon Healing. *Sci. Adv.* 2023, *9*, eadc9375.

106. Freedman, B.; Kuttler, A.; Beckmann, N.; Nam, S.; Kent, D.; Schuleit, M.; Ramazani, F.; Accart, N.; Rock, A.; Li, J.; et al. Enhanced Tendon Healing by a Tough Hydrogel with an Adhesive Side and High Drug-Loading Capacity. *Nat. Biomed. Eng.* **2022**, *6*, 1167–1179.
107. Luo, R.; Xiong, Y.; Li, J.; Xiao, M.; Bai, Y.; Xu, Z.; Luo, Z.; Li, C.; Liang, A.; Feng, H.; et al. Piezoelectric Injectable Anti-Adhesive Hydrogel to Promote Endogenous Healing of Tendon Injuries. *Adv. Mater.* **2025**, *37*, 2501306.
108. Chen, Z.; Zhang, H.; Fan, C.; Zhuang, Y.; Yang, W.; Chen, Y.; Shen, H.; Xiao, Z.; Zhao, Y.; Li, X.; et al. Adhesive, Stretchable, and Spatiotemporal Delivery Fibrous Hydrogels Harness Endogenous Neural Stem/Progenitor Cells for Spinal Cord Injury Repair. *ACS Nano* **2022**, *16*, 1986–1998.
109. Xu, D.; Fu, S.; Zhang, H.; Lu, W.; Xie, J.; Li, J.; Wang, H.; Zhao, Y.; Chai, R. Ultrasound-Responsive Aligned Piezoelectric Nanofibers Derived Hydrogel Conduits for Peripheral Nerve Regeneration. *Adv. Mater.* **2024**, *36*, 2307896.
110. Xuan, H.; Wu, S.; Jin, Y.; Wei, S.; Xiong, F.; Xue, Y.; Li, B.; Yang, Y.; Yuan, H. A Bioinspired Self-Healing Conductive Hydrogel Promoting Peripheral Nerve Regeneration. *Adv. Sci.* **2023**, *10*, 2302519.
111. Zhang, L.; Qiu, P.; Shen, S.; Zhang, C.; Qin, J.; Xu, Z.; Yixi, Z.; Lv, J.; Pu, H.; Lei, J.; et al. Polydopamine-Modified Hydrogel Nanofibers for Sustained SFRP2 Release: Synergistic Promotion of Angiogenesis and Nerve Regeneration. *NPG Asia Mater.* **2025**, *17*, 29.
112. Wang, K.; Xia, Z.; Yu, R.; Zhang, W.; Wang, Z.; Zhu, M.; Li, R.; Hu, Z.; Chen, Z.; Xu, K.; et al. Novel Hydrogel Adjuvant of Chinese Medicine External Preparations for Accelerated Healing of Deep Soft Tissue Injuries. *ACS Biomater. Sci. Eng.* **2024**, *10*, 4425–4436.
113. Wen, N.; Jiang, Y.; Song, Y.; Yang, J.; Long, J.; Wang, Y.; Yu, X.; Lu, S.; Zhou, T.; Huang, X. An Injectable Zwitterionic Hydrogels with Multiple Intermolecular Interactions for Effective Prevention of Abdominal Adhesions. *Adv. Sci.* **2025**, *12*, e11757.
114. Wu, D.; Eugenis, I.; Hu, C.; Kim, S.; Kanugovi, A.; Yue, S.; Wheeler, J.R.; Fathali, I.; Feeley, S.; Shrager, J.B.; et al. Bioinstructive Scaffolds Enhance Stem Cell Engraftment for Functional Tissue Regeneration. *Nat. Mater.* **2025**, *24*, 1364–1374.
115. Song, W.; Lee, C.; Jeong, H.; Kim, S.; Hwang, N.S. Sprayable Anti-Adhesive Hydrogel for Peritoneal Macrophage Scavenging in Post-Surgical Applications. *Nat. Commun.* **2024**, *15*, 8364.
116. Chen, J.; Li, J.; Zhang, S.; Zhu, D.; Yao, B.; Fang, X.; Perez, A.; Li, Y.; King, M.W.; Cheng, K. Local Microneedle Delivery of Calcium Channel Blockers for Preventing Abdominal Adhesions. *Cell Biomater.* 2025, *100251*.
117. Cherry, I.; Tarhini, L.; Doan, M.; De Buys Roessingh, A. Exploring the Place of Fish Skin Grafts with Omega-3 in Pediatric Wound Management. *J. Clin. Med.* **2024**, *13*, 112.
118. Seetharam, A.; Abad, J.; Baessler, A.; Badman, B.L. Use of a Nanofiber Resorbable Scaffold During Rotator Cuff Repair: Surgical Technique and Results After Repair of Small- to Medium-Sized Tears. *Orthop. J. Sports Med.* **2022**, *10*, 23259671221094848.
119. Boeckstyns, M.E.H.; Sørensen, A.I.; Viñeta, J.F.; Rosen, B.; Navarro, X.; Archibald, S.J.; Valls-Solé, J.; Moldovan, M.; Krarup, C. Collagen Conduit versus Microsurgical Neurorrhaphy: 2-Year Follow-Up of a Prospective, Blinded Clinical and Electrophysiological Multicenter Randomized, Controlled Trial. *J. Hand Surg.* **2013**, *38*, 2405–2411.
120. Fazio, V.W.; Cohen, Z.; Fleshman, J.W.; van Goor, H.; Bauer, J.J.; Wolff, B.G.; Corman, M.; Beart, R.W.; Wexner, S.D.; Becker, J.M.; et al. Reduction in Adhesive Small-Bowel Obstruction by Seprafilm® Adhesion Barrier After Intestinal Resection. *Dis. Colon Rectum* **2006**, *49*, 1–11.
121. Omar, U.F.; Lim, V.E.; Huang, S.; Tan, E.X.; Rajaratnam, V. Evaluation of Biodegradable Temporizing Matrix for Functional and Aesthetic Outcomes in Hand Soft-Tissue Defect: A 3-Year Retrospective Study. *Plast. Reconstr. Surg. Glob. Open* **2025**, *13*, e6909.

Article

Rational Electrolyte Formulation for Sodium Metal Batteries Operating in Extremely Cold Environments

Chuanlong Wang, Peiyu Wang, and Weiyang Li *

Thayer School of Engineering, Dartmouth College, Hanover, NH 03755, USA; weiyang.li@dartmouth.edu
Received: 3 March 2026; Revised: 27 March 2026; Accepted: 30 March 2026; Published: 31 March 2026

Abstract: Sodium metal batteries have shown considerable potential when operated at ambient temperatures. However, their performance in cold environments is constrained by increased electrolyte resistance with decreasing temperature and dendritic sodium plating associated with unstable solid electrolyte interphase (SEI), which are primarily influenced by the electrolyte composition. In this study, we present an electrolyte formulation that remains thermally stable down to −150 °C, which not only facilitates low internal resistance but also contributes to the formation of a protective SEI under cryogenic conditions. When cycled at −40 °C at 1 mA cm^{-2}, the sodium metal electrode exhibits a low overpotential of only 16 mV over 750 h; even at an ultra-low temperature of −80 °C, the electrode demonstrates remarkable long-term stability with a low overpotential of 54 mV sustained over 1500 h at 0.5 mA cm^{-2}. Furthermore, full cell evaluations when paring with $Na_3V_2(PO_4)_3$ cathode reveal a high average Coulombic efficiency exceeding 99.1% and a capacity retention over 83% after 100 cycles at both −40 °C and −80 °C.

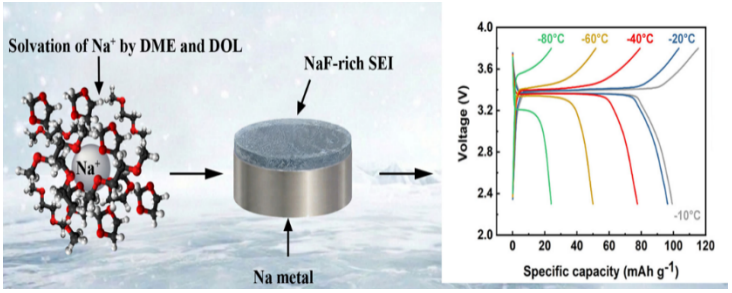

Keywords: sodium metal battery; low temperature; ether electrolyte; sodium hexafluorophosphate; solid electrolyte interphase

1. Introduction

Lithium-ion batteries (LIBs) are widely employed in portable electronics and electric vehicles owing to their high energy and power densities, as well as their prolonged cycle life [1–3]. However, LIBs suffer considerable energy and power losses at low operating temperatures, particularly below −20 °C [4,5]. This significantly restricts their applications under cold conditions [5,6], including military and aerospace, polar exploration, cold-chain logistics, and renewable energy storage in cold climates. To overcome the low-temperature operational hurdles, beyond LIB technologies, specifically those utilizing lithium metal anodes are being investigated with promising results [7–16]. Meanwhile, the escalating cost of lithium has compelled the research community to explore alternative energy storage technologies. Sodium (Na) metal emerges as a particularly attractive anode candidate for Na battery chemistry because of its high theoretical specific capacity (1166 mAh g^{-1}), low electrode potential (−2.714 V versus the standard hydrogen electrode), and much lower cost and high abundancy of Na resources compared to the lithium counterparts [17–22]. Yet, comprehensive understanding of the electrochemical behavior of Na metal anodes under low-temperature conditions remain elusive.

Formulating the appropriate electrolyte composition is critical for enabling the Na metal anode to work under cold conditions [23–30]. With decreasing temperature, the electrolyte resistance increases markedly, primarily due to elevated viscosity and decreased salt solubility. Moreover, the structure and composition of the solid electrolyte interphase (SEI) depend heavily on the electrolyte formulation and exhibit high sensitive to temperature fluctuations. It is well recognized that an electrolyte composed of sodium hexafluorophosphate ($NaPF_6$) salt dissolved in diethylene glycol dimethyl ether (DEGDME) in a standard salt concentration of 1 M exhibited high compatibility with Na metal anodes, rendering it a superior choice for stable cycling at room temperature [31]. Our previous research showed that $NaPF_6$ and sodium trifluoromethanesulfonate (NaOTf) exhibited intermediate

reduction potentials vs Na^+/Na with a moderate driving force to decompose before the decomposition of DEGDME, which may contribute to the formation of a smooth and inorganic-species-rich SEI film on the Na metal electrode at room temperature [23]. Nevertheless, $NaPF_6$ faces solubility challenges at low temperatures; salt precipitation was observed in the 1 M $NaPF_6$-DEGDME electrolyte system at −35 °C, leading to suboptimal electrochemical performance. Even at a reduced concentration of 0.5 M $NaPF_6$-DEGDME, a temperature limitation of −40 °C was still evident (Supplementary Figure S1), and similar temperature threshold was also observed with the NaOTf-DEGDME electrolyte system [23]. This phenomenon could be explained by the intrinsic molecular architecture of DEGDME. The presence of multiple oxygen atoms in DEGDME induces strong intermolecular interactions, causing sluggish diffusion of the solvated Na^+ ions, especially at low temperature [29]. Moreover, the multiple oxygen coordination sites facilitate a strong chelating affinity with Na^+ ions, which increases the number of solvent molecules within the solvation shell [29]. This feature is particularly detrimental for the SEI formation at low temperature, in which the salt solubility decreases and thus the decomposition of the salt is suppressed, leading to an unfavorable SEI dominated by organic species originated from the solvent molecules.

Herein we present an electrolyte formulation that replaces the widely employed DEGDME solvent for Na metal anode with monoglyme—1,2-dimethoxyethane (DME)—which enables superior performance for metallic Na anode at low temperatures down to −80 °C. X-ray photoelectron spectroscopy (XPS) characterization on the SEI layer reveals that DME facilitates the formation of an SEI that is more enriched with inorganic species compared to that formed in DEGDME counterpart at −80 °C. Symmetric cell testing shows that when cycled at −40 °C at 1 mA cm^{-2}, the Na metal electrode exhibits a low overpotential of only 16 mV over 750 h. Even at a high current of 3 mA cm^{-2}, the overpotential is only 82 mV at −40 °C. In addition, when cycled at an extremely cold temperature of −80 °C, the Na metal electrode displays impressive long-term stability with a low overpotential of 54 mV sustained over 1500 h at 0.5 mA cm^{-2}. Moreover, high Coulombic efficiency of 99.8% is achieved at −60 °C for Na asymmetric cell at 0.5 mA cm^{-2}. This performance is comparable to, and in many cases surpasses the reported state-of-the-art results for Na metal anodes cycling at current densities of ≥0.5 mA cm^{-2} at ultra-low temperatures (≤−40 °C), as summarized in Supplementary Table S1. Moreover, full cell evaluations when paring with $Na_3V_2(PO_4)_3$ cathode reveal a high average Coulombic efficiency exceeding 99.1% and a capacity retention over 83% after 100 cycles at both −40 °C and −80 °C.

2. Experimental Sections

2.1. Chemicals and Materials

Metallic Na chips were produced from Na metal cubes obtained from Sigma–Aldrich (Sigma-Aldrich, Inc., St. Louis, US). Prior to use, sodium hexafluorophosphate ($NaPF_6$, Sigma–Aldrich) was dried in an argon (Ar)-filled glove box, maintaining conditions of O_2 < 0.6 PPM and H_2O < 0.1 PPM (Mbraun). The solvents used for electrolyte preparation—diethylene glycol dimethyl ether (anhydrous, Sigma–Aldrich), 1,2-dimethoxyethane (anhydrous, Sigma–Aldrich), 1,3-dioxolane (anhydrous, Sigma–Aldrich), and tetrahydrofuran (anhydrous, Sigma–Aldrich)—were used directly without further purification.

2.2. Characterizations

A temperature chamber (MC-812 ESPEC Corp., Osaka, Japan) was utilized to maintain stable temperature conditions ranging from −80 °C to 20 °C. Coin cells were equilibrated at a specified temperature for a minimum of one hour to ensure thermal stability. X-ray photoelectron spectroscopy (XPS) analysis was conducted using a PHI Versaprobe II scanning XPS microprobe (ULVAC-PHI, Inc., Kanagawa, Japan), which has a system resolution of 0.47 eV and employs a monochromatic 1486.7 eV X-ray source. Samples were transferred into the XPS chamber using a sealed Ar-filled vessel to prevent exposure to air. Differential scanning calorimetry (DSC) was performed with a Netzsch DSC 204 F1 Phoenix (NETZSCH-Gerätebau GmbH, Selb, Germany), measuring both samples and a reference between −150 °C and 20 °C at a controlled heating rate of 10 °C min^{-1}. Additionally, ^{23}Na Nuclear Magnetic Resonance (NMR) was executed on a Bruker 600 MHz Advance III HD spectrometer (Bruker Corporation, Billerica, MA, USA) equipped with a 5 mm probe (Bruker BBFO). Scanning electron microscope (SEM) imaging was carried out using a field emission gun environmental SEM (XL 300 ESEM-FEG, FEI Company, Hillsboro, OR, USA).

2.3. Electrochemical Measurements

All electrolytes were prepared in an argon-filled glove box. Na || Na symmetric cycling was performed in 2032-type coin cells, which consisted of two identical Na chips and a separator (Celgard 2400) saturated with 40 μL

of the testing electrolyte. Asymmetric cells were assembled with stainless steel foil as the working electrode and freshly cut Na as the counter electrode, also using 40 μL of the electrolyte. Na metal full cells were constructed with $Na_3V_2(PO_4)_3$ cathodes and bare Na anodes utilizing the tested electrolytes. Details regarding the synthesis and processing of $Na_3V_2(PO_4)_3$, as well as cathode preparation, can be found in a prior study [18]. The active material loading for the cathodes is 2 mg cm^{-2}. Electrochemical evaluations of symmetric and asymmetric cells, along with Na metal full cells, were conducted using a standard battery tester (CT2001A, Wuhan LANHE Electronics Co., Ltd., Wuhan, China). Electrochemical impedance spectroscopy (EIS) measurements were carried out using an electrochemical workstation (VMP3, Bio-Logic Science Instruments, Seyssinet-Pariset, France) over a frequency range of 1 MHz to 0.1 Hz, with an AC amplitude of 5 mV. The total resistance of the electrolyte solution was measured through EIS in stainless steel (SS) || stainless steel (SS) cells [23]. A polymer membrane was sandwiched between two pieces of stainless steel in the coin cell with 40 μL electrolyte added. The ionic conductivity of the electrolyte solution was calculated based on the method detailed in our previous paper [23].

3. Results and Discussion

3.1. Screening and Electrochemical Evaluation of Different Electrolytes at Low Temperatures

We first investigated a series of electrolyte solutions composed of $NaPF_6$ salt with different solvents at −35 °C. Ethers including DEGDME, DME, 1,3-dioxolane (DOL), and tetrahydrofuran (THF) were chosen as candidate solvents due to their low melting points (Supplementary Table S2). Out of the twelve formulations tested, nine exhibited good solubility with 0.5 M $NaPF_6$ at −35 °C without obvious salt precipitation (Supplementary Table S3). Based upon our previous finding that a 2:8 volume ratio of DEGDME to DOL optimized the Na metal electrode performance at −80 °C [23], here we selected six representative systems (marked in Supplementary Table S3) for further systematic evaluation. To isolate the structural effects of linear ethers (DEGDME vs. DME) and cyclic ethers (DOL vs. THF), we primarily focused on the 2:8 ratio as a comparative benchmark to explore how molecular substitution—rather than concentration variance—governs low-temperature electrochemical behavior.

Repeated Na stripping and plating were performed in symmetric cells with two identical electrodes using 0.5 M $NaPF_6$ electrolytes at a current density of 0.2 mA cm^{-2} and a capacity of 0.1 mAh cm^{-2} across a temperature range from 0 °C to −80 °C (Figure 1a–c). As shown in Figure 1a, the electrolyte systems employing 0.5 M $NaPF_6$-DME/DOL (2:8 in volume fraction; all ratios hereafter refer to volume ratios) and 0.5 M $NaPF_6$-DEGDME/DOL (2:8) exhibit low overpotentials (less than 25 mV) and stable voltage profiles down to −80 °C. It is noted that the cell with 0.5 M $NaPF_6$-DME/DOL exhibits a stabler voltage profile, especially at −80 °C, compared to the one with DEGDME. A high percentage of DOL is necessary for maintaining stable voltage profiles, as the performance of the DME/DOL (5:5 and 8:2) electrolytes with higher volume ratio of DME was unsatisfactory (Figure 1b). The critical role of cyclic ether, DOL, can be mainly ascribed to the following reasons based on our prior study and previous reports [23,29,32]: (i) DOL has a much lower melting point (−95 °C) compared to DME (−58 °C), preventing the electrolyte from freezing at cold conditions and improving the ionic conductivity of the electrolyte; (ii) DOL is known as a weakly solvating solvent for Na^+ and Li^+ ions, which participates in the solvation shell and weakens the chelation of Na^+ ions with glyme-based electrolytes; (iii) DOL may contribute to a concentrated electron cloud around PF_6^- and result in the preferential salt decomposition rather than the solvent molecules. Additionally, replacing DOL with THF in the DGEDME/THF (2:8) and DME/THF (2:8) systems resulted in asymmetric voltage profiles and high overpotentials at low temperatures, especially at ultra-low temperature of −60 °C and −80 °C (Figure 1c).

In addition to symmetric cells, Na || stainless steel (SS) asymmetric cells were fabricated and tested at 0.5 mA cm^{-2} and 0.5 mAh cm^{-2}, with a cut-off voltage of 0.3 V (Figure 1d–f) at low temperatures ranging from −10 °C to −60 °C. While both the DEGDME/DOL (2:8) and DME/DOL (2:8) systems exhibit comparable performance in Na || Na symmetric configurations, the 0.5 M $NaPF_6$-DME/DOL (2:8) system displays smoother stripping and plating curves, featuring a lower nucleation overpotential of 47 mV and a high Coulombic efficiency (CE) of 99.84% at −60 °C (Figure 1d). In contrast, the 0.5 M $NaPF_6$-DEGDME/DOL (2:8) system has a higher nucleation overpotential of 60 mV and a much lower CE of 88.06% at −60 °C (Figure 1e). In addition, the CE of the 0.5 M $NaPF_6$-DME/DOL (2:8) at −10 °C, −20 °C and −40 °C is 99.84%, 99.93% and 99.60%, respectively; these numbers are slightly higher those of the 0.5 M $NaPF_6$- DEGDME/DOL (2:8), which gives a CE of 99.68% at −10 °C, 99.38% at −20 °C, and 99.28% at −40 °C. Meanwhile, the 0.5 M $NaPF_6$-DME/THF (2:8) system shows voltage profiles characterized by a stepwise stripping curve, with a distinct turning point at 0.15 V at −60 °C (Figure 1f). This phenomenon may suggest that Na dendrite fragments, formed due to sluggish kinetics at −60 °C, become partially isolated. The observed voltage step represents the stripping of this 'inactive' Na, which could only be recovered under increased overpotential. The CE values of the 0.5 M $NaPF_6$-DME/THF (2:8) at different temperatures are as follows: 99.92% at −10 °C, 99.83% at −20 °C, 99.84% at −40 °C and 92.93% at −60 °C.

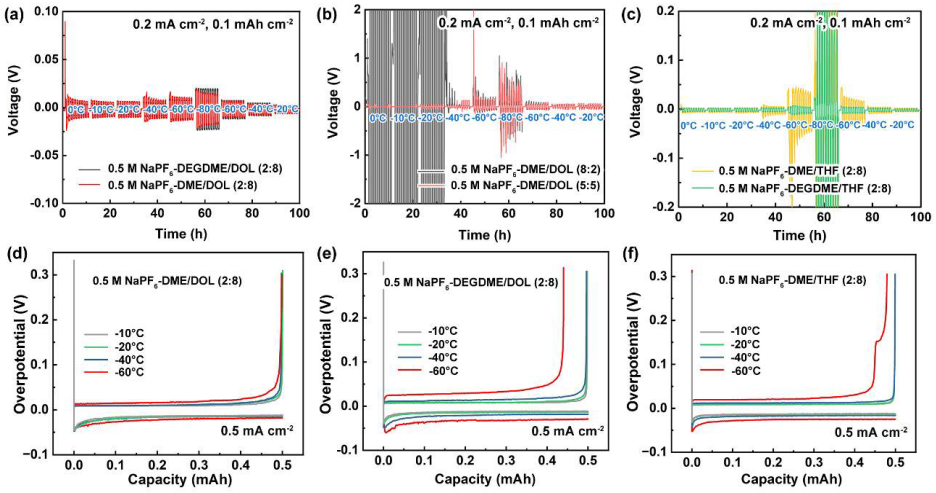

Figure 1. Temperature-dependent electrochemical screening of electrolyte formulations at low temperatures. Galvanostatic cycling of Na || Na symmetric cells at 0.2 mA cm^{-2} and 0.1 mAh cm^{-2} in 0.5 M electrolytes of (**a**) $NaPF_6$-DEGDME/DOL (2:8) and $NaPF_6$-DME/DOL (2:8); (**b**) $NaPF_6$-DME/DOL (8:2) and $NaPF_6$-DME/DOL (5:5); and (**c**) $NaPF_6$-DME/THF (2:8) and $NaPF_6$-DEGDME/THF (2:8); (**d**–**f**) Na plating/stripping profiles of Na || stainless steel (SS) asymmetric cells at 0.5 mA cm^{-2} and 0.5 mAh cm^{-2} with a cut-off voltage of 0.3 V in 0.5 M electrolytes of $NaPF_6$-DME/DOL (2:8), $NaPF_6$-DEGDME/DOL (2:8) and $NaPF_6$-DME/THF (2:8).

The 0.5 M $NaPF_6$-DME/DOL (2:8) electrolyte was then selected for further electrochemical evaluation due to its superior performance observed during the initial screening process. This assessment focused on rate capability and long-term cycling stability in symmetric cells at −40 °C (Figure 2). In the rate capacity measurement (Figure 2a), the cell exhibits stable performance with a low overpotential of less than 20 mV with a capacity increasing from 1 mAh cm^{-2} to 3 mAh cm^{-2} at a current density of 1 mA cm^{-2}. Meanwhile, as current density was increased from 1 to 2 mA cm^{-2} while maintaining a constant capacity of 1 mAh cm^{-2} (Figure 2b), the overpotential of the cell rises from about 16 mV to 48 mV; even at a high current density of 3 mA cm^{-2}, the cell only shows an overpotential of 82 mV, indicating fast kinetics at such low temperature. In addition, the 0.5 M $NaPF_6$-DME/DOL (2:8) electrolyte system demonstrates stable long-term cycling at −40 °C, maintaining an overpotential of approximately 15–16 mV for over 750 h at 1 mA cm^{-2} and 1 mAh cm^{-2}, without any discernible trend of increase (Figure 2c).

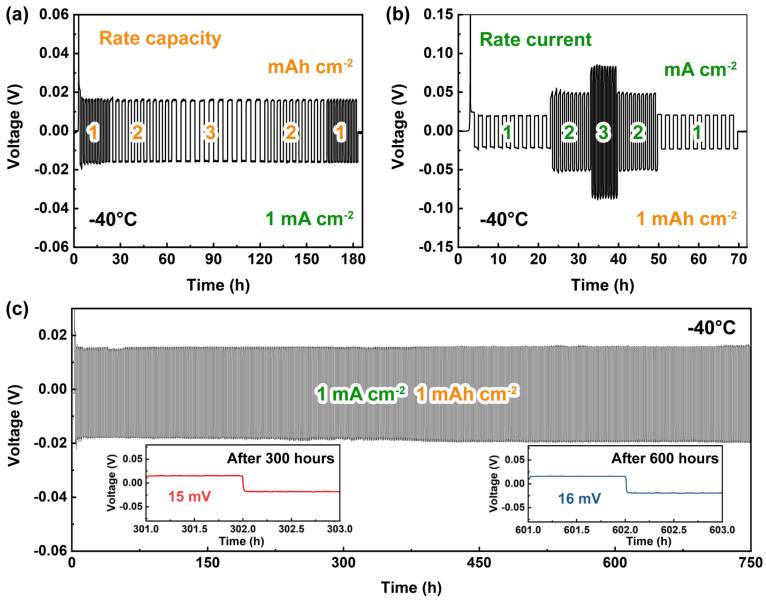

Figure 2. Galvanostatic cycling of Na || Na symmetric cells in 0.5 M $NaPF_6$-DME/DOL (2:8) electrolyte at −40 °C. (**a**) Rate capacity performance at various capacities up to 3 mAh cm^{-2} at 1 mA cm^{-2}; (**b**) Rate current performance at various current densities up to 3 mA cm^{-2} at 1 mAh cm^{-2}; (**c**) Long-term stability at 1 mA cm^{-2} and 1 mAh cm^{-2} (Insets: enlarged voltage profiles after 300 h and after 600 h).

3.2. Physicochemical Characterization of the Designed Electrolyte

To investigate the interaction between Na^+ ions and solvent molecules, we conducted ^{23}Na nuclear magnetic resonance (NMR) spectroscopy (Figure 3a). The relative peak intensities varied with different solvent species, providing insights for the solubility characteristics of the Na species (i.e., $NaPF_6$) in the medium [33]. Notably, $NaPF_6$ demonstrates higher solubility in DME and THF compared to DOL. The incorporation of a small fraction (20% in volume) of DME significantly enhanced salt solubility in the DME/DOL (2:8) mixture relative to pure DOL. This improved solubility was maintained even at temperatures as low as −80 °C (Figure 3b). No precipitation of salt was observed for the 0.5 M $NaPF_6$-DME/DOL (2:8) after storing at −80 °C for 24 h. Nevertheless, salt precipitation occurred in the 0.5 M $NaPF_6$-DME/THF (2:8) solution at −80 °C (Supplementary Figure S2), despite THF having a lower melting point and a higher dielectric constant at room temperature compared to DOL (Supplementary Table S2). Additionally, the chemical shifts reveals that DME caused a more pronounced downfield shift of ^{23}Na compared to DOL and THF, indicating a stronger deshielding effect on the ^{23}Na nucleus [34]. Consistent with the Gutmann donor theory, this shift suggests that DME possesses a higher coordination affinity for Na^+, effectively reducing the electron density surrounding the Na^+ through strong chelation.

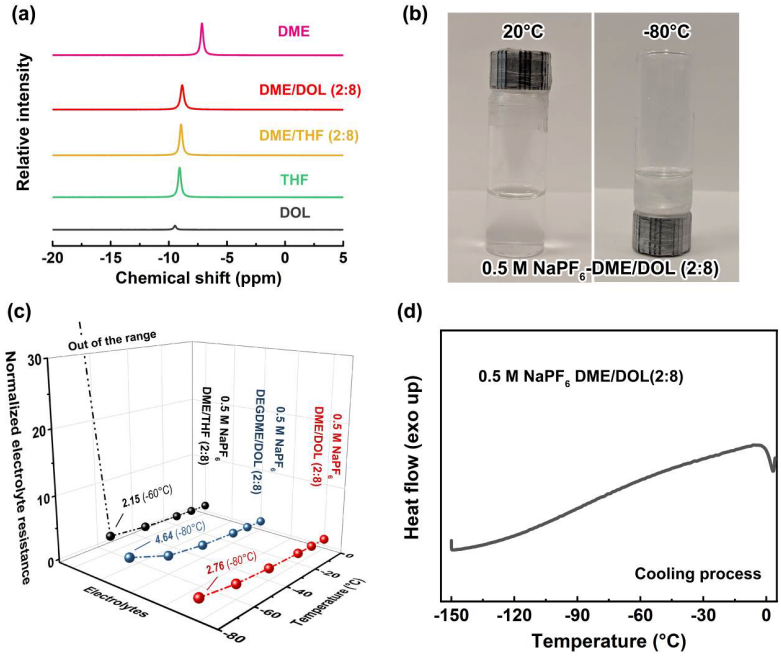

Figure 3. Physicochemical characterizations of $NaPF_6$-based electrolyte solutions. (**a**) ^{23}Na-NMR spectroscopy on the electrolyte solutions. Notably, the concentration of the $NaPF_6$-DOL system is below 0.5 M due to solubility limitation, whereas the other four systems were successfully prepared at 0.5 M; (**b**) Photo of 0.5 M $NaPF_6$-DME/DOL (2:8) after storing at 20 °C and −80 °C for 24 h. No precipitation of salts is observed at −80 °C; (**c**) Change in the resistance of the electrolyte solutions in the temperature range from 0 °C to −80 °C. The resistance values at different temperatures are normalized to those at 0 °C (the value of each electrolyte at 0 °C is treated as 1). Notably, the value for the 0.5 M $NaPF_6$-DME/THF (2:8) at −80 °C exceeds the plotted scale, shown as 'out of the range' in the figure; (**d**) DSC thermograms of 0.5 M $NaPF_6$-DME/DOL (2:8) electrolyte from 0 °C to −150 °C.

To elucidate the underlying mechanism for the enhanced performance, we examined the electrolyte resistance at various temperatures (Figure 3c). Electrochemical impedance spectroscopy (EIS) was used to measure the resistance of the electrolyte solution in SS || SS cells (see Experimental Sections for details). The resistance of 0.5 M $NaPF_6$-DME/DOL (2:8) was approximately 6.3 Ohms at 0 °C, which increased by a factor of 2.76 when the temperature decreased to −80 °C. This increase is half that observed for 0.5 M $NaPF_6$-DEGDME/DOL (2:8), which showed a 4.64-fold increase from 0 °C to −80 °C. In contrast, the resistance of the DME/THF (2:8) system increased by a factor of 2.15 when the temperature decreased to −60 °C and exceeded 30 times at −80 °C due to salt precipitation. Furthermore, the observed changes in electrolyte resistance correlate well with the trends in ionic conductivity (Supplementary Figure S3), where the 0.5 M $NaPF_6$-DME/DOL (2:8) system exhibits the slowest decline in conductivity with decreasing temperature. Differential scanning calorimetry (DSC) further confirmed the thermal stability of the 0.5 M $NaPF_6$-DME/DOL (2:8) system, indicating no phase transitions even down to −150 °C (Figure 3d).

3.3. Electrochemical Behavior at −80 °C and Post-Mortem Analysis

Extended cycling of Na || Na symmetric cells was performed utilizing 0.5 M $NaPF_6$-DME/DOL (2:8) at −80 °C at different current densities and capacities. At a current density of 0.2 mA cm^{-2} with a cycling capacity of 0.1 mAh cm^{-2}, the cell exhibits a low overpotential of approximately 20 mV, remaining stable for over 2000 h (Supplementary Figure S4). Furthermore, at a higher current density of 0.5 mA cm^{-2} with a capacity of 0.25 mAh cm^{-2}, stable performance was maintained for more than 1500 h (Figure 4a). The expanded voltage profiles (insets in Figure 4a) after 750 and 1500 h show smooth voltage responses without spikes with an overpotential of 53 mV and 54 mV, respectively. Scanning electron microscopy (SEM) imaging of the Na metal electrode after 50 cycles at −80 °C reveals a uniform morphology in the $NaPF_6$-DME/DOL (2:8) system, with no obvious porous structures on the surface or within the cross-section (Figure 4b). In contrast, the Na metal surface cycled with $NaPF_6$-DEGDME/DOL (2:8) exhibits rough and heterogeneous textures (Supplementary Figure S5).

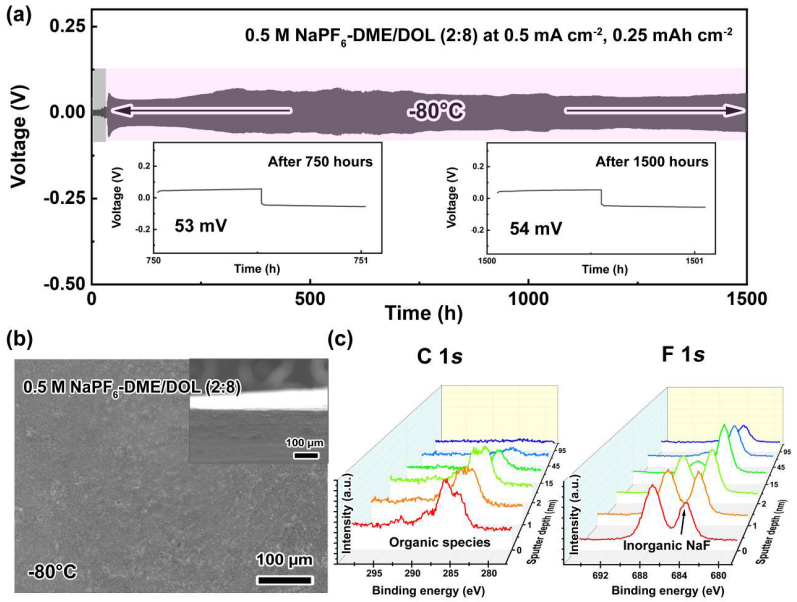

Figure 4. Electrochemical and physicochemical characterizations of Na metal electrodes cycled in 0.5 M $NaPF_6$-DME/DOL (2:8) electrolyte at −80 °C. (**a**) Galvanostatic cycling of Na || Na symmetric cells at 0.5 mA cm^{-2} and 0.25 mAh cm^{-2} (pink zone). Note that an initial stepwise temperature drop (gray zone) was applied to stabilize the cells (Insets: enlarged voltage profiles after 750 h and after 1500 h); (**b**) Ex situ postmortem SEM imaging of the surface of the Na metal electrode after cycling at −80 °C (Inset: corresponding cross-sectional SEM image); (**c**) XPS profiles of the C 1*s* and F 1*s* spectra recorded at various sputtering depths.

The chemical composition of the Na metal electrode surface using 0.5 M $NaPF_6$-DME/DOL (2:8) was characterized using X-ray photoelectron spectroscopy (XPS), as illustrated in Supplementary Figure S6. Binding energies for all elements were calibrated relative to the C 1*s* signal at 284.8 eV. In the C 1*s* spectrum, the peak at 293 eV corresponds to polycarbonate, and the peaks at 289.5 eV and 286.8 eV can be attributed to O–C=O/ CO_3^{2-} and C–O, respectively [19,31,33,35,36]. For the O 1*s* spectrum, the peaks at 532.5 eV and 526 eV can be assigned to O–P=O and Na_2O [19], respectively, while the peak at 537 eV is associated with Na KLL [19,35]. With respect to the F 1*s* spectrum, the peaks at 687.6 eV and 684.2 eV correspond to PF_6- and NaF species, respectively [19,35]. The P 2*p* spectrum shows doublets at 137.4 eV and 133.7 eV (for $2p_{3/2}$), which are assigned to PF_6^- and O-P=O. The signal of O-P=O is potentially originated from $Na_xPF_yO_z$, a major decomposition product of $NaPF_6$ [19]. The XPS results indicate a major composition of organic and inorganic species (mainly including NaF and Na_2O) on the Na metal electrode surface. Detailed identification of the XPS peaks is provided in Supplementary Table S4.

To further investigate the distribution of chemical species within the SEI formed with $NaPF_6$-DME/DOL (2:8), XPS depth profiling was conducted (Figure 4c and Supplementary Figures S6 and S7). The signal for the carbon content decreases with increasing depth and completely vanishes at around 95 nm beneath the surface, revealing that the organic debris predominantly resides in the upper layer of the SEI. This also indicates that the thickness of the SEI is approximately 95 nm. Moreover, the NaF content increases with depth till reaching around 15 nm, suggesting a higher percentage of NaF existing in the inner region of the SEI (Figure 4c). The NaF signal was still detectable while the signal of the carbon content disappeared, suggesting that the $NaPF_6$ salt decomposed

before the decomposition of the solvent molecules. For comparison, XPS characterization was also performed on the surface of the Na metal electrode using 0.5 M $NaPF_6$-DEGDME/DOL (2:8) at −80 °C (Supplementary Figure S8). It shows that the surface of the SEI contains much fewer inorganic species, especially NaF, in contrast to the SEI formed in the 0.5 M $NaPF_6$-DME/DOL (2:8), indicating that NaF is critical in maintaining the integrity of the SEI over cycling. Meanwhile, the signal of the O-P=O, which is associated with the $NaPF_6$ decomposition, is weaker in the SEI formed in the DEGDME system compared with that formed in the DME system. The XPS analyses revealed that the DME/DOL electrolyte system, in contrast to the commonly utilized DEGDME/DOL system, can facilitate the decomposition of the $NaPF_6$ salt at low operating temperatures. This could be attributed to the weaker binding affinity of the DME molecule for Na^+ ions, resulting from its fewer oxygen coordination sites than DEGDME; this reduces the number of solvent molecules within the solvation shell and subsequently promotes the salt decomposition [29].

3.4. Electrochemical Performance of Full Na Metal Cells at Low Temperatures

To evaluate the full cell performance of the formulated electrolyte of 0.5 M $NaPF_6$-DME/DOL (2:8), Na metal batteries utilizing $Na_3V_2(PO_4)_3$ as the cathode and Na metal as the anode were assembled and tested under a series of low temperatures ranging from −10 °C down to −80 °C (Figure 5). The charge–discharge voltage profiles at 0.2C (1C = 110 mA g^{-1}) (Figure 5a) reveal that both voltage hysteresis and capacity utilization are highly sensitive to the operating temperature. At a relatively mild low temperature of −10 °C, the cell delivers a specific capacity of ~100 mA g^{-1}, representing 91% of its theoretical capacity. As the temperature decreases, the discharge voltage plateaus become progressively shorter and shift to lower potentials due to increased internal resistance and sluggish diffusion kinetics. Notably, the cell still maintains great capacity retention at −40 °C and −60 °C, delivering 72% and 45% of its theoretical capacity, respectively. The detectable performance even at −80 °C highlights the exceptional low-temperature resilience of this system. The rate performance of the cells at −40 °C is illustrated in Figure 5b, demonstrating the viability of Na metal cycling in a full cell configuration using the formulated electrolyte under cold conditions. As the discharge current increases up to 1C, the specific discharge capacity decreases, with approximately 79% of the capacity achieved at 0.2C retained at 1C. It is noted that this capacity loss is reversible, with full recovery observed upon reverting the current rate to 0.2C (Figure 5b). For long-term cycling performance at −40 °C (Figure 5c), the battery exhibits an initial discharge capacity of 86.3 mAh g^{-1}, and 86% of this capacity was maintained after 100 cycles, accompanied by an average CE of 99.1%. At −80 °C, the system maintains a high CE of 99.3% with 83% capacity retention after 100 cycles.

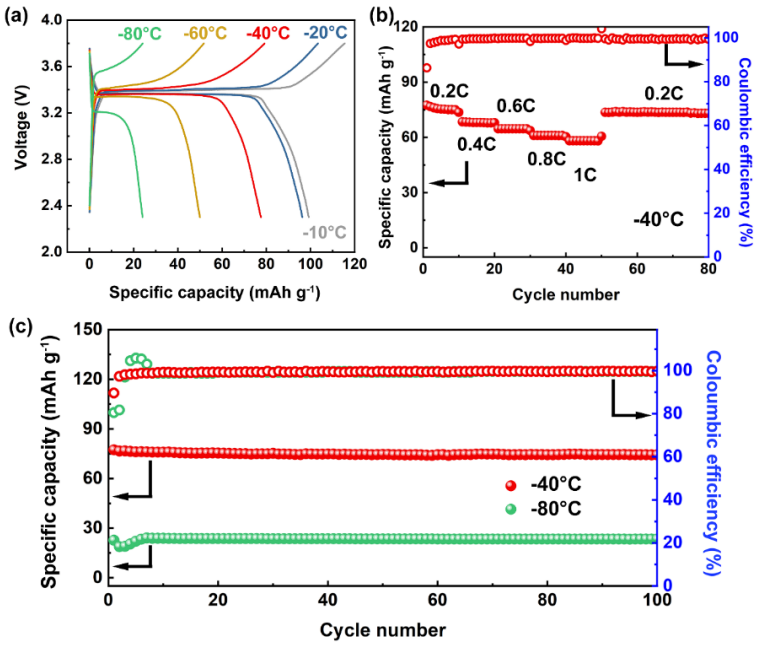

Figure 5. Electrochemical performance of Na || $Na_3V_2(PO_4)_3$ cells using the 0.5 M $NaPF_6$-DME/DOL (2:8) electrolyte at low temperatures. (**a**) Galvanostatic charge-discharge voltage profiles at 0.2C (1C=110 mA g^{-1}, based on the active material of $Na_3V_2(PO_4)_3$) from −10 °C to −80 °C; (**b**) Rate performance of cells up to 1C with voltage cutoffs of 2.3 and 3.8 V at −40 °C. c, Long-term galvanostatic cycling of cells at 0.2C at −40 °C and −80 °C.

4. Conclusions

In summary, we demonstrated that the monoglyme, DME, would be a better solvent option compared to the conventional DEGDME to formulate an electrolyte for Na metal electrode to work under extremely cold conditions. The optimized electrolyte formulation of 0.5 M $NaPF_6$-DME/DOL (2:8) enables stable cycling of Na metal down to −40 °C, exhibiting a low overpotential of 16 mV at 1 mA cm^{-2} with a capacity of 1 mAh cm^{-2} sustained for over 750 h. This low overpotential can be maintained even at a capacity of 3 mAh cm^{-2} (1 mA cm^{-2}), while a slightly elevated overpotential of 82 mV is observed at a higher current density of 3 mA cm^{-2} (1 mAh cm^{-2}). Furthermore, stable Na cycling at −80 °C is achieved with a small overpotential of 54 mV for over 1500 h at 0.5 mA cm^{-2}. The superior performance is attributed to a relatively modest increase in the electrolyte resistance, which rises by only 2.76 times from 0 °C to −80 °C. Additionally, the formation of a robust, NaF-rich SEI with a uniform morphology—characterized by SEM and XPS—contributes significantly to the observed electrochemical performance. As a proof of concept, Na metal batteries featuring $Na_3V_2(PO_4)_3$ as the cathode and Na metal as the anode exhibit stable cycling and high CE values during operation down to −80 °C.

Supplementary Materials: The following supporting information can be downloaded at: https://media.sciltp.com/articles/others/2603311457275841/MI-26030022-SM.pdf, Figure S1: Galvanostatic cycling of Na || Na symmetric cells at 0.2 mA cm^{-2} and 0.1 mAh cm^{-2} in an electrolyte composed of 0.5 M $NaPF_6$-DEGDME; Figure S2: Photos of 0.5 M $NaPF_6$-DME/THF (2:8) after storing at 20˚C and −80˚C for 24 hours (Salt precipitation was observed at the bottom of the vial at −80˚C); Figure S3: Temperature dependent ionic conductivity of 0.5 M $NaPF_6$-DME/THF (2:8), 0.5 M $NaPF_6$-DEGDME/DOL (2:8) and 0.5 M $NaPF_6$-DME/DOL (2:8); Figure S4: Galvanostatic cycling of Na || Na symmetric cells at 0.2 mA cm^{-2} and 0.1 mAh cm^{-2} at −80˚C; Figure S5: SEM image of Na metal surface after 50 cycles in 0.5 M $NaPF_6$-DEGDME/DOL (2:8) at −80˚C (Inset: corresponding cross-sectional SEM image); Figure S6: XPS depth profile analysis on the Na metal electrode after 50 cycles (symmetric Na || Na cells) at a current density of 0.5 mA cm^{-2} with a capacity of 0.5 mAh cm^{-2} in 0.5 M $NaPF_6$-DME/DOL (2:8) electrolyte at −80˚C; Figure S7: Contents of elements determined by ex-situ postmortem XPS depth profiling of the Na metal electrode (symmetric Na || Na cells) in 0.5 M $NaPF_6$-DME/DOL (2:8) after cycling at −80˚C; Figure S8: XPS profiles of C 1*s*, O 1*s*, F 1*s* and P 2*p* of the Na metal surface after 50 cycles (symmetric Na || Na cells) in 0.5 M $NaPF_6$-DEGDME/DOL (2:8) at 0.5 mA cm^{-2} and 0.5 mAh cm^{-2} at −80˚C; Table S1: Summary comparing performance of Na metal anodes (symmetric cells of Na/Na) cycling at current density ≥0.5 mA cm^{-2} and at low temperatures (≤40 °C). Table S2: Melting point, dielectric constant, and dynamic viscosity of DEGDME, DME, DOL and THF; Table S3: Summary of $NaPF_6$ salt dissolution in binary solvents at 0.5 M concentrations at −35°C; Table S4: Summary of identified XPS peaks. Reference [37] is cited in supplementary materials.

Author Contributions: C.W. and W.L.: conceived the idea; C.W.: conducted the electrolyte formulation and material characterization; C.W. and P.W.: performed electrochemical evaluation; C.W., P.W. and W.L.: cowrote the paper. All the authors discussed the results and commented on the manuscript

Funding: This work was funded by the U.S. Department of Energy, Office of Science, Basic Energy Sciences, under Award #DE-SC002624.

Data Availability Statement: Data are available from the corresponding author upon reasonable request.

Conflicts of Interest: The authors declare no conflict of interest.

Use of AI and AI-Assisted Technologies: No AI tools were used to prepare this paper.

References

1. Dunn, B.; Kamath, H.; Tarascon, J.-M. Electrical energy storage for the grid: A battery of choices. *Science* **2011**, *334*, 928–935.
2. Goodenough, J.; Park, K.-S. The Li-ion rechargeable battery: A perspective. *J. Am. Chem. Soc.* **2013**, *135*, 1167–1176.
3. Tarascon, J.-M.; Armand, M. Issues and challenges facing rechargeable lithium batteries. *Nature* **2001**, *414*, 359–367.
4. Zhang, S.; Xu, K.; Jow, T. The low temperature performance of Li-ion batteries. *J. Power Sources* **2003**, *115*, 137–140.
5. Xu, J.; Wang, X.; Yuan, N.; Ding, J.; Qin, S.; Razal, J.; Wang, X.; Ge, S.; Gogotsi, Y. Extending the low temperature operational limit of Li-ion battery to −80 °C. *Energy Storage Mater.* **2019**, *23*, 383–389.
6. Zhu, G. Materials insights into low-temperature performances of lithium-ion batteries. *J. Power Sources* **2015**, *300*, 29–40.
7. Yoon, S.; Cavallaro, K.; Park, B.; Yook, H.; Han, J.; McDowell, M. Controlling solvation and solid-electrolyte interphase formation to enhance lithium interfacial kinetics at low temperatures. *Adv. Funct. Mater.* **2023**, *38*, 2302778.
8. Gupta, A.; Manthiram, A. Designing advanced lithium-based batteries for low-temperature conditions. *Adv. Energy Mater.* **2020**, *10*, 2001972.
9. Dong, X.; Lin, Y.; Li, P.; Ma, Y.; Huang, J.; Bin, D.; Wang, Y.; Qi, Y.; Xia, Y. High-energy rechargeable metallic lithium battery at −70 °C enabled by a cosolvent electrolyte *Angew. Chem. Int. Ed.* **2019**, *58*, 5623–5627.
10. Thenuwara, A.; Shetty, P.; Kondekar, N.; Sandoval, S.; Cavallaro, K.; May, R.; Yang, C.; Marbella, L.; Qi, Y.; McDowell, M. Efficient low-temperature cycling of lithium metal anodes by tailoring the solid-electrolyte interphase *ACS Energy Lett.* **2020**, *5*, 2411−2420.

11. Holoubek, J.; Kim, K.; Yin, Y.; Wu, Z.; Liu, H.; Li, M.; Chen, A.; Gao, H.; Cai, G.; Pascal, T. et al. Electrolyte design implications of ion-pairing in low- temperature Li metal batteries. *Energy Environ. Sci.* **2022**, *15*, 1647–1658.
12. Tan, S.; Shadike, Z.; Cai, X.; Lin, R.; Kludze, A.; Borodin, O.; Lucht, B.; Wang, C.; Hu, E.; Xu, K.; et al. Review on low-temperature electrolytes for lithium-ion and lithium metal batteries *Electrochem. Energy Rev.* **2023**, *6*, 35.
13. Weng, S.; Zhang, X.; Yang, G.; Zhang, S.; Ma, B.; Liu, Q.; Liu, Y.; Peng, C.; Chen, H.; Yu, H. et al. Temperature-dependent interphase formation and Li+ transport in lithium metal batteries. *Nat Commun* **2023**, *14*, 4474.
14. Zhang, W.; Lu, Y.; Feng, Q.; Wang, H.; Cheng, G.; Liu, H.; Cao, Q.; Luo, Z.; Zhou, P.; Xia, Y. et al. Multifunctional electrolyte additive for high power lithium metal batteries at ultra-low temperatures *Nat Commun* **2025**, *16*, 3344.
15. Peng, Z.; Ding, K.; Lai, M.; Qiu, R.; Xiao, Y.; Shi, J.; Guan, X.; Cai, Y.; Xu, C.; Wang, F.; et al. Rational electrolyte solvent screening for high-energy lithium metal batteries at low temperatures *Nat Commun* **2026**, *17*, 590.
16. Holoubk, J.; Liu, H.; Wu, Z.; Yin, Y.; Xing, X.; Cai, G.; Yu, S.; Zhou, H.; Pascal, T.; Chen, Z.; et al. Tailoring electrolyte solvation for Li metal batteries cycled at ultra-low temperature *Nat Energy* **2021**, *6*, 303–313.
17. Wang, H.; Wang, C.; Matios, E.; Li, W. Critical role of ultrathin graphene films with tunable thickness in enabling highly stable sodium metal anodes. *Nano Lett*. **2017**, *17*, 6808–6815.
18. Wang, C.; Wang, H.; Matios, E.; Hu, X.; Li, W. A chemically engineered porous copper matrix with cylindrical core-shell skeleton as a stable host for metallic sodium anodes. *Adv. Funct. Mater.* **2018**, *28*, 1802282.
19. Wang, H.; Wang, C.; Matios, E.; Li, W. Facile stabilization of the sodium metal anode with additives: Unexpected key role of sodium polysulfide and adverse effect of sodium nitrate. *Angew. Chem. Int. Ed.* **2018**, *57*, 7734–7737.
20. Wang, H.; Matios, E.; Luo, J.; Li, W. Combining theories and experiments to understand the sodium nucleation behavior towards safe sodium metal batteries *Chem. Soc. Rev.* **2020**, *49*, 3783–3805.
21. Zhao, Y.; Adair, K.; Sun, X. Recent developments and insights into the understanding of Na metal anodes for Na-metal batteries *Energy Environ. Sci.* **2018**, *11*, 2673–2695.
22. Lee, B.; Paek, E.; Mitlin, D.; Lee, S. Sodium Metal Anodes: Emerging Solutions to Dendrite Growth *Chem. Rev.* **2019**, *119*, 8, 5416–5460.
23. Wang, C.; Thenuwara, A.C.; Luo, J.; Shetty, P.; McDowell, M.; Zhu, H.; Posada-Pérez, S.; Xiong, H.; Hautier, G.; Li, W. Extending the low-temperature operation of sodium metal batteries combining linear and cyclic ether-based electrolyte solutions. *Nat Commun.* **2022**, *13*, 4934.
24. Thenuwara, A.C.; Shetty, P.; Kondekar, N.; Wang, C.; Li, W.; McDowell, M. Enabling highly reversible sodium metal cycling across a wide temperature range with dual-salt electrolytes. *J. Mater. Chem. A* **2021**, *9*, 10992–11000.
25. Cheng, F.; Hu, J.; Zhang, W.; Guo, B.; Yu, P.; Sun, X.; Peng, J. Reviving ether-based electrolytes for sodium-ion batteries. *Energy Environ. Sci.* **2025**, *18*, 6874–6898.
26. Ge, B.; Deng, J.; Wang, Z.; Liang, Q.; Hu, L.; Ren, X.; Li, R.; Lin, Y.; Li, Y.; Wang, Q. et al. Aggregate-Dominated Dilute Electrolytes with Low-Temperature-Resistant Ion-Conducting Channels for Highly Reversible Na Plating/Stripping *Adv. Mater.* **2024**, *36*, 2408161.
27. Hu, X.; Matios, E.; Zhang, Y.; Wang, C.; Luo, J.; Li, W. Deeply cycled sodium metal anodes at low temperature and in lean electrolyte conditions. *Angew. Chem*. **2021**, *133*, 2–8.
28. Zhou, J.; Wang, Y.; Wang, J.; Liu, Y.; Li, Y.; Chen, L.; Ding, D.; Dong, S.; Zhu, Q.; Tang, M. et al. Low-temperature and high-rate sodium metal batteries enabled by electrolyte chemistry *Energy Storage Mater.* **2022**, *50*, 47–54.
29. Hu, L.; Deng, J.; Lin, Y.; Liang, Q.; Ge, B.; Weng, Q.; Bai, Y.; Li, Y.; Deng, Y.; Chen, G.; et al. Restructuring electrolyte solvation by a versatile diluent toward beyond 99.9% coulombic efficiency of sodium plating/stripping at ultralow temperatures. *Adv. Mater.* **2024**, *36*, 2312161.
30. Zhu, Q.; Yu, D.; Chen, J.; Cheng, L.; Tang, M.; Wang, Y.; Li, Y.; Yang, J.; Wang, H. A 110 Wh kg^{-1} Ah-level anode-free sodium battery at −40 °C *Joule* **2024**, *8*, 482–495.
31. Seh, Z.; Sun, J.; Sun, Y.; Cui, Y. A highly reversible room-temperature sodium metal anode. *ACS Cent. Sci.* **2015**, *1*, 449–455.
32. Cui, Y.; Ni, Y.; Wang, Y.; Wang, L.; Yang, W.; Wu, S.; Xie, W.; Zhang, K.; Yan, Z.; Chen, J. A temperature-adapted ultraweakly solvating electrolyte for cold-resistant sodium-ion batteries. *Adv. Energy Mater.* **2025**, *15*, 2405363.
33. Lutz, L.; Cortz, D.; Tang, M.; Salager, E.; Deschamps, M.; Grimaud, A.; Johson, L.; Bruce, P.; Tarascon, J. Role of electrolyte anions in the Na–O_2 battery: Implications for NaO_2 solvation and the stability of the sodium solid electrolyte interphase in glyme ethers. *Chem. Mater*. **2017**, *29*, 6066–6075.
34. Cresce, A.; Russell, S.; Borodin, O.; Allen, J.; Schroeder, M.; Dai, M.; Peng, J.; Gobet, M.; Greenbaum, S.; Rogers, R.; et al. Solvation behavior of carbonate-based electrolytes in sodium ion batteries. *Phys. Chem. Chem. Phys*. **2017**, *19*, 574–586.
35. Moulder, J.F. *Handbook of X-ray Photoelectron Spectroscopy: A Reference Book of Standard Spectra for Identification and Interpretation of XPS Data*; Physical Electronics Division, Perkin-Elmer Corporation Press: Eden Prairie, MI, USA, 1992.

36. Fiedler, C.; Luerssen, B.; Rohnke, M.; Sann, J.; Janek, J. XPS and SIMS analysis of solid electrolyte interphases on lithium formed by ether-based electrolytes. *J. Electrochem. Soc.* **2017**, *164*, A3742–A3749.
37. Aminabhavi, T.; Gopalakrishna, B. Density, viscosity, refractive index, and speed of sound in aqueous mixtures of N,N-dimethylformamide, dimethyl sulfoxide, N,N-dimethylacetamide, acetonitrile, ethylene glycol, diethylene glycol, 1,4-dioxane, tetrahydrofuran, 2-methoxyethanol, and 2-ethoxyethanol at 298.15 K. *J. Chem. Eng. Data* **1995**, *40*, 856–861.